Northumbria University
NEWCASTLE

Spectroscopy of Cu_2ZnSnS_4 nanoparticle inks and $Cu_2ZnSn(S,Se)_4$ solar cells

STEPHEN CAMPBELL

PhD

2020

Spectroscopy of Cu_2ZnSnS_4 nanoparticle inks and $Cu_2ZnSn(S,Se)_4$ solar cells

STEPHEN CAMPBELL

A thesis submitted in partial fulfilment of the requirements of the University of Northumbria at Newcastle for the degree of Doctor of Philosophy

Faculty of Engineering & Environment

May 2020

Abstract

Kesterite $Cu_2ZnSn(S,Se)_4$ (CZTSSe) is an encouraging candidate for thin film photovoltaic devices as it is a direct bandgap semiconductor with a high absorption coefficient. Its constituent elements are Earth-abundant which is advantageous for large scale commercialisation. Despite being adapted from $Cu(In,Ga)(S,Se)_2$ (CIGS) technology, CZTSSe PV performance is lacking in comparison to CIGS. To identify factors affecting the performance of CZTSSe PV, a comprehensive study using a number of characterisation techniques, such as photoluminescence spectroscopy, was performed on materials and interfaces within CZTSSe solar cells which were fabricated from Cu_2ZnSnS_4 nanoparticle inks by injection of metallic precursors into a hot surfactant.

To eliminate the carbon-rich CZTSSe fine grain layer usually found at the Mo back contact, the long carbon chain ligand oleylamine used in CZTS nanoparticle synthesis was replaced with low carbon content formamide. The substitution of the solvent removed the fine grain CZTSSe layer but no working device could be fabricated due to the porosity of the absorber film. Working solar cells were made by employing a dual layer of oleylamine/formamide CZTSSe absorbers, which reduced the height of the back contact barrier to $\sim$16 meV compared to the standard devices and improved device parameters.

The effects of precursor chemical quality on optoelectronic properties of CZTSSe absorber films were investigated. Sn loss was observed in films fabricated using lower grade chemical precursors. Deep level transient spectroscopy revealed the presence of an additional defect level in those films, suggesting the defect is Sn-related. Using higher grade precursor chemicals produced higher quality CZTSSe absorbers. However, improvement in film quality did not translate into increased performance in those devices, implying an issue other than defects in the bulk of the CZTSSe absorbers inhibits device performance.

In_2S_3 was used to replace buffer CdS commonly utilized in CZTSSe device structure. Photoemission spectroscopy demonstrated In_2S_3 formed a favourable Type I band alignment at the buffer/absorber interface, leading to increased open circuit voltage in the In_2S_3-based devices. Mott-Schottky analysis indicated increased defects at the buffer/absorber interface when using In_2S_3. Optimising the In_2S_3 layer and suppressing interface defects, using a barrier layer or passivating the absorber surface, could lead to the In_2S_3-based CZTSSe device outperforming devices using CdS due to better band alignment and increased current collection.

Contents

List of Figures

List of Tables

Acknowledgements

This has been quite a journey over the last six years from the point where I left a 24 year career in the police service and embarked on a degree in Physics at Northumbria University. Being out of academia for such a long time did present challenges along the way but I overcame them and I graduated three years ago. A PhD opportunity at Northumbria University presented itself under the supervision of Dr. Guillaume Zoppi. Wind the clock forward another three years and here I am, completing my thesis.

First and foremost, I wish to thank Guillaume Zoppi for his continuous support, encouragement and unwavering confidence in my abilities which allowed me the freedom to explore my ideas throughout the entire project. He was a constant source for inspiration.

I would also like to thank my second supervisor Dr. Neil Beattie whose enthusiasm for the field of Physics was what initially spurred me to enrol on the Physics degree course six years ago. His enthusiasm still has no bounds. He instilled in me a robust approach to scientific research methods and critical thinking. Dr. Vincent Barrioz was also an invaluable source of information, the depth of his knowledge regarding photovoltaics is unsurpassed.

Special thanks goes to Dr. Yongtao Qu. He has been there alongside me throughout the entirety of my PhD, providing me with support and assistance in all aspects of my research. His patience is boundless! My gratitude goes to the members of our research group, Dr. Xinya Xu, Dr. Stephen Nwankwo, Dr. Zara Ishwein and Nik Ahmad, who have made the last three years such an enjoyable experience. Thanks to you the time has flown by.

Finally, I'd like to thank my parents who have finally seen me realise my true potential, my children Abbie and Emily for 'just being there' and my long-suffering partner Angela, who has barely seen me over the last four months whilst I have been engrossed in completing my thesis. I thank you all.

Work done in conjunction with others

All of the work presented in this thesis was done by the author, with the following exceptions:

1. All CZTSSe solar cells used for this study were fabricated by Dr. Yongtao Qu, Department of Mathematics, Physics and Electrical Engineering, Northumbria University, UK.
2. Raman spectroscopy measurements presented in Chapters 4 and 6 were performed by Dr. Kate Nicholson, Department of Applied Sciences, Northumbria University, UK.
3. Additional time-resolved photoluminescence measurements in Chapter 5 were performed by Dr. Delphine Lagarde, Institut National des Sciences Appliquées, Toulouse, France.
4. Glow discharge optical emission spectroscopy measurements in Chapter 4 were performed by Dr. Patrick Chapon, Horiba France SAS, Palaiseau, France.
5. Inductively-coupled plasma mass spectroscopy measurements in Chapter 5 were performed by Dr. Chris Ottley, Department of Earth Sciences, Durham University, UK.
6. Deep level transient spectroscopy measurements in Chapter 5 were performed by Dr. Jon Major, Stephenson Institute for Renewable Energy, University of Liverpool, UK.
7. Photoemission spectroscopy measurements in Chapter 6 were performed by James Gibbon and Holly Edwards, Stephenson Institute for Renewable Energy, University of Liverpool, UK.

Declaration

I declare that the work contained in this thesis has not been submitted for any other award and that it is all my own work. I also confirm that this work fully acknowledges opinions, ideas and contributions from the work of others.

Any ethical clearance for the research presented in this thesis has been approved. Approval has been sought and granted by the University Ethics Committee on *31/01/2017*.

I declare that the Word Count of this thesis is 38,450 words.

Name: Stephen Campbell

Signature:

Date: May 7, 2020

List of publications

Papers

- **Stephen Campbell**, Yongtao Qu, James Gibbon, Holly J. Edwards, Vin Dhanak, Vincent Barrioz, Neil S. Beattie, Guillaume Zoppi. *Defect limitations and near infrared carrier extraction recovery in $Cu_2ZnSn(S,Se)_4$ solar cells utilising an In_2S_3 buffer layer.* Physica Status Solidi Rapid Research Letters (under review), 2020.

- **Stephen Campbell**, Yongtao Qu, Jonathan Major, Delphine Lagarde, Christophe Labbé, Pietro Maiello, Vincent Barrioz, Neil S. Beattie, Guillaume Zoppi. *Direct evidence of causality between chemical purity and band-edge potential fluctuations in nanoparticle ink-based $Cu_2ZnSn(S,Se)_4$ solar cells.* J. Phys. D:Appl. Phys. 135102, 52, 2019.

- **Stephen Campbell**, Yongtao Qu, Leon Bowen, Patrick Chapon, Vincent Barrioz, Neil S. Beattie, Guillaume Zoppi. *Influence of OLA and FA ligands on the optical and electronic properties of $Cu_2ZnSn(S,Se)_4$ thin films and solar cells prepared from nanoparticle inks.* Solar Energy. 101-109, 175, 2018.

- Yongtao Qu, See Wee Chee, Martial Duchamp, **Stephen Campbell**, Guillaume Zoppi, Vincent Barrioz, Yvelin Giret, Thomas J. Penfold, Apoorva Chaturvedi, Utkur Mirsaidov and Neil S. Beattie. *Real-Time Electron Nanoscopy of Photovoltaic Absorber Formation from Kesterite Nanoparticles.* ACS Applied Energy Materials, Publication Date (Web): 12 Dec 2019.

- Xinya Xu, Yongtao Qu, **Stephen Campbell**, Mathieu Le Garrec, Bethan Ford, Vincent Barrioz, Guillaume Zoppi, Neil S. Beattie. *Solution processing route to Na incorporation in CZTSSe nanoparticle ink solar cells on foil substrate.* Journal of Materials Science:Materials in Electronics, 7883-7889, 30(8), 2019.

- G. Kartopu, O. Oklobia, D. Turkay, D.R. Diercks, B.P. Gormand, V. Barrioz, **Stephen Campbell**, J.D. Major, M.K. Al Turkestani, S. Yerci, T.M. Barnes, N.S. Beattie, G. Zoppi, S. Jones and S.J.C. Irvine. *Study of thin film poly-crystalline CdTe solar cells presenting high acceptor concentrations achieved by in-situ arsenic doping.* Solar Energy Materials and Solar Cells, 259-267, 194, 2019.

- Stephen N. Nwankwo, **Stephen Campbell**, Ramakrishna K. T. Reddy, Neil S. Beattie, Vincent Barrioz and Guillaume Zoppi. *Temperature controlled properties of sub-micron thin SnS films.* Semicond. Sci. Technol. 065002, 33, 2018.

Conferences & Meetings

Stephen Campbell, Yongtao Qu, James Gibbon, Holly J. Edwards, Vin Dhanak, Vincent Barrioz, Neil S. Beattie, Guillaume Zoppi. *Defect limitations and near infrared carrier extraction recovery in $Cu_2ZnSn(S,Se)_4$ solar cells utilising an In_2S_3 buffer layer.* NECEM International Conference on Energy Materials and Interfaces 2019, Newcastle-upon-Tyne, UK. Poster presentation.

Stephen Campbell, Yongtao Qu, James Gibbon, Holly J. Edwards, Vin Dhanak, Vincent Barrioz, Neil S. Beattie, Guillaume Zoppi. *Defect limitations and near infrared carrier extraction recovery in $Cu_2ZnSn(S,Se)_4$ solar cells utilising an In_2S_3 buffer layer.* 10^{th} International Conference on Materials for Advanced Technologies 2019, Marina Bay Sands, Singapore. Oral presentation.

Stephen Campbell, Yongtao Qu, Jonathan Major, Delphine Lagarde, Christophe Labbé, Pietro Maiello, Vincent Barrioz, Neil S. Beattie, Guillaume Zoppi. *Spectroscopy of nanoparticle inks-based $Cu_2ZnSn(S,Se)_4$ (CZTSSe) solar cells.* European Materials Research Society 2018 Spring Meeting, Strasbourg Conference Centre, France. Poster presentation.

Stephen Campbell, Yongtao Qu, Jonathan Major, Delphine Lagarde, Christophe Labbé, Pietro Maiello, Vincent Barrioz, Neil S. Beattie, Guillaume Zoppi. *Spectroscopy of nanoparticle inks-based $Cu_2ZnSn(S,Se)_4$ (CZTSSe) solar cells.* North East Centre for Energy Materials Launch Event 2018, Newcastle-upon-Tyne, UK. Poster presentation.

Stephen Campbell, Yongtao Qu, Xinya Xu, Neil S. Beattie and Guillaume Zoppi. *Low temperature photoluminescence spectroscopy and IV measurements for analysis of $Cu_2ZnSn(S,Se)_4$ absorbers and solar cells.* North East Energy Materials Symposium 2017, Durham University, Durham, UK. Poster presentation.

Awards

Royal Society of Chemistry **Chemical Science Poster Prize**, NECEM International Conference on Energy Materials and Interfaces 2019. **Stephen Campbell**, Yongtao Qu, James Gibbon, Holly J. Edwards, Vin Dhanak, Vincent Barrioz, Neil S. Beattie, Guillaume Zoppi. *Defect limitations and near infrared carrier extraction recovery in $Cu_2ZnSn(S,Se)_4$ solar cells utilising an In_2S_3 buffer layer.*

Chapter 1

Introduction

Global warming induced by human activity has been identified as a major threat causing irrevocable change to the Earth's climate. The potentially catastrophic rise in global temperature is fuelled in part by the emission of 'greenhouse' gases such as CO_2, methane and nitrous oxide into the atmosphere by the burning of fossil fuels. The original Paris Agreement 2015 formulated by the United Nations Framework Convention on Climate Change (UNFCCC) outlined the goal of limiting the rise in global temperatures to 2 °C by the end of the 21^{st} Century [1]. To achieve this, emphasis needs to shift from fossil fuels to more sustainable, environmentally friendly energy sources. Photovoltaics (PV) harnessing the power of the sun are an ideal replacement energy production technology. The ultimate goal in PV is to fabricate solar cells that are efficient, low-cost, stable, non-toxic and flexible. Thin-film PV devices offer a viable alternative to market-dominant polycrystalline silicon PV and have the potential to be deposited on flexible substrates and incorporated into construction materials, so-called building-integrated photovoltaics (BIPV), eliminating the need for dedicated large area spaces required for silicon-based solar farms.

1.1 Thin Film Photovoltaics

As the name suggests, thin film photovoltaic (TFPV) technologies incorporate thin layers of semiconducting materials (typically $\sim$1 μm) with direct energy bandgaps and very high light absorption coefficients (between 10^4 – 10^5 cm^{-1}). Due to silicon having an indirect bandgap, Si-based PV require a thickness of between 200 to 500 μm to achieve similar light absorption. Thinner absorbers can be deposited on lightweight and flexible substrates such as polyimide and steel or

Mo foils making them ideally suited for new distributed applications requiring innovative and sustainable power sources. Unlike Si, most thin film semiconducting materials are intrinsically doped meaning they do not require further processing steps to extrinsically introduce an excess of charge carriers to give the materials *n*- or *p*-type conductivity. PV incorporating mono- and polycrystalline Si have been under development for over five decades and have achieved power conversion efficiencies (PCE) of 26.7 and 22.3%, respectively (for a single junction terrestrial cell measured under the standard solar irradiance air mass 1.5 spectrum (1000 W/m^2) at 25 °C) [2, 3]. Remarkably, TFPV technologies have exceeded the PCE of crystalline Si-based PV despite their shorter development period. A number of TFPV technologies have been developed based on inorganic materials such as III-V (GaAs, InP) and chalcogenide (CdTe, Cu(In,Ga)Se_2 (CIGS), $Cu_2ZnSn(S,Se)_4$ (CZTSSe)) compounds, hybrid organic-inorganic compounds (perovskite) and fully organic compounds (dye-sensitised). Figure 1.1.1 shows current certified record efficiencies of both Si- and thin film-based lab sized PV cells (area $\geq$1 cm^2), taken from the Solar Cell Efficiency Tables (Version 53) [4]. An important metric in the assessment of PV device performance is the Shockley-Queisser (SQ) limit on device parameters such as efficiency η, open circuit voltage V_{oc} and short circuit current density J_{sc} [5]. The SQ limit is based on maximum theoretical efficiency of a single *p-n* junction solar cell using 6000 K black-body emission as an approximation to the solar spectrum and where the only loss mechanism is radiative recombination in the solar cell. A maximum PCE of 30% was determined for a PV device containing a semiconducting absorber with a bandgap of 1.1 eV.

The dependence of PV device efficiency upon bandgap of the device absorber material is also shown in Figure 1.1.1. Most PV technologies show a considerable efficiency deficit in comparison to the theoretical SQ limit, indicating there is still further scope for improvement. In the case of TFPV technologies, the better performing devices are all composed of rare elements like indium, gallium or tellurium and/or toxic elements such as cadmium, arsenic or lead (in perovskites). Recently the European Commission classified these scarce elements as critical raw materials (CRM) which has ramifications on the cost and viability of using these materials in industrial scale production of TFPV [6]. The requirement for TFPV technologies incorporating low-toxicity, earth-abundant CRM-free materials led to the development of kesterite-based PV (Cu_2ZnSnS_4 (CZTS), $Cu_2ZnSnSe_4$ (CZTSe) and corresponding solid solution $Cu_2ZnSn(S,Se)_4$ (CZTSSe)), building on the well-established and closely related chalcopyrite CIGS platform. Research into CIGS-based

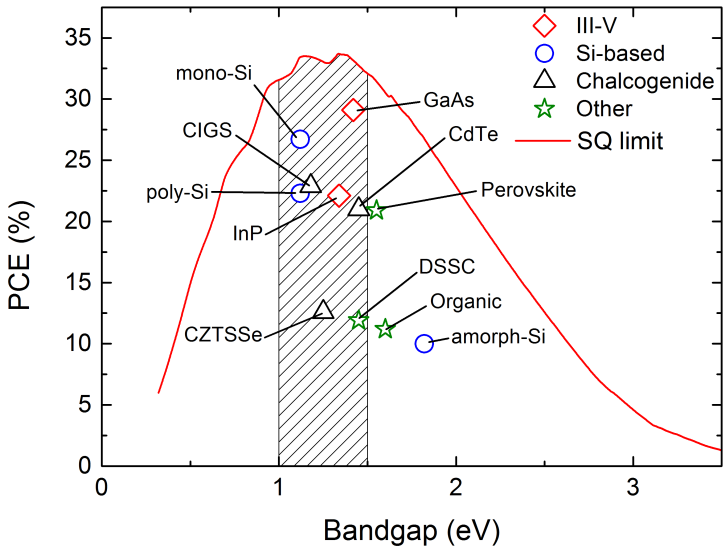

Figure 1.1.1: Record efficiencies of Si (monocrystalline, polycrystalline and amorphous), thin film III-V (GaAs and InP), chalcogenide (CdTe, CIGS and CZTSSe) and other thin film (perovskite, dye-sensitised solar cell (DSSC) and organic) based laboratory PV devices as a function of the band gap energy are shown, based on record efficiency table [4] and SQ limit [5] (Shockley Queisser detailed balance limit for a solar cell operated at 298.15 K under global AM1.5 spectral irradiance in accordance with standard solar test conditions). The crosshatched region shows the range of bandgap values for $Cu_2ZnSn(S_xSe_{1-x})_4$ where E_g = 1.0 eV when x = 0 and E_g = 1.5 eV when x = 1.

PV began in the 1970's with the first working $Cu(In,Ga)(S,Se)_2$ (CIGSSe) device produced in 1977 [7]. The technology has matured over the past four decades with the implementation of varying efficiency-enhancing strategies culminating in a current record PCE of 22.9% [8]. Interest in kesterite-based PV started during the 1990's as the technology was seen as a viable alternative to CIGS due to the similarity in crystal structure and optoelectronic properties.

1.2 Kesterite-based Photovoltaics

Kesterite and chalcopyrite materials belong to the chalcogenide family, which are a group of compounds containing one or more chalcogen elemnts (such as S, Se or Te) as a major constituent. Their crystal structure is derived from the face centred cubic lattice of zincblende. The kesterite CZTS cell differs from that of CIGSe by the substitution of half of the In/Ga sites with Zn and the other half with Sn, see Figure 1.2.1. Crystal properties of kesterite CZTS are shown in Table 1.2.1. Replacing the rare indium with readily available Zn and Sn does not alter the optical

and electronic properties of the semiconductor. Typical optoelectronic properties of CIGSe- and CZTS-based absorbers are compared in Table 1.2.2.

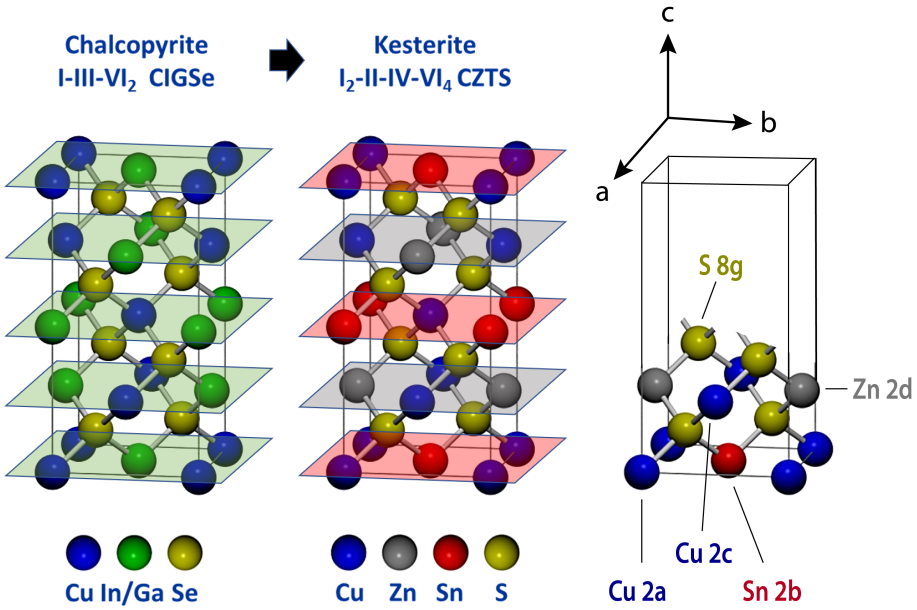

Figure 1.2.1: Conversion from chalcopyrite to kesterite cell structure by replacement of In/Ga sites with Zn and Sn together with Wyckoff labels for the constituent elements [9].

Table 1.2.1: Description of kesterite CZTS crystal structure [9].

Space group	Wyckoff label	Atomic position	Element
	2a	(0, 0, 0)	Cu
$I\bar{4}$	2b	(½, ½, 0)	Sn
No. 82	2c	(0, ½, ¼)	Cu
	2d	(0, ½, ¾)	Zn
	8g	(x, y, z)	S

Given the close similarities in the optical and electronic properties of kesterite and chalcopyrite materials, the most pertinent question to ask is - why are kesterite device efficiencies significany lower than chalcopyrite? In order to understand the issue, Giraldo *et al.* considered the relation between the bandgap of CIGSSe and CZTSSe absorbers and device efficiency [10]. In the case of narrow and wide bandgap absorbers (∼1.0 and ∼1.5 eV) the difference in device efficiencies was only 1-3%. However, for absorbers with an internediate bandgap of ∼1.2 eV, the difference was significant with efficiency of champion CIGSSe solar cells almost 10% higher than corresponding champion CZTSSe cells.

Table 1.2.2: A comparison of the optoelectronic properties of $Cu(In_{1-x}Ga_x)Se_2$ and $Cu_2ZnSn(S_xSe_{1-x})_4$ with bandgap, E_g, absorption coefficient, α, majority carrier type and concentration.

Absorber	E_g (eV)		α (cm^{-1})	Conductivity	Carrier density (10^{16} cm^{-3})
$Cu(In_{1-x}Ga_x)Se_2$	1.0 - 1.7 [11, 12]	for x = 0 to 1	10^4 - 10^5 [13]	*p*-type	2 [14]
$Cu_2ZnSn(S_xSe_{1-x})_4$	1.0 - 1.5 [15, 16]	for x = 0 to 1	10^4 - 10^5 [17]	*p*-type	3 [18]

One reason for the disparity in efficiency is the large open circuit voltage deficit, V_{oc-def} observed in kesterite devices. V_{oc-def} is the difference between the maximum V_{oc} achievable for a given absorber bandgap (SQ limit [5]) and the measured V_{oc} of the device. The V_{oc-def} for CIGSSe and CZTSSe devices as a function of absorber bandgap E_g is presented in Figure 1.2.2 [19]. Apparent is the monotonic increase in V_{oc-def} of kesterite devices and the deficit is greater than that observed in chalcopyrites at intermediate bandgaps. Possible explanations for this issue are explored in more detail in Chapter 2.

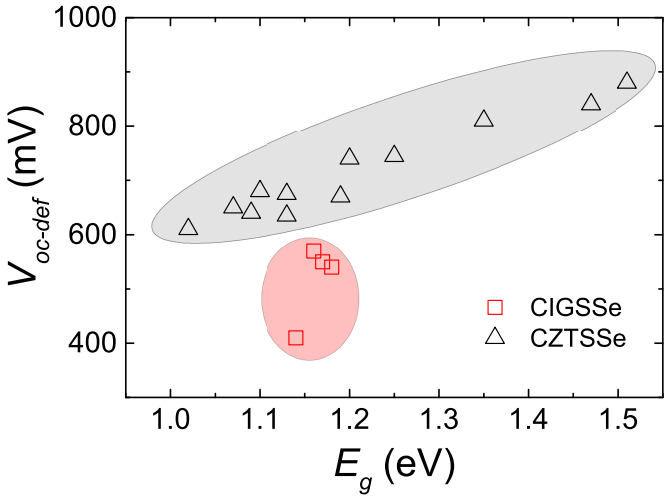

Figure 1.2.2: V_{oc} deficit in CIGSSe and CZTSSe as a function of bandgap, E_g. Adapted from [19].

To address the deficit in V_{oc} in kesterite one must look to relevant technological solutions discovered during the evolution of CIGSSe device efficiency over time. Initially, the typical substrate architecture of CZTSSe-based solar cells was copied from CIGSSe. Here, Mo (usually on a sodalime glass (SLG) substrate) forms the ohmic metal back contact with the absorber. CdS buffer is deposited on top of the absorber to produce a *pn*-junction followed by succesive window

(intrinsic ZnO) and transparent conducting oxide (TCO, such as indium tin oxide (ITO)) layers and finished with a Ni/Al metallic front contact, see Figure 1.2.3. Typical thickness of the stacked layers are: Mo, 500 - 1000 nm; CZTSSe, ∼1000 nm; CdS, ∼60 nm; *i*-ZnO, 50 - 100 nm; ITO, ∼250 nm.

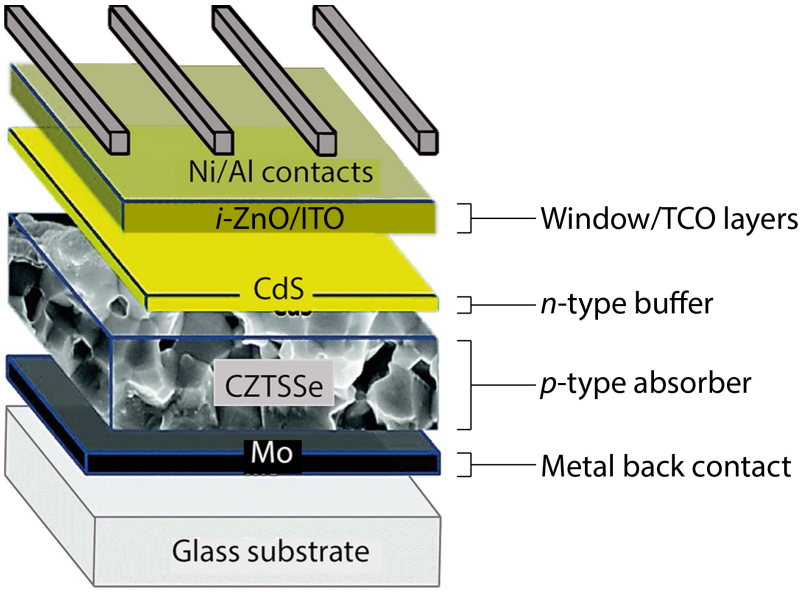

Figure 1.2.3: Typical CZTSSe solar cell structure.

Three key findings during the development of chalcopyrite-based solar cells have led to significant improvement in device efficiency: i) the incorporation of Na [20], ii) the post deposition treatment with alkali metals [21–23] and iii) alloying with Ga [24] These strategies have been adopted by the kesterite research community with some promising results. The introduction of Na into the kesterite absorber via doping or diffusion from SLG has a number of beneficial effects. In particular, enhanced grain growth, passivation of interfaces and grain boundaries together with increased carrier concentration have been demonstrated [25, 26]. By adding a NaF layer to their solution processed CZTSSe precursor films, Sutter-Fella *et al.* demonstrated an increase in device efficiency from 3.39% to 6.04%. Generally, the increase in efficiency has been attributed to increased grain size [25] and segragation of Na at grain boundaries and absorber surface [27], both of which lead to improvements in optoelectronic properties of the kesterite absorber.

Other alkali metals have been used to treat kesterite films during absorber fabrication and post-deposition. Li is perhaps the easiest alkali to incorporate into the lattice of kesterite phase due to the similar ionic radii (Li^+, 0.73 Å and Cu^+, 0.74 Å). Xin *et al.* found Li incorporation significantly increased the conductivity of the doped CZTSSe film producing an 11.8% efficient device

and Haass *et al.* discovered that using a 'high' Li concentration of 0.75 at% yielded a CZTSSe solar cell with 12.3% efficiency [28]. The mechanism on how Li doping/alloying improves device performance is unclear however some conclusions have been drawn: i) alloying CZTSSe with Li increases the bandgap of the absorber (bandgap increase of 0.15 eV in $(Cu_{1-x}Li_x)_2ZnSnS_4$ when x increases from 0 to 0.5) [29, 30] and ii) Li doping/alloying improves optoelectronic properties (increased fill factor and V_{oc}, reduction in tetragonal crystal distortion) regardless of the doping concentration [28]. Bulk potassium treatment of kesterite solar cells also leads to enhanced grain growth and improved device performance [31]. The addition of high concentrations of K in the CZTSSe absorber was observed to reduce Sn loss, helping to suppress the formation of detrimental Sn-related defects. Due to their large ionic radii, rubidium and caesium are less likely to be incorporated into the kesterite lattice and tend to be segragated at grain boundaries. Despite this, Rb- and Cs-treated kesterite devices still achieved efficiencies of 8.8% and 9.1%, respectively [28]. A comprehensive review of alkali-treated kesterite solar cells ranked their use in order of highest efficiencies as Li $>$ Na $>$ K $>$ Rb $>$ Cs [32].

Kesterite can also be alloyed with a number of isoelectronic elements from the same groups as Cu, Zn and Sn, the most common being Ge, Cd and Ag. The abundance of Ge in the Earth's crust makes it a viable substitution for Sn. Alloying with Ge helps to reduce Sn-related defects and allows the bandgap of the kesterite absorber to be tuned, dependent on the Ge/(Ge + Sn) ratio [33, 34]. Enhanced grain growth was also observed with Ge incorporation [35]. Kim *et al.* demonstrated a $Cu_2Zn(Sn_{1-x}Ge_x)Se_4$ (CZTGSe) device with 12.3% and attributed the performance to a greatly improved V_{oc} deficit (reducing from 0.647 eV for CZTSSe reference to 0.583 eV for CZTGSe) due to reduced band tailing [36].

Cadmium alloying of kesterite (CZCTS) has been suggested as a means to reduce the concentrations of Cu_{Zn} and Zn_{Cu} antisite defects responsible for Cu-Zn disorder [37]. Cd is expected to substitute Zn in the kesterite lattice and as the ionic radius is greater than that of Cu and Zn (0.78 Å for Cd compared to 0.60 Å for Cu and Zn), Cd incorporation increases the formation energy of disorder-inducing defect clusters from 0.22 eV for [Cu_{Zn}+Zn_{Cu}] to $\sim$0.32 eV, $\sim$0.62 eV and $\sim$1.36 eV for [Cd_{Cu}+Zn_{Cu}], [Cd_{Zn}+Zn_{Cu}+Cu_{Zn}] and [Cd_{Cu}+Zn_{Cu}+Cu_{Zn}], respectively. As a consequence, the Cu-Zn disorder and associated band tailing is reduced [38]. The substitution of Zn with Cd also improved grain size [39]. Here, Sun *et al.* found higher hole concentrations in the CZCTS-based device than the CZTSSe reference while the dominant recombination mecha-

nism changed from buffer/absorber interface in the reference device to bulk related. As a result, efficiency increased from 8.5% to 11.2% in the CZCTS device.

Silver incorporation into kesterite-based solar cells to improve performance has been extensively researched. In this instance, Ag partially substitutes Cu to form alloy $(Cu,Ag)_2ZnSn(S,Se)_4$ (CAZTSSe). Ag has a similar effect as the Cd substitution of Zn, again due to the larger Ag ionic radius and serves to reduce the concentration of Cu_{Zn} defects [40, 41]. The use of Ag is preferable to Cd due the toxic nature of Cd. Gershon *et al.* observed a 50% reduction in the Urbach tail of their Ag-substituted CZTSe solar cell with a device efficiency of 10.2% [42]. A summary of relevant elements in the doping/alloying kesterite thin films is shown in Figure 1.2.4.

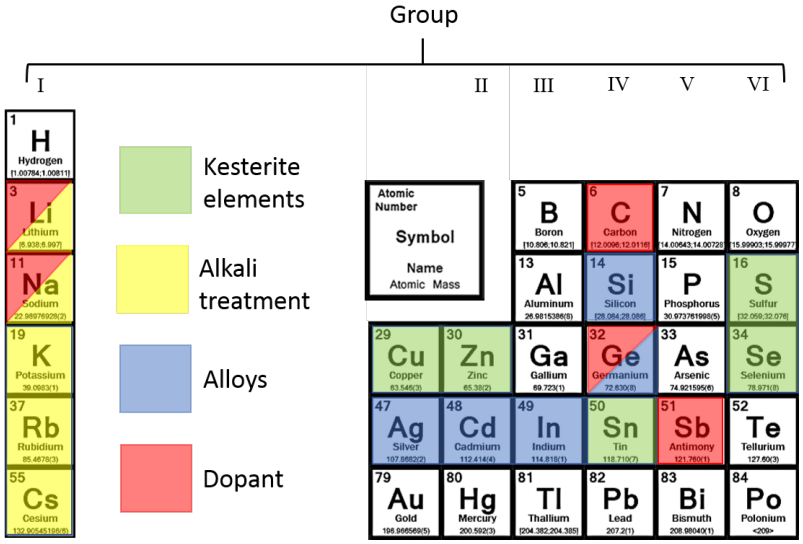

Figure 1.2.4: A summary of the relevant elements used to dope and alloy kesterite absorbers and to treat the absorber post-deposition. All strategies have shown demonstrable improvements in efficiency of kesterite-based PV.

There are a number of techniques for growing kesterite absorber thin films which fall into two categories, vacuum and non-vacuum processes. Vacuum methods include thermal evaporation of single compound kesterite, co-evaporation and co-sputtering of kesterite precursors. Some examples of non-vacuum methods are electrochemical deposition, hot-injection for kesterite nanoparticle synthesis and hydrazine-based precursor solution. All approaches have been developed over the last two decades with the hydrazine solution method for producing CZTSSe achieving the highest efficiency of 12.6% [43]. Table 1.2.3 lists optoelectronic properties of highest efficiency devices fabricated by vacuum and non-vacuum methods. In this study, the focus will be on CZTSSe PV fabricated from CZTS nanoparticle inks using the hot injection method [44].

Table 1.2.3: A comparison of the optoelectronic properties of highest efficiency CZTSSe solar cells fabricated using different growth techniques where V_{oc}, J_{sc} FF, η, J_0, E_g and V_{oc-def} are open circuit voltage, short circuit current density, fill factor, efficiency, reverse saturation current density, bandgap and open circuit voltage deficit, respectively.

Material	V_{oc} (mV)	J_{sc} (mA/cm^2)	FF (%)	η (%)	J_0 (mA/cm^2)	E_g (eV)	V_{oc-def} (mV)
CIGSSe[a] [45]	711	41.4	77.5	22.8	7x10^{-8}	1.09	420
CZTSSe[b] [43]	513	35.2	69.8	12.6	7x10^{-5}	1.13	617
CZTSSe[c] [46]	521	35.0	67.2	12.3	-	1.08	576
CZTSSe[a] [36]	527	32.2	72.7	12.3	4x10^{-5}	1.11	583
CZTSSe[d] [47]	583	33.6	55.9	11.0	-	1.20	548
CZTSSe[e] [48]	400	35.2	66.2	9.3	-	1.09	-

[a]Co-evaporation, [b]hydrazine solution, [c]DC-sputtering, [d]dimethylformamide solution, [e]nanoparticle ink

1.3 Objective of this investigation

The objective of this investigation was the methodical analysis of the CZTSSe absorber and its associated interfaces in nanoparticle inks-based CZTSSe solar cells. By using a number of spectroscopic techniques, the aim was to identify key areas within the device structure which were adversely affecting performance and provide possible solutions to overcome the issues. The following areas were investigated:

(i) Absorber-back contact interface - using a different capping ligand (formamide) as an alternative to oleylamine (typically used during CZTS nanoparticle synthesis) in order to remove the carbon-rich fine grain CZTSSe layer formed at the Mo/CZTSSe interface following selenisation of the absorber. This carbon-rich layer has been cited as potentially causing a current-blocking barrier at the absorber-metal contact junction [49, 50].

(ii) Absorber bulk - using CZTSSe absorbers fabricated from low and high grade purity chemical precursors in the CZTS nanoparticle phase of device fabrication in order to study their effect on the types of defect and their concentrations within the bulk of the absorber and subsequent impact on device performance.

(iii) Absorber-buffer interface - using an alternative *n*-type buffer material (such as In_2S_3) to the standard CdS in order to study the effect on energy band alignment at the buffer/CZTSSe absorber interface and the impact of the alternate buffer on V_{oc} in the comparative devices.

Chapter 2

Loss mechanisms in kesterite PV

2.1 Overview

Due to the limitations of other TFPV technologies such as GaAs, CdTe and CIGS, kesterite PV is being developed as a viable alternative in providing electricity on a terrawatt scale [51]. GaAs and CdTe have toxicity issues concerning the use of As and Cd and the scarcity of In is prohibitive in the large-scale commercialisation of CIGS. Despite intensive research into kesterite over the past two decades, improvement in device efficiency has stagnated. Therefore, it is important to understand the limiting factors which are thwarting the technology from attaining its true potential. The most cited reason for lower performance in kesterite-based PV is the large V_{oc} deficit compared to other TFPV technologies [52–55]. To address this issue, it is necessary to understand the fundamental loss mechanisms in kesterite PV. The device structure of a standard kesterite-based solar cell comprises of several layers (as shown in Figure 1.2.3) whose interfaces, if not optimised, can inhibit the efficient extraction of photogenerated carriers. A schematic energy band diagram of the interfaces in a typical CZTSSe thin film solar cell together with possible loss mechanisms and carrier recombination pathways is shown in Figure 2.1.1.

2.2 Absorber-back contact interface

Molybdenum is used ubiquitously as the metallic back contact in kesterite TFPV device architecture. The device structure was inherited from the more mature thin film CIGS technology from which kesterites were developed. CIGS device performance is enhanced by using a Mo back

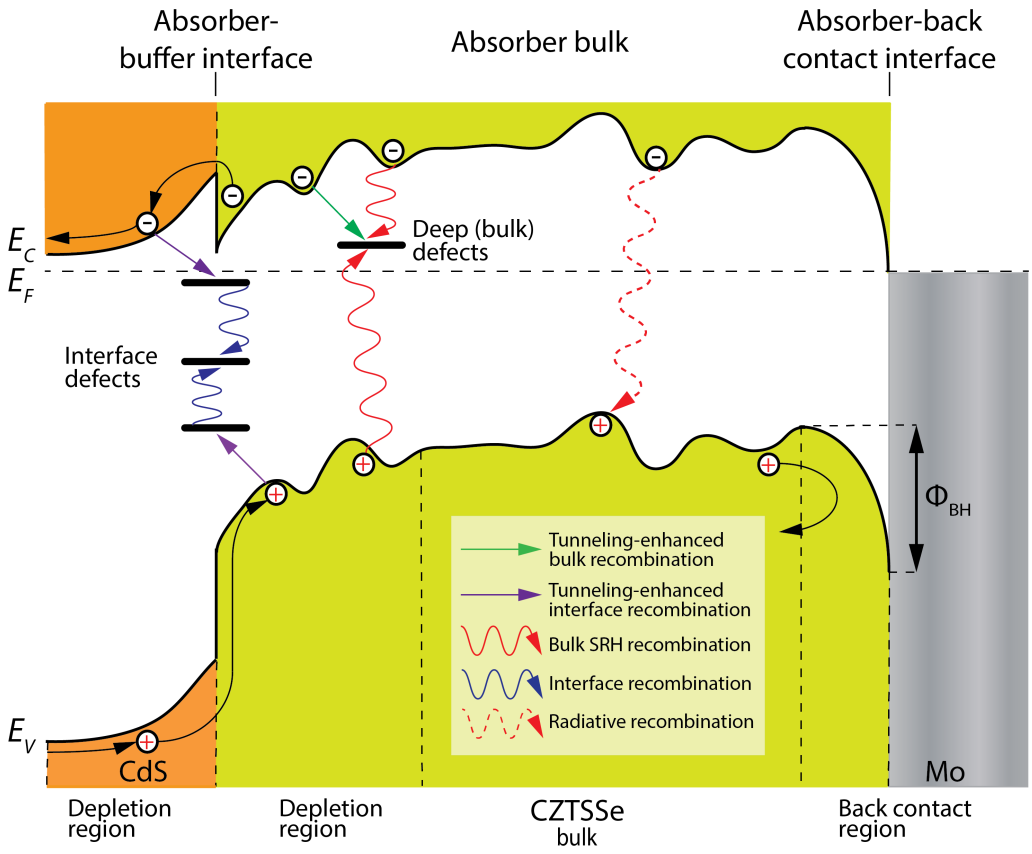

Figure 2.1.1: Schematic energy band diagram of a typical CZTSSe solar cell. A number of recombination pathways relating to the absorber/ buffer, absorber/back contact interfaces and absorber bulk are highlighted.

contact due to the formation of an ohmic contact, good adhesion properties and creation of an intermediate $MoSe_2$ layer which acts as a diffusion barrier [56]. Whether Mo is the best back contact material in kesterite TFPVs is still under debate. It has been demonstrated that when the thickness of the $MoSe_2$ layer in CZTSSe devices is not optimised by annealing temperature/Se vapour pressure, performance is negatively impacted (device efficiency of 2.95% with $MoSe_2$ thickness of ∼1300 nm compared to a similar device with efficiency of 5.95% with $MoSe_2$ thickness of 600 nm) [57]. During the selenisation (sulphurisation) process, $MoSe_2$ (MoS_2) forms at the CZTSe(CZTS)/Mo interface the thickness of which can have a detrimental effect on open circuit voltage and band alignment [58]. The formation of $MoS(e)_2$ is due to the instability of Mo at the Mo/CZTS(e) interface during the thermal processing step of device fabrication. The reaction at the interface can be described by [59]:

$$2Cu_2ZnSnS(e)_4 + Mo \rightarrow 2Cu_2S(e) + ZnS(e) + 2SnS(e) + MoS(e)_2 \qquad (2.2.1)$$

Shin *et al.* observed a ∼1300 nm thick $MoSe_2$ in a CZTSe device which increased cell series resistance and degraded V_{oc} [12]. Evidence of high series resistance related to $MoSe_2$ thickness in nanoparticle ink-based CZTSSe solar cells is shown in Figure 2.2.1 and the following section.

2.2.1 Back contact barrier

The issue of problematic high series resistance in CZTSSe devices was also highlighted by Gunawan *et al.* [52]. Following temperature-dependent standard diode analysis [60, 61], they observed a dramatic reduction in device efficiencies toward lower temperatures. This erroneous behaviour was ascribed to diverging dark series resistance with reducing temperature and is demonstrated as part of this work (see Figure 2.2.1).

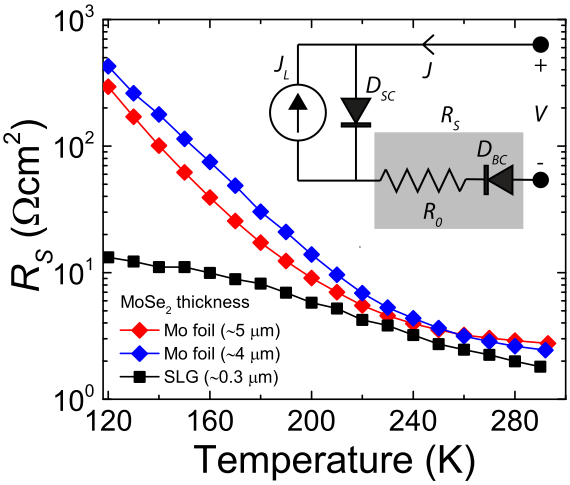

Figure 2.2.1: Temperature dependence of dark series resistance in CZTSSe solar cells on Mo foil and sodalime glass substrates with varying $MoSe_2$ thicknesses [62] and inset showing equivalent circuit diagram proposed by [63] incorporating a blocking back contact where D_{SC}, J_L and R_s are the solar cell diode, photogenerated current source and combined series resistance, respectively. The combined series resistance consists of the background series resistance R_0 and a blocking back contact diode D_{BC}.

It was speculated the cause of the diverging series at low temperature was the presence of a blocking contact barrier at the CZTSSe/back contact interface Φ_{BH}, as illustrated in Figure 2.1.1. The barrier would serve to suppress majority carrier (hole) transport. An equivalent circuit model was proposed to describe the temperature-dependent behaviour of device performance, see inset in Figure 2.2.1. The circuit is comprised of two diodes, i) main solar cell diode (D_{SC}) and ii)

back contact diode (D_{BC}) [63]. When the device is under forward bias, the back contact diode is in reverse bias. Under these conditions, the conduction of the back contact diode is limited by its reverse saturation current, which decreases rapidly at lower temperatures leading to a subsequent increase in series resistance.

Using the analysis method in [63], the back contact barrier height Φ_{BH} can be evaluated. Figure 2.2.2 shows Φ_{BH} values determined for a series of CZTSSe solar cells with varying $MoSe_2$ thickness. It would appear there is a direct correlation between the thickness of the $MoSe_2$ layer at the CZTSSe/Mo interface and the barrier height of the blocking contact. Therefore barrier height could be a contributing factor in the observed diverging series resistance with decreasing temperature. A current blocking back contact does not appear to be an issue in CIGS-based solar cells. Gunawan *et al.* compared the performance of hydrazine solution-processed CIGS and CZTSSe devices and found Φ_{BH} in the CZTSSe sample was significantly higher at 115 meV than that observed in CIGS at 5.6 meV [63].

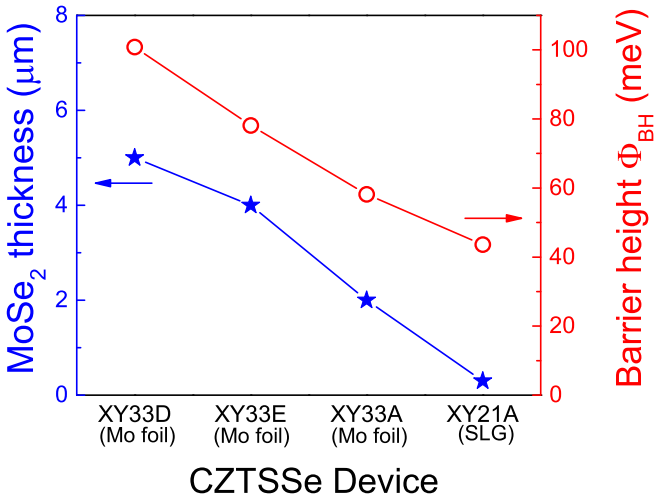

Figure 2.2.2: Correlation between thickness of $MoSe_2$ layer in CZTSSe devices on Mo foil or sodalime glass substrates and back contact barrier height Φ_{BH} [62], determined from *J-V(T)* analysis [61].

2.3 Absorber bulk

Fundamental to the operation of PV devices is the generation and recombination of charge carriers within the bulk of the absorber material. In order for efficient performance, the generated electron-hole (*e-h*) pairs have to be effectively separated and extracted from the solar cell be-

fore the carriers can recombine. Carrier recombination can happen through multiple relaxation channels, the main non-radiative processes being band Shockley-Read-Hall (SRH) trap-assisted recombination, Auger and surface recombination, as shown in Figure 2.1.1. The presence of these recombination pathways has a detrimental effect on the V_{oc} of the device due to increase of reverse saturation current density J_0.

2.3.1 Carrier diffusion

In most semiconductors, the absorption coefficient decreases with an increase in photon wavelength and approaches a minimum near to the bandgap of the material. Thus, photons with an energy around the bandgap are absorbed deeper into the absorber bulk and further away from the *p-n* junction. In most cases, the depletion (space charge) region does not extend to the full width of the absorber which means the generated *e-h* pairs have to diffuse over a longer distance increasing the probability of recombination. The increased probability of charge recombination could result in a reduction of quantum efficiency of a solar cell over longer wavelengths measurements, as exemplified in Figure 2.3.1.

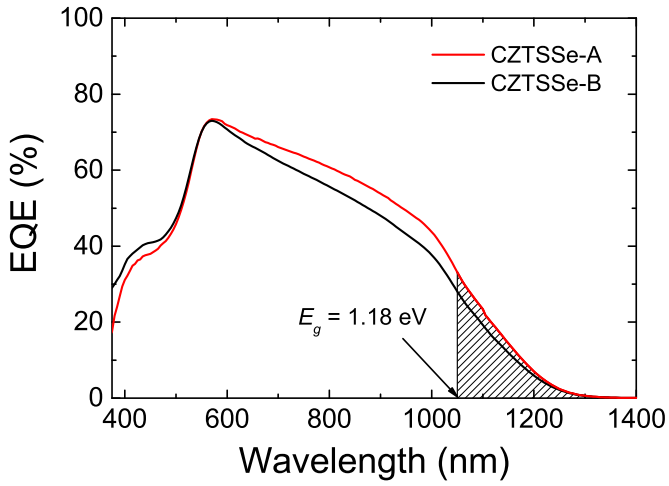

Figure 2.3.1: External quantum efficiency of sample CZTSSe devices. The reduction in carrier extraction efficiency over wavelength range 550 - 950 nm can be linked to poor minority carrier mobility and/or short carrier lifetime. The shaded area of the EQE curves shows the extent of band tailing into the bandgap of the CZTSSe absorbers [17].

Lower electron mobilites for CZTSSe (typically $\sim$40 cm^2/Vs) compared to CIGS thin films (typically $\sim$1000 cm^2/Vs) have been suggested as an explanation for reduced carrier extraction in CZTSSe devices [64]. Hole mobilities in these materials follow a similar trend with values of

$\sim$0.1 cm^2/Vs for CZTSSe and $\sim$10 cm^2/Vs for CIGS [65, 66]. Lower minority carrier mobility has been linked to the presence of charged defects which act as scattering centres. Low minority carrier lifetime τ has also been cited as a cause of poor carrier collection at longer wavelengths [67].

2.3.2 Bulk defects

Due to the complexity of the quaternary kesterite crystal structure (see Figure 1.2.1), the probability of large concentrations of defects in the absorber bulk, such as vacancies, antisites, interstitials and complexes, is high [37, 68]. Similarities in the ionic radii of the component elements promotes the formation of a variety of intrinsic defects. Energetically, the defects/complexes can be shallow donor and acceptor levels, mid-gap states and deep trap states all of which lie within the band gap of the kesterite absorber. Not all defects are detimental in nature: copper vacancies (V_{Cu}) form a shallow acceptor state $\sim$30 meV above the valence band maximum (VBM) and contribute to the *p*-type conductivity in CZTSSe. The formation of this defect is favoured under Cu-poor, Zn-rich growth conditions. Indeed, the most efficient CZTSSe devices reported in literature were grown under this regime [69, 70]. Other acceptor vacancies such as V_{Zn}, V_{Sn}, V_S and donor vacancy V_{Se} are not favourable as they form deeper states and negatively impact device performance. Also responsible for the *p*-type nature is the antisite defect Cu_{Zn} with an activation energy of $\sim$120 meV. Defect Cu_{Zn} is prevalent in CZTSSe regardless of growth conditions due to the lowest enthalpy of formation as determined by density funtional theory (DFT) calculations [37]. All other acceptor defects (Cu_{Sn} and Zn_{Sn}) have negligible impact on *p*-type conductivity and are deeper in nature and could act as non-radiative recombination centres. Interestingly, the presence of deep, partially compensated acceptor defects has also been cited as contributing to carrier 'freeze-out' and increasing series resistance at lower temperatures, see Figure 2.2.1 [43].

Regarding donor defects in CZTSSe, two shallow levels (Zn_{Cu} and Cu_i) and three deep levels (Sn_{Cu}, Sn_{Zn} and Zn_i) are possible. Given the preferred Cu-poor, Zn-rich growth conditions for efficient kesterite devices, Zn_{Cu} is expected to be the predominant donor. This antisite defect may agglomerate and behave like an electron sink and hole barrier, increasing non-radiative recombination and reducing device V_{oc}. Again, the deep donor levels are effective trap levels with deleterious effects on device performance. The negative effects of isolated Zn_{Cu} defects can be mitigated by the formation of [V_{Cu} + Zn_{Cu}] complex. High concentrations of this cluster

cause band-bending which assists in *e-h* pair separation. The valence band (VB) and conduction band (CB) edges are simultaneously lowered, repelling holes and increasing collection and onward transportation of electrons into the buffer layer [71, 72]. Most of the pernicious defects in CZTSSe are Sn-related and form mid-gap states, therefore it is important to control Sn composition during absorber growth and subsequent sulphurisation/selenisation processes.

2.3.3 Grain boundaries

As is the case in most polycrystalline semiconductors, the presence of grain boundaries (GBs) in kesterite absorbers is likely to be detrimental to solar cell performance. This is due to the structural defects and different crystal orientations associated with GBs which act as recombination centres. Using *ab initio* calculations, Li *et al.* found GBs formed mid-gap recombination states in CZTSe which may be a limiting factor in device efficiency [73]. They state the atoms at the GBs in CZTSe are unable to relax leading to the formation of deep traps. An example of GBs in a cross-section of a kesterite thin film is shown in Figure 2.3.2. Conversely, other studies have shown GBs have little effect on the electronic properties in Cu-poor/Zn-rich CZTS and CZTSSe PV devices [74, 75]. Using scanning Kelvin-probe microscopy, they demonstrated GBs act as an electrostatic potential barrier which facilitate charge separation near the GBs.

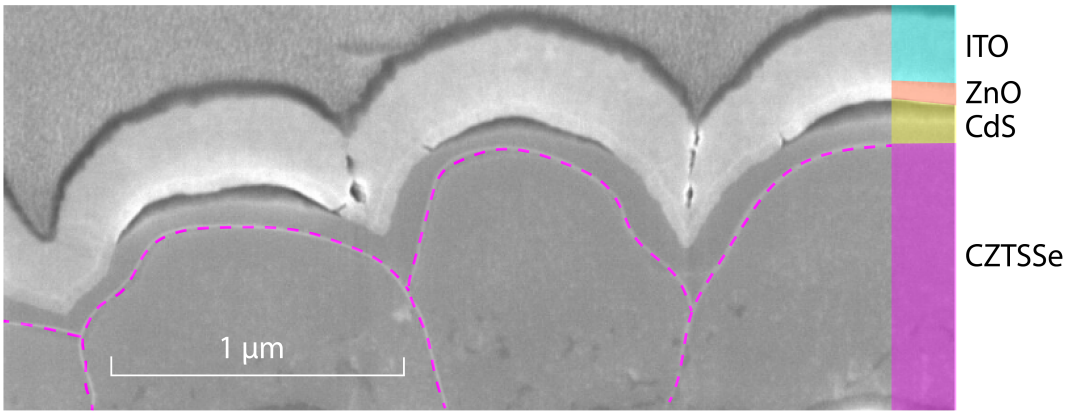

Figure 2.3.2: SEM cross-section image of a typical CZTSSe/CdS/ZnO/ITO stack prepared using a focused ion beam. The boundaries of the CZTSSe grains have been highlighted for clarity [76].

2.3.4 Band tailing

Absorption tails extending into the bandgap of a semiconductor are known to act as non-radiative recombination pathways which reduce the efficiency of PV devices. These band tails are perhaps the most important factor affecting the V_{oc} and have been extensively studied in order to identify the cause [54, 77–79]. High concentrations of V_{Cu}, Cu_{Zn} and Zn_{Cu} intrinsic defects and [V_{Cu} + Zn_{Cu}], [Cu_{Zn} + Zn_{Cu}] complexes (expected under Cu-poor, Zn-rich growth conditions), together with spatial deviations in the distribution of these defects/complexes induce potential fluctuations in the band structure. These band edge fluctuations can arise from microscale variations in the bandgap of the material and/or clustering of charged defects causing fluctuations in the electrostatic potential. Bandgap and electrostatic potential fluctuations are examined in more detail in Section 3.2.1. The extent of band tailing in CZTSSe films is shown in Figure 2.3.1 where there is extended absorption of photons with energies below the bandgap of the absorber.

2.4 Absorber-buffer interface

The band alignment of semiconductors at the *p-n* junction has a crucial role in the transfer of charge from the depletion region of a solar cell. Non-optimal band alignment will result in increased recombination at the absorber/buffer interface. Other factors contributing to interface recombination include the presence of secondary phases on the absorber surface which are dependent on kesterite film growth conditions and lattice mismatch between the absorber and buffer materials.

2.4.1 Band alignment

Band alignment at semiconductor interfaces can be categorised as Type I, II or III, however Type III are not pertinent to PV applications, see Figure 2.4.1. In Type I, the CB of the absorber is lower than that of the buffer (relative to the electron vacuum levels of the materials) forming a spike-like potential barrier which can hinder electron transport dependent on the magnitude of the conduction band offset (CBO). A theoretical optimal maximum value of 0.4 eV for the spike-like offset has previously been reported in CZTSSe [80]. If the CBO is below this threshold, electron transport is facilitated by tunnelling and/or thermionic emission. A small 'spike' CBO has been shown to create an absorber type inversion in the vicinity of the heterojunction which consequently

creates a large hole barrier [81]. In contrast, the CB of the absorber layer at a Type II interface is higher than that of the buffer layer forming a cliff-like alignment. Although there is no barrier for electrons to overcome when flowing from absorber to buffer, there may be high concentrations of holes near the semiconductor junction increasing the probability of interface recombination [81, 82]. Therefore, Type I and II CBO are preferable in order to achieve improvements in V_{oc} and short circuit current density J_{sc}, respectively.

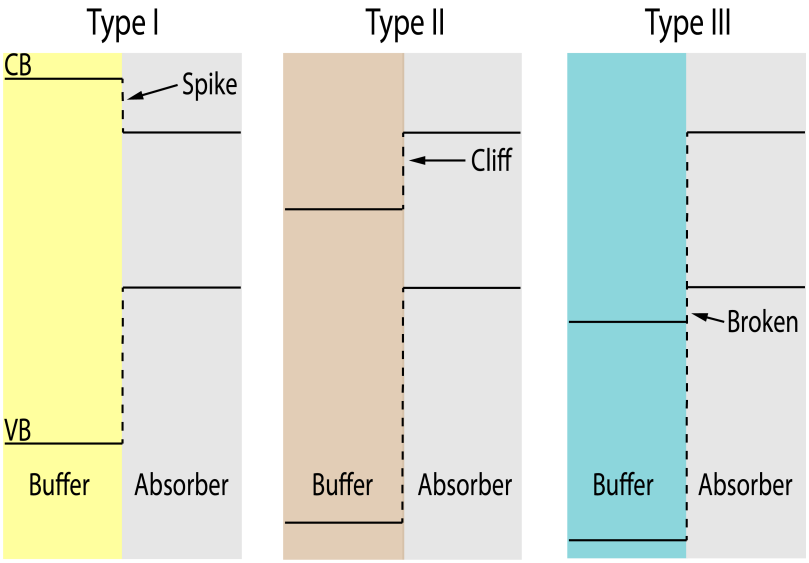

Figure 2.4.1: Different heterojunction band alignments where there is (a) spike, (b) cliff and (c) break between the CB at the interface of the buffer-absorber materials.

2.4.2 Interface recombination

CZTSSe film growth can result in a number of binary and ternary secondary phases due to variations in stoichiometry. In particular, films grown under the preferred Cu-poor, Zn-rich conditions promote the formation of ZnS(e) due to their large negative enthalpies [83]. ZnSe phase was observed at the CZTSe absorber surface resulting in a current blocking behavior and a reduced short-circuit current density in the associated device [84]. The presence of ZnSe containing a high concentration of Cu and Sn impurities on top of the CZTSe absorber layer was also detected by room temperature photoluminescence (PL) measurements [85]. The current-blocking behaviour arises from the large 'spike' CBO (1.32 eV) at the ZnS(e) and CZTS(e) interface [84, 86, 87]. Other secondary phases, such as SnS(e) and Cu_xS(e) have smaller bandgaps than CZTS(e) which contibutes to a reduced V_{oc}. Indeed the conduction band edge in $SnS(e)_2$ is much lower than

that of CZTS(e) which will increase interface recombination [88]. These secondary phases at the buffer/absorber interface can trap minority charge carriers or produce shunting pathways. Treating the CZTS(e) absorber surface with different chemical etchants can passivate and selectively remove secondary phases. This is evidenced in Figure 2.4.2 where PL intensity from CZTSSe thin films is enhanced following chemical etches, suggesting passivation of non-radiative defects at the film surface.

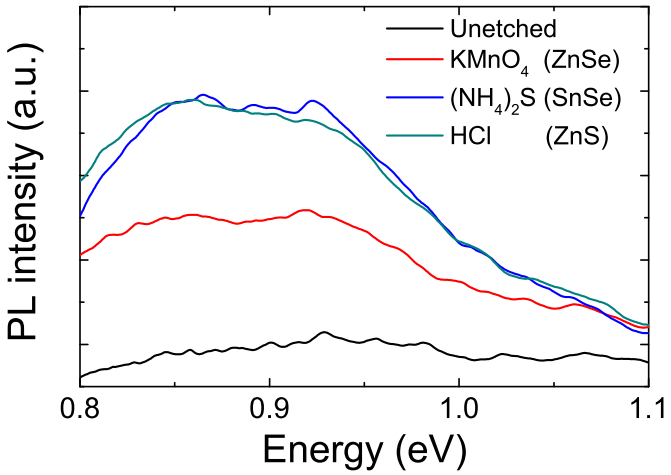

Figure 2.4.2: Room temperature photoluminescence from similar CZTSSe thin films subjected to different surface etching. $KMnO_4$, $(NH_4)_2S$ and HCl etchants were used to remove ZnSe,SnSe and ZnS secondary phases, respectively.

By performing $V_{oc}(T)$ analysis of CZTSSe solar cells, the activation energy E_A of the dominant recombination pathway can be determined which indicates the type of recombination mechanism prevalent in the devices, see Figure 2.4.3 [89]. By extrapolating the linear region of the V_{oc} versus T plot, E_A/q (eV) is evaluated at T = 0 K.

It is apparent the activation energy of the example CZTSSe device is significantly lower than the indicated bandgap of the CZTSSE absorber. The large discrepancy suggests that the recombination mechanism in the device is strongly influenced by interface recombination which will negatively impact V_{oc} at room temperature.

To summarise, some of the factors which currently inhibit performance in kesterite TFPV have been examined. By understanding the loss mechanisms in kesterite, a targeted approach can be adopted in order to identify key areas for improvements and provide informed solutions to increase performance in CZTSSe PV. The following chapter will look at the different experimental

methods and characterisation/analytical techniques to achieve this objective.

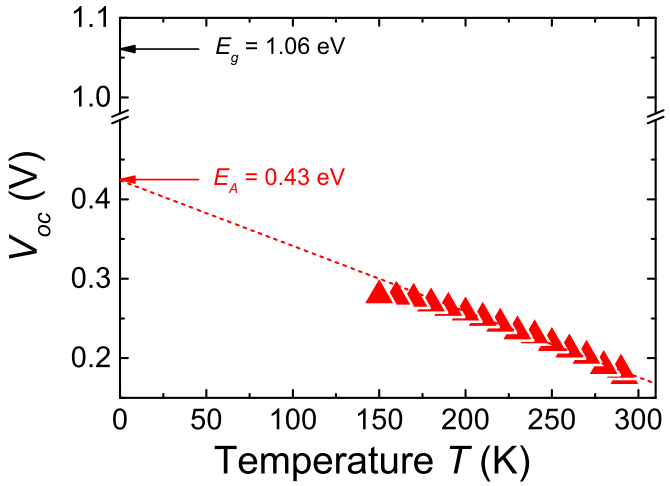

Figure 2.4.3: Temperature dependence of the open circuit voltage V_{oc} of a CZTSSe device. The activation energy E_A of the dominant recombination mechanism is determined by extrapolation of the linear region of the plot to 0 K. The significant difference between the activation energy and bandgap of the CZTSSe absorber indicates substantial recombination at the absorber/buffer interface.

Chapter 3

Experimental methods, characterisation and analysis

This chapter will detail the fabrication of CZTSSe absorbers and solar cells from CZTS nanoparticle inks using the hot injection method. A number of optical and electronic characterisation techniques will be considered together with relevant data analysis methodology.

3.1 Solar cell fabrication

3.1.1 CZTS nanoparticle synthesis

CZTS nanoparticles in this study were produced by injection of metallic precursors and sulphur into a hot solvent. Oleylamine (OLA) with long hydrocarbon chain was firstly chosen as the capping ligand to prevent the agglomeration of nanoparticles during fabrication [44]. Alternatively, formamide (FA) was chosen as the solvent in the synthesis of CZTS nanoparticles [90].

CZTS OLA recipe

1.34 mmol of copper(II) acetylacetonate, 0.95 mmol of zinc acetylacetonate, 0.75 mmol of tin(IV) bis(acetylacetonate) dichloride were dissolved into 10 ml OLA in a three neck flask connected to the Schlenk line. The reaction mixture was put under vacuum and purged with nitrogen twice to remove residual water and oxygen dissolved in the solvent. After the degassing process, the temperature of the mixture was then increased to the reaction temperature of 225 °C after which 3 ml 1M sulphur-OLA solution was then injected into the solvent. The reaction solution was

then held at the reaction temperature for 30 min to allow the growth of the CZTS nanoparticles. After reaction, the CZTS nanoparticles were collected and washed twice using isopropyl alcohol (IPA) and toluene. The CZTS OLA nanoparticle ink was prepared by dispersing nanoparticles into hexanethiol with the aid of sonication.

CZTS FA recipe

Firstly, 4.8 mmol of copper(II) acetate monohydrate, 3.3 mmol of $SnCl_2$, 3.12 mmol of $ZnCl_2$ were dissolved successively into 20 ml FA to make the metal solution in a glass bottle. Next, 13.2 mmol thioacetamide (TAA) was dissovled into 10 ml FA at room temperature in a three necks flask connected to the Schlenk line. The TAA solution was put under vacuum and purged with nitrogen twice to remove residual water and oxygen dissolved in the solvent. After the degassing process, the temperature of the mixture was then increased to the reaction temperature of 170 °C after which 2.5 ml metal solution was injected into the TAA solution. The reaction was held for 2 min before immersing the reaction flask into a cold water bath to cease the reaction. After the reaction, ethanol and FA were used to precipitate and wash the CZTS nanoparticles twice before suspending nanoparticles in ethanol to yield the CZTS FA nanoparticle ink.

3.1.2 Spin-coating

Approximately 50 μl of the concentrated ink was applied onto a square (2.5 cm x 2.5 cm) Mo-coated glass substrate at a speed of 1200 rpm for 5 seconds. The samples were then dried on a hot plate at ∼150 (∼100) °C for 30 seconds and then at ∼300 (∼200) °C in air for 30 seconds for OLA (FA) samples to remove the residual solvents. The spin coating and soft-baking procedures were repeated 10 times to yield thin films with a thickness of ∼1μm.

3.1.3 Selenisation of CZTS films

The thin films comprising CZTS nanoparticles were selenised in a tube furnace in order to promote grain growth, resulting in CZTSSe absorbers. Selenium pellets were placed directly under the substrate of the as-deposited precursor thin films encapsulated in a graphite box. The furnace was evacuated (6.0 x 10^{-3} mbar) and an argon atmosphere (∼10 mbar) was provided before the temperature was increased (∼20 °C /min) to 500 °C. This temperature was then held for 20 minutes before being cooled down rapidly (∼ 20 °C /min) to 300 °C, followed by a slower cooling rate of ∼4 °C /min until the selenised films reached room temperature [91]. The annealing

temperature during selenisation of the CZTS films is an important factor as it is directly correlated to the Se vapour pressure inside the tube furnace. In order to achieve large grain growth, the CZTS film is maintained at 500 °C for the determined time period with $Se_{(g)}$ supplied at a vapour pressure close to its saturation vapour pressure (which occurs when Se pellets are heated to 500 °C and above). These conditions result in selenisation of the film in a saturated $Se_{(g)}$ atmosphere. The selenisation conditions have also been optimised by controlling the annealing temperature and duration to minimise the thickness of the $MoSe_2$ layer at the Mo/CZTSSe interface. A thicker layer of $MoSe_2$ can increase the series resistance of the subsequent device [92, 93]. Also, the concentration of chalcogen vacancy defects (V_S, V_{Se}) is assumed to be inversely proportional to the chalcogen vapour pressure. Thus, sufficient Se vapour pressure will reduce these defects within the CZTSSe absorber bulk [94].

3.1.4 Chemical bath deposition of buffer layers

CdS buffer

The CdS buffer layer was deposited using a chemical bath. Deionized water was first poured into a double-walled beaker. After the temperature inside the beaker stabilized at 70 °C, $CdSO_4$(2 mM) and ammonium hydroxide (1.5 M) were successively added while a magnetic bar was continuously stirred to form the solution. The CZTSSe films were then soaked in the solution for 2 min before thiourea (12 mM) was mixed into the solution. After the reaction, the samples were removed from the bath, rinsed with deionized water and dried under a nitrogen stream and then annealed at 200 °C for 10 min in air.

In_2S_3 buffer

For In_2S_3 deposition, samples were immersed in a solution composed of indium chloride (10 mM), thioactamide (0.1 M) and acetic acid (0.1 M) at 70 °C to form an In_2S_3 coating on CZTSSe [95, 96]. After the deposition, the samples were removed from the bath, rinsed with deionized water and dried under a N_2 stream. The buffer coated samples were then annealed at 200 °C in open air for 2 min.

3.1.5 Completion of CZTSSe solar cells

The solar cells were integrated into a device configuration of Mo/CZTSSe/CdS/*i*-ZnO/ITO/Ni-Al, see Figure 1.2.3. *i*-ZnO ($\sim$ 35 nm) and ITO ($\sim$ 200 nm) layers were then deposited by magnetron

sputtering to act as the transparent conducting oxide (TCO) layers. Front contact grids which are composed of Ni ($\sim$ 50 nm) and Al ($\sim$ 1 μm) layers were deposited through a shadow mask by electron beam evaporation. Finally, nine ~ 0.16 cm^2 cells were defined by mechanical scribing on each substrate. A typical complete set of CZTSSe solar cells is shown in Figure 3.1.1.

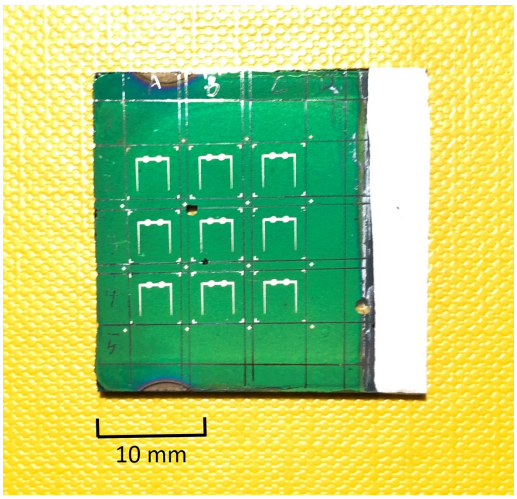

Figure 3.1.1: Typical CZTSSe solar cells.

3.2 Materials characterisation and analysis

3.2.1 Photoluminescence

Photoluminescence (PL) is an optical process involving (i) the absorption of photons by atoms within a luminescent material generating electron-hole (*e*-*h*) pairs in the respective conduction and valence bands (photoexcitation), (ii) the thermalisation of the photogenerated charge carriers to the energy band edges (relaxation) and (iii) the re-emission of photons due to the recombination of the *e*-*h* pairs (radiative recombination). Thus, PL spectroscopy is a non-destructive technique used in the analysis of defects within a semiconductor and is particularly sensitive to shallow defects within the bandgap of the absorbing material. A number of radiative recombination transitions are possible but only those relating to highly doped and compensated materials, such as kesterite CZTSSe, will be discussed. A material is classed as highly doped and compensated when there are similar concentrations of acceptor and donor defects and the average distance between defects is less than the Bohr radius of a defect state [97]. In the case of an *n*-type semiconductor, if the heavy doping condition $N_d a^3 > 1$ is satisfied, there are no localised single donor states (N_d

is the donor concentration and a is the Bohr radius of the donor state). When this condition is satisfied, the kinetic energy of an electron localised in space s (average distance between donors $\approx N_d{}^{-1/3}$) exceeds the attractive Coulomb energy due to the donor. The defect level is displaced to an energy band and the semiconductor becomes degenerate. For a heavily doped semiconductor, this defect level broadens into a defect band due to the many-body interactions between all defects and carriers and results in significant densitiy of states tails within the bandgap. A similar case exists for acceptor states in a *p*-type semiconductor although these states tend to be deeper due to the larger effective mass of holes compared to that of electrons. In fact, the high doping and strong compensation conditions in *p*-type kesterites are more readily satisfied for electrons than holes. This is due to the significantly larger effective mass of holes compared to that of electrons (hole effective mass $m_h^\star = 0.21m_0$, electron effective mass $m_e^\star = 0.08m_0$ where m_0 is the mass of free electron [16]). High concentrations of donors cause donor wave-functions to overlap due to their small spatial separation whereas acceptors remain non-degenrate and therefore can be treated like classical particles [97, 98]. The considerable band tailing seen in strongly compensated polycrystalline semiconductors is highlighted in the PL spectra of a CZTSSe absorber compared to that of a epitaxially grown GaAs absorber, see Figure 3.2.1.

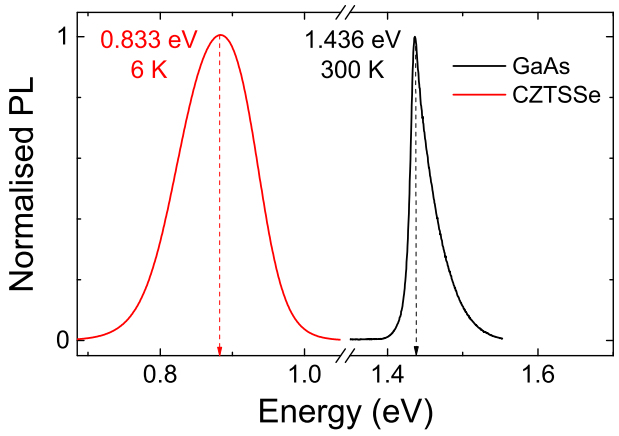

Figure 3.2.1: PL spectra of a highly doped, compensated semiconductor, such as CZTSSe and a non-compensated semiconductor, such as intrinsic GaAs. Note the significant band tailing below the indicated PL peak position of the CZTSSe sample. The PL emission occurs around the bandgap of the GaAs sample (1.42 eV) whereas emission from the CZTSSe sample occurs well below its bandgap of 1.12 eV, indicating PL emission is defect-mediated.

Such band tailing is manisfested as a consequence of spatial inhomogeneities in the absorber material leading to fluctuations in the bandgap, clusters of charged defects creating fluctuations

in the elecrostatic potential or thermal vibrations of the crystal lattice (Urbach tails). Electrostatic potential fluctuations are characterised as a constant bandgap with parallel shifts in the valence and conduction band energies. Conversely, bandgap fluctuations in kesterites are caused by microscopic variations in the stoichiometry of the material and/or the presence of secondary phases resulting in small modulations of the absorber bandgap. These band edge fluctuations are represented schematically in Figure 3.2.2.

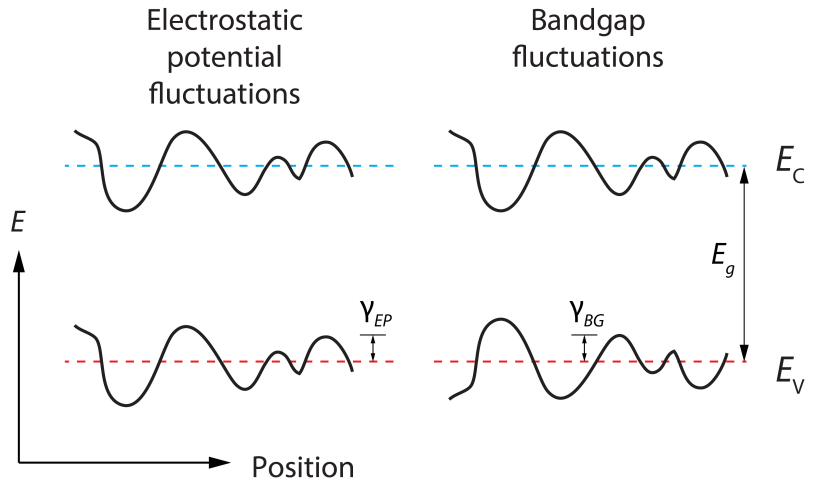

Figure 3.2.2: Schematics of electrostatic potential and bandgap fluctuations of the conduction and valence band edges of a heavily doped and compensated semiconductor. γ_{EP} and γ_{BG} are the root mean square depths of the electrostatic potential and bandgap fluctuations, respectively.

In the case of electrostatic potential fluctuations in a compensated semiconductor, the net doping density ($N_a{}^+$+$N_d{}^-$) is significantly lower than the dopant concentration (N_a+N_d). The minority defects lose their charge carriers to the majority defects, leaving the defects ionised without producing free charge carriers which would normally screen the fixed space charges. As these defects are distributed randomly within the material, areas of higher concentrations of positively charged donors and negatively charged acceptors are formed. Due to the low density of free charges, the variation in fixed space charge cannot be screened resulting in non-uniform distortion of the band edges arising from spatial fluctuations of the electrostatic potential. The average depth of the fluctuation γ within a volume r^3 depends on the total charged defect concentration (N_t = $N_a{}^+$+$N_d{}^-$) [98]:

$$\gamma_{EP} = \frac{e^2}{4\pi\epsilon_0\epsilon_r}\frac{\left(N_t r^3\right)^{1/2}}{r} \tag{3.2.1}$$

where ϵ_0 is permittivity of vacuum and ϵ_r is relative permittivity (or dielectric constant). Due to

the screening effects of free carriers, the maximum range r_s of the fluctuations is dependent on the hole density *p* such that:

$$r_s = \frac{N_t^{1/3}}{p^{2/3}} \tag{3.2.2}$$

This gives the average potential fluctuations within a screening volume ${r_s}^3$:

$$\gamma_{EP} = \frac{e^2}{4\pi\epsilon_0\epsilon_r}\frac{N_t^{2/3}}{p^{1/3}} \tag{3.2.3}$$

It is worth noting that fluctuations greater than r_s are screened by free carriers. As electrons and holes are localised in spatially separated potential wells, radiative recombination is facilitated by tunneling. The tunneling length r_t is dependent on γ_{EP}, i.e. $r_s = \hbar/\sqrt{m_r\gamma_{EP}}$ and substituting r_t into 3.2.1 gives [99]:

$$\gamma_{EP}^5 = \left(\frac{e^2}{4\pi\epsilon_0\epsilon_r}\right)^4 \frac{N_t^2\hbar^2}{m_r m_0} \tag{3.2.4}$$

where m_r is the reduced effective mass given by $m_r = (m_e m_h)/(m_e + m_h)$, m_e is the effective electron mass, m_h is the effective hole mass, m_0 is the electron mass and $\hbar$ is the reduced Planck's constant. The screening of the Coulomb potential of charge carriers is an important factor which affects the depth of electrostatic potential fluctuations. The screened Coulomb potential *ϕ(r)* takes the form of Poisson's equation using the Fermi-Thomas approximation (system is maintained at a constant electron chemical potential (Fermi level E_F) and at low temperature [100]) and the solution includes a Coulomb potential multiplied by an exponential damping term, k_0:

$$\phi(r) = \frac{Q}{4\pi\epsilon_0 r}e^{(-k_0 r)} \quad \text{where} \quad k_0 = \sqrt{\frac{3e^2\rho}{2\epsilon_0 E_F}} \tag{3.2.5}$$

where ρ is the density of free charge carriers. The effect of increasing free carrier density on the screened Coulomb potential is shown in Figure 3.2.3. For example, an increase in carrier generation due to increasing laser excitation intensity causes a reduction in r_s by an injection of free charge carriers and/or reduced concentrations of ionised donors and acceptors. Thus, according to Equation 3.2.3, a reduction in r_s has an associated reduction in γ_{EP}. This is illustrated in Figure 3.2.4 where γ_{EP} values for CZTSSe thin films with different buffer materials show a marked decrease above a certain excitation intensity and can be attributed to Coulomb screening of the electrostatic potential.

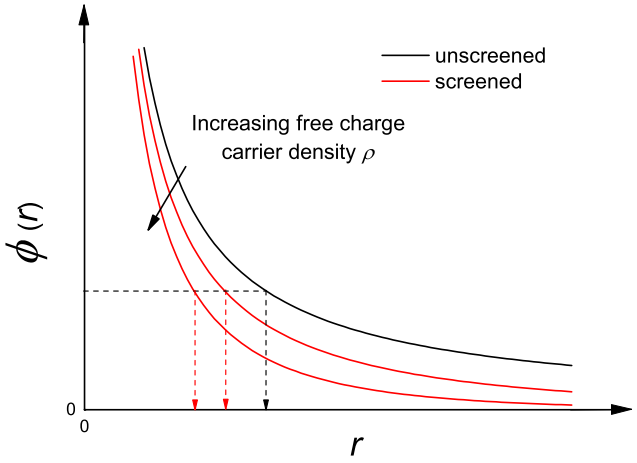

Figure 3.2.3: Plot of Coulomb potential ϕ as a function of distance between interacting bodies r. An increase in free charge carrier density ρ leads to ϕ being screened over a shorter distance.

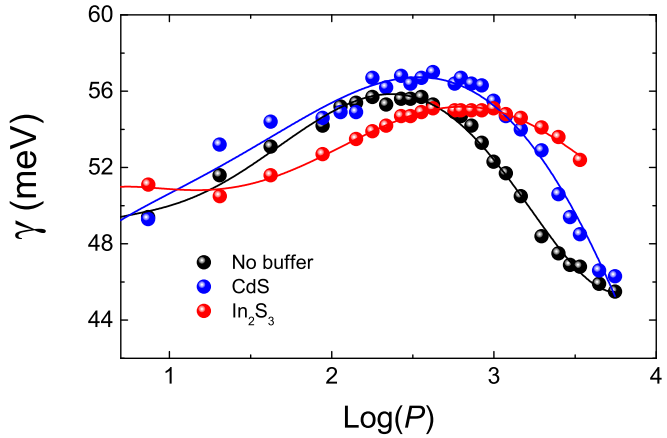

Figure 3.2.4: Average potential fluctuation depth γ as a function of laser excitation power P of CZTSSe thin films with different buffers. Note the reduction in γ above a certain laser power, which can be attributed to Coulomb screening due to increased generation of charge carriers, further discussed in Chapter 6.

Evidence of the presence of a fluctuating electrostatic potential is the significant red-shift of the energy of the maximum of the PL peak (E_{PL}) compared to the bandgap of the material. The spectral shape of PL emission lines from a semiconductor with fluctuating potential of the energy bands is determined by the density of states (DOS) of charge carriers. A model has been proposed where the absorption tails due to an electrostatic potential fluctuation are treated like a Gaussian distribution of defects. The low energy tail of emissions *I(E)* (see CZTSSe PL spectra in Figure

3.2.1) can therefore be described by [101]:

$$I(E) \sim exp\left(-\frac{(E-E_0)^2}{2\gamma_{EP}^2}\right) \tag{3.2.6}$$

where E_0 is the average emission energy in the case of fluctuating potentials. The values of γ_{EP}, and therefore N_t, can be deduced from the defect-model Gaussian fit. There are two main models for understanding the dominant recombination mechanism involving sub-bandgap defect states in CZTSSe: (i) electrostatic potential fluctuation as previously detailed and (ii) quasi donor acceptor pair (QDAP) model [102, 103] and both are fundamentally linked. Indeed, the only distinction between the models is the concentration of donor defects and depth of the defects in relation to the CB tail. In the case of QDAP recombination, the donor defects form discrete levels below the CB tail. However, with increasing donor concentrations seen in strongly compensated semiconductors, discretisation of the localised donor states is lost as the states merge with the CB tail, see Figure 3.2.5.

The QDAP model describes the distribution of radiative donor/acceptor states (which are a proportion of N_t) that contribute to this potential fluctuation. The spectral position of the QDAP PL maximum E_{PL} can be described as [103]:

$$E_{PL} = E_g - (E_D + E_A) + \frac{e^2}{4\pi\epsilon_0\epsilon_r s} \tag{3.2.7}$$

where E_D and E_A are the donor and acceptor energy levels separated from the conduction band minimum (CBM) and valence band maximum (VBM), respectively and s is the separation distance between donor and acceptor. The last term in Equation 3.2.7 describes the Coulomb potential which exists due to the attraction of the donor- and acceptor-like defects. A blue-shift in E_{PL} is observed with increasing excitation intensity. More donor and acceptor states become populated with escalating intensity, reducing the separation between these charge clusters and increasing their Coulomb interaction. This induces a shift of the emission peak towards higher energy and is a charcteristic of QDAP recombination observed in excitation-dependent PL spectra [102].

Previous reports [104, 105] have estimated the QDAP density using Equation 3.2.7 by making the following assumptions: (i) at low laser intensity, the spatial separation of charged defects is large enough such that there is no Coulombic interaction between the charged acceptor and donor clusters and (ii) there is maximum Coulombic attraction when all QDAP states are occupied which occurs when the QDAP peak saturates. Thus, the average separation distance s between

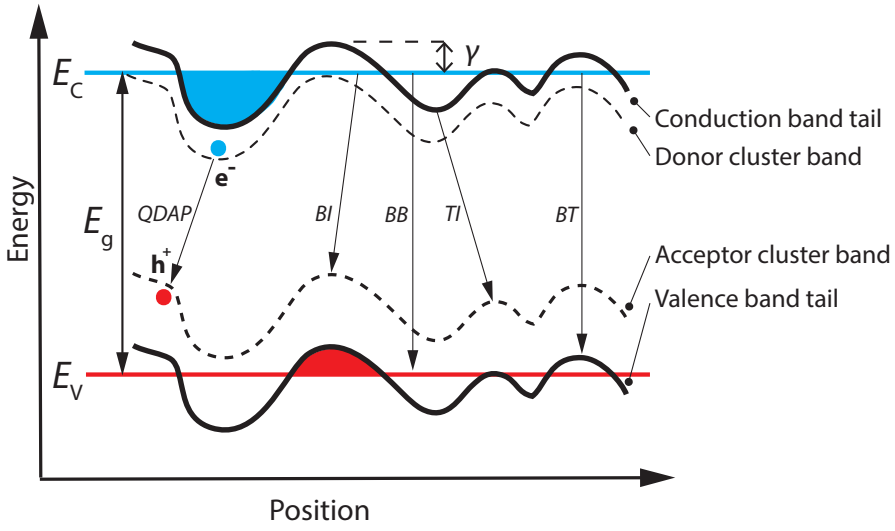

Figure 3.2.5: Schematic of electrostatic potential fluctuation where a strong perturbation of the energy bands is caused by a high density of localised charged defects resulting in deeper band-tail states (the solid colour shows a potential well region). Possible radiative transitions are shown where (i) the shallow CB donor level is discrete and (ii) the shallow CB donor level merges with the CB tail: (i) quasi donor acceptor pair (QDAP) and (ii) band-impurity (BI), band-band (BB), tail-impurity (TI) and band-tail (BT).

donor and acceptor can be estimated by equating the magnitude of blue-shift to the Coulombic interaction term in Equation 3.2.7. Consequently, the QDAP density N_D can be estimated by assuming [98]:

$$\Delta E = \frac{e^2}{4\pi\epsilon_0\epsilon_r s} \tag{3.2.8}$$

$$s = \left(\frac{4\pi N_D}{3}\right)^{-\frac{1}{3}} \tag{3.2.9}$$

In the case of electrostatic potential fluctuations where the donor band and CB tail merge, a number of radiative transitions are possible, see Figure 3.2.5:

- Tail-to-Impurity (TI): Electrons localised in states in the CB tail recombine with holes localised in deeper acceptor (impurity) states above the VB;
- Band-to-Impurity (BI): Free electrons in the CB recombine with holes in deeper acceptor (impurity) states;
- Band-to-Tail (BT): Free electrons recombine with holes localised in deep VB tail states;

- Band-to-Band (BB): Recombination between free electrons and free holes.

Further information regarding the nature of radiative recombination processes can be gleaned from the temperature dependence of PL emission from semiconducting materials. The changes in PL peak position and line shape with temperature are associated with recombination via defects. The activation energy (E_a) of such defects can be determined from Arrhenius analysis, which gives information on the depth of the defect state from the energy band edge and the density of non-radiative states resposible for quenching PL emission. Thermal quenching of PL due to a single radiative recombination channel can be described by [106]:

$$I(T) = \frac{I_0}{1 + C_1 T^{\frac{3}{2}} + C_2 T^{\frac{3}{2}} exp\left(-\frac{E_a}{kT}\right)} \tag{3.2.10}$$

where I_0 is the integrated intensity extrapolated to T= 0 K, k is the Boltzmann constant, C_1 and C_2 are the process rate parameters and E_a is the thermal activation energy for the involved defect state. In the case where a single recombination channel does not adequately describe the observed temperature-dependent behaviour, a more complex Arrhenius model involving two defect activation energies can be used [107]:

$$I(T) = \frac{I_0}{1 + C_1 exp\left(-\frac{E_{a1}}{kT}\right) + C_2 exp\left(-\frac{E_{a2}}{kT}\right)} \tag{3.2.11}$$

Here E_{a1} is the first activation energy, which is dominant over the higher temperature region and E_{a2} is the second activation energy, which is dominant over the lower temperature region, see Figure 3.2.6.

In considering the shift in PL maxima peak position with increasing excitation intensity or temperature, it is possible to identify the type of radiative recombination processes occuring in a highly doped and compensated semiconductor. However, this is not a trivial task as there may be concurrent transitions involving different acceptor and/or donor defects. Nevertheless, this type of analysis is still a useful tool to indicate the type of defect(s) within the absorber material. A general overview of the peak shifts with increasing excitation power and temperature are summarised in Table 3.2.1.

In this study, PL spectra were measured using a Horiba Jobin Yvon iHR320 fully automated spectrometer fitted with an InGaAs PMT detector cooled to -30 °C to reduce noise. A 532 nm continuous wave diode-pumped solid state (CW-DPSS) laser (MGL III-532 200 mW) was used as an excitation source. Power-dependent PL measurements (0.02 - 48.9 mW) were performed

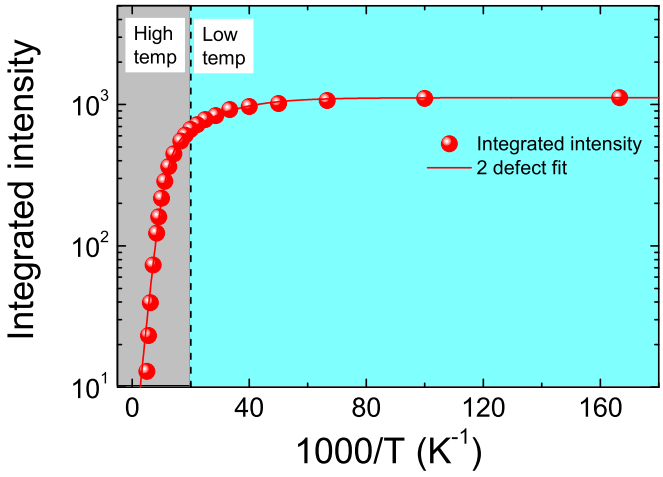

Figure 3.2.6: Example of Arrhenius plot for the temperature dependence of PL spectral lines in a CZTSSe thin film sample, fitted using a two activation energy model as in Equation 3.2.11 [17].

Table 3.2.1: Observed shift in PL peak maxima with increasing excitation intensity and temperature for radiative transitions in highly doped and strongly compensated semiconductors.

Shift	QDAP	TI	BI	BT	BB
Increasing P	Blue	Blue	Blue	Blue	None
Increasing T	Red	Red	Blue	Red	Blue

by adjusting the intensity of the laser beam using the MGL PSU-III-LED controller. PL measurements at varying temperatures (6 - 300 K) were performed by placing the sample in a Janis SHI-4-2 closed cycle refrigeration cryostat using compressed He gas coupled with a Lakeshore Model 335 temperature controller. The laser light was chopped and focused onto the sample inside the cryostat and luminescence from the sample was focused into the entrance slit of the 320 mm focal length monochromator, containing a grating with 900 grooves/mm. In order to avoid higher order artefacts arising from laser radiation, the luminescence was filtered with a long-pass filter with a cut-off wavelength of 760 nm. The chopped signal was detected with the thermoelectrically cooled InGaAs detector and amplified with a Stanford Research Systems SR810 DSP lock-in amplifier connected to the chopper signal. A schematic of the experimental PL setup with integrated time-resolved PL system is illustrated in Figure 3.2.7.

For accurate analysis of PL emission, all PL spectra were fitted using an emperical asymmetric

double sigmoidal function in the form [108]:

$$y = y_0 + A\left[\frac{1}{1+exp\left(\frac{x-x_c+w_1/2}{w_2}\right)}\right]\left[1-\frac{1}{1+exp\left(\frac{x-x_c-w_1/2}{w_3}\right)}\right] \tag{3.2.12}$$

where y_0 is an offset, x_c is the centre, A is the amplitude, w_1 is the full width of half maximum, w_2 is the variance of low-energy side, w_3 is the variance of high-energy side of the curve. The intensity of all PL spectra were corrected for wavelength-to-energy conversion.

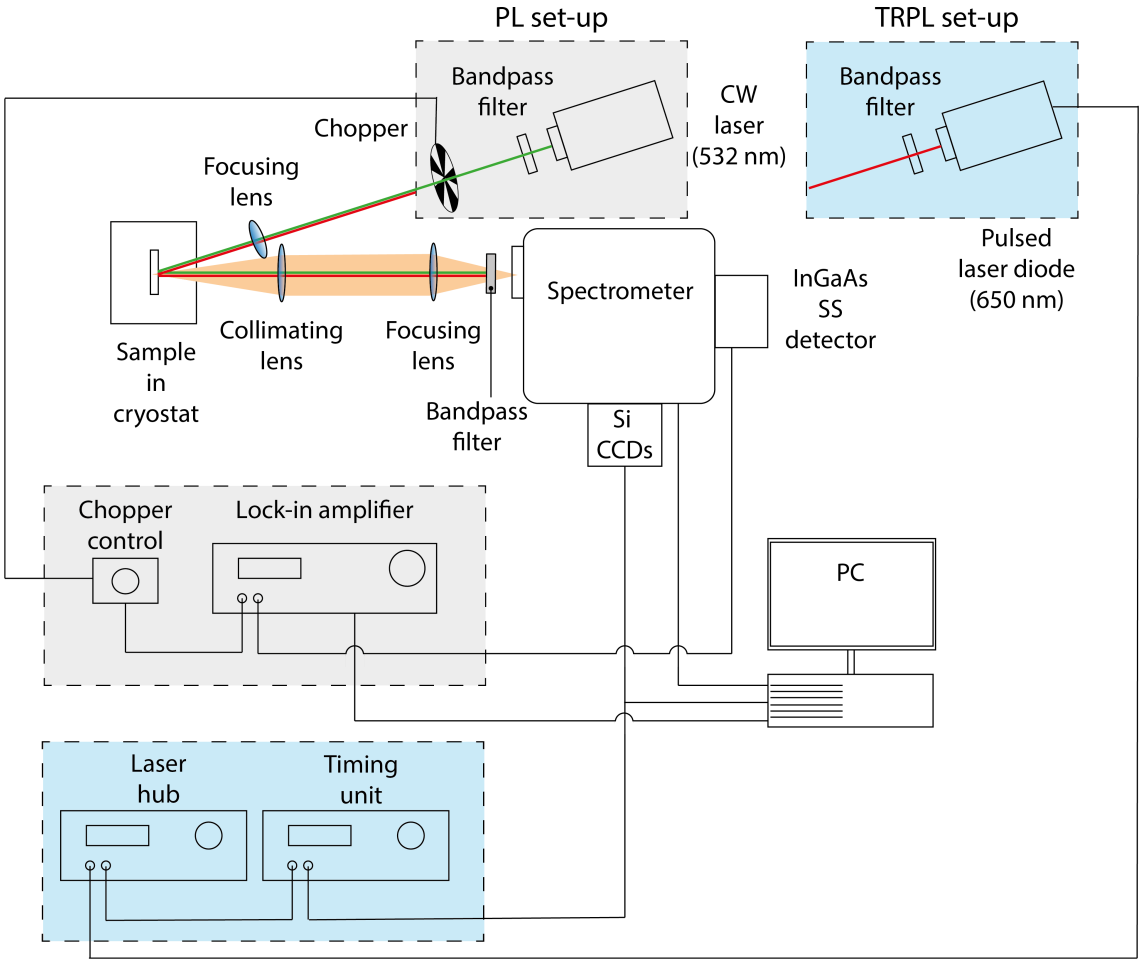

Figure 3.2.7: PL experimental setup.

3.2.2 Time-resolved photoluminescence

Time-resolved photoluminescence (TRPL) uses short pulses of incident photons (primarily from coherent laser sources) to generate excess charge carriers within a semiconducting material and the time dependence of PL emission from recombination of the carriers is measured. The decay time of excess carrier recombination is correlated with minority carrier lifetime. It is also a measure

of the degree of charge carrier localisation, which is particularly relevant to kesterite compounds with high defect densities. Carriers trapped in defects and low energy CB and/or VB tail states are bound to those states, trapped in potential wells caused by electrostatic and/or bandgap fluctuations (see Figure 3.2.5). In this case, the tunneling probability of electrons/holes from these potential wells to recombine with the corresponding carrier is low. The result is a long recombination lifetime. Conversely, carriers in higher energy band tail and band states have a higher degree of freedom and mobility and recombination lifetimes involving these states is predictably short. Thus, performing TRPL measurements at cryogenic temperatures traps the carriers in the lowest energy states giving an insight into the degree of charge localisation and electronic structure within the semiconductor. It has been demonstrated that a direct link exists between minority carrier lifetimes and the V_{oc} and efficiency of CIGS solar cells [60, 109].

Generally, TRPL decay curves are fitted by a bi-exponential function:

$$I_{PL}(t) = A_1 e^{-\left(\frac{t}{\tau_1}\right)} + A_2 e^{-\left(\frac{t}{\tau_2}\right)} \tag{3.2.13}$$

where $I_{PL}(t)$ is the luminescence intensity at time t after the excitation pulse, A_1 and A_2 are are the PL intensities corresponding to the injection regimes and τ_1 and τ_2 are the fast and slow decay times. The initial fast decay τ_1 can be ascribed to high carrier injection immediately after the excitation pulse and the long tail τ_2 attributed to the minority carrier lifetime of the material [52, 67].

Two TRPL systems were used to perform carrier lifetime measurements. The first was an integrated Horiba time-correlated single photon counting (TCSPC) system comprising of a Delta-Diode DD-650L 650 nm 100 MHz diode laser with DeltaDiode Controller and DeltaHub timing units using DeltaStation software. TRPL signals were detected using a Horiba PPD-900 Si CCD based picosecond photon detector mounted on a Horiba Jobin Yvon iHR320 fully automated spectrometer. The system was incorporated into an in-house bespoke PL/TRPL setup as shown in Figure 3.2.7. Additional TRPL experiments were performed at 6 K using 800 nm 1.5 ps laser pulses generated by a tunable mode-locked Ti:Sa laser with a repetition rate of 80 MHz. The laser beam is focused onto the sample on a 1/e^2 diameter spot of $\sim$100 μm and an average power of 20 mW. The PL signal is dispersed by a f-6.5 spectrometer and detected by a synchro-scan Hamamatsu streak camera with an overall time resolution of 15 ps. These measurements were done at Institut National des Sciences Appliquées, Toulouse.

3.2.3 Optical spectroscopy

When light is incident on a medium a proportion will be transmitted, absorbed and refected. The intensity of the transmitted light *I* shows an exponential decay dependant on the thickness *x* and wavelength-dependent absorption coefficient α such that $I = I_0(exp(-\alpha x))$. where I_0 is the intensity of the incident light. By measuring the transmittance T and reflectance R of a material using a spectrophotometer, α can be determined by:

$$\alpha(\lambda) = \frac{1}{x} ln \left[\frac{(1 - R(\lambda))^2}{T(\lambda)} \right] \tag{3.2.14}$$

where T and R are expressed as a fraction. The optical absorption spectrum of a semiconductor yields information on the energy band structure of the material. A sharp edge is observed in the absorption coefficient where the incident photons with energy lower than the optical bandgap of the material are not absorbed. In a direct bandgap semiconductor such as CZTSSe, α has a square root dependence on photon energy (in an ideal semiconductor [110]). According to Tauc *et al.*:

$$(\alpha h\nu)^n = A\,(h\nu - E_g) \tag{3.2.15}$$

where n = 2 for direct transitions and n = 1/2 for indirect transitions, h is Planck constant, ν is the frequency of the electromagnetic radiation and A is a constant of proportionality. For a direct bandgap semiconductor, the density of states (DOS) function (derived from the density per unit volume and energy of the number of solutions to Schrödinger equation) is given by:

$$g\,(\hbar\omega) = \frac{1}{2\pi^2} \left(\frac{2m^\star}{\hbar^2} \right)^{\frac{3}{2}} (\hbar\omega - E_g)^{\frac{1}{2}} \quad \text{for} \quad \hbar\omega > E_g \tag{3.2.16}$$

$$g\,(\hbar\omega) = 0 \quad \text{for} \quad \hbar\omega < E_g \tag{3.2.17}$$

where $g(\hbar\omega)$ is the joint conduction-valence density of states (i.e. the density of pair of states; one occupied valence state, one empty conduction state), $\hbar$ is reduced Planck constant ($\hbar = h/2\pi$), ω is angular frequency ($\omega = 2\pi\nu$) and $m^\star$ is the effective electron-hole mass. In terms of photon absorption in a semiconductor, the quantum mechanical transition rate depends upon the strength of the coupling between the initial and final quantum electron states and the number of ways the transition can occur. According to Fermi's golden rule, the transition probability λ_{if} takes the

form:

$$\lambda_{if} = \frac{2\pi}{\hbar} |M_{if}|^2 \, g(\hbar\omega) \tag{3.2.18}$$

where M_{if} is a coupling term called the matrix element for the transition. A transition will proceed more rapidly if the coupling between the initial and final states is stronger. For photon energies greater than the bandgap of the semiconductor, the transition rate is proportional to the DOS and, therefore, proportional to the material absorption coefficient such that (see Figure 3.2.8(a)):

$$g(\hbar\omega) \propto \alpha(\hbar\omega) \propto (\hbar\omega - E_g)^{\frac{1}{2}} \tag{3.2.19}$$

According to Equations 3.2.15 and 3.2.19, n will be equal to 2 for a direct bandgap semiconductor. An example of a Tauc plot is shown in Figure 3.2.8(b). Extrapolating the linear region of the plot to the abscissa yields the bandgap of the semiconductor.

(a)

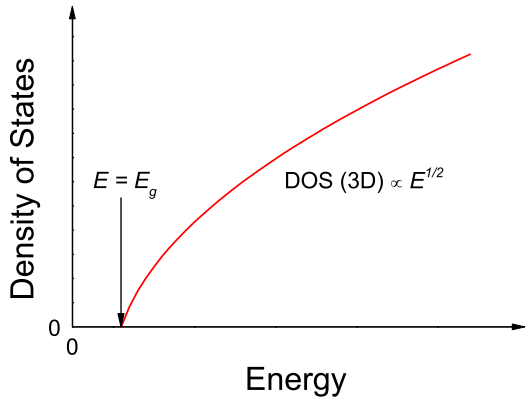

(b)

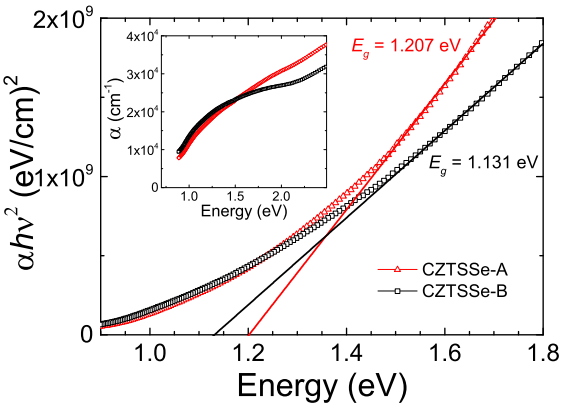

Figure 3.2.8: (a) Free-electron DOS in 3-dimensional k-space and (b) bandgap energies of two different CZTSSe thin films determined from Tauc plot with inset showing the absorption edge of the same films [17].

In a non-ideal semiconductor with high defect density, band tail states allow the absorption of photons with sub-bandgap energy. This sub-bandgap absorption in CZTSSe can be modeled in a number of ways, (i) Urbach tail (exponential), (ii) bandgap fluctuations (Gaussian) and (iii) electrostatic potential fluctuations. With regards to Urbach tails, the exponential tail appears in low crystalline, poor crystalline, disordered and amorphous materials because these materials have localized states which extended into the band gap. Urbach's rule takes the form [111]:

$$\alpha = \alpha_0 exp\left[\sigma\frac{(E - E_0)}{k_B T}\right] \tag{3.2.20}$$

where E_0 and α_0 are characteristic parameters of the semiconductor, σ is the steepness parameter and k_B is the Boltzmann constant. The Urbach energy E_u, which is temeprature-dependent, is defined as $E_u = k_B T/\sigma$ and is a measure of the exponential width of the sub-bandgap absorption tail. An example of Urbach tail fitting of the absorption edge in CZTSSe thin films is shown in Figure 3.2.9.

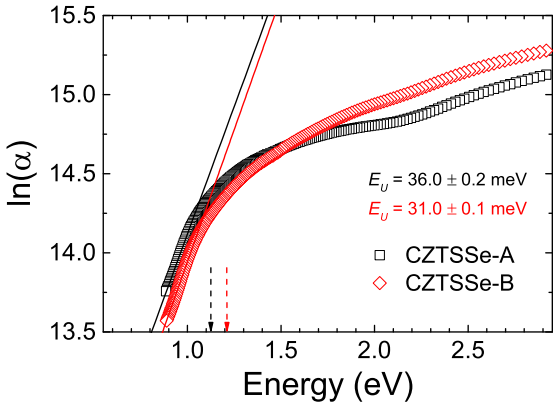

Figure 3.2.9: Determination of Urbach energy E_u from absorption coefficient of two different CZTSSe thin films. Fitted using Equation 3.2.20. The dashed arrows indicate the bandgaps of the respective absorbers [17].

Sub-bandgap absorption is also related to the presence of fluctuating potentials in the energy bands of the semiconductor. Regarding bandgap fluctuations a model assumes a Gaussian distribution of bandgap energies being centred at $E_{g.mean}$ and characterised by a standard deviation σ [54, 112]:

$$\alpha \propto \int_0^\infty \frac{1}{\sqrt{2\sigma}} exp\left[\frac{-(E_g - E_{g.mean})^2}{2\sigma^2}\right] \alpha_0(h\nu, E_g) dE_g \tag{3.2.21}$$

In the case of electrostatic potential fluctuations, the absorption coefficient can be described by

the mean amplitude of fluctuations y_{opt} (due to a random distribution of charged defects) such that:

$$\alpha \propto \exp\left[-\frac{2}{5\sqrt{\pi}}\left(\frac{E_g - h\nu}{\gamma_{opt}/2}\right)^{-\frac{5}{4}}\right] \tag{3.2.22}$$

Thus, it is possible to quantify the origin of band-tailing which is seen in non-ideal semiconductors such as CZTSSe. The absorption coefficient is also proportional to the internal quantum efficiency (IQE) of photovoltaic devices and depends on the density of states in the fluctuating potentials. Liu and Sites demonstrated IQE is also dependent on the effective carrier diffusion length L_d and the depletion region width w_d, $IQE = 1 - [exp(-\alpha w_d)/\alpha L_d + 1]$ [113]. Rearranging the equation gives:

$$\alpha \propto -ln(1 - IQE(h\nu)) \tag{3.2.23}$$

which is valid for small values of α/IQE (typically IQE < $\sim$ 0.3). In the absence of absorption data, the band-tailing parameter(s) can be determined from IQE measurements on complete solar cells. Therefore, the above absorption models can be applied to a plot of α vs. $h\nu$, see Figure 3.2.10.

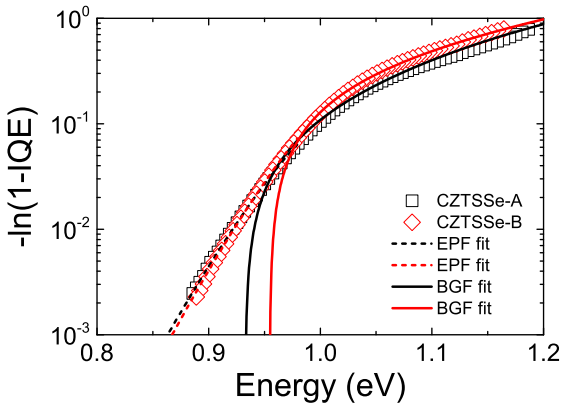

Figure 3.2.10: Plot of IQE data as a function of photon energy for two different types of CZTSSe solar cells. The IQE data is proportional to the absorption coefficients of the individual CZTSSe absorbers in the devices (Equation 3.2.23). Fits corresponding to the electrostatic potential fluctuation (EPF) and bandgap fluctuation (BGF) models are shown by dashed and solid lines, respectively.

It is apparent that the application of a single absorption model to the data of two different CZTSSe thin films does not adequately describe the observed behaviour. In this instance, a combination

of electrostatic potential fluctuations (EPF) and bandgap fluctuations (BGF) provide the best data fit.

Optical spectroscopy measurements were performed using a Shimadzu UV-2600 spectrophotometer fitted with an integrating sphere.

3.2.4 X-ray diffraction and grazing incidence X-ray diffraction

X-ray diffraction (XRD) is an analytical technique used to determine the crystalline properties of a material, such as unit cell dimensions. Monochromatic X-rays, typically generated from a Cu $K\alpha$ source, are directed towards the sample where they interact with the atoms within the material. The interaction of the incident rays with the sample produces constructive interference (and a diffracted ray) when conditions satisfy Bragg's Law, $n\lambda = 2dsin\theta$ (d is the crystal lattice spacing). The diffracted X-rays are then detected and counted. By scanning the detector through a range of 2θ angles a comprehensive diffraction peak pattern is compiled, see Figure 3.2.11. These diffraction peaks are correlated to unique d lattice spacings which are then compared to standard reference patterns to enable identification of the crystalline phases of the material.

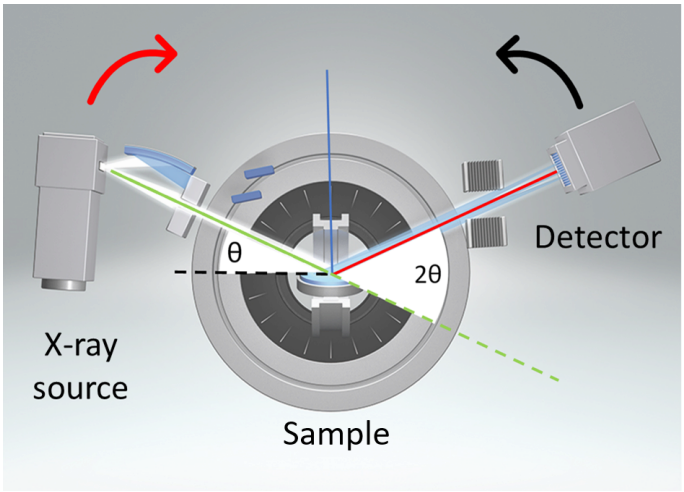

Figure 3.2.11: Schematic diagram of a typical XRD setup.

The penetration depth of the incident X-rays into the material being examined directly depends on the X-ray angle of incidence. Therefore, using small incident angles for the impinging X-rays allows the diffraction to become surface-sensitive. This is a technique called grazing incidence X-ray diffraction (GIXRD). Examples of GIXRD measurements of a thin film of CdS on soda lime glass (∼70 nm) and CdS/CZTSSe/Mo stack are shown in Figure 3.2.12. For the

CdS/CZTSSe/Mo thin film, as the X-ray grazing angle is increased from 0.10° to 0.35° the diffraction peaks associated with crystalline kesterite increase in intensity as the X-rays penetrate deeper into the thin film.

In this study, a Siemens D-5000 diffractometer using a Cu $K\alpha$ radiation source ($\lambda = 0.154$ nm) was used at beam voltage 40 kV and beam current 40 mA.

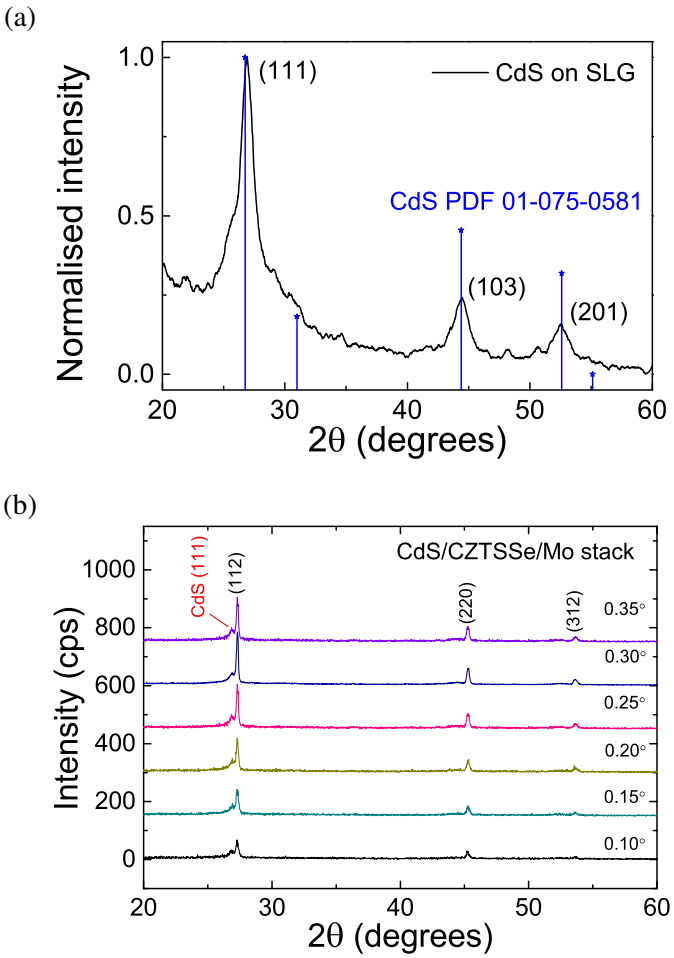

Figure 3.2.12: (a) GIXRD diffraction pattern of a 70 nm thick CdS film on soda lime glass at incidence angle 0.25° which matches standard pattern for cubic phase of CdS and (b) evolution of XRD peaks of a CdS/CZTSSe/Mo stack with increasing grazing incidence angle. Peaks at (112), (220) and (312) planes are assigned to kesterite CZTSe (PDF 052-0868).

3.2.5 X-ray photoelectron spectroscopy and inverse photoemission spectroscopy

X-ray photoelectron spectroscopy (XPS) is another analytical spectroscopic technique employing X-rays to probe the surface (typically $\sim$ 10 nm) of a material in order to determine the chemical and electronic states of the constituent elements in the material. Rather than measuring the

diffracted X-rays, as is the case for standard XRD analysis, photoelectrons generated within the surface of the material by X-ray irradiation are collected and analysed by an electron spectrometer to determine the photoelectron intensity and kinetic energy. As the energy of an X-ray with a particular wavelength is known (for X-rays from an Al $K\alpha$ source, the photon energy E_{photon} is 1486.6 eV) together with the kinetic energies of emitted electrons, the binding energy of each of the emitted electrons can be determined from $E_{binding} = E_{photon} - (E_{kinetic} + \phi)$, where ϕ is the work function which is dependent on both the material and electron spectrometer. The work function is adjusted to factor the loss of energy of the photoelectron when it is absorbed by the detector of the instrument. An example of an XPS spectrum from the surface of a CZTSSe thin film is shown in Figure 3.2.13.

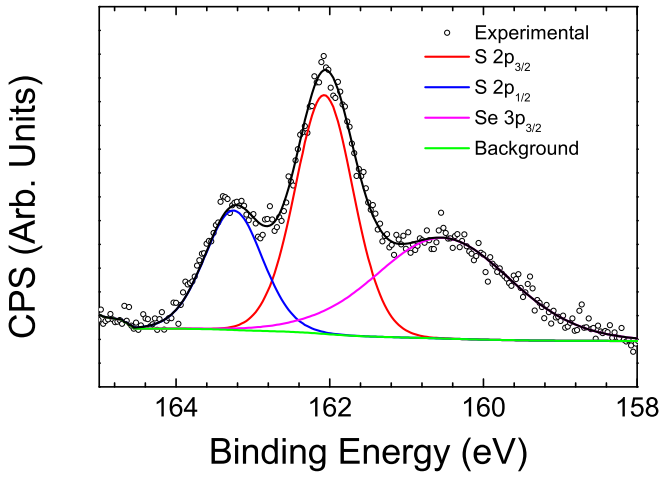

Figure 3.2.13: XPS spectrum from the surface region of a CZTSSe absorber thin film showing the electron binding energies of S 2p and Se 3p orbitals.

Inverse photoemission spectroscopy (IPES) is a form of photoemission spectroscopy which uses a beam of low energy electrons (< 20 eV) to probe the surface region of a sample. Electrons are absorbed by the material into high-lying unoccupied electronic levels and bremsstrahlung photons are emitted as the absorbed electrons decay to lower-lying states. Due to the low energy, the incident electrons are absorbed within a few atomic layers. Therefore, IPES is used to examine the unoccupied states in the CB (*i.e.* those states above the Fermi level E_F) whereas XPS measures the occupied states of the core-levels and VB [114, 115]. As the energy of the emitted photons E_{photon} can be measured and the energy of the incident electrons $E_{incident}$ is known, the final energy state of the absorbed electron E_{final} after it relaxes to the lower unoccupied energy level

in the CB can be derived due to conservation of energy law, $E_{incident} = E_{final} + h\nu$. The energy of the unoccupied state to relative to the Fermi level.

XPS measurements were performed in a standard ultra-high vacuum (UHV) chamber, which had a base pressure <2 x10^{-10} mbar, the main residual gas of which was hydrogen. A monochromatic Al Kα SPECS XR 50 M source ($h\nu$ = 1486.6 eV) operating at a nominal power of 250 W was used in conjunction with a PSP Vacuum Technology Ltd Resolve 120 MCD5 electron energy analyzer. The calibration of the spectrometer was performed by aligning the Ag $3d_{5/2}$ and Fermi level to their known energy positions of a clean polycrystalline Ag foil. By fitting the Fermi-Dirac distribution to the Ag Fermi level, the experimental resolution of the analyzer is found to be 0.37 $\pm$0.05 eV. The measured spectra are charge-corrected to the C 1s peak at 285.00 eV, due to adsorbed, adventitious carbon. The spectra were analysed using the CasaXPS software. Core-levels were fitted with pseudo-Voigt functions atop a Shirley background. VBM positions were found by linear extrapolation to the background. The errors on core-level binding energies and the VBM were determined to be $\pm$0.05 eV. IPES were performed in the same chamber using a PSP Vacuum Technology BaO cathode dispenser electron source and an isochromat NaCl photon detector, both of which were at 45° to the sample normal. The lowest unoccupied molecular orbital of a thick C_{60} multilayer, deposited in situ, was used to calibrate the photoemission spectra. The spectrometer resolution was determined to be 1.00 $\pm$0.10 eV from fitting the Fermi level of a clean, polycrystalline Ag foil. To obtain the interfacial samples, a PSP Vacuum Ltd ISIS 3000 ion source was used to Ar^+ ion (E_k = 0.25 keV) etch material away from the sample with an ion flux of 6.25 x10^{13} ions $cm^{-2}s^{-1}$ until the interface was visible in XPS measurements. This typically corresponds to an overlayer thickness of 2-3 nm. All XPS/IPES measurements were performed at the Stephenson Institute for Renewable Energy, University of Liverpool.

3.2.6 Scanning electron microscopy and energy dispersive X-ray spectroscopy

Scanning electron microscopy (SEM) uses a focused beam of high energy electrons ($\sim$ keV) to raster scan the surface of a sample to produce high magnification images. As in IPES, the electrons interact with atoms as they penetrate into the surface region of the sample material. A number of interactions can occur, producing various signals that contain information about the surface topography and composition of the sample, see Figure 3.2.14. Low-energy secondary electrons (SE) are ejected from the uppermost region ($\sim$ 5 - 10 nm) and are used to build a topographical image of

the surface. The brightness of the signal/image depends on the number of secondary electrons reaching the SE detector. In a sample with a rough surface, the angle of incidence of the scanning electron beam varies from perpendicular which increases the interaction volume and results in more secondary electrons being emitted from the sample. Thus steep surfaces and edges tend to be brighter than flat surfaces, which results in images with a well-defined, three-dimensional appearance. This effect can clearly be seen in the top and cross-sectional SEM images of CdS thin films deposited on SLG (Figure 3.2.15). The large agglomerates which formed during the chemical bath deposition appear as bright 'islands' on top of a conformal coating of CdS.

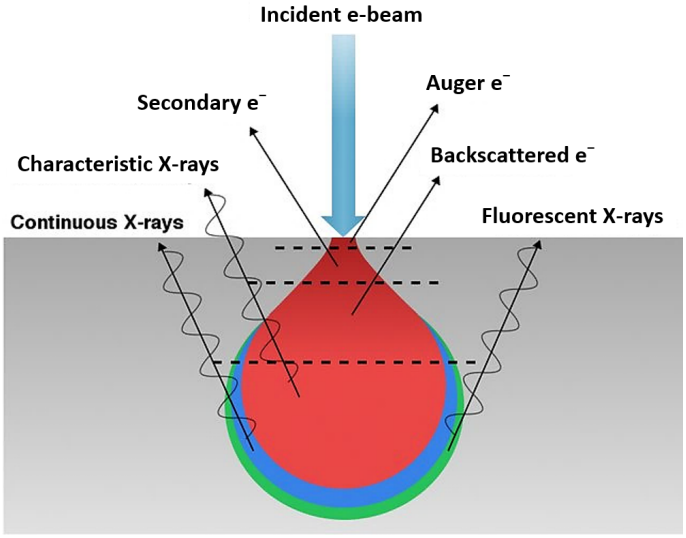

Figure 3.2.14: The interaction volume of an electron beam produces a number of effects depending on the penetration depth of the incident beam. SEM uses radiated secondary electrons for imaging whereas EDS utilises characteristic X-rays for elemental analysis [116].

In energy-dispersive X-ray spectroscopy (EDS) a high energy electron beam is used to stimulate the emission of characteristic X-rays.The number and energy of the X-rays emitted from a specimen is then measured by an energy-dispersive spectrometer. X-rays are emitted when an electron excited to a higher state by the incident beam relaxes to a lower energy state. This energy difference directly relates to the electron shells of the atomic structure of the radiating element and EDS allows the elemental composition of the specimen to be measured [117].

In this work, a Tescan Mira 3 FEG SEM was used for SEM imaging together with an Oxford Instruments X-Max X-ray spectrometer fitted with a 20 mm^2 detector operating at 10-20 kV for EDS measurements.

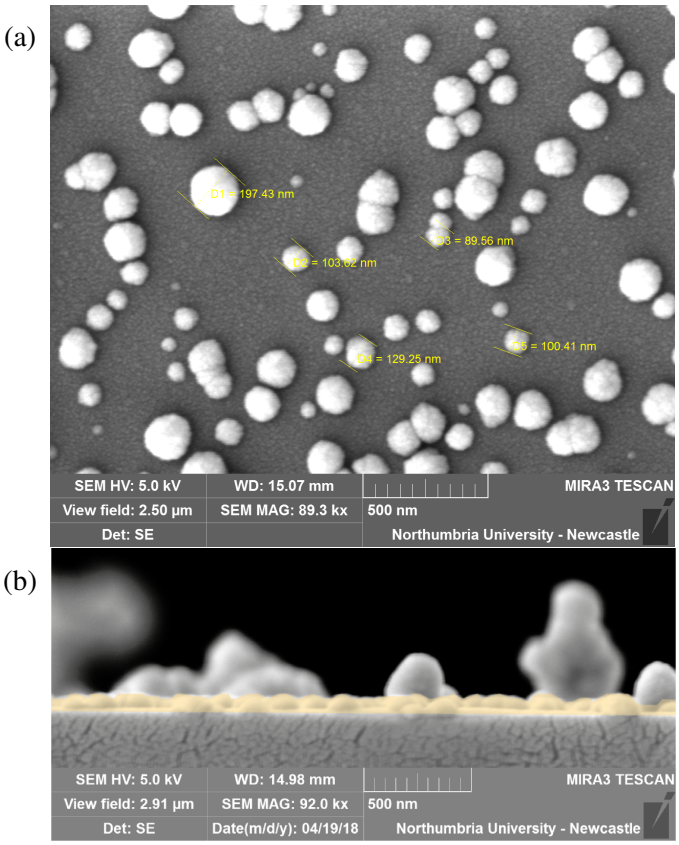

Figure 3.2.15: (a) Top SEM view of a thin CdS film on sodalime glass and (b) cross-sectional view of the same CdS sample showing large agglomerates on top of a $\sim$ 70 nm conformal CdS layer (shown in orange).

3.2.7 Raman spectroscopy

Raman spectroscopy is a non-destructive optical analysis technique providing detailed information on chemical structure, phase and crystallinity together with molecular interactions within the material. The main principle is the interaction of high intensity light source (usually a laser) with the chemical bonds within the molecules of the material which scatter the incident light. The vast majority of the scattered light is at the same wavelength as the laser source (Rayleigh scattering) but a minute proportion (typically 10^{-7}%) is scattered at different wavelengths induced by the vibrational mode of the molecules (Raman scattering). A Raman spectrum features a number of peaks, showing the intensity and wavelength position of the Raman scattered light. Each peak corresponds to a specific molecular bond vibration and a Raman spectrum typically has a number of peaks which provide a distinct chemical 'fingerprint' relating to a particular material. This allows easy identification of a material based on its Raman spectrum using comprehensive Raman spectral libraries. In kesterite compound CZTSSe, a number of secondary phases such as ZnSe

and Cu_2SnSe_3 may be present which cannot be easily identified as they have the same main (112) diffraction peak ($2\theta \sim 27.3°$). Raman spectra of these materials is different and each individual material can be distinguished.

Raman spectroscopy was performed with a Horiba microscope using a 632.8 nm HeNe ion laser.

3.2.8 Glow discharge optical emission spectroscopy

Glow discharge optical emission spectroscopy (GDOES) is a form of optical spectroscopy providing both quantitative and qualitative determination of elemental composition through a cross-section of material [118]. Typically, metallic samples are used as a cathode in a direct current plasma. Using a beam of argon ions, successive layers are removed from the sample by sputtering. The ejected atoms from the sample diffuse into the plasma and photons of a wavelength characteristic to the element are emitted from these excited atoms. The optical emission is then detected using a spectrometer. Non-metallic sample can also be analysed by using a high-frequency alternating voltage for plasma generation. An example of a GDOES profile of a CZTSSe/Mo thin film is shown in Figure 3.2.16.

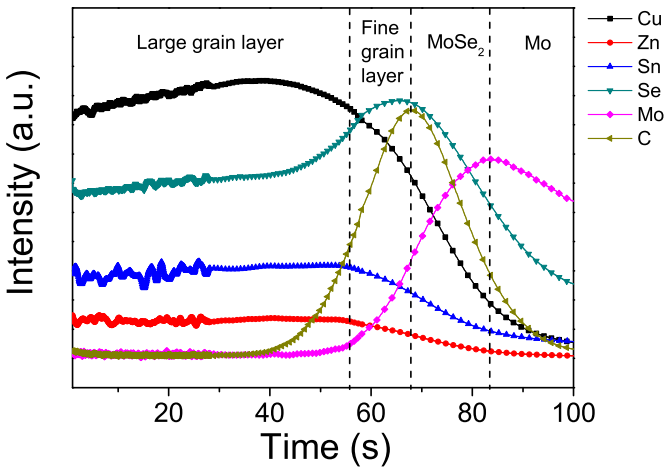

Figure 3.2.16: GDOES elemental depth profile of a CZTSSe thin film on Mo and sodalime glass. The analysis shows a high carbon content in the fine grain CZTSSe layer due to the oleylamine capping ligand used during CZTS nanoparticle ink synthesis [76].

Elemental depth profling in this study was performed by glow-discharge optical emission spectroscopy using a Horiba GD-profler 2 with sputtering done by an Ar^+ plasma with a crater size

of 4 mm in diameter. GDOES measurements were performed by Horiba Scientific, Longjumeau, France.

3.2.9 Inductively coupled plasma mass spectroscopy

Inductively-coupled plasma mass spectroscopy (ICPMS) uses a high-frequency inductively coupled plasma as ionisation source to fully decompose a sample into its constituent elements and transform those elements into ions.The ions are detected by a mass spectrometer used as a mass-charge filter device. ICPMS is a very sensitive technique capable of detecting elemental concentrations in the range of parts per billion (ppb).

A ThermoFischer Element Series 2 HR-ICP-MS system was used in this study for the compositional analysis of the precursor chemicals used to fabricate CZTS nanoparticle inks. ICPMS measurements were performed at Durham University.

3.3 Device characterisation

3.3.1 Current density-voltage measurement

Current density-voltage (*J*-*V*) measurements of solar cells under illumination and in the dark over a range of temperatures provide information on a number of device parameters, such as series R_s and shunt R_{sh} resistances, V_{oc}, J_{sc}, FF, η to name a few. Using a standard diode analysis of a thin-film solar cell [61, 119], R_s is extracted from the *y* intercept of the *dV/dJ* versus *1/(J+*J_L*)* plot according to:

$$\frac{dV}{dJ} = R_s + \frac{nkT}{q(J + J_L)} \tag{3.3.1}$$

where *n, k, T, q and* J_L are the diode ideality factor, Boltzmann constant, temperature, electron charge and photogenerated current density, respectively. Dark (as opposed to illuminated) series resistance was chosen to avoid any light-induced fluctuations in the series resistance that may occur under illumination. In this case, $J_L = J_{sc} = 0$. In the case of a PV device with a blocking back-contact (Schottky) barrier, the total series resistance $R_{s,D}$ in the solar cell is given by:

$$R_{s,D} = R_0 + \frac{k}{qA^*T} exp\left(\frac{\Phi_{BH}}{kT}\right) \tag{3.3.2}$$

where A^* is the effective Richardson constant, Φ_{BH} is the barrier height, R_0 is the background series resistance, due to top contact and bulk resistance which is usually small and approximately constant and therefore neglected in this analysis. From *ln(R_sT)* versus *1/kT* plot, Equation 3.3.2 is fitted to the high temperature region (low *1/kT*) of the curve and the slope yields the barrier height Φ_{BH}. An example of this type of analysis is shown in Figure 3.3.1, where a standard CZTSSe device on a SLG substrate is compared to a device on a flexible Mo foil subtrate.

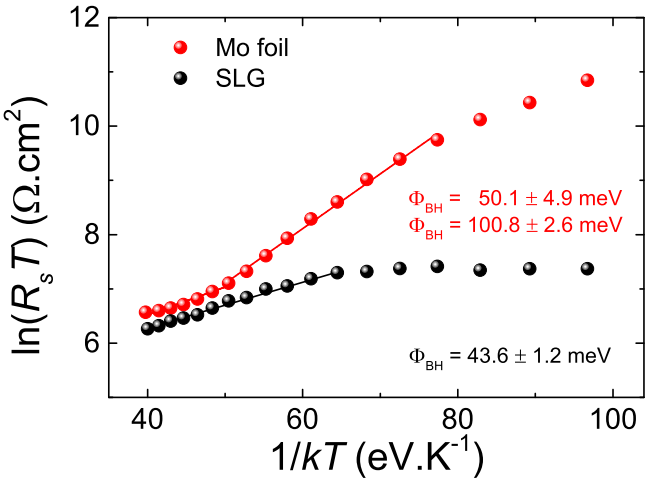

Figure 3.3.1: Barrier height extraction from ln(R_sT) vs 1/T plot of a standard CZTSSe solar cell on sodalime glass substrate and a cell on flexible Mo foil [62]. The solid line is the fit to Equation 3.3.2. The fitting to the cell on Mo foil suggests the presence of two barriers at the back contact (possibly due to a thick $MoSe_2$ layer which formed during selenisation of CZTS nanoparticle film).

Solar cell *J-V* parameters were measured using an Abet Technologies solar simulator at 1-sun (100 mW/cm^2) illumination equivalent to air mass 1.5 global spectrum with the light power density calibrated using a Si reference cell. A Keithley 2400 series source-meter in a four probe configuration was used to perform a voltage sweep from -0.8 V to 0.8 V with compliance current of 100 mA.

3.3.2 External quantum efficiency (including light/voltage biased) measurement

The external quantum efficiency (EQE) of a solar cell is the ratio of the number of photogenerated carriers collected by the device to the number of photons of a given energy or wavelength incident on the device. In an ideal solar cell, where all photons of a certain wavelength are absorbed and the resulting minority carriers are collected, the response curve takes the form of a Heaviside function

with a unity(zero) value for photon energies greater(lower) than the material bandgap. An example of an EQE curve is shown in Figure 3.3.2.

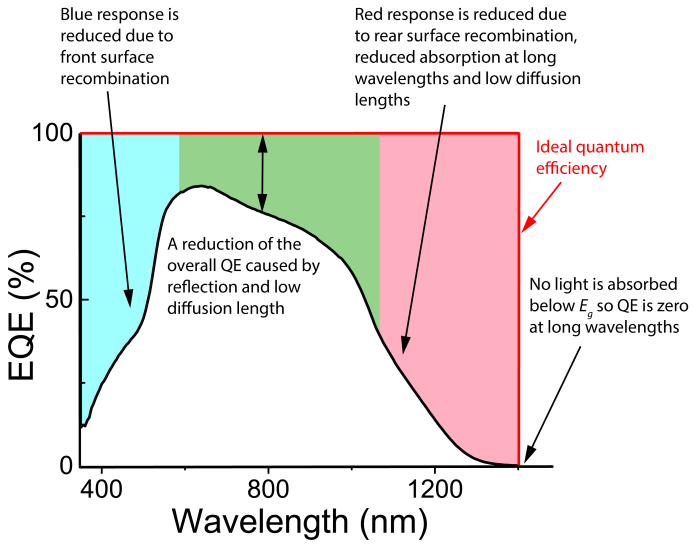

Figure 3.3.2: A typical EQE spectral response curve of a CZTSSe-based solar cell.

Inspection of the spectral response curve can provide qualitative information regarding the nature of loss mechanisms within the solar cell. For example, a reduced red response would suggest recombination at the rear absorber interface and low minority carrier diffusion length. It can also be seen that reflection of photons from the front surface of the device generally reduces the overall efficiency which can be overcome by the application of an anti-reflection coating (ARC) such as MgF_2. As such, the internal quantum efficiency (IQE) can be determined from EQE and reflectance data *R*, $IQE(\lambda) = EQE(\lambda)/(1 - R(\lambda))$. As discussed previously in section 3.2.3, $\alpha \propto -ln(1 - IQE(h\nu))$. Thus, measuring IQE of a solar cell allows the type and degree of band-tailing to be quantitatively determined, see Figures 3.2.10 and 3.3.3.

The minority carrier diffusion length L_d of an absorber material can also be evaluated from the spectral response of the associated device. Based on the assumption that the short circuit current density contribution J_{sc} for a given wavelength λ can be approximated by [120]:

$$J_{sc}(\lambda) = q[1 - R(\lambda)]N_{ph}(\lambda)\left[\frac{L_d}{(L_d + 1/\alpha)}\right] \tag{3.3.3}$$

where N_{ph} is the incident photon flux, L_d can be determined from EQE or IQE data as follows. From the known relation between EQE/IQE and J_{sc}:

$$EQE(\lambda) = \frac{J_{sc}(\lambda)}{qN_{ph}(\lambda)} = \frac{hc}{q\lambda}SR(\lambda) = IQE(\lambda)[1 - R(\lambda)] \tag{3.3.4}$$

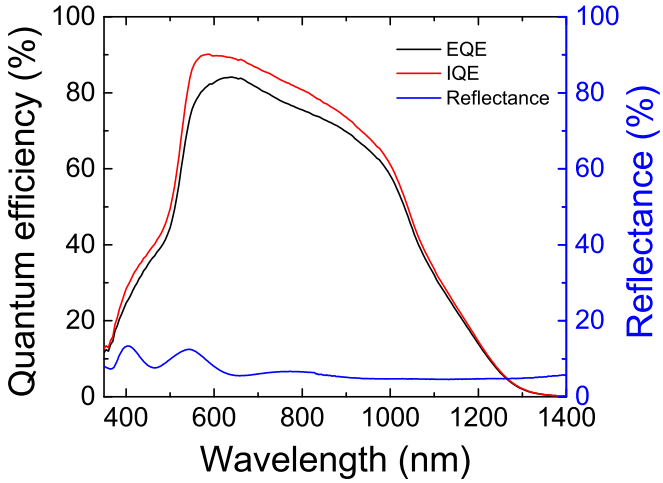

Figure 3.3.3: IQE and EQE measurements of a CZTSSe solar cell with reflectance data for the same device [17].

where SR is the Spectral Response (ratio of the current generated by the solar cell to the power incident on the solar cell), substituting for J_{sc} in Equation 3.3.4 and rearranging gives:

$$1/IQE(\lambda) = \frac{(L_d + 1/\alpha)}{L_d} \tag{3.3.5}$$

$$1/EQE(\lambda) = \frac{1}{1 - R(\lambda)} \left[\frac{(L_d + 1/\alpha)}{L_d} \right] \tag{3.3.6}$$

Therefore a plot of IQE^{-1} or EQE^{-1} versus α^{-1} should be linear with intercept on the α^{-1} axis equal to L_d [121].

Further information regarding solar cell parameters and performance can be gleaned by performing voltage-biased and light-biased EQE measurements. Incomplete collection of minority carriers generated beyond the 'effective' diffusion length ($L_{eff} = w_d + L_d$) into the absorber layer can be a significant loss mechanism. As the space charge region w_d around the *pn*-junction within a solar cell is voltage-dependent, applying a reverse bias extends the depletion region deeper into the bulk of the absorber. This provides insight into whether effective charge collection is affected by low L_d. Applying a white light bias during EQE measurements of an ideal solar cell will have a negligible effect on the spectral response. However, in thin film solar cells where there is a propensity for high concentrations of defects, charge collection may be affected due to charge trapping and photoconductivity [122].

External quantum efficiency measurements were performed using a Bentham Instruments

TM300 spectral response system with double grating monochromator and chopped light source. A voltage bias was applied using a Keithley 2400 series source-meter and light bias was provided by an integrated halogen lamp.

3.3.3 Capacitance-voltage and capacitance-frequency measurement

The space charge region (SCR) around the *pn*-junction of a solar cell behaves like a parallel plate capacitor such that:

$$C = \frac{\epsilon_0 \epsilon_r A}{w_d} \tag{3.3.7}$$

where C is the junction capacitance and A is the cell junction area. For a junction with an applied bias voltage *V* the width of the space charge layer is defined by:

$$w_d = \sqrt{\frac{2\epsilon_0 \epsilon_r (V_{bi} - V)}{q} \left(\frac{N_A + N_D}{N_A N_D} \right)} \tag{3.3.8}$$

where V_{bi} is the built-in voltage of the unbiased junction, N_A and N_D are the acceptor and donor densities, respectively. In the case of an abrupt junction of a *p*-type semiconductor where the *n*-side of the junction is heavily doped (pn^+), $N_D \gg N_A$ and $N_A + N_D \simeq N_D$, Equation 3.3.8 reduces to:

$$w_d = \sqrt{\frac{2\epsilon_0 \epsilon_r (V_{bi} - V)}{q N_A}} \tag{3.3.9}$$

Substituting for w_d in Equation 3.3.7 and rearranging gives:

$$\frac{1}{C^2} = \frac{2(V_{bi} - V)}{q \epsilon_0 \epsilon_r A^2 N_A} \tag{3.3.10}$$

A plot of $1/C^2$ versus V shows a linear relationship and $N_A \propto [d(1/C^2)/dV]^{-1}$. The space charge region width w_d can be determined by using Equation 3.3.7 at zero bias. An example of *C-V* measurements of CZTSSe solar cells with different buffer layers is shown in Figure 3.3.4.

C-V and *C-f* measurements were performed using an Agilent E4980a LCR meter and Ametek VersaSTAT 3 potentiostat/galvanostat, respectively.

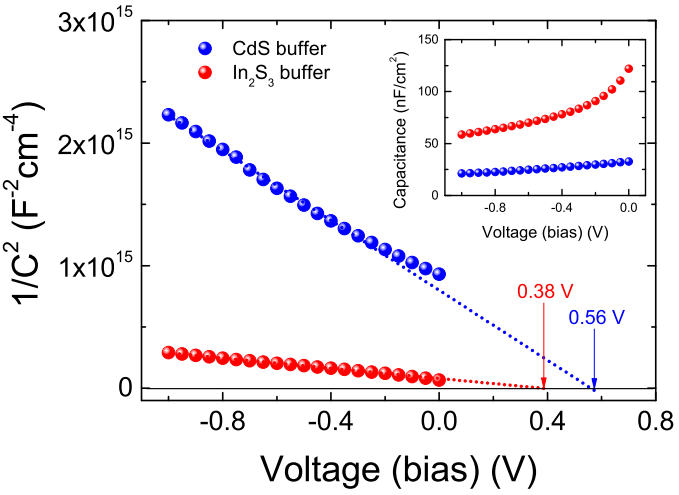

Figure 3.3.4: Determination of built-in voltage V_{bi} of two CZTSSe solar cells incorporating different buffer layers according to Equation 3.3.10 from *C-V* measurements shown in inset.

3.3.4 Deep level transient spectroscopy

As the name suggests, deep level transient spectroscopy (DLTS) is a temperature-dependent experimental tool used to identify defect traps which lie deep within the bandgap of a semiconductor. This measurement probes the effect of voltage pulses on the charge state of defects located within the SCR of the material. The voltage pulse causes the defects to become charged as free carriers penetrate the space charge region. This is possible as the voltage pulse reduces the electric field within the space charge region and the defects enter a non-equilibrium state. When the voltage returns to a steady state, trapped carriers at the defect sites begin to be thermally emitted. A capacitance transient is caused while the defects return to equilibrium. The voltage pulse followed by the defect charge state recovery are cycled allowing an application of different signal processing methods for defect recharging process analysis. The process results in an exponential capacitance change, where the emission rate e_T is the reciprocal of the emission rate constant τ_e. The emission rate is temperature-dependent and can be described by:

$$e_T(T) = \frac{1}{\tau_e} = \sigma_n v_{th} N_{C,V} exp\left[-\frac{(E_{C,V} - E_T)}{k_B T}\right] \tag{3.3.11}$$

where σ_T is the carrier capture cross-section, $N_{C,V}$ is the density of states in the conduction or valence bands, v_{th} is electron thermal velocity, $E_{C,V}$ is the conduction band minimum or valence band maximum, E_T is the trap level, k_B is Boltzmann's constant and T is temperature [123].

Equation 3.3.11 takes the form of an Arrhenius formula :

$$k = Ae^{\frac{-E_a}{k_B T}} \tag{3.3.12}$$

where A and E_a are the pre-exponential factor and activation energy for the process, respectively. Therefore, an Arrhenius plot will result in a linear relation where the activation energy $E_a \equiv E_{C,V} - E_T$ can be determined from the slope and carrier capture cross-section σ_T from the intercept.

The change in capacitance ΔC (from the capacitance immediately after the voltage pulse to the equilibrium capacitance) is also temperature-dependent. A plot of ΔC versus T reveals a spectrum where a maximum (minimum) in the curve indicates the presence of hole (electron) trap state, see Figure 3.3.5 [124]. The trap concentration N_T can be determined from the height of the peaks on the DLTS spectrum:

$$\frac{\Delta C}{C_0} \approx \frac{N_T}{2N_d} \tag{3.3.13}$$

where ΔC is the amplitude of the transient, C_0 is the equilibrium capacitance and N_d is the doping concentration. One type of DLTS signal processing method is deep level transient Fourier spectroscopy (DLTFS). Here the capacitance-time transients are discretised and converted to Fourier coefficients via numerical Fourier transformation. These coefficients are used to evaluate time constant and amplitude of the transients for the discrete trap levels.

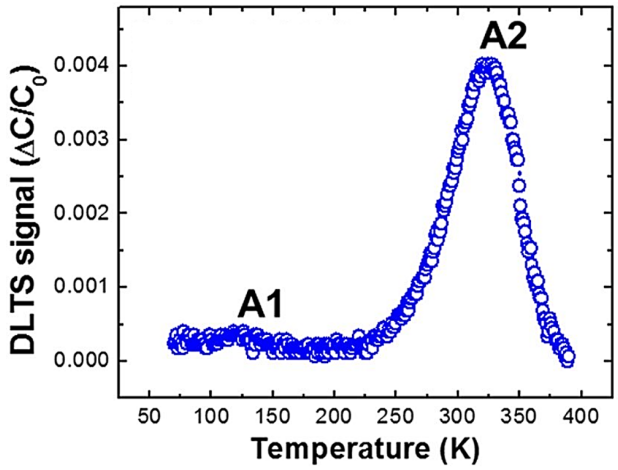

Figure 3.3.5: Example of a DLTS spectrum of a CZTSSe device showing the presence of hole trap states [17].

DLTS analysis was performed using a PhysTech FT1230 HERA DLTS system. Emission

capacitance transients were recorded using reverse and pulse biases of 5 V and 0 V respectively with a pulse duration of 10 ms. Three transient period widths were recorded 19.2 ms, 192 ms and 480 ms with time constants for the transients being determined via Fourier transform analysis [123]. Quality of the diodes was assessed prior to DLTS measurements using capacitance-voltage (*C-V*) and current density-voltage (*J-V*) analysis with *C-V* measurements being used to calculate shallow acceptor concentration N_A. A temperature range of 80-300 K was used however samples showed significant variation in reverse capacitance values above 220 K hence only data < 220 K was analyzed. DLTS measurements were performed at the Stephenson Institute for Renewable Energy, University of Liverpool.

Chapter 4

Absorber-back contact interface

The current record of 12.6% for a CZTSSe-based device has been obtained with a solution approach using reactive hydrazine as the solvent [43]. In a less hazardous environment, Cu_2ZnSnS_4 (CZTS) nanoparticle inks annealed in the presence of Se has resulted in a device with efficiency as high as 9.3% [48]. However, one of the current limitations of this method is the presence of a fine grain (FG) layer between the CZTSSe large grain (LG) layer and the back contact which is likely to reduce device performance via carrier recombination through traps, interface states and increased grain boundary density. This FG layer is a direct result of the use of a long carbon chain ligand, oleylamine (OLA), for the nanoparticle inks synthesis step. Alternative nanoparticle ink-based approaches have also been suggested [125].

Huang *et al.* recently suggested the use of formamide (FA) instead of OLA to produce single CZTS absorber layer without the FG layer [90]. Surprisingly, despite a complete comparison of the microstructure properties of the absorber layer [126], there is no functional device reported from nanoparticle synthesized with FA. In this chapter, working solar cells are demonstrated using a dual ligands approach via a stack of FA and OLA based absorbers: the FA absorber is used to provide a reduced back contact barrier height while the OLA absorber ensures a functioning *pn*-junction. Furthermore, the detailed luminescence properties of the two types of absorber and device parameters of working solar cells using dual ligands are presented.

4.1 Material properties

CZTS nanoparticles in this study were produced by injection of metallic precursors and sulphur into a hot solvent. OLA with long hydrocarbon chain was firstly chosen as the capping ligand to prevent the agglomeration of nanoparticles during fabrication (CZTS nanoparticles referred to as CZTS OLA). Alternatively, FA was chosen as the solvent in the synthesis of CZTS nanoparticles (referred to as CZTS FA). The resulting nanoparticle inks are then spin coated on Mo-glass substrates to make CZTS thin films. The thin films comprising CZTS nanoparticles were selenised in a tube furnace in order to promote grain growth, resulting in CZTSSe absorbers. The selenisation of CZTS thin films and subsequent fabrication of CZTSSe solar cells is previously described using methods detailed in Chapter 3.

XRD was first used to confirm and compare the crystal structure of the selenised films. In addition to the peaks belonging to Mo and $MoSe_2$, both spectra reveal distinct peaks of (112), (220), (312) planes that can be assigned to kesterite CZTSe (PDF 052-0868) as shown in Figure 4.1.1(a). However, these characteristic peaks are slightly shifted to higher angles as residual sulphur is present in the lattice (from EDS data Table 4.1.1). Due to the increased Cu/(Zn + Sn) and decreased Zn/Sn ratios, a zinc loss process was observed after selenisation for both samples. In addition, a difference in the selenium and sulphur exchange process (i.e. Se/(Se+S) ratio) is observed between the two samples. For the CZTSSe OLA sample, 89% of sulphur is replaced by selenium and this increases to 98% for the CZTSSe FA sample. Compared with the dense CZTS OLA precursor film, the porous structure of the CZTS FA sample (see Figure 4.1.2) is likely to facilitate more selenium diffusion and incorporation into the thin films.

The crystal quality of both samples was further studied by Raman spectroscopy to rule out possible binary and ternary compounds existing in the samples. As shown in Figure 4.1.1(b), the two sharp peaks at 172 and 195 cm^{-1}, and a weak peak at 235 cm^{-1} correspond to CZTSe [127]. The shoulder peak at 245 cm^{-1} belonging to $MoSe_2$ which formed at the back contact has low intensity when measured from the top of dense and homogeneous films [107]. Additionally, for the CZTSSe OLA sample, a wide peak at 328 cm^{-1} can be attributed to the A1 mode of residual CZTS [128]. This peak is negligible for CZTSSe FA sample as only 2% S remains in this sample after the selenisation process. Although derived from different solvent systems, both CZTSSe thin films have a high quality kesterite crystal structure with no obvious secondary phases observed.

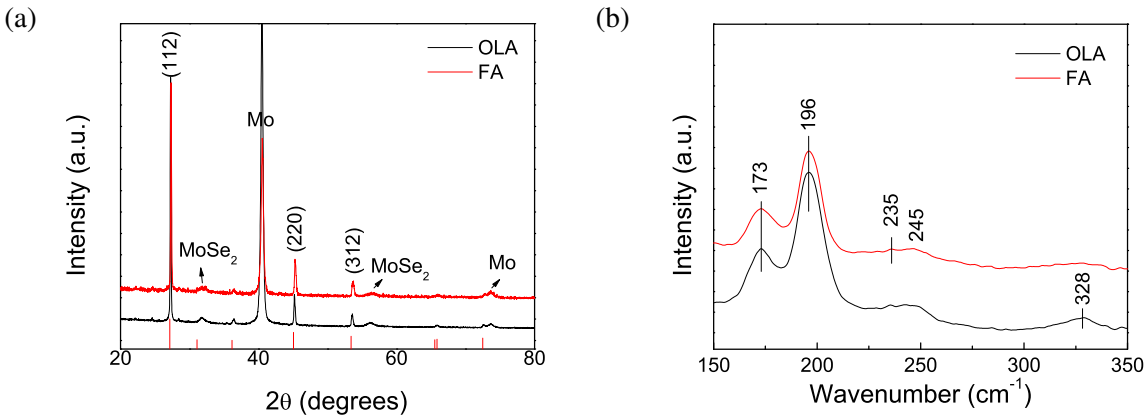

Figure 4.1.1: (a) XRD patterns and (b) Raman spectra of selenised CZTSSe absorber made from CZTS OLA and CZTS FA nanoparticles [76]. The distinct XRD peaks in (a) matched with the reference pattern of CZTSe (PDF 052-0868) given at the bottom.

Table 4.1.1: The composition of precursor and selenised CZTSSe thin films using OLA and FA ligands on bare SLG.

Solvent		Cu $(at\%)$	Zn $(at\%)$	Sn $(at\%)$	S $(at\%)$	Se $(at\%)$	$\frac{Cu}{Zn+Sn}$	Zn/Sn	$\frac{Se}{Se+S}$
OLA	Precursor	24.0	16.2	14.1	45.7		0.79	1.15	
	Selenised	22.4	12.6	12.7	5.8	46.6	0.89	1.00	0.89
FA	Precursor	21.8	16.3	12.8	49.1		0.76	1.30	
	Selenised	19.0	12.2	11.2	1.9	55.7	0.81	1.09	0.98

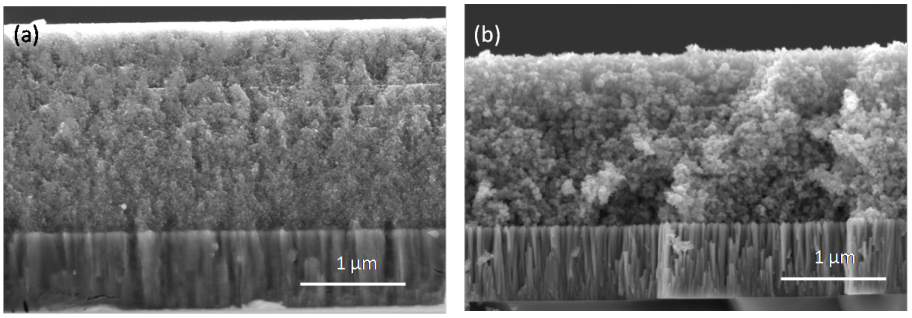

Figure 4.1.2: Cross-sectional SEM images of precursor thin films made from (a) CZTS OLA nanoparticles and (b) CZTS FA nanoparticles [76].

Further to the crystal property study above, the cross-sectional morphology of thin films after selenisation are given in Figure 4.1.3. The CZTSSe OLA thin film, shown in Figure 4.1.3(a) reveals a four-layer structure. The bottom layer is the columnar grain structured Mo with $MoSe_2$

layer on top formed under the selenium-rich annealing conditions. Above the metal contact, the CZTSSe absorber is composed of a bilayer structure with a top layer consisting of densely packed large grains (LGs) and a bottom layer composed of fine grains (FGs). In CZTSSe FA thin film however, the absorber is only composed of a single LG CZTSSe layer as shown in Figure 4.1.3(b) in agreement with [126]. Figure 4.1.3 also shows the relative carbon depth profiles in both absorber. CZTSSe OLA shows the characteristic high concentration of carbon in the FG layer while CZTSSe FA present a uniform signal throughout the absorber.

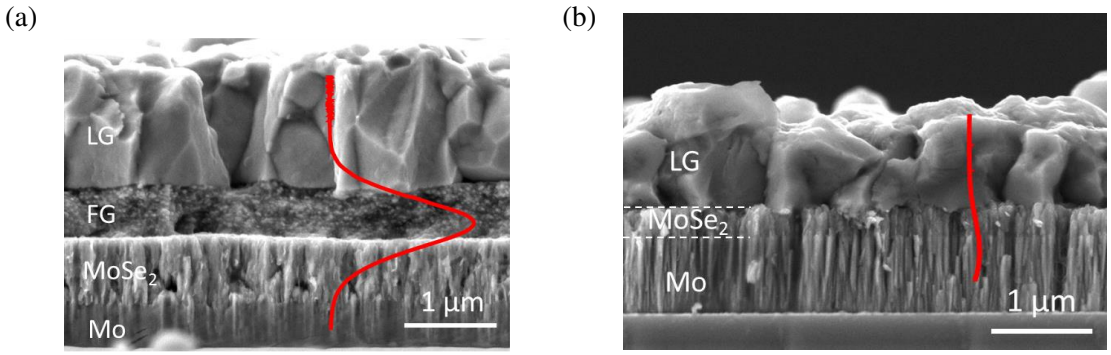

Figure 4.1.3: Cross-sectional SEM images of selenised absorber made from (a) CZTS OLA and (b) CZTS FA nanoparticle films [76]. The depth profiles of carbon measured by GDOES across the absorbers are given as the red curve in the figures, which are a qualitative indicator of the carbon-rich FG layer.

4.2 Excitation-dependent PL

The power-dependent PL spectra of the OLA and FA samples, measured at 6 K under equivalent experimental conditions, are presented in Figure 4.2.1. The luminescence for both samples is dominated by a broad asymmetric band with peak energies of ∼0.91 (∼0.86) eV for OLA (FA) samples. The lower peak energy value of the FA sample could be attributed to the higher Se content, see Table 4.1.1. From the figure, the saturation of the PL peak is evident as all the defect states become populated with increasing excitation intensity.

The blue-shifting PL peak together with the emergence of a higher-energy shoulder at higher excitation intensity observed in both OLA and FA samples are indicative of QDAP defects as the dominant recombination mechanism. The significant shift to lower energy of the PL peak compared to the energy bandgap (E_g) of the absorbers (∼ 1.14 eV for both OLA and FA) and broad asymmetric PL spectra also suggest the presence of charged defect clusters forming band

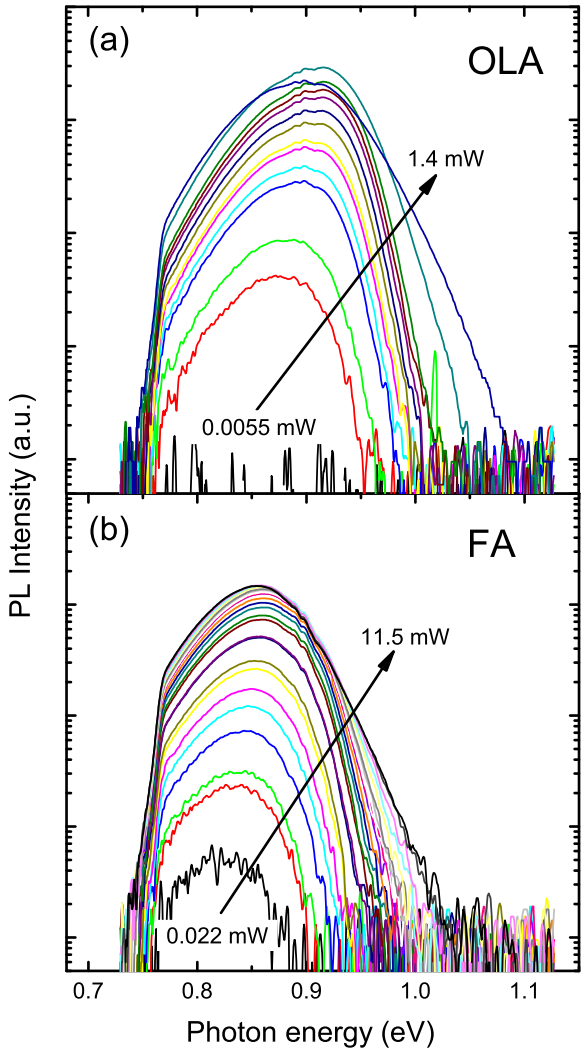

Figure 4.2.1: Excitation intensity dependencies of PL spectra in sample OLA (a) and sample FA (b) measured at 6 K [76].

tails, which consequently induce electrostatic potential fluctuations in the conduction and valence bands of the material.

The emergence of a higher-energy shoulder upon saturation of the PL peak is a further indicator that the lower-energy luminescence does not involve the bands. When the QDAP defects contributing to the PL peak saturate, further excitation injects carriers into extended band-type states and radiative recombination involves band-impurity or band-tail emission. A higher-energy shoulder was observed in both samples at excitation intensity exceeding the saturation threshold.

A power relationship $I \sim P^k$ was suggested [129] as a means of determining whether recom-

bination is band-to-band BB ($k > 1$) or involves defect states ($k < 1$), as previously discussed. The k power coefficient is evaluated by measuring the gradient of log-log plots of $I(P)$ as shown in Figure 4.2.2. For CZTSSe OLA sample, the estimated value of k is 0.75 ± 0.02. However, the plot for the FA sample suggests two linear regions which can be fitted by the power relation, with estimated k values of 1.23 ± 0.06 and 0.70 ± 0.02. It should be noted that $k > 1$, while suggesting band-related transitions, is not a general behaviour and it has been shown values $k > 1$ can also be observed for defect-related transitions involving neutral donors in CZTSSe absorbers [130]. Here, Levcenko *et al.* showed that the k value for a BI transition can approach values up to twice the k value for a DAP transition. Also, the saturation of the PL intensity with increasing excitation power could indicate the full occupation of the finite number of radiative defects. Nonetheless, it appears that several defect-related recombination mechanisms are present in the FA sample.

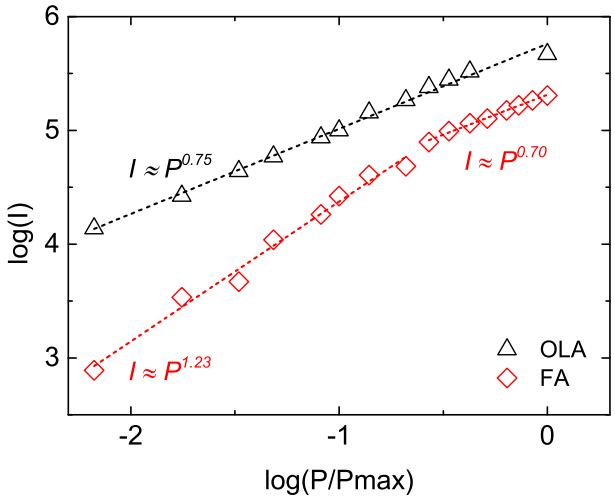

Figure 4.2.2: Log-log plot of the integrated PL intensity I as a function of excitation power for sample CZTSSe OLA and CZTSSe FA at 6 K [76]. The supralinear behaviour of the CZTSSe-FA data could indicate the saturation of radiative defects in this sample.

The shape $I(h\nu)$ of the PL spectra were fitted with the emperical double sigmoidal function proposed in [108, 131], see Figure 4.2.3. Thus, the blue-shift magnitude ΔE can be derived and QDAP separation s is derived from Equation 3.2.8 and substituting for s in 3.2.9 yields the QDAP density N_D. The calculated and experimental values of the dielectric constant and effective mass for CZTSSe from previous reports were used [16, 132]. The fit of the low energy tail of emissions described by Equation 3.2.8 yields the average amplitude of electrostatic potential fluctuations γ and the total defect density N_t can be derived using Equation 3.2.4. It should be noted that

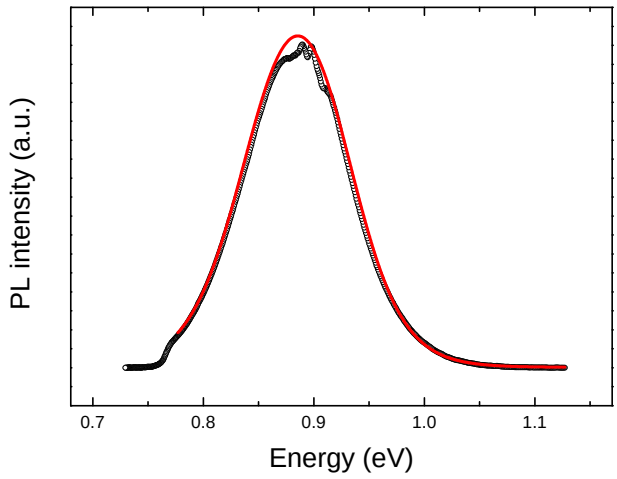

Figure 4.2.3: The PL spectrum (circle symbols) of sample OLA measured at 6 K, fitted with asymmetric double sigmoidal function (solid red line) [76]. The oscillation in the PL signal around 0.9 eV is due to water vapour absorption.

oscillations in the PL signal around 0.9 eV are due to water vapour absorption.

The optical parameters of OLA and FA absorbers are summarised in Table 4.2.1. Both samples show evidence of the presence of a fluctuating electrostatic potential with similar average amplitude γ and are comparable to those observed in hydrazine-based CZTSSe samples studied in [54]. The QDAP density in sample FA ($\sim 10^{16}$ cm^{-3}) is several orders of magnitude less than the OLA samples ($\sim 10^{18}$ cm^{-3}), whereas N_t in all samples is similar ($\sim 10^{19}$ cm^{-3}). The smaller proportion of QDAP defects to total defects in sample FA suggests a larger number of non-radiative defects are present in the sample. The QDAP defect clusters also have a greater spatial separation in sample FA.

In the fluctuating electrostatic potential model, electrons and holes are spatially separated and localised in potential wells within the valence and conduction bands as in Figure 3.2.5. In that case, any likely radiative recombination process requires the tunneling of charge carriers, thus an increase in the separation distance of the charged defect centres lowers the probability of a radiative transition.

Table 4.2.1: List of optical parameters of samples OLA and FA.

	OLA	FA
E_{PL} (meV)	0.907	0.861
ΔE (meV)	29.6	19.0
k	0.75	(1) 1.23
		(2) 0.70
γ (meV)	57.5	51.2
E_a (meV)	(1) 60.3 ± 8.2	39.3 ± 3.3
	(2) 7.6 ± 0.6	
E_0 (meV)	0.923	0.873
Defect spacing s (nm)	6.05	15.87
QDAP density N_D (cm^{-3})	1.08 x 10^{18}	5.97 x 10^{16}
Defect density N_t (cm^{-3})	9.34 x 10^{19}	6.98 x 10^{19}

4.3 Temperature-dependent PL

Temperature-dependent PL was measured using a laser power (4 mW) just below the power at which E_{PL} saturates for each sample, meaning the PL emission likely stems from pure QDAP recombination. Figure 4.3.1 shows the PL spectra of the OLA and FA samples as a function of temperature for a fixed laser power.

At 6 K, the spectrum is dominated by a peak at ∼0.91 (∼0.86) eV for the OLA (FA) sample. For the OLA sample, increasing the temperature causes this peak to red-shift up to approximately 100 K before blue-shifting. This behaviour has also been observed by Dirnstorfer *et al.* in $CuInGaSe_2$ (CIGSe) [99] and by Lin *et al.* in CZTSSe [133]. The behaviour can be explained by assuming carriers are trapped in different potential wells due to a lack of complete thermalisation, leading to an incomplete filling of the least energetic wells. Upon increasing temperature, the carriers become more dynamic and populate the deepest wells leading to a red-shift of E_{PL}. When all carriers occupy deeper potentials, E_{PL} reaches a minimum at the characteristic temperature of T=100 K for sample OLA. If the temperature is increased beyond the characteristic temperature, there is a blue-shift in E_{PL}, as shown in Figure 4.3.2(a).

The more distant carrier pairs are increasingly transferred to the bands leaving the close pairs thus producing a blue-shift in the emission peak. This red-shift to blue-shift behaviour in E_{PL} is indicative of the competition between QDAP transitions and band-impurity (BI) transitions with

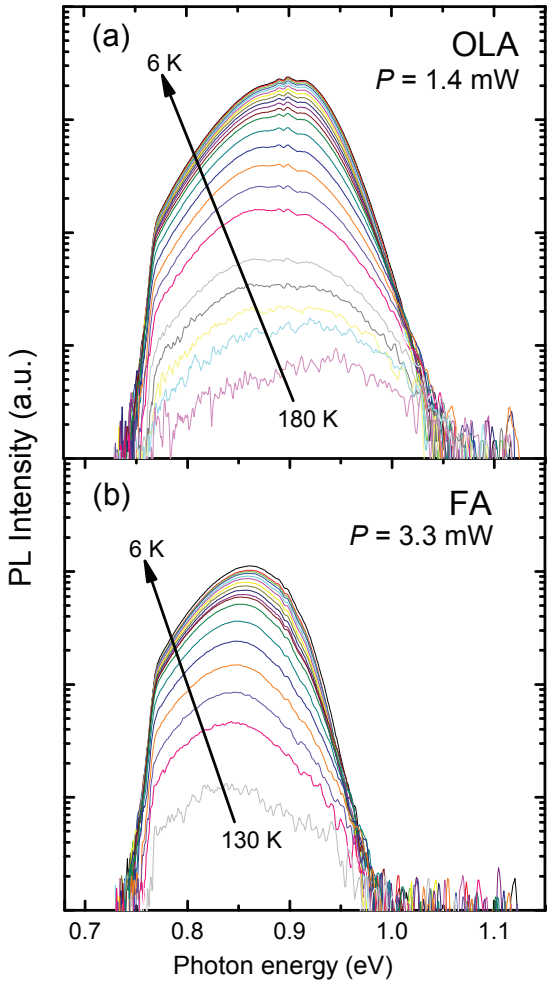

Figure 4.3.1: Temperature-dependent PL of sample OLA and FA with laser power below peak saturation intensity to avoid band-related recombination [76].

increasing temperature [134]. Also it was observed that temperature dependence of E_{PL} is different for both types of recombination [135], where a red-shift suggests QDAP recombination and a blue-shift indicates BI transitions. This is in agreement with the results of this study. Sample FA only exhibits a red-shift in E_{PL} before the emission is quenched $\sim$ 140 K, indicating that QDAP recombination is the only radiative mechanism. A schematic of the proposed recombination mechanisms for both types of absorber is illustrated in Figure 4.3.3.

To determine the activation energy of the defects involved in the recombination process, a one activation energy model was proposed [106] in the form of Equation 3.2.10. This model was used to fit the Arrhenius plots of both samples, the fitted curve for sample FA is shown in Figure 4.3.2(b). The one activation energy model provides a good fit to the experimental data for sample

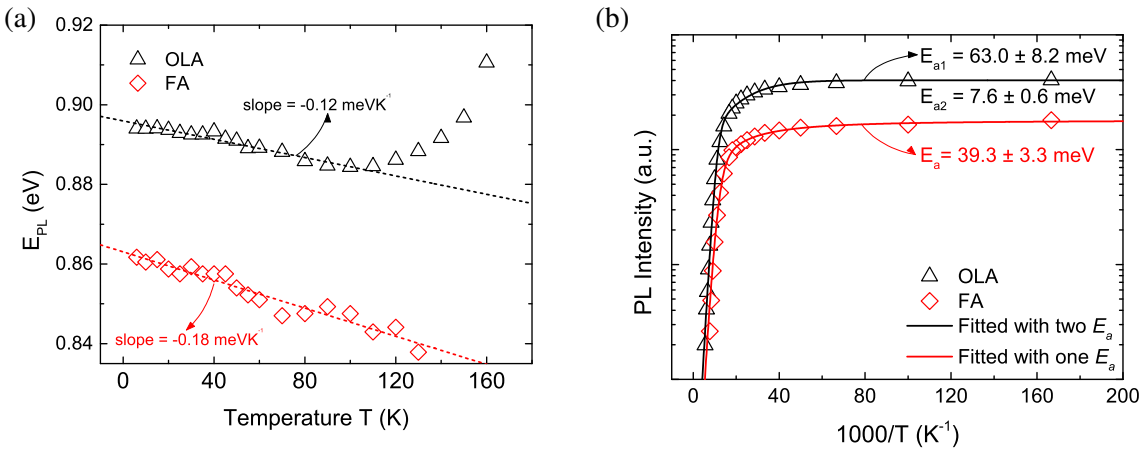

Figure 4.3.2: (a) Evolution of PL peak positions with increasing temperature T for sample OLA and FA, and (b) Arrhenius plot of the integrated intensities of the PL spectra of sample OLA and FA [76]. A two-defect model was used to fit the experimental data for sample OLA whereas a one-defect model was used to fit the sample FA data.

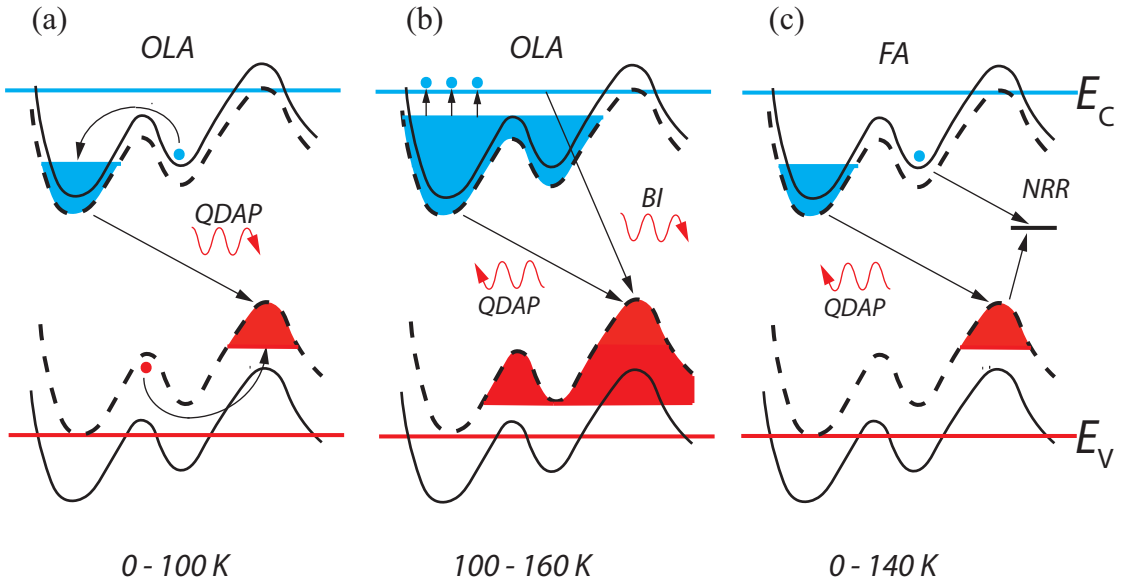

Figure 4.3.3: Schematic of the proposed recombination mechanisms in OLA and FA absorbers, (a) in OLA absorber at low temperature, carriers are trapped in different potential wells and least energetic wells are not completely filled. As temperature increases, carriers become more mobile and populate the deeper wells causing a red-shift in E_{PL} of QDAP transition in both absorbers, (b) above the characteristic temperature (100 K) in OLA absorber, the potential wells are filled and carriers are thermalised to the bands and radiative recombination occurs via BI transitions with a blue-shift in E_{PL} (c) in FA absorber, there are a higher proportion of non-radiative defect levels and non-radiative recombination (NRR) is more prevalent, preventing the deeper wells from being completely filled.

FA. However, the fitted curve is not accurate in the higher temperature regime of the Arrhenius plot for sample OLA. Therefore, a two activation energy model in the form of Equation 3.2.11 [107] was used to fit the experimental data. Here E_{a1} is the first activation energy, which is dominant for

the high temperature region (T>100 K for sample OLA) and E_{a2} is the second activation energy, which is dominant for the low temperature region (T<100 K for sample OLA).

By applying the above models values for activation energies of E_{a1} = 63.0 ± 8.2 meV, E_{a2} = 7.6 ± 0.6 meV and E_a = 39.3 ± 3.3 meV were determined for sample OLA and FA, respectively. These values are in reasonable agreement with those reported in [136] where $Cu_2ZnSnSe_4$ thin films were studied. The authors proposed a recombination model with an acceptor level above the valence band and a shallow donor level below the conduction band with an electrostatic potential fluctuation in the valence and conduction bands of the semiconductor.

For sample OLA at temperatures above the characteristic temperature, the shallow donor is ionised and the transition changes from QDAP to BI transition. The BI recombination involves electrons in the conduction band and distorted acceptor levels above the valence band. Conversely, sample FA did not exhibit this change in recombination mechanism and confirms QDAP transitions are the dominant recombination process. By considering the activation energy of the defect levels in the OLA and FA absorbers in conjunction with the kesterite defect study by Chen *et al.*, it is speculated that a defect complex ($[V_{Cu}{}^{-} + Zn_{Cu}{}^{+}]$ or $[Zn_{Sn}{}^{2-} + 2Zn_{Cu}{}^{+}]$) is present in sample OLA while a shallow acceptor antisite defect (V_{Cu} or Cu_{Zn}) is present in sample FA [37].

4.4 Device fabrication and analysis

FA and OLA CZTSSe absorbers were made into complete device structures as described in Chapter 3. While OLA-based device performed reasonably well (see later analysis) it was not possible to fabricate working solar cells using FA CZTSSe. Although Figure 4.1.3(b) showed a uniform FG layer-free absorber, large pores and voids are still present in the films even after a double selenisation process to densify the films (as shown in Figure 4.4.1).

As a result, any device made using FA CZTSSe resulted in shunted diode with no power output. In an effort to remove the FG layer from the interface with the back contact in a working device a dual layer structure was prepared: a FA CZTS precursor was selenised to provide a carbon poor back contact interface while OLA CZTSSe was used on top to provide a compact, void-free absorber. This results in the FG layer being sandwiched between two LG layers. Consequently, any voids between the CZTSSe FA grains are filled with the FG CZTSSe OLA material to ensure a continuous film as shown in Figure 4.4.2.

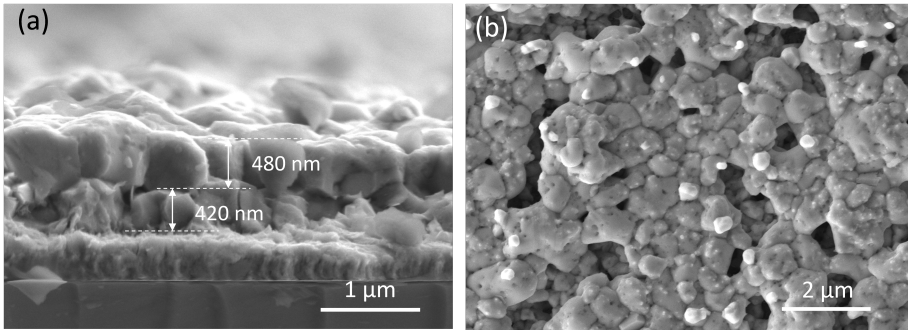

Figure 4.4.1: Cross sectional and top view SEM images of the double selenised CZTSSe FA thin film [76]. Five layers CZTS FA film was selenised followed by the selenisation of another five layers CZTS FA on top to attempt densifying the absorber. As shown in (a), the double selenised CZTSSe FA thin film is composed of two large grain layers. However, the thin film is still highly porous as shown in (b).

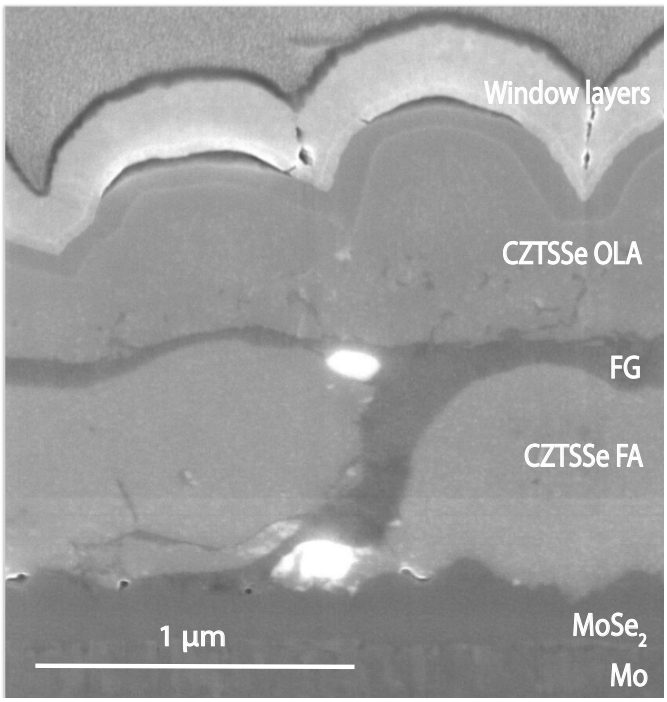

Figure 4.4.2: Cross-sectional SEM image of the device with a dual layer structure [76]. Focused ion-beam was used to prepare this specimen. The bright areas in the FG layer are indicative of a secondary phase identified as ZnSe from EDS.

Working devices were produced as a result of the elimination of shunting pathways following the deposition of the OLA layer. The distribution of cell parameters of all devices across the substrate are shown in Figure 4.4.3. For both types of device, open circuit voltages (V_{oc}) and fill factor (FF) variations are uniform across each substrate.

The OLA devices showed greater V_{oc} (40 mV on average) compared to OLA+FA while FF

was significantly lower (13%). The short circuit current density (J_{sc}) values were similar across both type of devices resulting in OLA+FA based devices outperforming those made from OLA only absorber. The light and dark *J-V* curves together with parameters of the best performing devices from each type of absorber are shown in Figure 4.4.4(a) and Table 4.4.1. Illuminated series resistance ($R_{s,L}$) for the OLA cell was 2.9 Ωcm^2 compared to a lower value of 0.6 Ωcm^2 for the OLA+FA cell with illuminated shunt resistance ($R_{sh,L}$) values of 175 and 122 Ωcm^2 for OLA and OLA+FA cells, respectively. The OLA+FA device exhibited an improvement in reverse saturation current density J_0 in contrast to the OLA device, with J_0 values of 2.8 x 10^{-2} and 4.8 x 10^{-1} mA/cm^2 for OLA+FA and OLA cells, respectively.

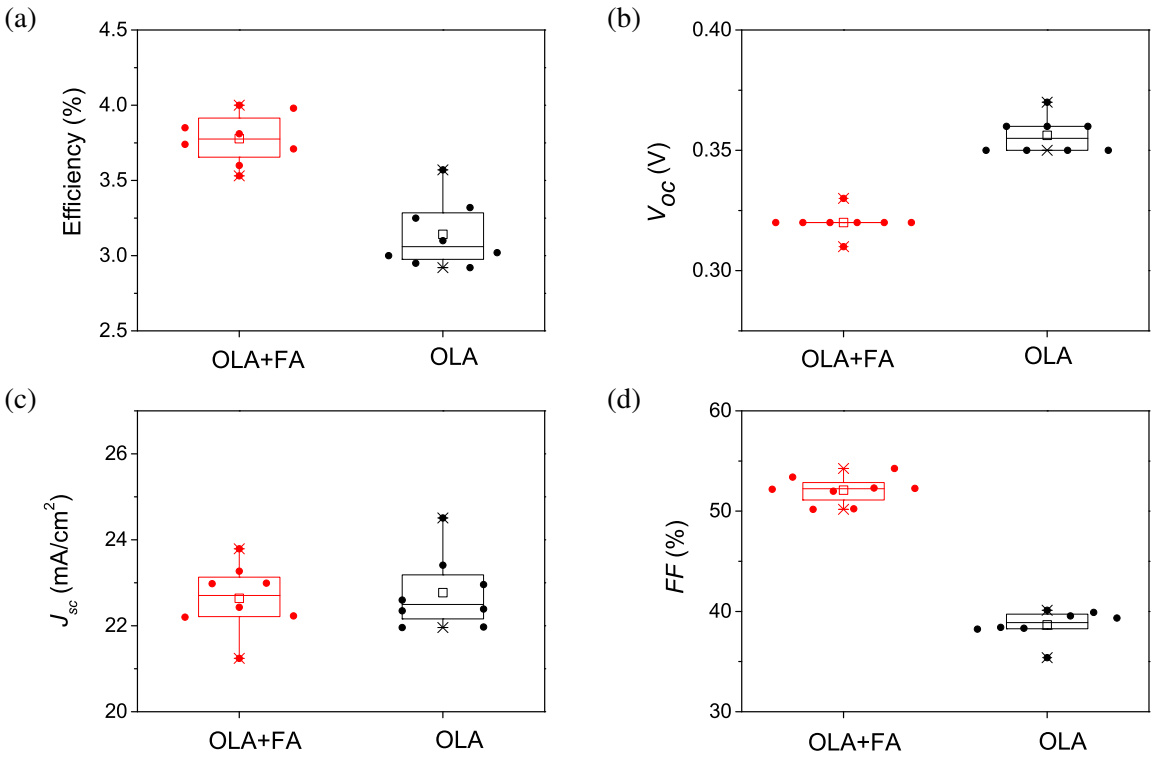

Figure 4.4.3: Box plots of the distribution of (a) efficiency, (b) V_{oc}, (c) J_{sc} and (d) *FF* of all devices on each substrate [76]. □ is the average value. × is the minimum and maximum position. The three horizontal lines of each box stand for the 25%, 50% and 75% of the reading distribution. The whisker range is determined by the standard deviation of the readings.

In-depth analysis of the most efficient OLA+FA device showed reduced dark series resistance ($R_{s,D}$ = 3.8 Ωcm^2) compared with the OLA only device ($R_{s,D}$ = 7.3 Ωcm^2). The temperature dependence of the dark series resistance ($R_{s,D}$) was studied using a standard diode analysis of a thin-film solar cell [61, 119] see Chapter 3. *J-V(T)* measurments were performed to determine R_s according to Equation 3.3.1.

Table 4.4.1: Device parameters for the best performing CZTSSe cells at room temperature with average values shown in brackets. $R_{s,L}$, $R_{sh,L}$, n and J_0 are the series resistance, shunt resistance, ideality factor and reverse saturation current respectively, measured using the light *J-V* data. All parameters were determined using methods described in Chapter 3.

CZTSSe cell	η (%)	*FF* (%)	V_{oc} (V)	J_{sc} (mA/cm^2)	$R_{s,L}$ (Ω cm^2)	$R_{sh,L}$ (Ω cm^2)	n	J_0 (mA/cm^2)
OLA	3.6	39.4	0.37	24.5	2.86	175	2.26	4.82 x 10^{-1}
	(3.2)	(38.9)	(0.36)	(23.1)				
OLA+FA	4.0	54.3	0.32	23.8	0.57	122	1.96	2.75 x 10^{-2}
	(3.8)	(52.1)	(0.32)	(22.6)				

Figure 4.4.4(b) shows the diverging dark series resistance of the OLA and OLA+FA cells towards lower temperature. $R_{s,D}$ of the OLA cell increases $\sim$17 fold from 300 to 130 K compared to only $\sim$4 fold increase for the OLA+FA cell. An explanation for this diverging series resistance is the presence of a blocking back-contact (Schottky) barrier as proposed by [52]. The presence of the barrier would act to suppress the hole transport across the Mo back contact to the CZTSSe absorber layer. In this Schottky diode model , the total series resistance $R_{s,D}$ in the solar cell is given by Equation 3.3.2.

From *ln(R_sT)* versus *1/kT* plot, Equation 3.3.2 is fitted to the high temperature region (low *1/kT*) of the curve and the slope yields a barrier height Φ_{BH} of 15.6 and 35.8 meV for the OLA+FA and OLA cells, respectively (see Figure 4.4.4(c)). The low barrier height for the OLA+FA device could be considered a quasi-ohmic contact, as evidenced by lower $R_{s,D}$ and higher *FF* compared to the OLA device. A similar trend in device parameters was reported by [52].

Both devices showed crossover of the dark and light *J-V* curves, as indicated by the solid circles in Figure 4.4.4(a). These crossover points occur at a lower current value for the OLA cell than the OLA+FA cell also demonstrating the presence of a larger barrier in the OLA device [137]. An alternate explanation for the observed divergence of $R_{s,D}$ has been hypothesised. Admittance spectroscopy analysis of CZTSSe solar cells by [132] showed the apparent divergent behaviour in $R_{s,D}$ arises out of a carrier freeze-out effect due to lack of shallow acceptors in the CZTSSe absorbers.

The temperature dependence of n for both devices are shown in Figure 4.4.5(a). It is evident that the ideality factor for both types of device increases above two as temperature reduces, sug-

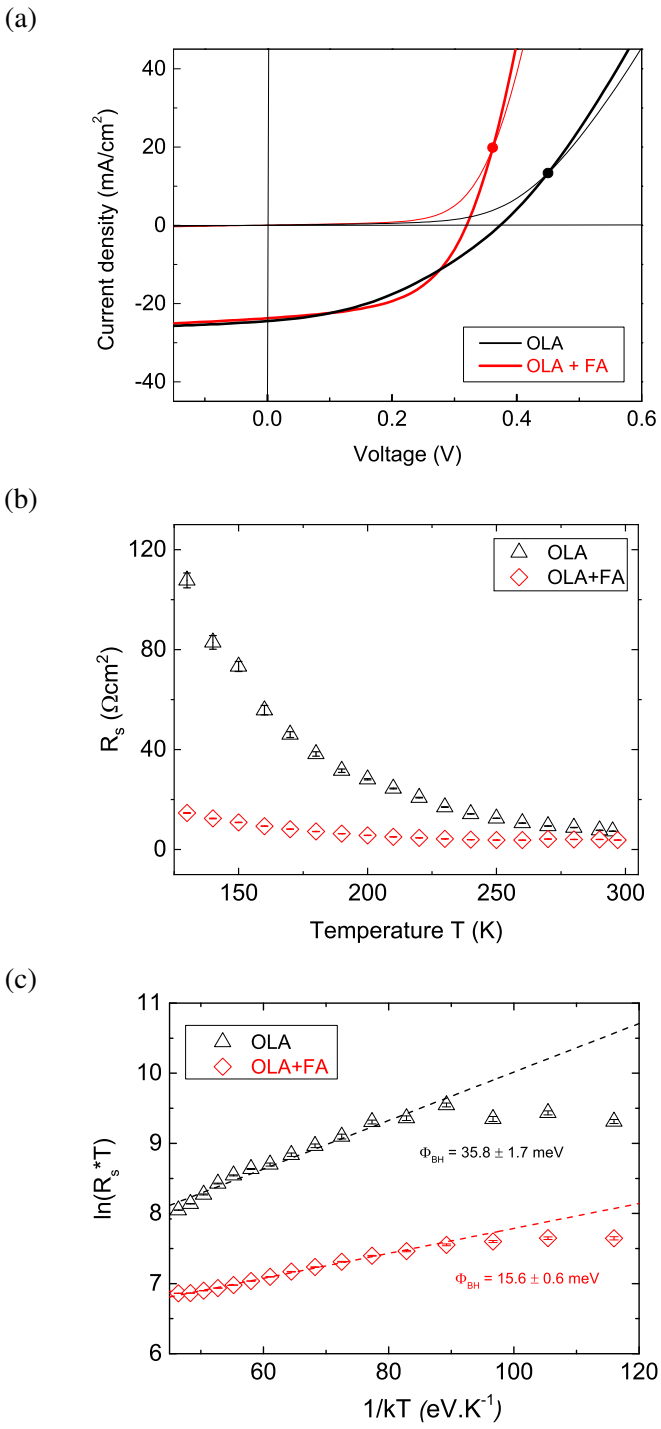

Figure 4.4.4: (a) Light (thick curves) and dark (thin curves) *J-V* charactersitics of OLA and OLA+FA CZTSSe solar cells [76]. Solid circles mark the cross-over point between light and dark *J-V* curves, (b) temperature-dependent dark series resistance and (c) barrier height extraction from $\ln(R_sT)$ vs $1/T$ plot, the dashed line is the fit to Equation 3.3.2.

gesting a mechanism other than Shockley-Read-Hall (SRH) recombination is present. Regarding SRH recombination, n assumes values between one and two and is almost independent of temper-

ature. A number of factors influence the value of n, such as recombination centre(s) energy, their capture cross-section, distribution and location within the absorber [61, 138–140].

One explanation for the temperature dependent behaviour of n relates to a tunneling-enhanced recombination mechanism, where the SRH recombination rate is augmented by contributions from tunneling [89, 138, 141]. Tunneling enhanced recombination can occur (i) in the depletion region of the *pn*-junction due to high densities of mid-gap defect states (*bulk*-dominated tunneling-enhanced recombination) and (ii) at the heterojunction between absorber and buffer due to high densities of interface defect states (*interface*-dominated tunneling-enhanced recombination). Such a tunneling-enhanced recombination model is frequently applied to Cu(In,Ga)(S,Se)$_2$ (CIGSSe) and CdTe based solar cells [140] where the tunneling-enhanced recombination current is found to increase with increasing characteristic tunneling energy (E_{00}) and decreasing temperature. Application of this model reveals a continuous transition of n to values greater than two as the temperature is decreased, similar to the ideality factor data for the CZTSSe devices presented here.

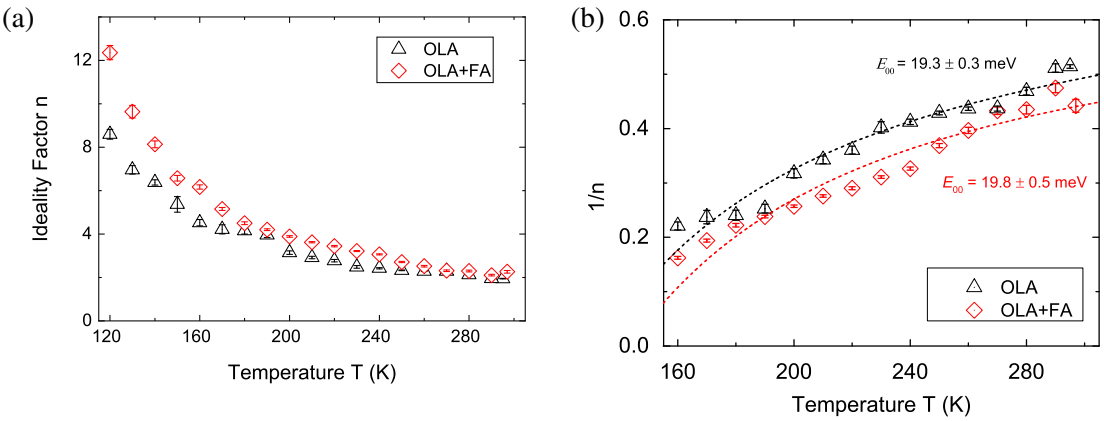

Figure 4.4.5: (a) Temperature-dependent ideality factor n in the dark and (b) $1/n(T)$ vs T plot [76]. The solid fitted lines to the data represent a fit to Equation 4.4.1 for the measured data.

In considering *bulk*-dominated tunneling-enhanced recombination mechanism, the ideality factor can be expressed as:

$$\frac{1}{n} = \frac{1}{2}\left(1 - \frac{E_{00}^2}{3(kT)^2} + \frac{T}{T^*}\right) \tag{4.4.1}$$

where E_{00} is the characteristic tunneling energy and kT^* is the characteristic energy of the distribution of trap states near the band edge associated with band-tailing or potential fluctuations [142]. Fitting Equation 4.4.1 to $1/n$ versus T plots in Figure 4.4.5(b) yields an estimate of E_{00} values of 19.3 and 19.8 meV for sample OLA and OLA+FA respectively, comparable to values determined

by Hages *et al.* [142]. Nadenau *et al.* showed a close relationship between open-circuit voltage V_{oc} and the characteristic tunneling energy E_{00}, where a link was established between efficiency gain in use of Ga-rich $CuGaSe_2$ absorbers and decreased tunneling rates. They suggest device modifications such as the change of CdS deposition temperature have beneficial effects of lowered E_{00} and increased V_{oc} [89].

It is apparent that a tunneling enhanced mechanism dominates in both devices at low temperature with a reducing tunneling contribution as T approaches 300 K. The possibility of *interface*-dominated tunneling-enhanced recombination was considered but discounted following analysis of the experimental data. In the limit of *interface*-dominated tunneling-enhanced recombination mechanism, the ideality factor follows:

$$n = \frac{E_{00}}{kT} coth\left(\frac{E_{00}}{kT}\right) \tag{4.4.2}$$

However, analysis of *n(T)* according to Equation 4.4.2 did not provide a good fit for the experimental data, see Figure 4.4.6. Applying this model to the data yields E_{00} values of $\approx$ 56 and $\approx$ 64 meV for sample OLA and OLA+FA, respectively. In order to ascertain which recombination mechanism is dominant in the OLA and OLA+FA devices, the origin of the characteristic tunnelling energy can be considered, according to [138]:

$$E_{00} = \left(\frac{q\hbar}{2}\right)\left(\frac{N_A}{m^*\epsilon_s}\right)^{\frac{1}{2}} \tag{4.4.3}$$

where $\hbar$ is the reduced Planck constant, N_A is the net doping density , m^* is the effective tunneling mass, and ϵ_s is the dielectric constant of the semiconductor material whose values determined by [16, 132] were used. If *bulk* tunneling-enhanced recombination is assumed to be the dominant mechanism, using Equation 4.4.3 results in a net doping density N_A of $\approx$ 6 x 10^{17} and $\approx$ 7 x 10^{17} cm^{-3} for the OLA and OLA+FA devices, respectively. The estimate of the net doping density is reasonable under the *bulk*-dominant tunneling enhanced recombination mechanism, specifically for recombination in the SCR near the junction where high defect densities are to be expected [142]. However, using Equation 4.4.3 to evaluate the net doping density from E_{00} values assumed under the *interface*-tunneling model gives N_A values of $\approx$ 8 x 10^{18} cm^{-3}. This would indicate a substantially high recombination current at the CdS/CZTSSe interface and would lead to a significant reduction in J_{sc}. Such a reduction was not observed in either device under study. Furthermore, Hages *et al.* state that the *bulk* tunneling-enhanced recombination mechanism correlates with the

potential fluctuations model (as discussed previously) from $J_0(T)$ analysis [142].

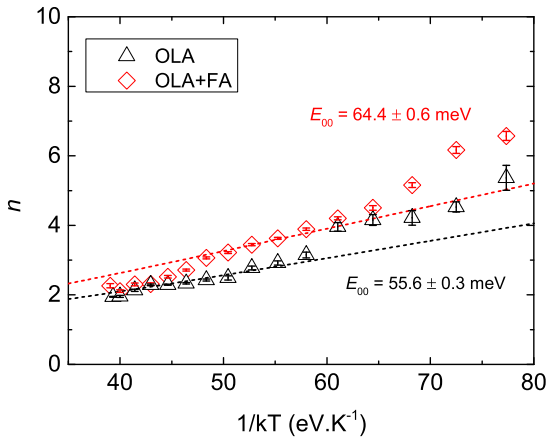

Figure 4.4.6: $n(T)$ vs $1/kT$ plot [76]. The dashed lines represent a fit to Equation 4.4.2.

4.5 Summary

The luminescence properties of CZTSSe thin film layers prepared from CZTS nanoparticle inks have been investigated with respect to the ligand type used during the nanocrystal synthesis. It is suspected that QDAP is the dominating recombination mechanism in both type of absorbers showing similar level of potential fluctuation ($\sim$ 50 meV). The temperature-dependent PL analysis revealed a shift in recombination mechanism in OLA CZTSSe from QDAP to BI as temperature increases while QDAP remained the sole recombination process in FA CZTSSe. Due to the porosity of the FA CZTSSe layer it was not possible to produce solar devices however when using a dual layer FA+OLA this was found to outperform devices based on OLA CZTSSe alone. The main reason for this was the reduction of the back contact barrier height in OLA+FA devices yielding lower series resistance, reverse saturation current, diode ideality factor and higher fill factor. This is a consequence of the removal of the fine grain layer at the Mo back contact interface and gives promising new outlook for this particular synthesis route. The next chapter will look at factors affecting CZTSSe device performance arising from the absorber material bulk.

Chapter 5

Absorber bulk

In this chapter, the behaviour of nanoparticle-based CZTSSe absorbers and solar cells made from relatively low and high quality grade chemicals is investigated with a view to improving cost-effectiveness of the ink-based fabrication process. PL spectroscopy revealed the presence of similar shallow acceptor plus shallow donor states in both low and high purity precursor absorbers. A relationship is demonstrated between the average depth of energy band-edge potential fluctuations and absorber quality where the higher grade chemical precursor-based absorber outperforms the lower purity version. In addition, the low purity precursor absorber had a higher total defect density resulting in a 10 meV increase in the average electrostatic potential fluctuations. Deep level transient spectroscopy (DLTS) in solar devices indicated the presence of detrimental deep defect states in both types of absorber. Notwithstanding the high purity precursor absorber with lower defect density, the power conversion efficiencies of both types of CZTSSe solar cells were similar ($\sim$5%), implying an issue other than defects in the absorber bulk inhibits device performance as evidenced by quantum efficiency analysis and current-voltage measurements (in this range of efficiency values).

Polycrystalline thin-film solar cells are inherently susceptible to the formation of mid-gap defects, which act as electron traps within the bulk of the absorber, and defects at the buffer-absorber interface which inhibit charge transport. Due to the complexity of the pentanary kesterite crystal structure, a variety of intrinsic lattice defects can form which influence the optical and electronic properties of the CZTSSe absorber [37]. Density functional theory and first principle calculations have been employed to identify a number of intrinsic defects in bulk CZTSSe, which range from charged point defects such as elemental vacancies, antisites and interstitials to neutral

defect complexes. Some defects, like shallow acceptors V_{Cu}^{-} and Cu_{Zn}^{-}, are beneficial and are responsible for the *p*-type conductivity of the absorber. Conversely, deleterious defects such as deep donor antisites Sn_{Cu}^{3+} and Sn_{Zn}^{2+}, form mid-gap traps which act as effective electron-hole recombination centres.

Band-tails may also be present within the kesterite bulk which have been suggested as contributing to SRH recombination [143]. Two rudimentary processes are understood to cause band-tailing: i) an elevated concentration of highly-compensated charged defects which result in an electrostatic potential fluctuation of the valence and conduction bands (VB and CB, respectively) and ii) changes in compositional and/or crystalline homogeneity of the absorber, which cause the VB and CB edges to waver, inducing bandgap fluctuations [54].

Complementary PL and DLTS techniques were used to study nanoparticle-based CZTSSe thin films and devices fabricated from low and high purity precursor chemicals (subsequently referred to as film LP and HP, respectively). The evolution of PL spectra over a range of cryogenic temperatures can be used to elucidate details of shallow defects within both types of CZTSSe absorber, whereas DLTS is used to probe deeper, mid-gap states. Employing both techniques in conjunction provides comprehensive quantitative information on root-mean-square potential fluctuation depths of band egdes (γ), defect activation energies (E_A), defect concentrations (N_t) and defect capture cross-sections (σ_t) of both types of absorber, which is correlated to the structural quality of the material.

5.1 Material properties

Low and high quality grade metallic sources and solvent oleylamine were used for the CZTS nanoparticle synthesis to investigate their influence on the absorber's behaviour and subsequent solar cells performance. Low and high purity nanoparticle inks were prepared by varying the metallic sources and solvent as listed in Table 5.1.1. The purity of the technical grade solvent OLA used in LP CZTS ink synthesis is signicantly less than that used in the HP recipe. However, the most significant cost difference is observed when high purity Cu and Zn precursor chemicals are used. Impurity analysis of both types of dried and powdered CZTS nanoparticle inks was performed using ICPMS. The results of ICPMS analysis of LP and HP CZTS inks is shown in Figure 5.1.1. Higher concentrations of Al, Hg and Pb impurities were identified in the low purity

CZTS nanoparticle powder. Substitution of Pb for Cu and Hg for Zn can occur in the kesterite crystal structure of CZTS [144, 145]. Such substitutions could impact on the optical and electronic properties of the material as well as the introduction of impurity defect levels.

Table 5.1.1: Chemical composition and concentration details of low/high purity CZTS nanoparticle recipe. Key - *SA*, Sigma Aldrich; *AA*, Alfa Asear; *Cu(acac)$_2$*, copper(II) acetylacetonate; *Zn(acac)$_2$*, zinc acetylacetonate; *Sn(acac)$_2$Cl$_2$*, tin bis(acetylacetonate); *OLA*, oleylamine.

	Low purity recipe			High purity recipe		
	Purity	*Cost(/g)*	*Supplier*	*Purity*	*Cost (/g)*	*Supplier*
$Cu(acac)_2$	97%	£0.31	*SA*	99.99%	£2.88	*SA*
$Zn(acac)_2$	*not provided by supplier*	£0.38	*AA*	99.995%	£9.90	*SA*
$Sn(acac)_2Cl_2$	95%	£6.82	*AA*	98%	£5.32	*SA*
Sulphur (S)	99.98%	£1.20	*SA*	99.98%	£1.20	*SA*
OLA	*technical grade* 70%	£0.20	*SA*	98%	£0.15	*SA*

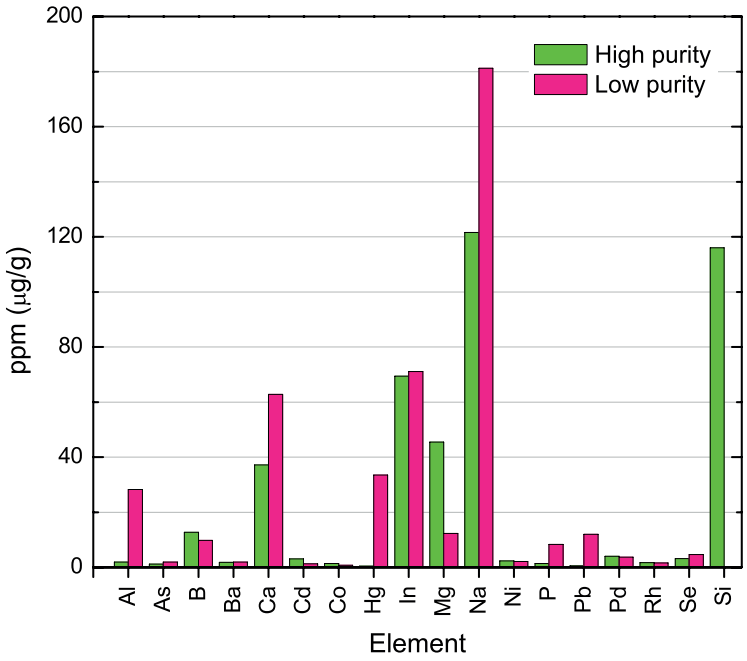

Figure 5.1.1: Concentrations of residual impurities in LP and HP CZTS dried nanoparticle ink powders.

5.2 Excitation-dependent PL

CZTSSe is considered a highly-doped and highly-compensated semiconductor due to a high defect density such that the average distance s between defects is less than the defect Bohr radius [98]. The defects tend to be charged and a random distribution of these unscreened charged defects results in electrostatic potential fluctuations inducing band tails [146]. The presence of both donor and acceptor defects within the material bulk infers that the material is also highly-compensated. Electrostatic potential fluctuations manifest as parallel shifts in valence and conduction band (VB and CB) edges with constant bandgap energy E_g [76]. The consequential band tails with energy lower than E_g have an exponentially decaying density of states which produce a broad asymmetric PL spectrum at room temperature [97]. Similarly, bandgap fluctuations in the CZTSSe material may be induced by Cu-Zn disorder in the kesterite lattice structure [147, 148], leading to the formation of non-stoichiometric defect complexes such as [V_{Cu}^{-} + Zn_{Cu}^{+}] and [Zn_{Sn}^{2-} + 2Zn_{Cu}^{+}] [37]. Slow-cooling at a rate of 10 ^{o}C/hr after the high-temperature annealing stage of CZTSSe absorber fabrication has been shown to promote clusters of ordered and disordered areas suggesting the random distribution of charged antisite defect Cu_{Zn}^{-} is reduced [87, 149]. Consequently, a reduction in local variations of Cu-Zn disorder produces clusters of lower and higher E_g phases which induces potential fluctuations in the VB and CB of the material.

The normalised 6 K PL spectra of the selenised LP and HP films at excitation intensity just below E_{PL} peak saturation are illustrated in Figure 5.2.1. The broad asymmetric shape of the PL bands for both absorbers show a gradual rise in PL intensity on the low energy side and sharper decline on the high energy side of the PL peak, indicating significant band-tailing in the materials. The PL peak maxima are located at 0.86 and 0.84 eV for LP and HP films, respectively. The energy peaks are considerably red-shifted from the corresponding room temperature bandgap energy of 1.19 eV, determined from EQE data (discussed later in this section) for both types of absorber. Such a large red-shift could be explained by the presence of deep donor defect Sn_{Zn} with an energy level $\sim$420 meV below CBM or deep acceptor states V_{Sn} or Cu_{Sn} with energy levels $\sim$400 and 420 meV above VBM, respectively [37]. The full width at half maximum (FWHM) of the PL spectra exhibit a slight decrease from 96 meV for film LP to 92 meV for film HP, with maximum intensity of the PL band of film HP half the intensity of film PL. It has been observed that a narrower PL band is indicative of a better structural quality of the material due to lower

defect concentrations [150].

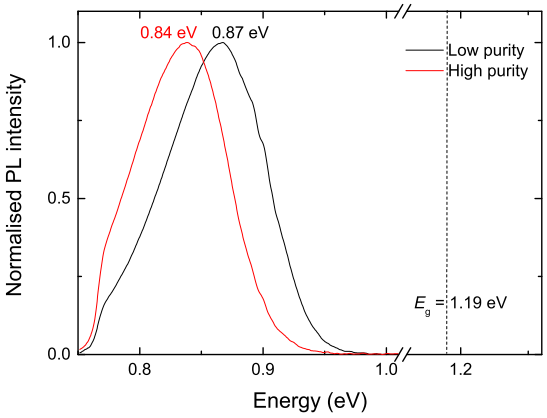

Figure 5.2.1: PL of sample LP and HP at 6 K with laser power below PL peak saturation intensity to avoid band-related recombination [17]. The dashed line indicates room temperature bandgap energy E_g of both types of sample.

The low temperature excitation-dependent intensity of the PL spectra for both absorbers is shown in Figure 5.2.2(a). The PL band intensity saturates at lower laser power for film HP and a high energy shoulder at ∼0.92 eV emerges upon increasing excitation beyond the threshold intensity (see Figure 5.2.2(b)). Above the threshold, the lower energy peak red-shifts as the high energy shoulder increases in intensity. Gershon *et al.* observe similar behaviour in CZTS films and state the high energy shoulder is due to a recombination process associated with extended band states and only appears after all localised (QDAP) states are fully saturated [151]. This is further evidence QDAP radiative recombination is dominant in the CZTSSe films studied here. The appearance of a high energy shoulder was not observed in the PL bands for film LP, indicating that not all QDAP states are occupied. An emperical asymmetric double sigmoidal function was used to fit the PL spectra in order to evaluate the peak maxima at each excitation intensity [108, 131]. Both films exhibit a substantial blue-shift of PL peak maxima with increasing laser power until reaching saturation point of PL emission. Figure 5.2.2(c) shows the evolution of PL band peaks E_{PL} for the CZTSSe samples over a laser intensity range up to the threshold value.

Changes in excitation intensity produce a shift in E_{PL} (β) at a rate of β equals 14 and 15 meV/decade and an energy blue-shift magnitude ΔE of 30 and 37 meV for HP and LP films, respectively. Oscillations in the PL bands around 0.9 eV are associated with water vapour absorption of light.

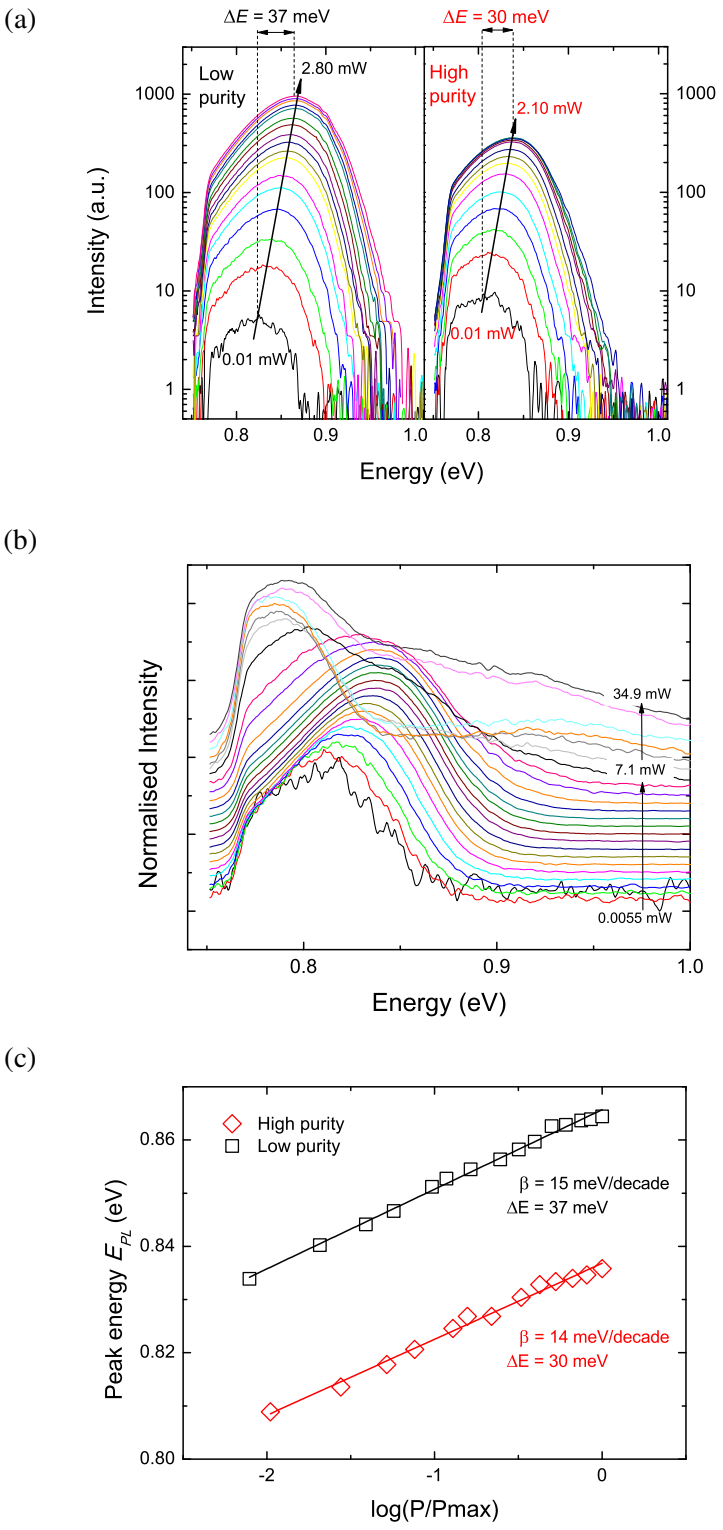

Figure 5.2.2: (a) Excitation-dependent PL spectra of sample LP and HP with laser power P up to saturation point of PL emissions together with respective ΔE blue-shift values in E_{PL}, (b) emergence of high energy 'shoulder' in PL spectra of film HP indicating saturation of QDAP defects and an increasing contribution to PL intensity from band-related radiative recombination and (c) evolution of PL band maxima with increasing P of LP and HP films with associated shift rates β at 6 K [17].

Evidence of a significant red-shift in E_{PL} compared to E_g together with large ΔE plus β values for both LP and HP films indicate QDAP defects are predominantly responsible for potential fluctuations in the VBM and CBM of the CZTSSe absorbers. As both films were slow-cooled after annealing (see Chapter 3), it is expected that any bandgap variations contributing to the potential fluctuations should be reduced as the rapid cooling process promotes a more disordered kesterite structure. The fit of the low energy tail of emissions described by Equation 3.2.6 yields the average amplitude of electrostatic potential fluctuations γ. It is evident that electrostatic potential fluctuations exist in both films with γ values of 48.6 and 58.7 meV for films HP and LP, respectively which are similar to those previously reported [54]. QDAP defect density N_D was derived from the magnitude of QDAP PL peak shift ΔE using Equations 3.2.8 and 3.2.9. It was found that N_D in film LP (2.1 x10^{18} cm^{-3}) is double that of film HP (1.1 x10^{18} cm^{-3}) and correlates to a reduction in average defect separation *s* from 6.0 to 4.8 nm in films HP and LP, respectively. Here, electrons and holes are spatially separated and localised in potential wells within the energy band edges and any radiative recombination requires tunneling of charge carriers from one potential well to another. Increasing the separation distance of the defect centres reduces the probability of radiative emission. The concentration of net (free) charge carriers reduces as the charged QDAP defect density increases. Reducing the density of free carriers lowers the screening effect on the charged defects which, in turn, increases perturbation in the depth of the fluctuating potential γ. The QDAP density is a measure of the shallow donor and acceptor defect concentration responsible for radiative recombination within the material and may not represent the total defect density N_t as the presence of deep and/or non-radiative defects is not accounted for. Therefore the total defect density can be estimated from γ values derived from PL spectra of both films [99]. The optical parameters of LP and HP films are outlined in Table 5.2.1.

5.3 Temperature-dependent PL

Temperature dependence of the PL bands was measured at an excitation power slightly lower than the threshold value (at which the high energy shoulder emerges - 1.7 mW for LP and 4.0 mW for HP films) in order to prevent contributions to PL emissions from band-related transitions. PL spectra of both films over a range of cryogenic temperatures are presented in Figure 5.3.1(a). It is apparent that PL emissions are quenched at a lower temperature in film HP and both films exhibit

Table 5.2.1: List of optical parameters of low and high purity CZTSSe samples.

	Low purity	High purity	Defect
γ (meV)	58.7	48.6	
ΔE (meV)	36.8	29.6	
Defect spacing s (nm)	4.8	6.0	
QDAP density N_D (cm^{-3})	2.1 x 10^{18}	1.1 x 10^{18}	
Defect density N_t (cm^{-3})	2.3 x 10^{19}	1.4 x 10^{19}	
E_a (meV)	(1) 38.3 ± 3.8	(1) 40.1 ± 6.4	V_{Cu}
	(2) 3.2 ± 0.5	(2) 5.9 ± 0.5	Sn_{Cu}

a red-shift in E_{PL} with increasing temperature. The magnitude of the red-shift in E_{PL} (κ) for both types of absorber are shown in Figure 5.3.1(b). Initially E_{PL} red-shifts with rising temperature at a similar rate of 0.05 and 0.09 meV/K for films LP and HP, respectively. PL emission from film HP is then quenched at a temperature of ~100 K, whereas κ increases rapidly above ~80 K at a rate of 0.84 meV/K in film LP before emissions are finally quenched at ~140 K. Thermal quenching can be surmised to originate from the thermal depopulation of defect states and/or the activation of non-radiative recombination centres. Similar behaviour was observed by Grossberg *et al.* in an optical study of defect clusters in CZTS polycrystals [152]. They state the observed evolution of E_{PL} with increasing temperature in CZTS polycrystals followed the temperature dependence of the bandgap energy of the material [153]. Another study by Yakushev *et al*. revealed comparable temperature trends in PL spectra of CZTSe thin films with varying Cu content [131].

The Varshni equation was used to fit the asymptotic low temperature behaviour of E_{PL} in both LP and HP films [154],

$$E_g(T) = E_g(0) - \left(\frac{AT^2}{T+B}\right) \tag{5.3.1}$$

where $E_g(0)$ is the bandgap of the semiconductor at 0 K and A, B are fitting parameters specific to the absorber material. Using the fitting parameters extracted from application of the Varshni model, $E_g(0)$ values of 1.24 eV for both films were extrapolated from the room temperature E_g estimate of 1.19 eV. Similar shifts in E_g of CZTS were observed in [152, 155]. E_{PL} in both films appear to follow the E_g trend at lower temperatures until ~80 K where it deviates markedly in film LP. If electrostatic potential fluctuations of the VBM and CBM are present in the absorbers due to clusters of charged QDAP defects, shallow and deep potential energy wells which follow the

(a)

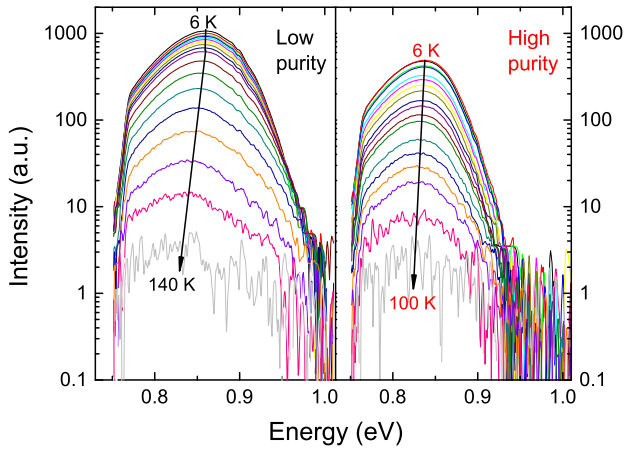

(b)

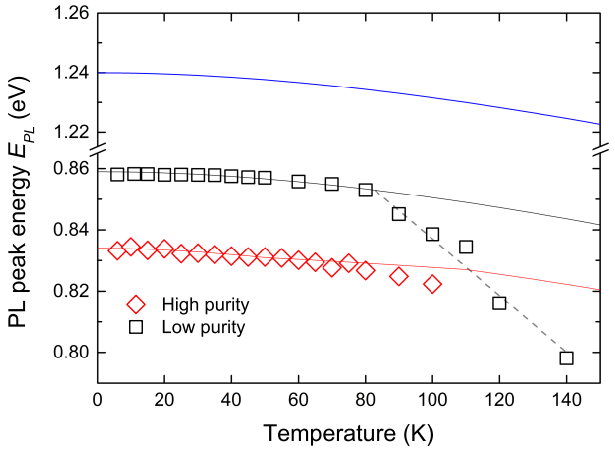

Figure 5.3.1: (a) Temperature-dependent PL of sample LP and HP with laser power below PL peak saturation intensity to avoid band-related recombination and (b) evolution of PL band maxima E_{PL} of LP and HP films with increasing temperature [17]. Equation 5.3.1 was used to extrapolate room temperature E_g values to 0 K (blue curve) and temperature-dependent E_{PL} data fitted with same equation (red/black curves). The dashed black line shows the linear red-shift of E_{PL} with temperature increasing above 80 K in sample LP.

fluctuating band edges are formed. Due to a lack of thermal energy at low temperature, carriers are trapped in shallow wells resulting in incomplete occupation of deeper/least energetic wells. As temperature increases the carriers are energised and liberated to fill the deepest wells with a consequent red-shift in E_{PL}. PL emission is quenched in both films due to increasing activation of non-radiative mid-gap recombination centres with rising temperature. The large red-shift in E_{PL} of film LP at temperatures >80 K suggests a different defect is involved in radiative transitions. This red-shift appears linear in nature (dashed black line in 5.3.1(a)) where this phenomenon has been observed in [108].

As temperature increases (up to ∼80 K) carriers are ionised and redistributed into other radiative and non-radiative defect states which quench PL emission (T>140 K). Activation energies of the defects involved in radiative recombination can be determined by analysis of the temperature-dependent PL spectra intensity using a two activation energy model proposed by [107] (see 3.2.11). Application of the model to the Arrhenius plots for both films (Figure 5.3.2(a)) yields estimated activation energies of E_{a1} = 40.1 ± 6.4 meV, E_{a2} = 5.9 ± 0.5 meV and E_{a1} = 38.3 ± 3.8 meV, E_{a2} = 3.2 ± 0.5 meV for film HP and LP, respectively. The low activation energies indicate the presence of shallow donor (3-6 meV) and shallow acceptor (38-48 meV) states in both films. A kesterite defect study by Chen *et al.* would suggest Sn_{Cu} and V_{Cu} are the corresponding donor and acceptor states. They state the Sn 5p electron has a high orbital energy which can be easily ionised, hence the Sn_{Cu} (0/+) defect is located just below the conduction band minimum, which is in agreement with the very shallow donor level observed in both types of absorber [37]. Also the ionised $V_{Cu}{}^{-}$ defect is the predominant acceptor responsible for *p*-type conductivity in these CZTSSe absorbers producing a reasonably high concentration of holes (in the region of 10^{15} - 10^{16} cm^{-3}). The presence of an additional Sn-related acceptor defect (V_{Sn}, Zn_{Sn} or Cu_{Sn}) could explain the anomalous red-shift in E_{PL} observed in film LP (see Figure 5.3.1(b)). An alternative explanation for this anomalous temperature-dependent PL behaviour was proposed by Krustok *et al.* in [108]. The weak temperature dependence of E_{PL} in temperature region 6 - 80 K arises from the gradual thermal escape of electrons localised in shallow potential wells in the CB and become free carriers. Once all of these shallow potential wells in the CB are depopulated, the free electrons then recombine radiatively with holes localised at deeper impurity tail states in the VB (T > 80 K) resulting in a larger red-shift in E_{PL} linked to band-to-tail (BT) recombination.

The minority carrier dynamics of LP and HP CZTSSe thin films were studied using TRPL decays, see Figure 5.3.2(b). Similar to PL, electron-hole (*e-h*) pairs are generated, in this case, by a short pulse of incident photons and the time-dependence of the emitted light from recombination of *e-h* pairs is monitored. The minority carrier lifetime τ is determined from the decay time of charge carrier recombination.

In order to evaluate τ, the TRPL decay curves were fitted with a double exponential function [60]:

$$I_{PL}(t) = A_1 e^{-\left(\frac{t}{\tau_1}\right)} + A_2 e^{-\left(\frac{t}{\tau_2}\right)} \tag{5.3.2}$$

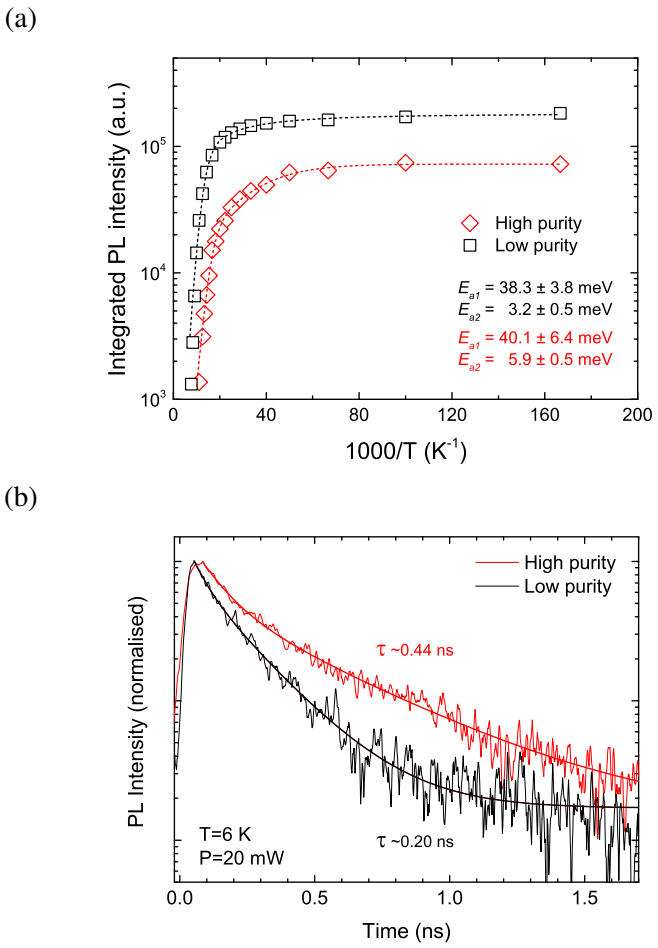

Figure 5.3.2: (a) Arrhenius plots of integrated PL intensities and (b) TRPL decays at 6 K for films LP and HP [17]. The solid lines are results of fitting with bi-exponential function.

where $I_{PL}(t)$ is the luminescence intensity at time t after the excitation pulse, A_1 and A_2 are are the PL intensities corresponding to the injection regimes and τ_1 and τ_2 are the fast and slow decay times. The initial fast decay τ_1 can be ascribed to high carrier injection immediately after the excitation pulse and the long tail τ_2 attributed to the minority carrier lifetime of the material [52, 67].

Lifetimes of 0.20 and 0.44 ns were observed for films LP and HP, respectively. The lower τ value for film LP would suggest more non-radiative bulk/surface recombination centres are present in the absorber, which is in agreement with the total defect density N_t determined from excitation-dependent PL measurements. Raadik et *al.* propose the shorter carrier lifetime could be related to a higher degree of Cu/Zn disorder in the bulk of the CZTSSe absorber [156]. Therefore different recombination processes may be active in LP and HP films. The unexpectedly low carrier lifetime at 6 K observed in this study could be due to high recombination rates at the unpassivated absorber

surface.

5.4 Electrical characterisation

In order to probe deep defect levels in the CZTSSe devices beyond the scope of PL spectroscopy, deep level transient spectroscopy (DLTS) is employed to quantify trap activation energies E_T, trap densities N_T and their capture cross-sections σ_T in devices. Figure 5.4.1 show DLTS spectra for samples LP and HP respectively. In this measurement setup positive ΔC peaks are indicative of hole trap levels with energy values measured with respect to the valence band. Peak positions are analysed over three different transient period widths (19.2 ms, 192 ms, 480 ms) and for a range of correlator functions [123], used to generate Arrhenius plots shown in Figure 5.4.2. Values for E_T and σ_T are extracted from fitting to the Arrhenius plot whilst the trap density is determined from the magnitude of the capacitance change relative to the reverse bias capacitance (see Table 5.4.1).

Table 5.4.1: List of electronic parameters of low and high purity CZTSSe samples determined from DLTS.

Purity		Trap level E_T (meV)	Capture cross-section σ_T (cm^2)	Trap density N_T (cm^{-3})	Possible defect
Low	(1)	86 ± 7	(1.08 ± 0.95) x 10^{-20}	(1.70 ± 0.22) x 10^{14}	Cu_{Zn}
	(2)	167 ± 10	(2.20 ± 1.99) x 10^{-20}	(3.17 ± 0.32) x 10^{13}	Cu_{Sn}, Zn_{Sn} or V_{Sn}
High	(1)	87 ± 6	(3.61 ± 1.59) x 10^{-21}	(6.38 ± 0.05) x 10^{14}	Cu_{Zn}

For sample HP a single peak is clearly visible at an energy of E_T = 87 $\pm$ 6 meV. The peak is very broad indicating the observed peak may in fact be a distribution of deep levels closely spaced in energy. Attempts were made to separate these levels via a Laplace analysis method [157] however such analysis did not give a definitive answer and was too dependent on the analysis conditions used i.e. number of overlapping transients permissible. This sample also showed some evidence of a negative peak, indicative of an electron trap, at $\sim$170 K. On closer inspection, this was found to predominantly occur for short period widths and is in fact measurement artifact related to the recovery time of the capacitance signal. Sample LP showed the same deep level present at E_T = 86 $\pm$ 9 meV, although the lower purity sample displayed a slightly lower concen-

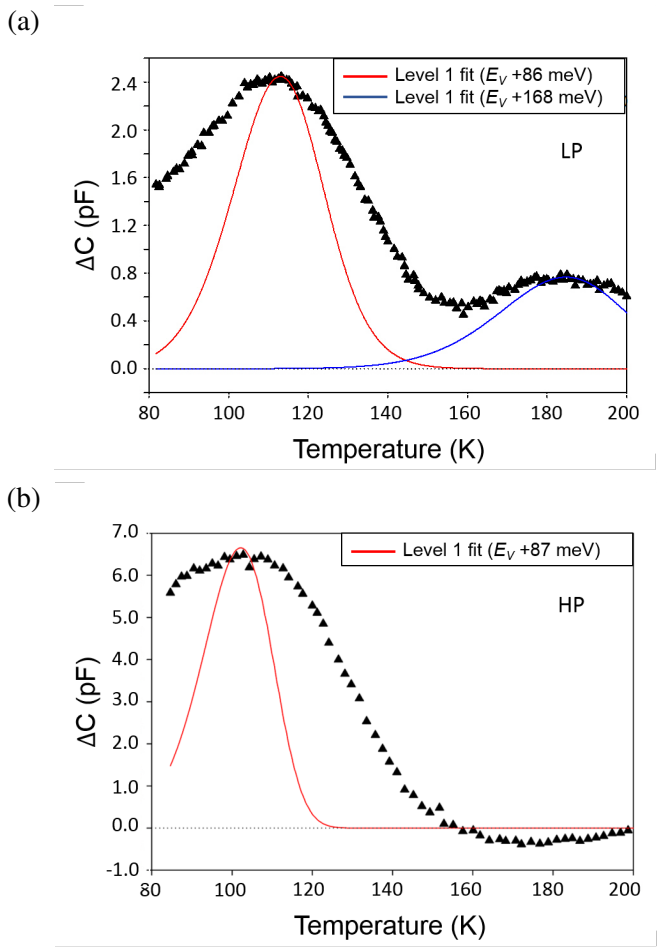

Figure 5.4.1: Example DLTS spectra recorded for (a) sample LP and (b) sample HP [17].

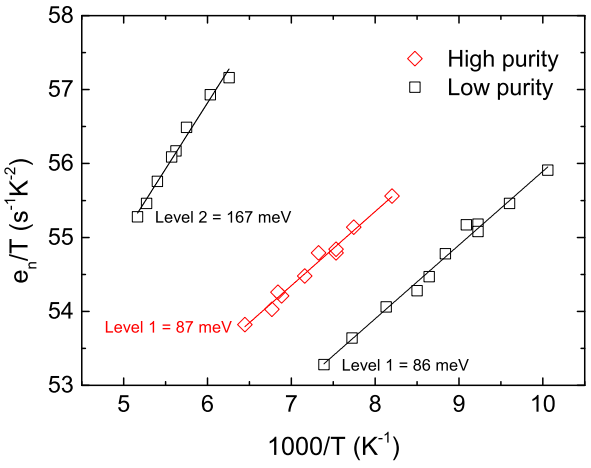

Figure 5.4.2: Extracted Arrhenius plots from DLTS spectra for samples LP and HP [17].

tration of this trap level. A second trap state not observable in the HP sample was also observed at an energy of E_T = 167 $\pm$ 10 meV but an order of magnitude lower density, 3.17 x10^{13} cm^{-3},

than for the shallower level. The natural assumption would be that this secondary trap level has arisen as a result of some contaminant within the process solution. It is assumed that the same trap level at 86-87 meV above the VBM in both types of absorber is antisite Cu_{Zn} [37]. Although the concentration of this defect is higher in device HP than LP, their potentially deleterious effect is mitigated by a lower carrier capture cross-section (σ_{HP} ~4 x10^{-21} cm^2 compared to σ_{LP} ~1 x10^{-20} cm^2). *Ab initio* calculations show that the additional defect level in film LP could be Sn-related (V_{Sn}, Cu_{Sn} or Zn_{Sn}) with the likelihood of the defect being Zn_{Sn}, considering the LP absorber is Cu-poor and Zn-rich (see Table 5.4.2). The concentration of any Sn-related defects in film HP should be reduced as the film is compositionally closer to the preferred Cu/(Zn+Sn) ratio of 0.8, see Table 5.4.2 [69, 70]. CZTSSe films which have low Cu/(Zn+Sn) and high Zn/Sn ratios are predisposed due to the presence of high populations of [Zn_{Sn}+2Zn_{Cu}] charge compensated clusters which are one of the defect complexes responsible for non-stoichiometry in this type of absorber material.

Table 5.4.2: Cu/(Zn+Sn) and Zn/Sn ratios of LP and HP thin films and solar cell parameters of subsequently fabricated best devices (with average values in brackets).

	Low purity	High purity
Cu/(Zn+Sn)	0.84	0.82
Zn/Sn	1.07	1.08
V_{oc} (V)	0.31 (0.31)	0.32 (0.32)
J_{sc} (mA/cm^2)	27.2 (26.0)	25.6 (23.7)
FF (%)	59.9 (57.9)	61.9 (56.7)
Efficiency η (%)	5.1 (4.7)	5.1 (4.2)
Carrier lifetime τ (ns)	0.20	0.44
Carrier diffusion L_d (nm) length	203	369

Further studies of the electronic properties of LP and HP solar cells were performed using current density-voltage (*J*-*V*), capacitance-voltage (*C*-*V*) and external quantum efficiency (EQE) analysis. Figure 5.4.3(a) shows the *J*-*V* plots of the best performing LP and HP devices under 1-sun illumination with the inset showing the average device open circuit voltage V_{oc} and short circuit current density J_{sc}. It is noted that the average V_{oc} of HP cells was slightly higher that that of the LP cells, see inset of Figure 5.4.3(a). Conversely, LP devices have a higher J_{sc} value (26.1 mA/cm^2) in comparison to that seen in HP devices (23.7 mA/cm^2). Similar observations were

made by Yakushev et *al.* for $Cu_2ZnSnSe_4$ (CZTSe) devices with varying Cu/(Zn+Sn) and Zn/Sn ratios and were attributed to the degree of Cu-Zn order/disorder in the crystal lattice [131]. EQE plots for LP and HP devices are shown in Figure 5.4.3(b), where it can be seen that device LP has enhanced carrier extraction in the wavelength range 600-1000 nm. This anomalous behaviour could be explained by a lower concentration of free charge carriers and will be explored in more detail later in this section.

(a)

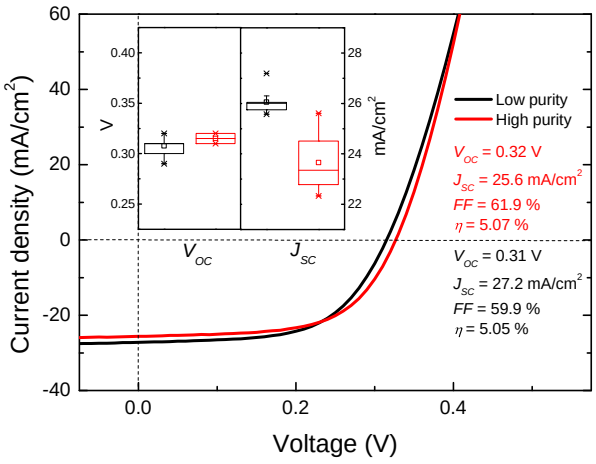

(b)

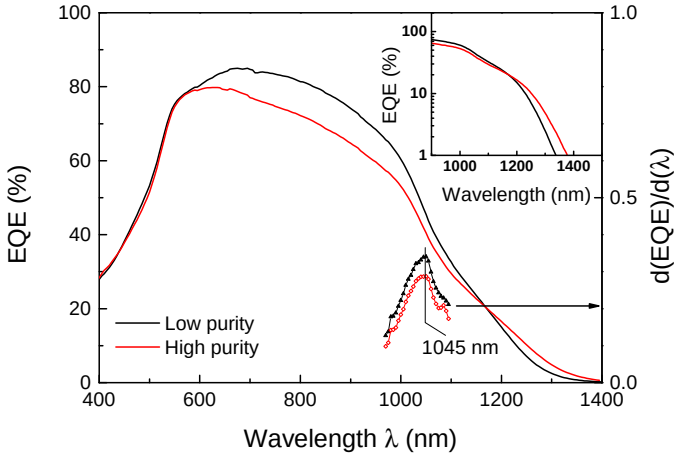

Figure 5.4.3: (a) J-V curves of best performing devices for samples LP and HP with inset showing box plots of average device V_{oc} and J_{sc} parameters and (b) EQE plots with inset showing extended absorption due to tail states in sample HP [17].

The minority carrier diffusion length L_d for both types of absorber was calculated from EQE measurements in conjunction with optical absorption coefficient α measurements (determined from transmittance/reflectance data, see Figure 5.4.4) using a method by Courel et *al.* [121].

It was shown that EQE^{-1} is a linear function of α^{-1} such that:

$$EQE(\lambda)^{-1} = \frac{1}{(1 - R(\lambda))}\left(1 + \frac{\alpha(\lambda)^{-1}}{L_d}\right) \tag{5.4.1}$$

where $R(\lambda)$ is the reflectance of the cell with an intercept on the α^{-1} equal to L_d, see Figure 5.4.4(c). Diffusion length values of 203 and 369 nm were determined for LP and HP devices respectively. The reported L_d values are significantly lower than the value of 750 nm observed in the CZTSSe solar cell with record efficiency of 12.6% [43]. The longer diffusion lengths of carriers in film HP strongly correlates with higher carrier lifetimes measured in CZTSSe bulk. *C-V* measurements were performed to estimate the depletion region width *w* and doping density N_A in the CZTSSe absorber layers of devices LP and HP. The inset in Figure 5.4.4(c) shows the plot of $1/C^2$ versus reverse bias voltage where $\langle w \rangle = A\varepsilon_0\varepsilon_r/C$ is determined from the measured capacitance value at zero bias and N_A is derived from the slope $d(1/C^2)/dV$. Very short space charge regions widths of 63 and 61 nm were observed for devices LP and HP respectively, with corresponding apparent doping densities of 2.5 x10^{16} and 3.3 x10^{16} cm^{-3}, in agreement with those observed by Qu *et al*. [158]. A high doping density is usually associated with a short depletion width in CZTSSe solar cells as $w \propto N_A$ [159, 160].

Following the selenisation of the CZTS nanoparticle films, EDS compositional analysis of the LP and HP CZTSSe absorbers revealed a greater Cu and Sn loss was observed in LP films, whereas HP films suffered a larger Zn loss, see Table 5.4.3. Subsequent Cu/Zn+Sn and Zn/Sn ratios of 0.84, 0.82 and 1.07, 1.08 for respective LP and HP absorbers demonstrate HP films are closer to the preferred CZTSSe composition of Cu/Zn+Sn = 0.8 and Zn/Sn = 1.2 [69, 70]. With regard to the elemental losses, it would be reasonable to assume that there could be higher concentrations of Cu- and Sn-related defects in LP films. Recent studies have shown the degree of Cu-Zn order/disorder has a significant impact on the bandgap and crystallinity of CZTSSe absorbers and may be the main cause of bandgap and electrostatic potential fluctuations within the material, as shown in Figure 5.4.5 [77, 147, 161, 162].

Considering the small decrease in Cu/Zn+Sn and small increase in Zn/Sn ratios in HP films compared to LP films, higher concentrations of A-type defects ([V_{Cu}+Zn_{Cu}] neutral complexes) may be present in HP films together with higher concentrations of B-type defects ([Zn_{Sn}+2Zn_{Cu}] neutral complexes) in LP films [163, 164]. Although the presence of Zn_{Cu} donor defect was not directly observed in either film, their presence can be inferred as high populations of benign

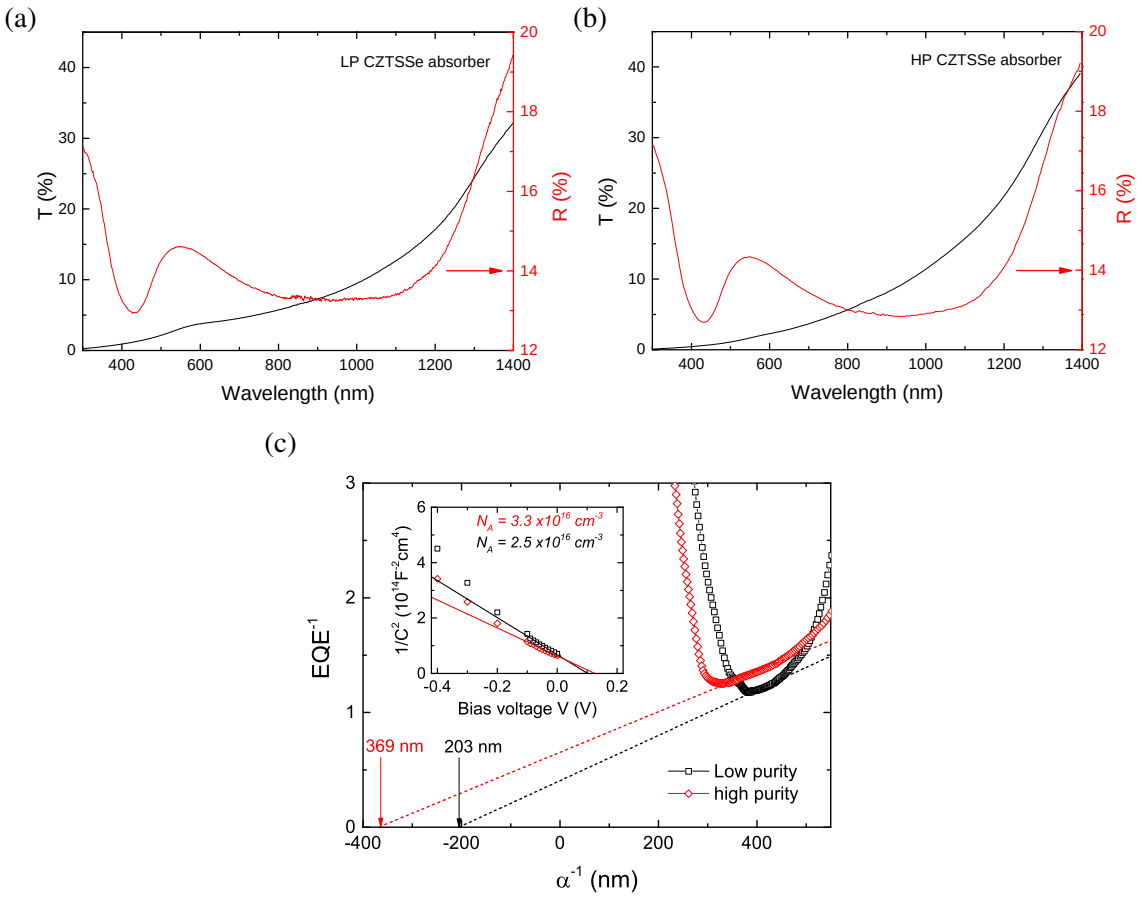

Figure 5.4.4: Transmission and absorption data of CZTSSe absorbers deposited on bare soda lime glass of (a) film LP and (b) film HP and (c) calculation of depletion region width w_0 and apparent doping density N_A [17].

Table 5.4.3: The composition of precursor and selenised films on bare SLG

Film		Cu $(at\%)$	Zn $(at\%)$	Sn $(at\%)$	S $(at\%)$	Se $(at\%)$
HP	Precursor	23.93	16.88	14.24	45.95	
	Selenised	20.61	13.13	12.12	5.57	48.53
LP	Precursor	23.17	14.3	14.16	48.04	
	Selenised	19.09	11.80	11.02	5.02	53.06

[V_{Cu}+Zn_{Cu}] clusters are expected in non-stoichiometric CZTSSe absorbers [37].

Perhaps the most interesting observation in this study is the presence of an additional acceptor defect in the LP device located ∼167 meV above the VBM, speculatively attributed to antisite Zn_{Sn}. Chen *et al.* have shown the Zn_{Sn} defect has negligible impact on *p*-type conductivity but could contribute to luminescence and act as recombination centres [37]. The presence of

radiative Zn_{Sn} defects could explain the increased QDAP density and PL intensity seen in film LP compared to film HP. The significant red-shift of the PL peak in film LP at temperatures greater than 80 K could be attributed to radiative recombination involving the Zn_{Sn} acceptor. The lower QDAP concentration in film HP could also account for quenching of the PL signal at a lower temperature ($\sim$100 K) in this film compared to film LP ($\sim$140 K). It is also possible the anomalous temperture-dependent PL behaviour in film LP could involve Cu_{Zn} - Sn_{Cu} QDAP due to the thermal escape of holes from the shallower V_{Cu} acceptor state to the slightly deeper Cu_{Zn} state, see Figure 5.4.5. According to Chen *et al*. a number of self-compensated defect clusters can be formed in quaternary kesterites. They show the overall formation energy of these defect clusters is significantly decreased relative to the sum of the individual defects. As the clusters are charge-neutral and bound by strong Coulomb attraction, their presence should not be detected directly by PL analysis. However, some defect clusters can produce a significant shift in the valence and conduction band edges, effectively reducing the bandgap of the absorber. Large populations of clusters [$2V_{Cu}$+Sn_{Zn}] or [$2Cu_{Zn}$+Sn_{Zn}] could exist in both types of absorber given the observed large red-shift of E_{PL} in comparison to the bandgap of the absorbers at 6 K ($\sim$300 meV) which cannot be solely attributed to QDAP defects. The presence of neutral defect clusters would reduce the concentration of shallow acceptor defects which contribute to the overall p-type conductivity of the absorber material. From capacitance-voltage measurements, film LP has a slightly lower apparent doping density N_A in comparison to that of film HP indicating the degree of compensation is greater in this film. The measured concentration of V_{Cu} antisite defects (which are mainly responsible for the p-type conductivity of Cu-poor/Zn- rich CZTSSe films) is around 10^{19} cm^{-3} in both types of absorber whereas both films show N_A $\sim 10^{16}$ cm^{-3} confirming the material is highly compensated.

All optical and electronic parameters indicate films prepared from high purity precursor chemicals are of a higher quality than those fabricated from lower grade materials. However, this improvement in film quality does not translate to an increase in completed device efficiency as both types of device have similar best η values of $\sim$5.1 $\%$. In Chapter 4, a study of CZTSSe solar cells fabricated using the same nanoparticle inks-based method has revealed the devices typically have a contact barrier height of $\sim$40 meV between the CZTSSe absorber and Mo back contact. This low barrier height would suggest the back contact of both types of device is not a factor constraining cell performance and, therefore, attention should be focused on improving buffer/absorber

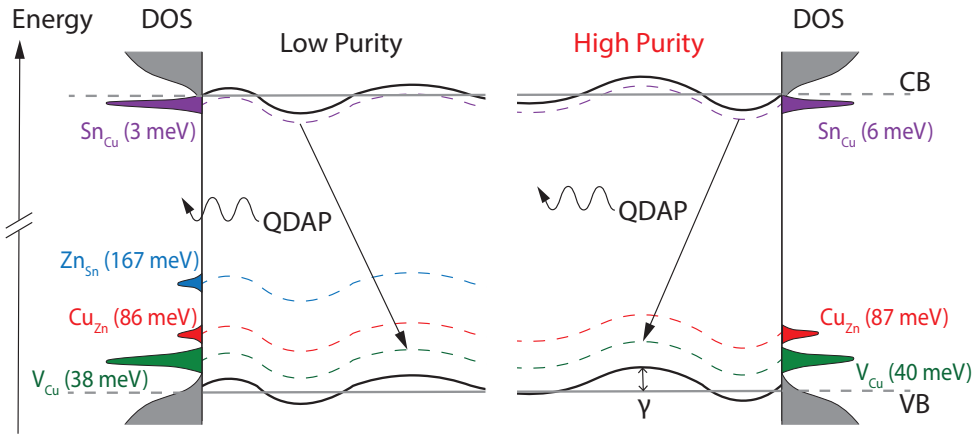

Figure 5.4.5: Schematic of electrostatic potential fluctuations in the band edges of LP and HP absorbers with associated defects and densities of state (DOS). The predominant radiative recombination process in both samples involves QDAP defects Sn_{Cu} and V_{Cu}.

junction and other components in the device architecture.

One important parameter which could be utilised to indicate the quality of CZTSSe absorbers is the mean depth of potential fluctuations γ. Considering a high concentration of Zn_{Sn} defects present in absorber LP (which could contribute to an elevated QDAP density), we see a direct correlation of such QDAP density with γ, suggesting γ is a useful indicator of the presence of specific defects which generate band tails in the material. Yakushev *et al.* observe a similar reduction in γ values when the studied CZTSe films became Cu-poorer and Zn-richer, attributing this change to improved ordering of Cu-Zn atoms within the crystal lattice of the thin film [131]. A similar reduction in γ values are noted in this study. Bourdais *et al.* investigated the effect of Cu-Zn disorder on the V_{oc} deficit in kesterite solar cells also noted that ordering of the CZTSSe absorbers by slow cooling improved the V_{oc} deficit in their devices by 40 meV. Therefore, a reduction in γ value could indicate a reduction in Cu-Zn disorder with an associated increase in V_{oc} [40]. Figure 5.4.5 highlights the main results of the combined optical and electronic studies, principally:

(i) Fluctuations in the band edges of both types of absorber, predominantly caused by variations in electrostatic potential, with an average depth of γ equal to 59 and 49 meV in films LP and HP respectively.

(ii) Same shallow donor (Sn_{Cu}) and shallow acceptor (V_{Cu}, Cu_{Zn}) defects present in the bulk of both types of CZTSSe absorber.

(iii) Additional deep Sn-related acceptor defect (probably Zn_{Sn}) located 167 meV above the VBM present in sample LP.

(iv) Radiative recombination primarily involving QDAP donor Sn_{Cu} and acceptor V_{Cu} defects located 3-6 meV below CBM and 38-40 meV above VBM.

(v) V_{Cu} chiefly responsible for *p*-type conductivity in both types of thin film.

5.5 Summary

In depth optical spectroscopy and electronic studies of CZTSSe absorber layers and solar cells fabricated from low and high purity precursor chemicals are presented. The high purity chemical recipe produced Cu-poorer and Zn-richer CZTS nanoparticles. Following selenisation of the stacked spin-coated CZTS films, a Zn loss was observed in the HP absorber while a Sn loss was seen in the LP absorber. Comprehensive temperature and excitation dependent analysis of PL spectra together with DLTS enabled identification of shallow and deep defects and QDAP recombination as the predominant recombination mechanism in both types of thin film. The loss of Sn could account for the presence of additional Sn-related defects identified in the LP film. Notwithstanding the improvement in quality of film HP, detailed analysis of the electronic properties of LP and HP solar cells revealed similar performance in both types of device. This implies an underlying issue other than defects in the absorber bulk inhibits device performance which warrants further investigation. The next chapter will look at factors affecting CZTSSe device performance arising from issues with the absorber-buffer interface.

Chapter 6

Absorber-buffer interface

Currently, the typical kesterite $Cu_2ZnSn(S,Se)_4$ (CZTSSe) device architecture incorporates a CdS *n*-type buffer which is non-ideal due to the presence of toxic Cd with other buffers such as In_2S_3 and Zn(O,S) proposed as alternatives. In this chapter, optical and electronic characterisation techniques together with device analysis and simulation were used to assess nanoparticle-based CZTSSe absorbers and solar cells with CdS and In_2S_3 buffers. Photoluminescence spectroscopy indicated CZTSSe absorbers with In_2S_3 buffer had a lower density of detrimental non-radiative defects and a higher concentration of copper vacancies $V_{Cu}{}^{+}$, responsible for *p*-type conductivity in CZTSSe, in comparison to the absorber with CdS buffer. Capacitance-voltage (*C*-*V*) measurements revealed the In_2S_3 buffer-based CZTSSe devices had a three times higher apparent doping density and a consequently narrower SCR than devices with a CdS layer, resulting in poorer collection of photo-generated charge carriers in the near-IR region despite a more favourable band alignment as determined by X-ray photoelectron and inverse photoelectron spectroscopy. The presence of interfacial defect states in In_2S_3 devices as determined by *C*-*V* and biased quantum efficiency measurements are also responsible for the loss in open-circuit voltage compared with reference devices with CdS. Additional near-IR recovery can be activated by employing thin dual In_2S_3/CdS layer.

The current record efficiency of 12.6% for CZTSSe-based solar cells [43] was achieved in 2013, whereas counterpart CIGSSe-based devices achieved efficiencies up to 22.9% [4]. The large disparity in performance between kesterite and chalcopyrite PV devices is primarily attributed to a severe open circuit voltage (V_{oc}) deficit of about 650 mV in CZTSSe solar cells compared to values around 400 mV in CIGSSe devices with comparable bandgaps of around 1.15 eV [43, 165].

Several reasons for the V_{oc} deficit have been cited: i) high densities of intrinsic defects in the kesterite bulk, such as vacancies (e.g. V_{Zn}, V_{Sn}), antisites (e.g. Sn_{Cu}, Sn_{Zn}) and interstitials (e.g. Zn_i) which act as effective electron-hole recombination centres [37], ii) band tailing which is also related to high concentrations of defects in conjunction with a high degree of charge compensation causing electrostatic potential fluctuations [54, 143, 166] or heterogeneous spatial variations in crystallinity and/or composition leading to nanoscale bandgap fluctuations [40, 77, 162] and iii) enhanced buffer/absorber interface recombination due to nonoptimal band alignment depending on buffer selection, see Chapter 2 [52, 54, 167].

A suitable strategy to reduce the V_{oc} deficit in kesterite-based solar cells is the investigation of band alignments at the buffer/absorber interface to facilitate selection of suitable *n*-type buffer materials with an optimal conduction band offset (CBO). The CBO is most relevant in the conjunction of *n*-type buffer with *p*-type absorbers, where the minority charge carriers are electrons. In this instance, electrons are promoted to the conduction band (CB) of the *p*-type absorber and optimum device performance is governed by efficient transport of electrons across the interface into the *n*-type buffer for onward extraction from the device.

In kesterite solar cells, CdS is used ubiquitously as the *n*-type material in device architecture despite the buffer having a slightly larger than optimal CBO with CZTSSe which can lead to enhanced interface recombination [88, 168]. As an alternative, In_2S_3 has been considered due to the material having a more favourable CB alignment with CZTSSe and a larger energy bandgap [169, 170]. In fact, Jiang *et al.* successfully incorporated a thin In_2S_3 layer in a CZTS-based device achieving an efficiency of 6.9% [95] and Mitzi *et al.* demonstrated CZTSSe devices with lowest V_{oc} deficit by applying a double In_2S_3/CdS emitter [171].

The aim of this chapter is to demonstrate how replacing the conventional CdS buffer with In_2S_3 in nanoparticle based CZTSSe device architecture can potentially lead to an improvement in V_{oc}. First, the nature of the CBO at the buffer/absorber heterojunction is determined using X-ray photoemission (XPS) and inverse photoemission (IPES) spectroscopy to ascertain which material forms a more favourable band alignment with CZTSSe absorbers fabricated from nanoparticle inks. Then the deposition method of the buffer layer is investigated to elucidate whether the method can affect changes in the chemical and electronic properties of the absorber material in the region near the interface. To this end, temperature and excitation dependent PL measurements of as-deposited, CdS- and In_2S_3-buffered CZTSSe thin films are conducted to elucidate

details of the main recombination mechanism present in the absorbers and associated shallow defects which contribute towards such recombination. By applying a number of electrical characterisation techniques, quantitative demonstration is made on how the application of different buffers impacts device performance. Furthermore, device modelling using solar cell capacitance simulations (SCAPS) was done to gain an insight on the relationship between CdS/CZTSSe and In_2S_3/CZTSSe interface defects and device performance.

6.1 CdS and In_2S_3 material properties

Buffer layers of CdS ($\sim$60 nm) and In_2S_3 ($\sim$70 nm) were prepared by chemical bath deposition (CBD). Specific details are given in Chapter 3. SEM images of annealed CdS and In_2S_3 thin films grown on soda lime glass deposited by CBD are shown in Figure 6.1.1.

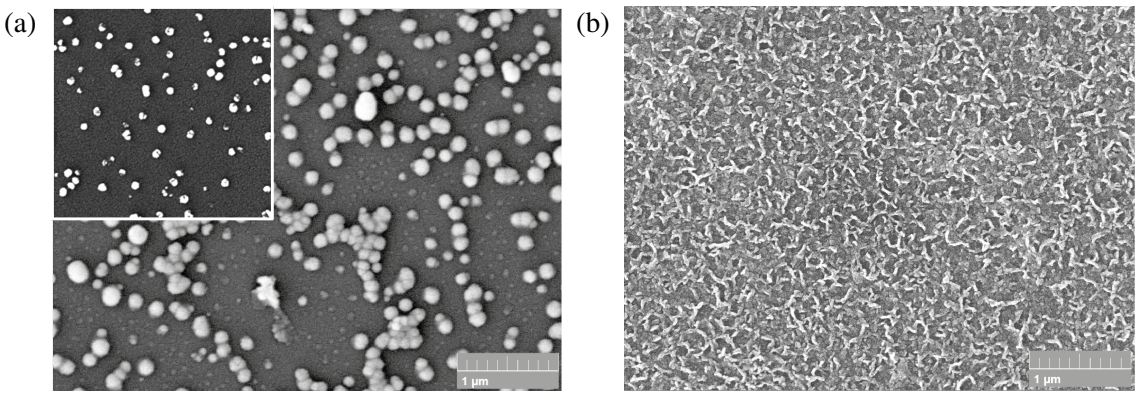

Figure 6.1.1: SEM images of annealed (a) CdS and (b) In_2S_3 thin films grown by chemical bath deposition on soda lime glass. The inset in (a) shows the CdS film after cleaning with a CO_2 snow jet.

The films show significant differences in morphology with the CdS layer forming large agglomerates on the surface. The large agglomerates on the surface of the film can be removed by application of a CO_2 snow jet. Similar worm-like structures in the In_2S_3 film were observed by [172]. Despite the structural differences, cross sectional SEM images of both films show conformal coatings.The bandgap of the films was determined from their respective transmission spectra measured by UV-VIS. In_2S_3 can have both a direct and indirect bandgap resulting in two absorption edges, however the probability of an indirect transition between the parabolic CB and VB is less likely as a change in crystal lattice momentum is required to facilitate the transition. In order to determine the transition type, both indirect and direct models were applied to the absorption

data. Here the absorption spectra obey the relation $(\alpha E)^{1/2}$ for indirect and $(\alpha E)^2$ for direct transitions with the results shown in Figure 6.1.2. The dashed lines in both plots represent the best fitting to the theoretical models.

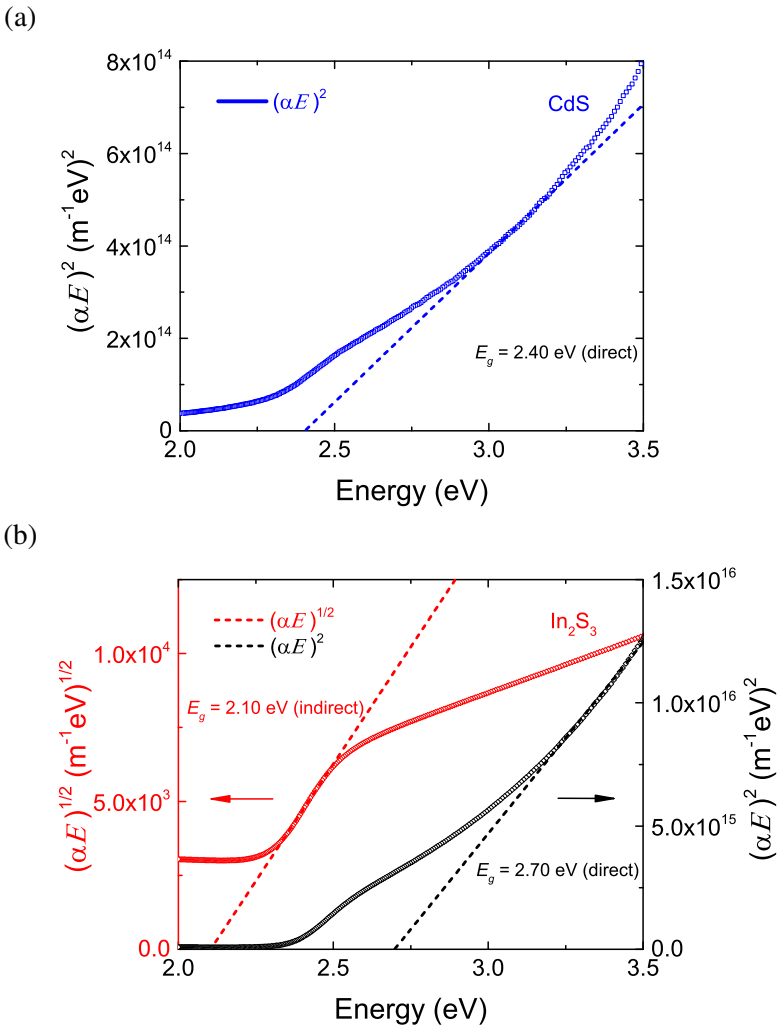

Figure 6.1.2: (a) $(\alpha E)^2$ vs. E spectra for CdS and (b) $(\alpha E)^{1/2}$, $(\alpha E)^2$ vs. E spectra for In_2S_3 thin films.

Optical bandgaps of 2.40 eV (direct) and 2.10 (indirect), 2.70 eV (direct) were determined for CdS and In_2S_3 films, respectively. Sandoval-Paz *et al.* observed similar results in chemically deposited In_2S_3 polycrystalline films and inferred the indirect bandgap was due to a cubic structure (resulting from a mixture of α and β phases) and the direct bandgap arose from the tetragonal β phase [169]. A wider bandgap buffer material is desirable for the transmission of shorter wavelengths of the solar spectrum to the absorber layer.

6.2 Band alignment at buffer/CZTSSe interface

The Kraut method is frequently used to experimentally determine the band alignments at semiconductor interfaces [173–175]. This method uses the photoelectron spectra of a series of three samples to determine the band offsets at an interface, namely a thick overlayer sample (buffer), a substrate sample (CZTSSe) and an interfacial sample in which the core-levels from both the substrate and the overlayer (buffer/CZTSSe) are visible. By determining the relative energy positions of the core-levels ($E_{cl}^{over,sub}$) to the VBM (ξ_{VBM}^{sub}) and the difference in energies of the core-levels in the interfacial sample, the valence band offset (ΔE_v) can be determined by:

$$\Delta E_v = (E_{cl}^{over} - \xi_{VBM}^{over}) - (E_{cl}^{sub} - \xi_{VBM}^{sub}) - (E_{cl}^{over} - E_{cl}^{sub}) \tag{6.2.1}$$

The bandgaps of the semiconductors are given by $E_g^{over,sub} = \xi_{VBM}^{over,sub} + \xi_{CBM}^{over,sub}$, thus the CBO ($\Delta E_c$) can be derived from:

$$\Delta E_c = E_g^{over} - E_g^{sub} - \Delta E_v \tag{6.2.2}$$

In order to determine the band alignment at the CdS/CZTSSe and In_2S_3/CZTSSe interfaces, the valence band offset (VBO) and CBO are measured for individual 3d core levels in Cd, In, Sn and Se and 2p core levels in S, Cu and Zn and the final VBO and CBO for the semiconductor interfaces is obtained from the mean of the individual core level values (experimental core level values are listed in Table 6.2.1) .

Figures 6.2.1(a), 6.2.1(c) and 6.2.1(e) show the determination of the VBM as measured by XPS and 6.2.1(b), 6.2.1(d) and 6.2.1(f) show the CBM as measured by IPES for CdS, In_2S_3 and CZTSSe films, respectively. Note that the spectra show states tailing into the band gap, which is an artefact of instrumental broadening and not a measure of defect states. Using the aforementioned method, VBO values of ΔE_v = -1.98 $\pm$ 0.10 eV and -1.21 $\pm$ 0.10 eV and CBO values of ΔE_c = -0.68 $\pm$ 0.14 eV and 0.39 $\pm$ 0.14 eV were determined for CdS and In_2S_3 buffered samples, respectively. The calculated band alignment for each sample are represented schematically in Figure 6.2.2(a). It is apparent CdS forms a large cliff-like CBO (Type II) at the heterojunction with CZTSSe prepared here (far greater than other reported values [168, 176, 177]) whereas In_2S_3 forms a modest spike-like CBO (Type I). Device simulation has shown that the ideal CBO is a moderate spike in the range 0 – 0.4 eV [178–180]. However, as the experimentally determined

Table 6.2.1: A summary of the parameters used to obtain band offsets at the CdS/CZTSSe and In_2S_3/CZTSSe interfaces using the Kraut method.

Sample	core level	$E_{cl}^{over,sub}$ (eV)	$\xi_{VBM}^{over,sub}$ (eV)	E_g (eV)	ΔE_v (eV)	ΔE_c (eV)
CdS (overlayer)	Cd $3d_{5/2}$	405.41	1.96	2.45	-	-
	S $2p_{3/2}$	161.82	1.96	2.45	-	-
CZTSSe (substrate)	Cu $2p_{3/2}$	932.47	0.39	1.15	-1.92	-0.62
	Zn $2p_{3/2}$	1021.96	0.39	1.15	-1.98	-0.68
	Sn $3d_{5/2}$	486.55	0.39	1.15	-2.02	-0.72
	Se $3d_{5/2}$	54.39	0.39	1.15	-1.98	-0.68
In_2S_3 (overlayer)	In $3d_{5/2}$	445.34	1.94	2.75	-	-
	S $2p_{3/2}$	161.82	1.94	2.75	-	-
CZTSSe (substrate)	Cu $2p_{3/2}$	932.47	0.39	1.15	-1.22	0.38
	Zn $2p_{3/2}$	1021.96	0.39	1.15	-1.12	0.48
	Sn $3d_{5/2}$	486.55	0.39	1.15	-1.33	0.27
	Se $3d_{5/2}$	54.39	0.39	1.15	-1.16	0.44

CdS/CZTSSe CBO is -0.68 eV, this cliff barrier inhibits the flow of injected electrons from buffer to absorber under forward bias conditions causing an accumulation of electrons at the interface. Charge carrier recombination is therefore elevated at the heterojunction and V_{oc} is reduced as a consequence [179].

Scheer demonstrated the activation energy of interface recombination in a generic heterojunction PV device is equivalent to the energy difference between the CBM of the buffer and VBM of the absorber layers [82]. Thus, with regard to interface recombination, a cliff-like CBO will result in a lower activation energy than the absorber bandgap leading to a reduction in V_{oc}. The spike-like CBO of +0.39 eV at the *pn*-junction of the In_2S_3-buffered CZTSSe sample is almost at the threshold for efficient electron transport across the buffer/absorber interface (0.4 eV [80]). Notwithstanding the magnitude of the spike offset in this sample, interface recombination is still expected to be reduced due to a limited supply of holes at the junction caused by absorber type inversion [81]. Band alignment can also influence the degree of quasi Fermi level splitting at the het-

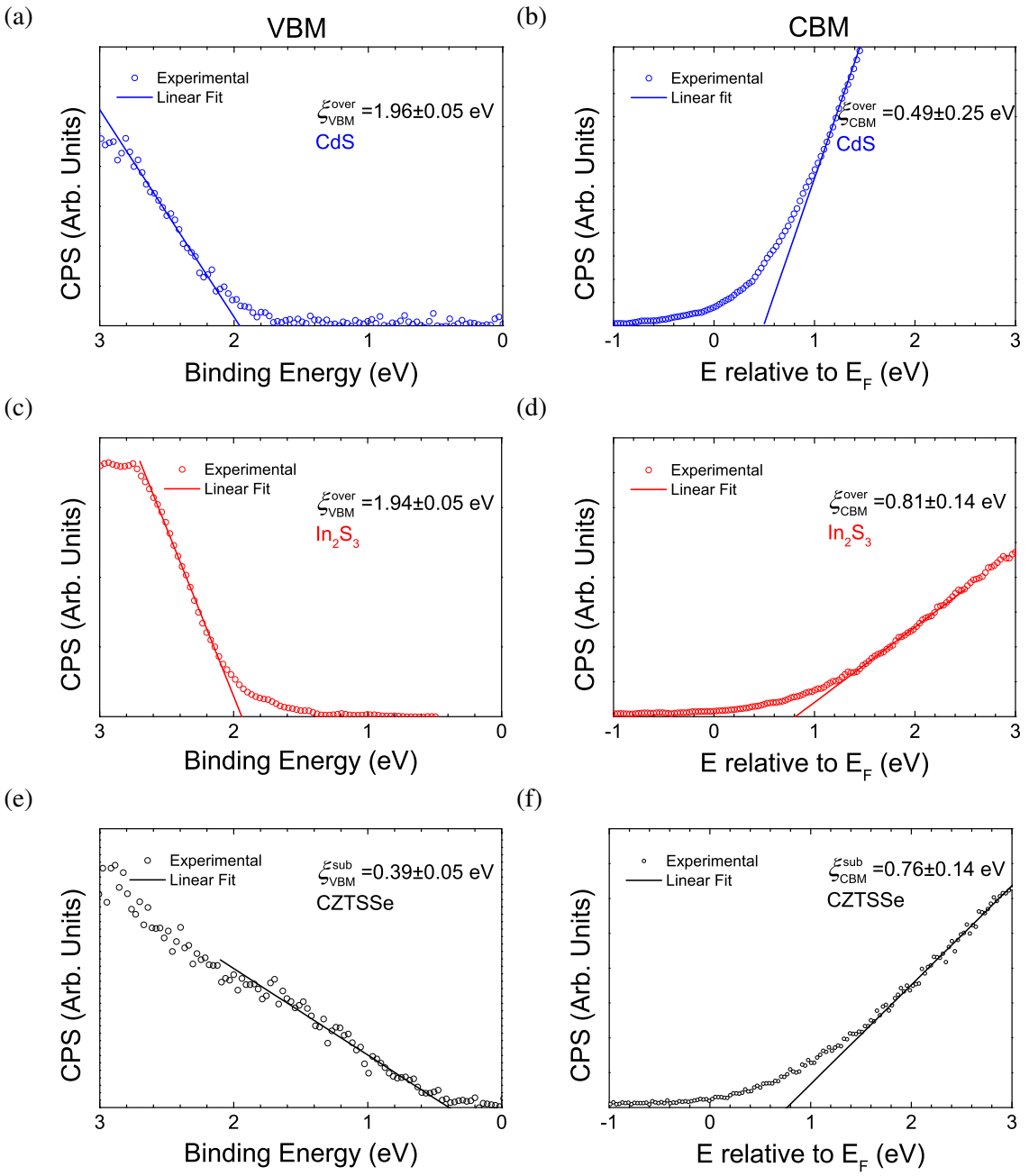

Figure 6.2.1: Valence band maximum regions as measured by XPS for thick samples of (a) CdS, (c) In_2S_3 and (e) CZTSSe and conduction band minimum as measured by IPES for the same samples (b) CdS, (d) In_2S_3 and (f) CZTSSe. Combining XPS/IPES data gives estimated bandgaps of 2.45, 2.75 and 1.15 eV for CdS, In_2S_3 and CZTSSe, respectively. These values are in good agreement with bandgap values of 2.42, 2.72 and 1.14 eV determined from UV-VIS measurements, respectively.

erojunction under illumination, depicted schematically by the dashed lines in Figure 6.2.2(a). V_{oc} is enhanced by the spike-like CBO at the In_2S_3/CZTSSe interface in comparison to cliff-like offset at the CdS/CZTSSe junction. Based on XPS and IPES measurements of nanoparticle-derived

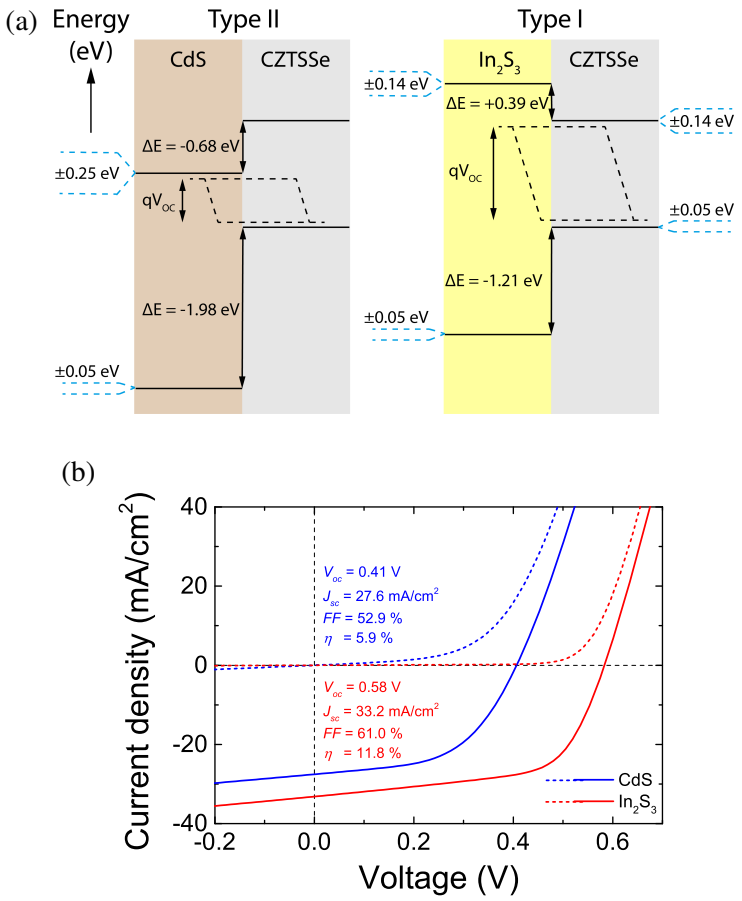

Figure 6.2.2: (a) Experimentally determined band alignment from XPS/IPES data for CdS/CZTSSe (left) and In_2S_3/CZTSSe (right) interfaces. A small 'spike' in the conduction band offset at the In_2S_3/CZTSSe interface theoretically increases V_{oc} compared to that of a 'cliff' alignment at the CdS/CZTSSe interface. The dashed lines represent the degree of quasi fermi level splitting at the buffer/absorber interface and (b) SCAPS device modelling showing increased V_{oc} in In_2S_3-buffered CZTSSe device related to better band alignment. The dashed lines are *J-V* measurements in the dark and solid lines under 1-Sun illumination. Data for the CZTSSe has been derived from experiments on nanoparticle absorbers.

CZTSSe device-like stacks, In_2S_3 is a more appropriate buffer material to enhance device V_{oc} than conventional CdS. Furthermore, SCAPS simulations on CdS- and In_2S_3-buffered CZTSSe devices were performed using the XPS/IPES data, see Figure 6.2.2(b). It is clearly evident the 'spike' CBO in the In_2S_3 based device translates to a significant improvement in V_{oc} compared to the device with CdS buffer.

6.3 Photoluminescence measurements

In order to rule out the existence of possible binary and ternary compounds, Raman spectroscopy was performed to investigate the crystal quality of as-deposited CZTSSe reference, CdS- and

In_2S_3-buffered CZTSSe absorbers fabricated from the same batch of nanoparticle inks, see Figure 6.3.1. The two sharp peaks at 173 and 196 cm^{-1} correspond to CZTSe [127]. All three CZTSSe thin films have a high quality kesterite crystal structure with no obvious secondary phases observed and confirmed the CZTSSe absorbers are identical.

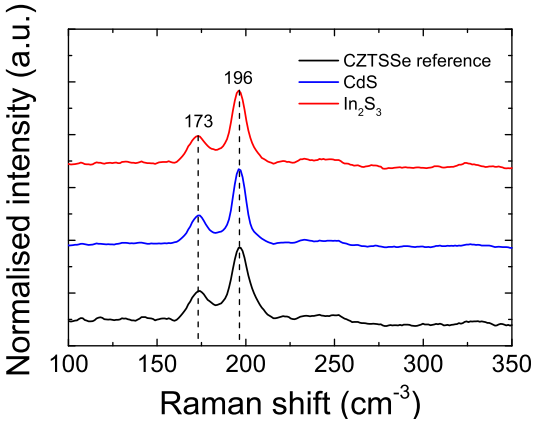

Figure 6.3.1: Raman spectra of as-deposited reference, CdS- and In_2S_3-buffered CZTSSe absorber thin films.

To determine whether the deposition of different buffers causes any modification to the surface region of CZTSSe films, low temperature excitation intensity PL measurements were made on as-deposited CZTSSe reference, CdS and In_2S_3 buffered CZTSSe absorbers fabricated from the same batch of nanoparticle inks. As the absorption coefficient α of CZTSSe is $\sim$4 x10^4 cm^{-1} for the laser excitation wavelength of 532 nm, it can be assumed the incident laser light is fully absorbed within the first 250 nm of the CZTSSe absorber in all three samples, see Figure 5.4.4 [17]. The results of the excitation dependent PL of all CZTSSe samples at 6 K are presented in Figures 6.3.2 and 6.3.3.

PL spectra for all samples exhibit a broad asymmetric shape where the shallower low energy slope is related to the joint density of states (JDOS) of CB/VB tails [97, 101, 108] and the steeper high energy slope depends on the photogenerated carrier distribution [162], see Figure 6.3.2. The asymmetric nature of the PL bands is indicative of a semiconductor with a high degree of band tailing due to spatial fluctuations of VB and/or CB edges [150]. For all samples, the PL peak maxima exhibit strong blue-shifts with increasing excitation intensity up to a saturation point with no increase in PL intensity or peak shift upon higher excitation. A distinct high energy 'shoulder' is observed as the excitation intensity is escalated over several orders of magnitude, which is congruent with the activation of an additional radiative recombination mechanism. The

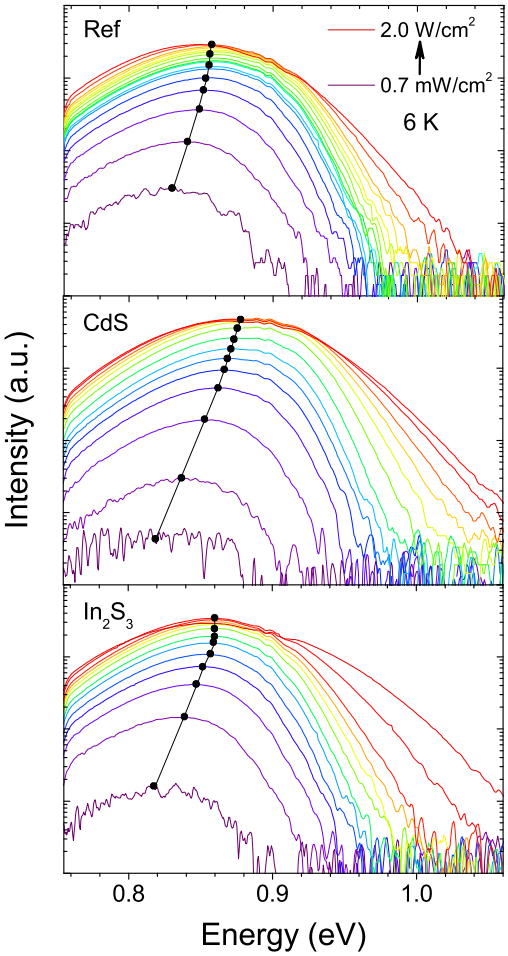

Figure 6.3.2: Excitation intensity dependence of the PL spectra with laser power P for as-deposited reference, CdS- and In_2S_3-buffered CZTSSe films at 6 K (the black line is a guide for the eye to show PL peak shift).

high energy shoulder is predominant in the buffered CZTSSe films, see Figure 6.3.4. An indication of the radiative process is given by evaluating the so-called k value which can be determined from the power law relation between the integrated PL intensity and excitation power, $I_{PL} \propto P^k$ see Chapter 3. Values of $k > 1$ are expected for band-related recombination whereas $k < 1$ indicates defect-mediated recombination. Figure 6.3.3(a) shows a log-log plot of the dependence of I_{PL} on P for all CZTSSe absorber samples, where k can be evaluated from the gradient of a straight fit to the data. The k values for all samples are less than unity (k-Ref = 0.76 $\pm$ 0.04, k-CdS = 0.81 $\pm$ 0.03 and k-In_2S_3 = 0.80 $\pm$ 0.04) suggesting the main recombination mechanism is related to defects within the bandgap of the absorber and remains unchanged regardless of buffer deposition. The presence of charge carriers localised at defects with energy levels above (below) the VB (CB) is further indicated by the strong blue-shift of PL peak maxima with increasing excitation intensity

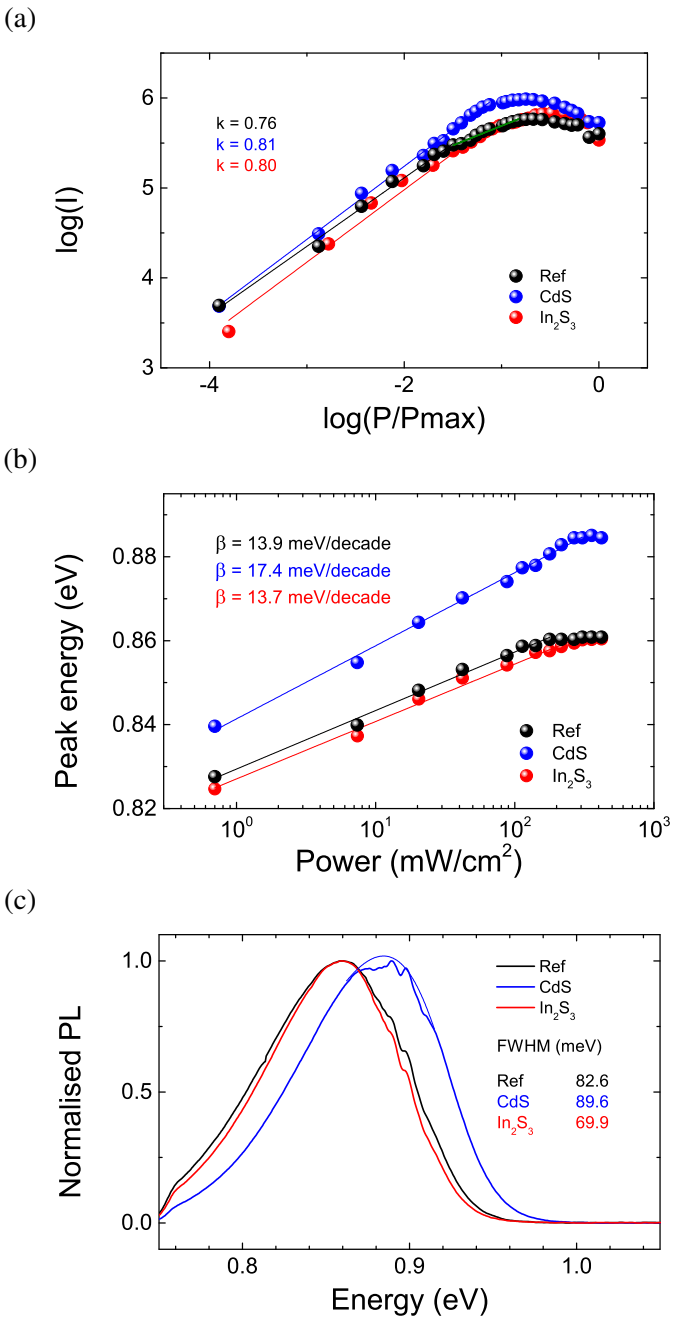

Figure 6.3.3: (a) Derivation of k parameter from $I \approx P^k$, (b) evolution of PL band maxima with increasing P and (c) normalised 6 K PL spectra of all films excited with same laser intensity showing significant shift of PL peaks from estimated room temperature bandgap of ∼1.14 eV (the oscillations around 0.9 eV are due to water vapor absorption, the thin blue line is asymmetric double sigmoidal fit to PL spectra).

(solid black lines in Figure 6.3.2).

The blue-shifting PL energy maxima for CZTSSe samples as a function of increasing laser power are shown in Figure 6.3.3(b). The energetic shift parameter β has a similar value of ∼14 meV/decade for the as-deposited reference and In_2S_3-buffered absorbers which increases to

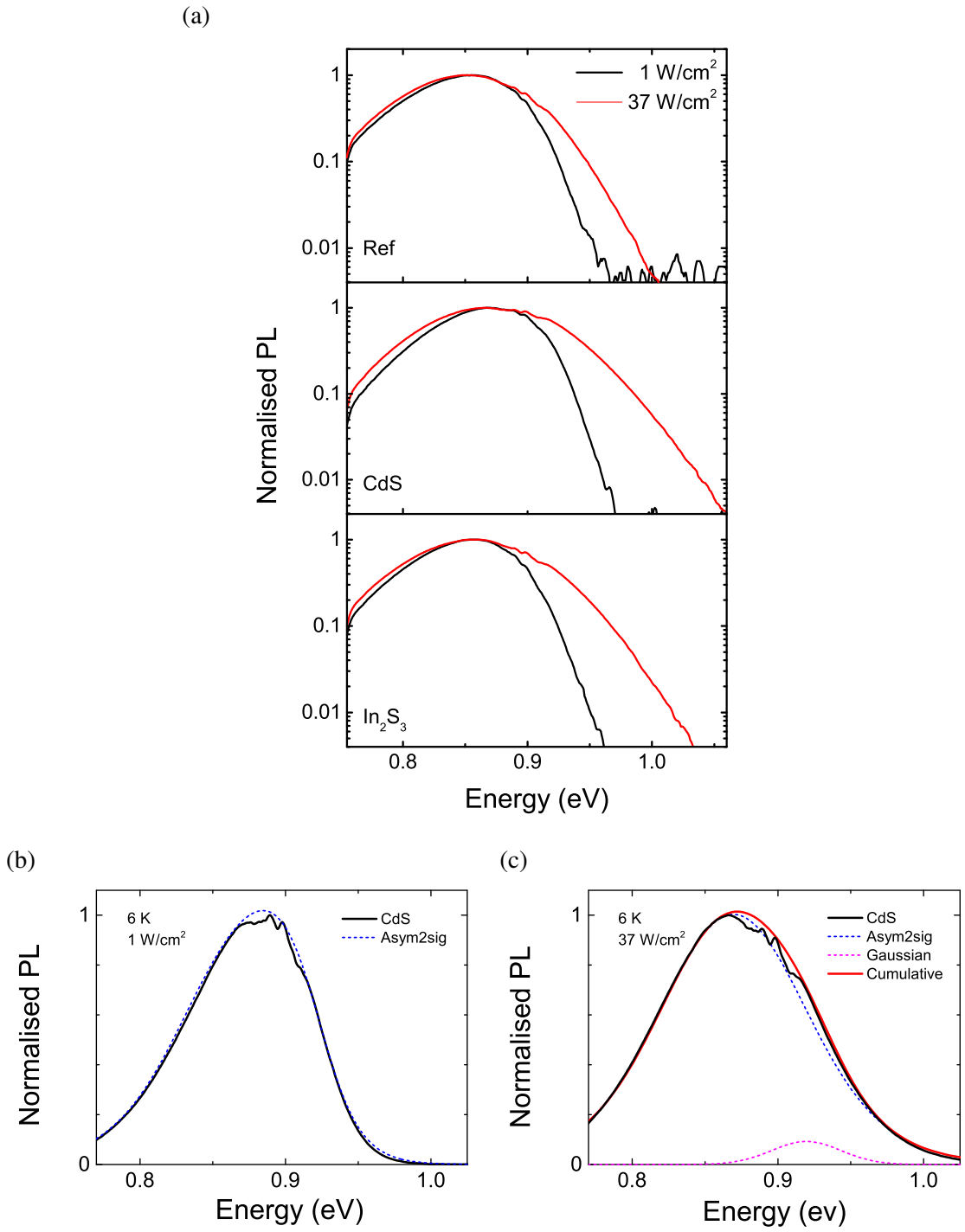

Figure 6.3.4: (a) Emergence of high energy 'shoulder' in PL spectra of as-deposited, CdS and In_2S_3 based CZTSSe films indicating saturation of QDAP defects and an increasing contribution to PL intensity from band-related radiative recombination, (b) asymmetric double sigmoidal peak fit at 0.885 eV of 6 K PL spectra from CdS based CZTSSe film under low excitation and (c) cumulative peak fitting of PL spectra from the same film under high excitation. Fitted with asymmetric double sigmoidal at 0.872 eV and gaussian at 0.920 eV which shows the emergence of another radiative transition. Note oscillations around 0.90 eV are due to water vapour absorption of light.

$\sim$17 meV/decade for the CdS sample. The increase in β value for CdS-buffered absorber also indicates a higher degree of charge compensation than the other CZTSSe based films. Here radiative recombination can be explained by different models: i) QDAP and ii) spatial electrostatic potential fluctuations [76, 99, 102, 105, 181]. In considering the energetic blue-shift of PL peak maxima with increasing excitation intensity, Zacks and Halperin conclude the expected β values for the QDAP model should only be $\sim$8(2) meV/decade for CZTS(CZTSe) [182]. In comparison, the β values determined for both types of CZTSSe film studied here are significantly higher, which would indicate the observed excitation dependent behaviour is also influenced by electrostatic potential fluctuations. Evidence of this is illustrated in Figure 6.3.5 where increasing numbers of photogenerated carriers (due to increasing excitation intensity) screen the Coulomb potential of the charged defects, consequently flattening the band edge fluctuations. The average depth of these potential fluctuations γ is inversely proportional to the generated free carrier density (see Equation 3.2.3 and Figure 3.2.3), thus γ reduces as the excitation intensity increases. Electrostatic potential fluctuations give rise to a number of radiative transitions, such as tail-to-impurity (TI) where electrons trapped in CB tail states recombine with holes localised at acceptor levels and exhibit similar behaviour to QDAP at low temperatures, see Chapter 3.

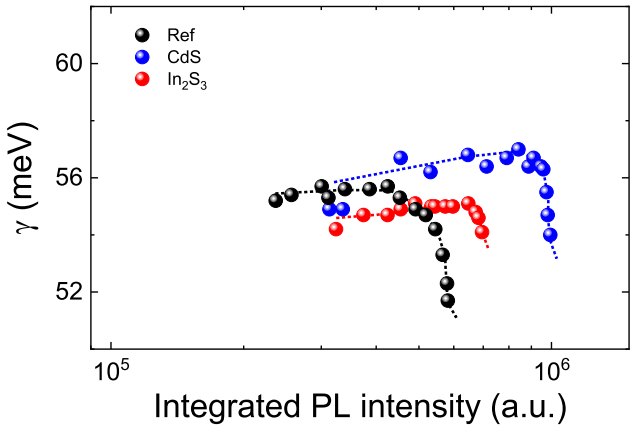

Figure 6.3.5: Plot of root mean square depth of energy band edge potential fluctuations γ versus PL intensity. The reduction in γ over a certain arbitrary unit range in PL intensity can be attributed to Coulomb screening due to increased generation of charge carriers. The contribution to γ due to electrostatic potential fluctuations is inversely proportional to the free carrier density, which in turn is related to PL intensity. As the excitation intensity increases and generates additional free carriers, the electrostatic potential fluctuations start to flatten, see Equation 3.2.3. The dashed lines are a guide for the eye.

The blue-shift of PL energy maxima is correlated to increasing Coulombic attraction between

charged acceptor and donor defect clusters [104, 105, 181]. Maximum Coulombic attraction occurs when all QDAP defect states are occupied and the blue-shift of the PL energy maxima saturates, where ΔE is the magnitude of the associated blue-shift (see Figure 6.3.3(b)).

According to Equations 3.2.8 and 3.2.9, QDAP densities of 1.8 ± 0.1 x10^{18}, 4.7 ± 0.2 x10^{18} and 2.3 ± 0.1 x10^{18} cm^{-3} were estimated from ΔE values of 33, 46 and 36 meV for as-deposited, CdS-buffered and In_2S_3-buffered CZTSSe absorbers, respectively. Both absorbers with buffer layers show an increase in the QDAP density compared to the as-deposited reference and most notable is the almost threefold increase in defect density in the CdS-buffered thin film. The augmented QDAP densities could be attributed to the diffusion of elements such as In and Cd across the buffer/absorber interface during buffer deposition forming additional acceptor and donor defects in the absorber near the heterojunction. Alternatively, the deposition of a buffer layer could act to passivate the CZTSSe film surface by reducing the number of non-radiative defect centres. The large QDAP density and β value determined for the CdS-buffered sample would suggest higher concentrations of self-compensated defect cluster in the CZTSSe material. The CZTSSe absorbers in all thin film samples studied here are non-stoichiometric, grown in a Cu poor and Zn rich environment. Under such conditions, the concentrations of self-compensated defect clusters [V_{Cu} + Zn_{Cu}] and [Zn_{Sn} + 2Zn_{Cu}] are expected to be high [88]. The observed increase in compensation in the absorbers with buffer layers (albeit slight in the case of In_2S_3) could be accounted for by the formation of additional antisite defects such as Cd_{Cu} and In_{Sn} promoted by buffer deposition conditions [95, 183–187]. Due to the valencies of Cd and In atoms, antisites Cd_{Cu} and In_{Sn} form donor and acceptor defects, respectively. In the case of Cd_{Cu}, high concentrations in the top region of CZTSSe would contribute to *n*-type doping effectively reducing the overall *p*-type doping, increasing charge compensation and enlarging the depletion region. Conversely, *p*-type doping would rise in the interface region of CZTSSe absorber due to acceptor state In_{Sn}. It has also been reported by several groups that Cu diffuses from the CZTSSe absorber into the CdS as a result of an annealing step following buffer deposition [184, 188, 189]. The resulting rise in density of V_{Cu} point defects can further increase the Cu depletion and *p*-type doping of the CZTSSe surface region. The effect of buffer deposition on apparent doping density will be discussed later (doping and depletion region width from *C-V* profiling and effects of interface defects from *C-f* measurements). Further evidence of structural/electronic modification of the upper absorber layer in the CdS/CZTSSe film is shown in Figure 6.3.3(c). The normalised PL spectra for all films at 6 K

illustrate a significant red-shift in peak position from the bandgap of the films at room temperature ($\sim$ 1.14 eV) estimated from IQE measurements (see Figure 6.4.3(a)). This is additional confirmation the main radiative recombination channel is mediated by defects within the bandgap of the absorbers. The oscillations around 0.9 eV are due to water vapour absorption. PL spectra were fitted with asymmetric double sigmoidal function (DSF) proposed in [108] so as to determine the position of the PL peak maximum. The PL peaks of the as-deposited reference and In_2S_3-buffered films are coincidental and red-shifted by $\sim$30 meV compared to the CdS-buffered film. This suggests the CdS deposition conditions modify the absorber structure near the interface. Yan *et al.* investigated the effect of a 300 °C post-deposition heat treatment on CdS/Cu_2ZnSnS_4 (CZTS) heterojunction and found an interdiffusion of Cd and Zn between the buffer and absorber with diffusion depths of 200 and 15 nm for Cd and Zn, respectively [183]. High-angle annular dark-field (HAADF) imaging confirmed the presence of Cd_{Cu} antisite defects in the top region of the CZTS film. It is also possible for Cd to occupy Zn sites forming alloy $Cu_2Cd_xZn_{1-x}SnS_4$ (CCZTS) with a different bandgap to the bulk material. Both observations could account for the shift in PL peak position illustrated in Figure 6.3.3(c). The average depth of band edge potential fluctuations γ is directly proportional to the total charged defect density N_t (which includes both radiative and non-radiative defects) [98, 99, 105]. Siebentritt *et al.* determined the low energy tail in PL spectra $I_{PL}(E)$ followed a Gaussian distribution which accurately described the defect-related nature of absorption tails caused by electrostatic potential and/or bandgap fluctuations [101].

Using Equation 3.2.6, γ values of 54.8 ± 0.1, 55.0 ± 0.1 and 56.8 ± 0.1 meV were determined for as-deposited reference, In_2S_3-buffered and CdS-buffered absorbers, respectively. The increase in γ for the CdS-buffered sample could be ascribed to an increase in charge compensation. For a highly compensated *p*-type material with a fixed acceptor density such as CZTSSe, $\gamma \propto N_t$ (where N_t is the sum of charged acceptor ${N_A}^+$ and donor ${N_D}^-$ concentrations and $N_A \approx N_D$), therefore an increase in donor concentration N_D will result in an increase in potential fluctuation depth γ. In this case, the total number of ionised defects increases together with the level of compensation which in turn reduces the number of free holes. The screening length is thereby reduced which also contributes to an increase in γ.

The results of temperature-dependent PL measurements are presented in Figures 6.3.6 and 6.3.7. Here PL spectra were obtained using laser excitation intensity just below the saturation of PL peak energy to ensure emission stems from QDAP recombination alone (and not from

additional contributions due to band-related recombination, see Figure 6.3.4(a)). In Figure 6.3.6, the PL signal for the as-deposited film is fully quenched at temperatures greater than 160 K which suggests carriers are efficiently redistributed into non-radiative states. The appearance of a PL peak around 0.96 eV as temperature rises to 300 K in CdS- and In_2S_3-buffered films indicates another radiative recombination mechanism becomes predominant. The evolution of PL peak maxima with increasing temperature for all films is illustrated in Figure 6.3.7(a).

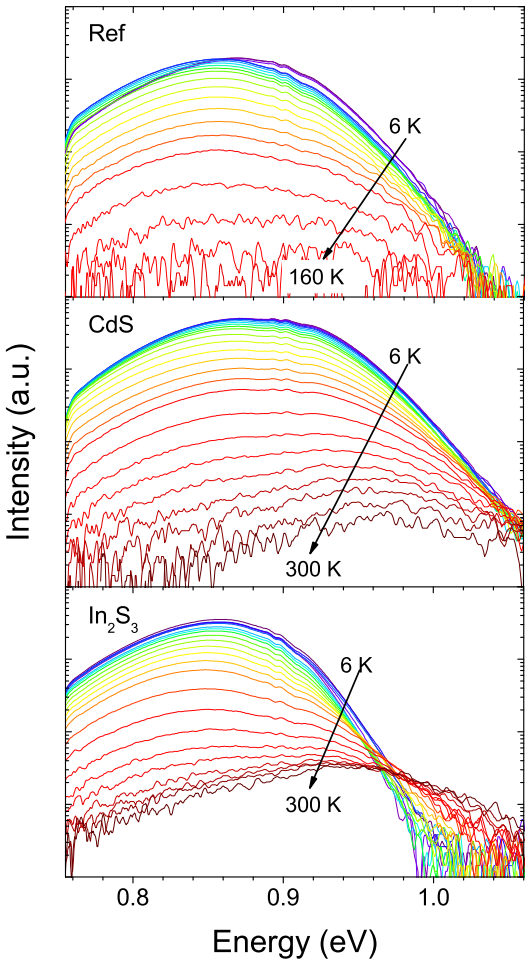

Figure 6.3.6: Temperature dependence of PL spectra for as-deposited reference, CdS- and In_2S_3-buffered CZTSSe films at laser power P = 1.7 W/cm^2.

The PL peak in the as-deposited film shows a slight red-shift in temperature range 6 - 60 K before exhibiting a slight blue-shift as temperature is increased up to 160 K, whereupon PL emission is thermally quenched. The buffered films demonstrate a different behaviour. Both buffered films show a red-shift of the band maximum at a greater rate than the as-deposited film as temperature rises from 6 K. The PL peaks of both films then blue-shift significantly at temperatures higher

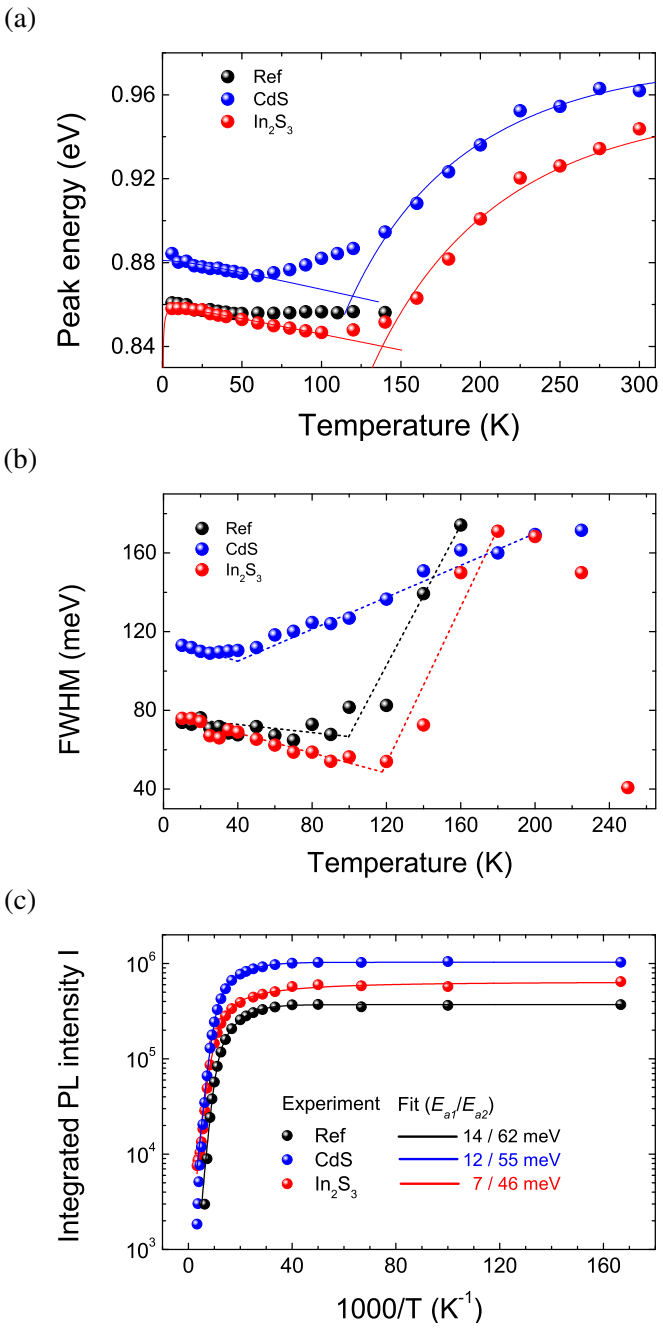

Figure 6.3.7: (a) Maximum PL peak position vs. temperature showing bandgap dependence in low temperature regime changing to band tail related dependence at higher temperatures with overall 'S'-type behaviour according to Equation 6.3.1 (b) and temperature dependence of full width half maximum (FWHM) of PL spectra showing 'V'-type behaviour of all films and (c) Arrhenius plot of integrated PL with derived defect activation energies.

than T_{min} = 60 K and 100 K for CdS-buffered and In_2S_3-buffered samples, respectively. Similar QDAP behaviour was observed for CZTSSe solid solutions [130, 188, 190]. The temperature dependence of PL emission peak has been described previously in semiconductor materials with

multiple quantum wells using a modified Varshni relation [154, 191, 192],

$$E_g(T) = E_g(0) - \left(\frac{AT^2}{T+B}\right) - \left(\frac{\sigma^2}{k_B T}\right) \tag{6.3.1}$$

where $E_g(0)$ is the material bandgap at 0 K, A and B are Varshni coefficients and σ is the degree of localisation of charge carriers within the quantum wells. It is evident the simple Varshni relation E_{PL}(T) = E_g(0) - (AT^2)/(B+T) is a good approximation of the PL peak behaviour for all films at low temperature (see Figure 6.3.7(a)). As temperature increases above T_{min} in the buffered films, the behaviour is more readily described by the band-tail model proposed by Eliseev *et al*, E_{PL}(T) = E_g(0) - ($\sigma^2/(k_B T)$) [193]. Thus, the temperature dependence of the PL energy peak in these films exhibits 'S-shaped' behaviour. Increasing the temperature of the films also leads to broadening of the high energy side of the PL spectra, associated with carrier thermal redistribution between quantum wells in the fluctuating band edges. Figure 6.3.7(b) shows the evolution of PL spectra FWHM with increasing temperature. The PL spectra for the CdS-buffered film are the broadest of all films, again indicating this film has the highest defect concentration. All films exhibit a slight reduction in bandwidth with increasing temperature from 6 K until reaching a minimum value around T_{min}. Further temperature rise reveals significant broadening of PL bandwidth for the as-deposited reference and In_2S_3-buffered films. The broader PL spectra and gradual increase in bandwidth above T_{min} could suggest the presence of an unresolved PL band in PL emission from the CdS-buffered film. That notwithstanding, FWHM of the PL spectra of all films demonstrate 'V-shaped' behaviour commensurate with redistribution of localised carriers in potential wells of different depths. Further analysis of the temperature dependence of PL spectra reveals the activation energies of defects involved in the recombination mechanisms for the studied films. A two-defect model (Figure 6.3.7(c)) best describes the observed thermal quenching (Equation 3.2.11). Defect activation energy E_{a1} relates to temperature range $T < T_{min}$ and E_{a2} to range $T > T_{min}$. The determined activation energies E_{a1} and E_{a2} are 14 $\pm$ 1, 12 $\pm$ 1, 7 $\pm$ 1 meV and 62 $\pm$ 8, 55 $\pm$ 3, 46 $\pm$ 7 meV for as-deposited reference, CdS-buffered and In_2S_3-buffered films, respectively.

Previous studies have attributed the shallow level E_{a1} to the CB average potential well depth rather than a discrete defect level based on temperature-dependent PL peak behaviour for $T < T_{min}$ [130, 188]. Krustok *et al*. theorise in heavily doped materials electrons with very small effective mass are unable to localise in smaller diameter potential wells created by electrostatic potential

fluctuations [190]. However, bandgap fluctuations create slightly larger diameter potential wells within which electrons can become localised. The average depth of bandgap fluctuations γ_{BG} can be estimated from the magnitude of the red-shift in PL peak position at temperatures below T_{min}. From Figure 6.3.7(a) a red-shift in PL maxima of 3, 11 and 12 meV were determined for as-deposited reference, CdS-buffered and In_2S_3-buffered films. These values are significantly lower than the average band-edge fluctuations ~56 meV extracted from the low energy slope of PL spectra. The presence of electrostatic potential fluctuations of average depth γ_{EP} would account for the discrepancy. The coexistence of bandgap and electrostatic potential fluctuations has also observed in other kesterite compounds [162, 194]. Rey *et al.* proposed the total fluctuation depth is a combination of γ_{EP} and γ_{BG} such that $\gamma^2 = {\gamma_{EP}}^2 + {\gamma_{BG}}^2$. Given the low values of γ_{BG} in all three films, electrostatic potential fluctuations are the predominant cause of the spatial band-edge fluctuations. Unlike electrons, holes have larger effective mass and can be trapped in the deeper potential wells in the VB caused by clusters of acceptor defects. Thus the JDOS (determined from the low energy slope of PL spectra) represents electron states affected only by bandgap fluctuations and hole states additionally affected by electrostatic potential fluctuations [190].

Alternatively, with an increase of effective-mass donors in strongly compensated semiconductors, discretisation of localised electron states is lost as the states merge with the CB [102]. Acceptor states remain discrete due to their larger effective mass. Recombination would involve radiative transitions between this CB tail and acceptor impurity (TI transition) which manifests as a red-shift in E_{PL} with increasing temperature. Activation energy E_{a2} is associated with radiative recombination in the temperature regime $T_{min} < T < 295$ K. Given the similarity in γ and E_{a2} values for all three CZTSSe films, it would be reasonable to assume radiative transitions involve tail states as T approaches room temperature. However, in a compensated material the PL peak is expected to red-shift with increasing T, which is not the case here where a strong blue-shift in E_{PL} with increasing T is observed. Levcenko *et al.* saw very similar temperature-dependent PL behaviour in their CZTSSe films and concluded the deeper defect level E_{a2} is more probably a donor state in a *p*-type absorber [130].

Room temperature excitation-dependent PL behaviour of the CdS-buffered and In_2S_3-buffered CZTSSe films is shown in Figure 6.3.8(a). The PL peaks at 0.962 eV (CdS-buffered) and 0.944 eV (In_2S_3-buffered) are significantly red-shifted from their respective bandgaps at 1.14 eV determined from IQE measurements (see Electrical device characterisation Section, Figure 6.4.3(a)).

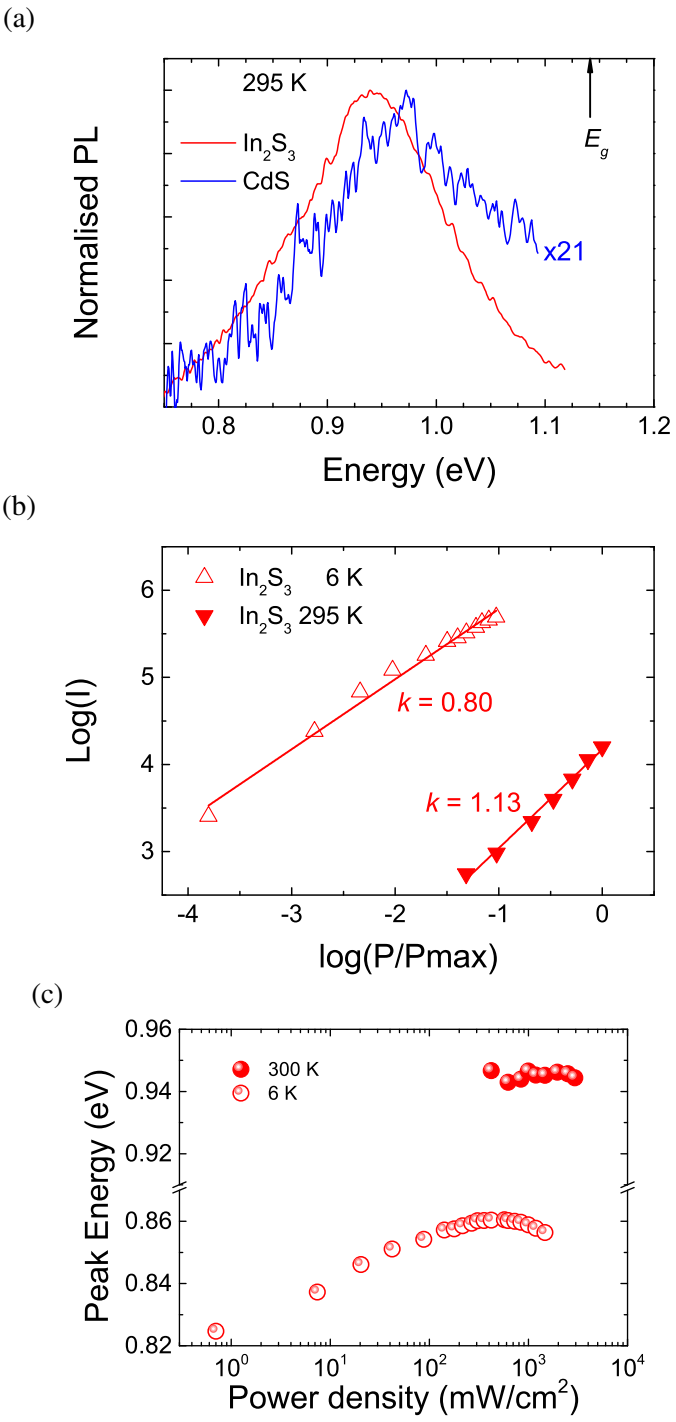

Figure 6.3.8: (a) Room temperature normalised PL spectra for CdS- and In_2S_3-buffered CZTSSe films, (b) intensity dependent PL plot showing change in k parameter of In_2S_3 based film between 6 K and room temperature and (c) evolution of PL band maxima with increasing excitation intensity for the In_2S_3-buffered CZTSSe film at 6 and 300 K. No PL peak shift was observed for the film at 300 K indicating the radiative transition stems from band-related recombination.

Figure 6.3.8(b) shows the excitation-dependent PL response of the In_2S_3-buffered film at 6 K and 295 K. A change in k value indicates a change in the main radiative recombination process

from defect mediated at 6 K ($k < 1$, $k = 0.80$) to band-related at 295 K ($k > 1$, $k = 1.13$). Further evidence of a band-related transition is shown in Figure 6.3.8(c) where there is no shift in the PL peak with increasing excitation at room temperature. As the CZTSSe absorber has *p*-type conductivity, a CB-acceptor transition is most likely responsible for the room temperature PL observations. Although the PL signal from the CdS-buffered film was too low to analyse accurately, it is reasonable to assume the same acceptor defect is also present in this film. The magnitude of the PL peak red-shift from room temperature bandgap is roughly equivalent to the activation energy of the acceptor defect, giving values of 182 meV and 200 meV for CdS-buffered and In_2S_3-buffered films, respectively. These activation energies are in agreement with the DLTS study of CZTSSe solar cells in Chapter 5. Based on all PL observations, radiative recombination in the CZTSSe-based films changes from QDAP at low temperature to band-to-impurity (BI) at higher temperatures. QDAP recombination involves a donor defect with activation energy in the range 46-62 meV and acceptor defect with activation energy in the range 182-200 meV.

The BI transition involves recombination between the CB and same deep acceptor defect. *Ab initio* DFT calculations [37] reveal donor defects such as Zn_{Cu}, Sn_{Cu} antisites and Cu_i are shallow in nature whereas Sn-related acceptor defects such as V_{Sn}, Cu_{Sn} and Zn_{Sn} have formation energies in the range of the observed activation energies of acceptor defects found in the CZTSSe-based films studied here. Given the Cu-poor and Zn-rich growth conditions of the absorber films, it is reasonable to assume the donor and acceptor defects present are antisites Zn_{Cu} and Zn_{Sn}. Such conditions also promote higher concentrations of free hole carrier defect V_{Cu} and associated benign defect clusters [V_{Cu} + Zn_{Cu}] and [Zn_{Sn} + 2Zn_{Cu}] which are expected in all analysed CZTSSe-based films. Given the antisite defect Cd_{Cu} forms a shallow donor level with formation energy similar to Zn_{Cu} [195] and Cd diffusion into CZTSSe absorbers has been demonstrated experimentally [183, 184], it is reasonable to assume the presence of Cd_{Cu} defects and [V_{Cu} + Cd_{Cu}] clusters in the surface region of the CdS-buffered CZTSSe film studied here. It would account for the increase in the degree of charge compensation and QDAP density determined from PL measurements for this thin film.

Based on all PL observations, radiative recombination in the CZTSSe-based films probably changes from QDAP or TI at low temperature to BI at higher temperatures involving the same deep acceptor defects, which are most likely Sn-related, see Figure 6.3.9.

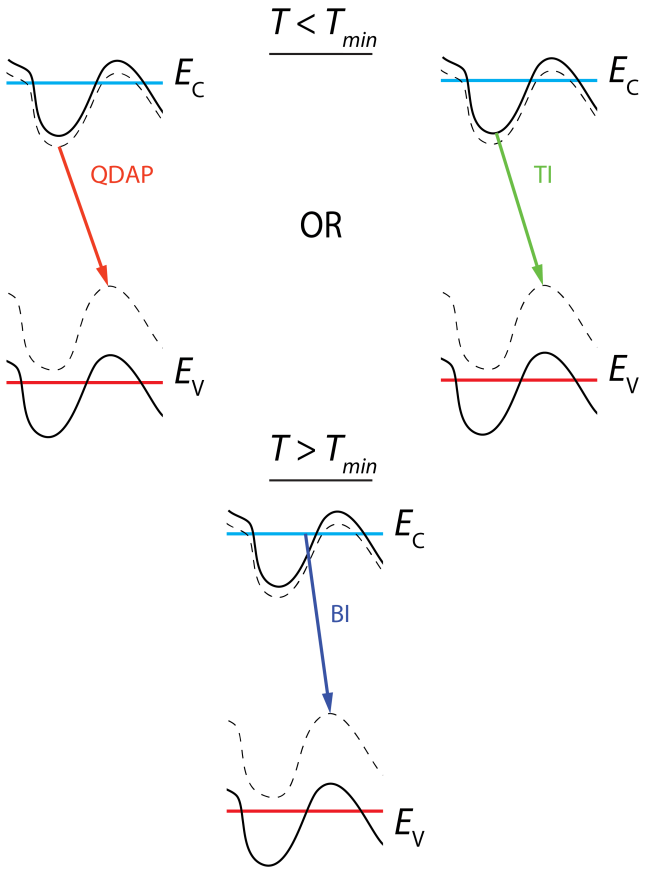

Figure 6.3.9: Possible radiative recombination pathways in CdS- and In_2S_3-buffered CZTSSe thin films involving shallow donor states or CB tail and deep acceptor states at temperatures below T_{min} gradually changing to recombination from the CB to the same deep acceptor impurity above T_{min}.

6.4 Electrical device characterisation

The results of electrical device characterisation of CdS-buffered and In_2S_3-buffered CZTSSe solar cells are presented in Figure 6.4.1 and device parameters shown in Table 6.4.1. The *J*-*V* curves for the best performing devices measured in the dark and under 1-sun illumination are plotted in Figure 6.4.1(a). It is evident the In_2S_3-based device shows a clear drop in V_{oc} and suffers from poor shunt resistance R_{sh} ($\sim$35 Ωcm^2) compared to the CdS-based device ($\sim$96 Ωcm^2), despite device simulations (Figure 6.2.2(b)). As a consequence, the fill-factor (*FF*) is also reduced. The cause of the low shunt resistance is not immediately apparent as SEM images reveal a conformal layer of In_2S_3 of thickness $\sim$60 nm following CBD (see Figure 6.4.2). Also highlighted are the crossover points in the dark and illuminated *J*-*V* curves. Such a crossover can occur as a result of a voltage-dependent photocurrent due to a low built-in potential, the cause of which may be the

presence of a Schottky barrier at the back contact or a depleted front layer [196]. In Chapter 4, there was no evidence of a blocking barrier at the back contact, which suggests that the crossover issue may be due to the buffer-absorber interface.

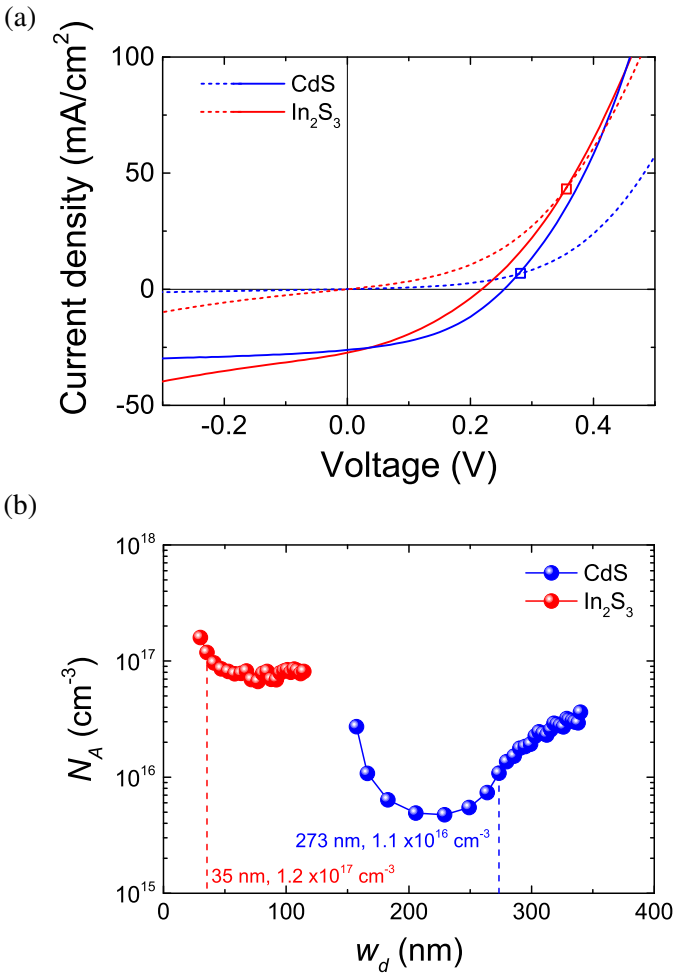

Figure 6.4.1: (a) *J-V* curves of solar cells with CdS and In_2S_3 buffers measured in the dark (dashed lines) and under 1-Sun illumination (solid lines) with crossover points highlighted by □ and (b) *C-V* depth profiles with indicated w_d and N_A values at zero bias.

To gain an insight into the reduced V_{oc}, capacitance-voltage (*C-V*) measurements were conducted at a frequency of 100 kHz. The *C-V* profile curves for CZTSSe devices with different buffers are presented in Figure 6.4.1(b). The carrier concentration N_A and depletion region width w_d for both devices at zero voltage bias are indicated on the plot. In terms of N_A, an increase in doping density of around one order of magnitude from 1.1 x 10^{16} cm^{-3} to 1.2 x 10^{17} cm^{-3} is observed for the In_2S_3-buffered compared to the CdS-buffered device. According to [197] the change in V_{oc} can be estimated by $\Delta V_{oc} = kT/q\ ln(N_{A1}/N_{A2})$, assuming a change only in the doping density of the absorbers being compared. The increase in doping density in the In_2S_3-based

Table 6.4.1: Device parameters for the CZTSSe cells at room temperature. $R_{s,L}$, $R_{sh,L}$, n and J_0 are the series resistance, shunt resistance, ideality factor and reverse saturation current respectively, measured using the light *J-V* data (parameters were determined using methods described in [61]). E_g, N_A, w_d and L_d are the bandgap, apparent doping density, depletion region width and effective diffusion length, respectively.

CZTSSe buffer	η (%)	FF (%)	V_{oc} (mV)	J_{sc} (mA/cm^2)	$R_{s,L}$ (Ω cm^2)	$R_{sh,L}$ (Ω cm^2)	A	J_0 (mA/cm^2)	E_g (eV)	N_A (cm^{-3})	w_d (nm)	L_d (nm)
CdS	3.2	42.6	255	26.1	1.64	106.3	2.0	4.9 x 10^{-2}	1.145	1.1 x 10^{16}	273	532
In_2S_3	2.3	35.3	220	27.3	2.27	25.4	1.6	1.4 x 10^{-3}	1.144	1.2 x 10^{17}	35	681

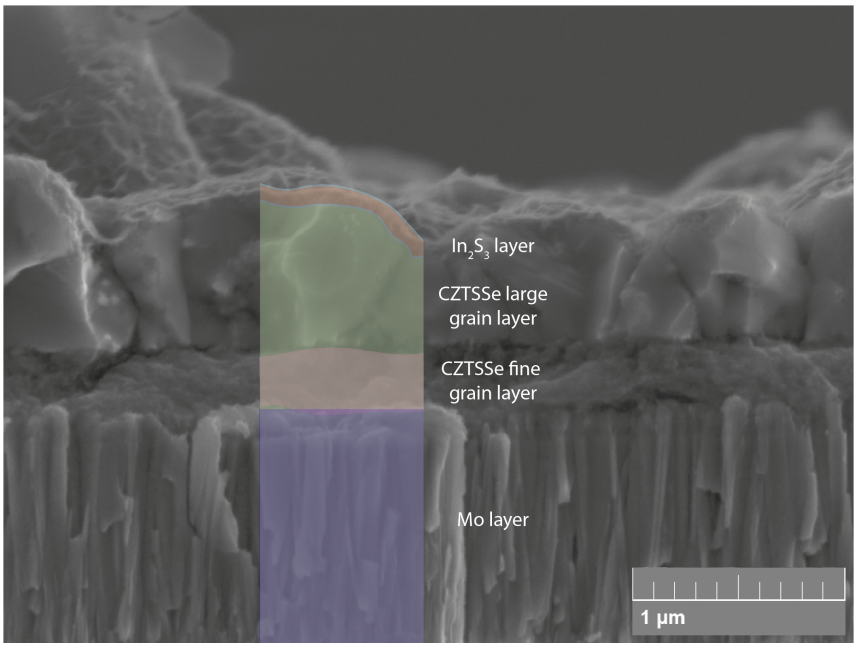

Figure 6.4.2: Cross-sectional SEM image of In_2S_3-buffered CZTSSe thin film showing conformal coating of In_2S_3 layer.

device should have an associated V_{oc} improvement of 61 mV. As V_{oc} is inversely proportional to shunt conductance G_{sh}, this anomaly can be explained in terms of increased G_{sh} compared to the CdS-based device (G_{sh} (In_2S_3) = 39.3 mS/cm^2, G_{sh} (CdS) = 9.4 mS/cm^2) [186]. Similar carrier concentrations were observed in CZTSSe devices with In_2S_3 buffer layers and CZTSSe absorbers intentionally doped with In [171, 186, 198]. The elevated hole concentrations in these devices and ones studied here is mainly due to the substitution of Sn^{4+} with In^{3+}, facilitated by the similarity in their ionic radius [185]. The depletion region width w_d in the In_2S_3-buffered device is 35 nm, which is almost eight times shorter than that of the CdS-buffered device (w_d = 273 nm). As effective charge separation occurs in the depletion region in the absorber material of a solar cell, such a small w_d due to high hole concentration in CZTSSe adversely affects carrier collection. The effective carrier collection length L_{eff} is also related to the diffusion length of the minority carrier L_d and is roughly equal to $w_d + L_d$.

The bandgaps of the In_2S_3- and CdS-buffered CZTSSe absorbers were determined from IQE data, see Figure 6.4.3(a), giving values of ∼1.14 eV for both types of absorber. IQE measurements can also provide additional information on solar cell parameters. It has been shown that the shape of the IQE curve is determined by the absorption coefficient α and carrier collection efficiency within the solar cell [113]. Generally, for small IQE (where IQE < ∼0.3), $\alpha \propto$ -ln (1-

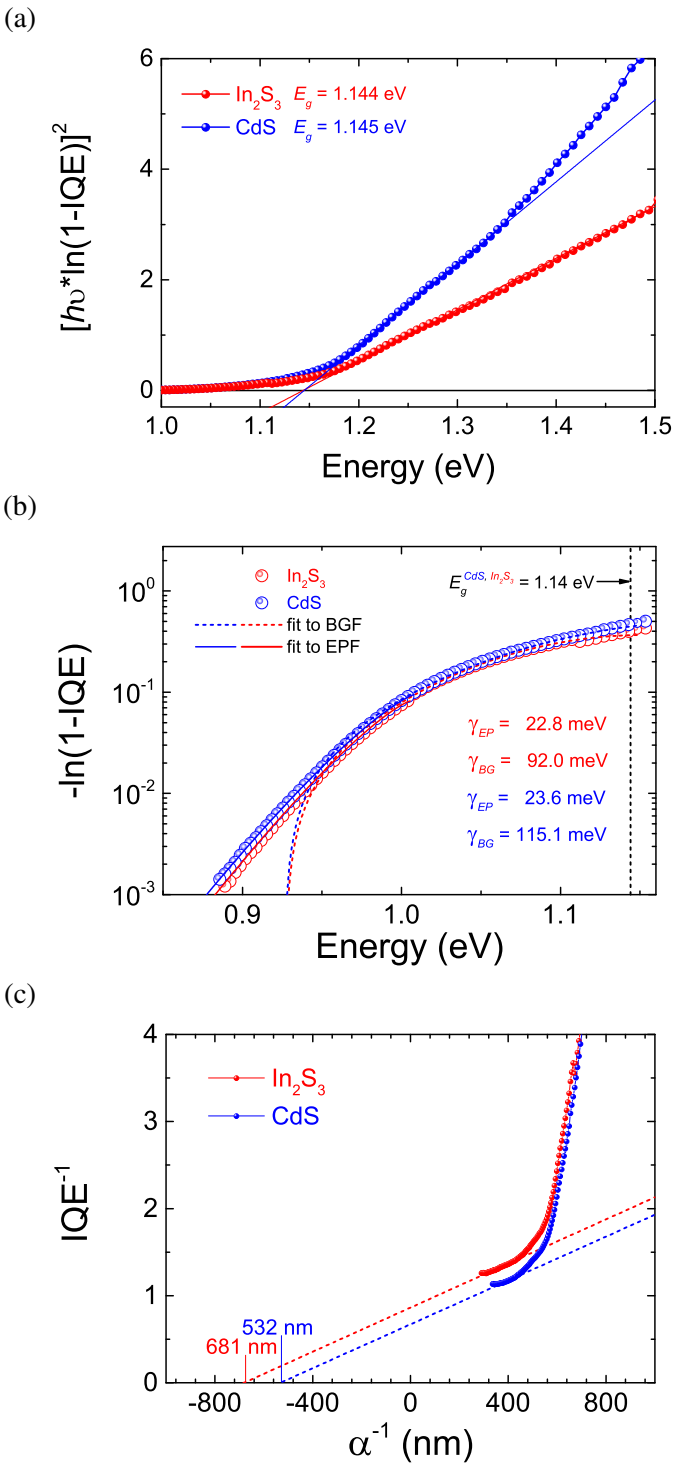

Figure 6.4.3: (a) Bandgap determination for CdS- and In_2S_3-buffered CZTSSe devices from internal quantum efficiency (IQE) measurements, (b) fitting of the absorption coefficient α below the bandgap of both types of device to estimate the magnitude of electrostatic potential fluctuations γ_{EP} (solid line) and bandgap fluctuations γ_{BG} (dashed line) and (c) effective carrier diffusion length L_{eff} extracted from absorption coefficient/IQE data for CdS and In_2S_3 based devices.

IQE($h\nu$)). A plot of α vs. energy ($h\nu$) is shown in Figure 6.4.3(b) where the extent of band tailing in both types of device is clearly evident. The absorption due to band tailing can be equivalently described by a superposition of bandgap and electrostatic potential fluctuations. With regard to bandgap fluctuations, a probability-based Gaussian distribution model can be applied, where σ_g and $E_{g,mean}$ are the standard deviation (average fluctuation depth) and the mean of the spatially varying bangap, respectively (see Equation 3.2.21). This model assumes the tailing in the absorption spectra arises from tailing in the local density of states which are proportional to the local absorption coefficient. For electrostatic potential fluctuations, there are no spatial variations in E_g and the fluctuations result from random distributions of charged defects (see Chapter 3). According to [98], the absorption coefficient below E_g can be described by Equation 3.2.22 in order to determine the average electrostatic potential fluctuation depth relevant for optical transitions, γ_{opt} (σ_g and γ_{opt} are equivalent to γ_{BG} and γ_{EP}). According to Equations 3.2.21 and 3.2.22, γ_{BG} values of 92.0 and 115.1 meV and γ_{EP} values of 22.8 and 23.6 were determined for the In_2S_3- and CdS-buffered devices, respectively. It is apparent that bandgap fluctuations are predominantly responsible for the large band tailing observed in both types of device at room temperature, whereas electrostatic potential fluctuations dominate at cryogenic temperatures, as discussed in the previous section. A reduction in electrostatic potential fluctuations with increasing temperature is to be expected due to the additional Coulomb screening from thermally activated and photogenerated carriers which serve to flatten the band edge distortions. According to $\gamma^2 = {\gamma_{EP}}^2 + {\gamma_{BG}}^2$, the total bend edge fluctuation depth γ for the In_2S_3 and CdS based solar cells was calculated to be 94.8 and 117.5 meV, respectively. Analysis of the low energy slope of the room temperature PL spectra (detailed in Chapter 3) of the In_2S_3-buffered CZTSSe absorber revealed a γ value of 97.4 meV, which is in very good agreement with γ values obtained from absorption data. Due to poor PL signal from the CdS-buffered absorber, no value for γ for this absorber was available. Such band edge fluctuations could originate from high concentrations of self-compensated [$2Cu_{Zn}$ + Sn_{Zn}] defect clusters due to Cu-Zn disorder in the kesterite crystal lattice [37]. Rey *et al.* observed similar bandgap fluctuations in CZTS, CZTSe and CZTSSe devices which were also attributed to [$2Cu_{Zn}$ + Sn_{Zn}] clusters [162].

From further analysis of α and IQE data (see Figure 6.4.3(c)), L_d values of 532 nm and 681 nm were extracted for CdS-buffered and In_2S_3-buffered CZTSSe solar cells, respectively. Due to the narrow SCR in the In_2S_3-based device, the effective carrier collection length is significantly larger

in the CdS-based device (L_{eff} (CdS) = 805 nm and L_{eff} (In_2S_3) = 716 nm). Reduced carrier collection from longer wavelength photons in the In_2S_3-buffered solar cell is also evident in the EQE plots for both devices, see Figure 6.4.4(a).

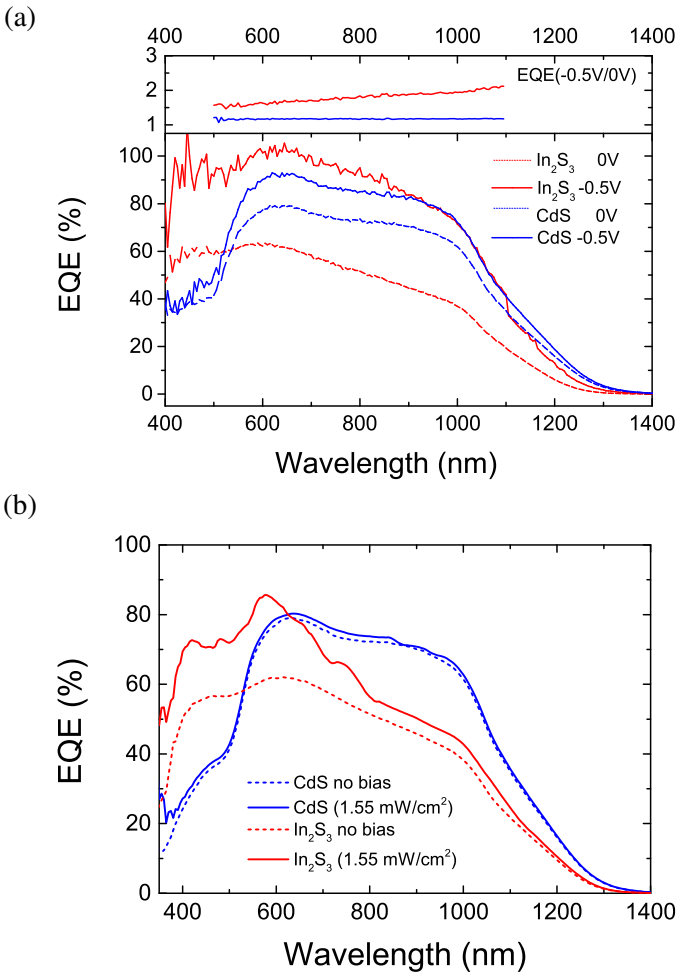

Figure 6.4.4: (a) Reverse-bias EQE plots with EQE ratio -0.5/0 V and (b) light-biased EQE plots with CZTSSe solar cells under 1.55 mW/cm^2 illumination.

The unbiased EQE curves demonstrate the In_2S_3-buffered device is generally less efficient at carrier extraction than the CdS counterpart except in the sub 500 nm wavelength region where extraction is enhanced due to the higher bandgap and transparency of the In_2S_3 layer. The overall lower efficiency would suggest there is a greater barrier for electron transport in this device. The -0.5 V reverse biased EQE curves are also shown in Figure 6.4.4(a). By applying a reverse bias, photogenerated electrons can overcome the barrier leading to an enhancement in the EQE signal. The application of a reverse bias to the In_2S_3-buffered device results in a significant increase in EQE response. The ratio between unbiased and biased curves for the In_2S_3-based solar cell shows

a gradual increase over the wavelength range 500 – 1100 nm indicating improved extraction of carriers at longer wavelengths. Reverse-biasing a solar cell increases the SCR in the absorber and facilitates the carrier collection deeper into the absorber bulk. These observations are concurrent with lower effective carrier diffusion length in the In_2S_3-buffered device. Complimentary EQE measurements with and without white light bias (1.55 mW/cm^2) were performed, as shown in Figure 6.4.4(b). Considering the CZTSSe device with CdS buffer, the EQE response under light bias is slightly lower than that with light bias over the entire spectrum. Comparable results were observed in CZTS devices with CdS buffer layers [198, 199]. The reduction in EQE was attributed to increased recombination in the SCR. Conversely, the In_2S_3-buffered device exhibits a substantial increase in EQE over the wavelength region below 800 nm upon light bias application. It would appear that the In_2S_3/CZTSSe interface is photoactive and the increase in photoconductivity of the In_2S_3 layer increases the depletion region width leading to the observed higher collection efficiencies.

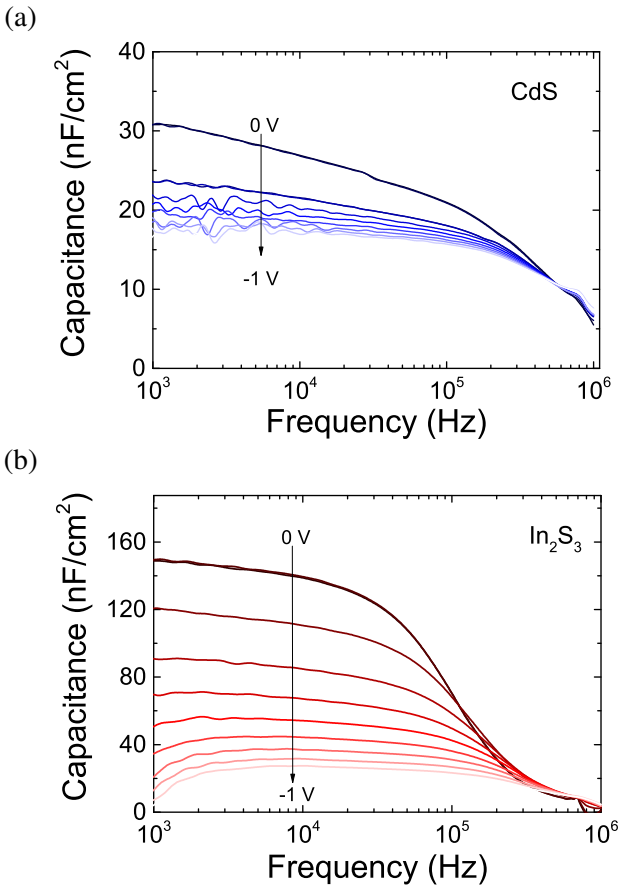

Figure 6.4.5: *C-f* sweeps in reverse bias range 0 to -1 V of CZTSSe devices with (a) CdS and (b) In_2S_3 buffers.

To gain a better understanding of the buffer/absorber interface capacitance-frequency (*C-f*) sweeps at different bias voltages were performed to evaluate interface and/or bulk defect characteristic frequencies f_{def}. *C-f* plots show a sharp decrease of capacitance at higher frequencies (see Figure 6.4.5) and the inflection point in the capacitance curve corresponds to the defect characteristic frequency. The bias voltage dependence of f_{def} is illustrated in Figure 6.4.6.

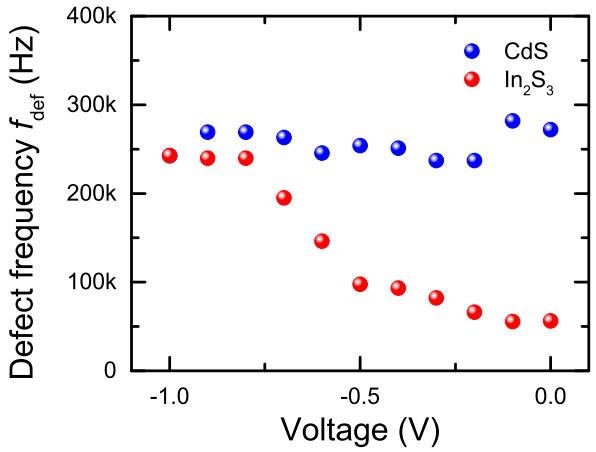

Figure 6.4.6: Voltage bias dependence of defect characteristic frequency f_{def}.

Varying the bias voltage changes the band bending near the buffer/absorber interface and adjusts the crossing point of the interface defect level E_t and Fermi level E_F, see Figure 6.4.7 . A shift of f_{def} with bias voltage indicates a predominance of interface defect states [200]. The characteristic defect frequency for the CdS-buffered device is roughly constant over the bias measurement range whereas the defect frequency for the In_2S_3 counterpart rises from ∼60 kHz up to ∼250 kHz. The presence of high concentrations of interface defects in the In_2S_3-based CZTSSe solar cell could account for the lower V_{oc} observed in the device.

With regard to In_2S_3/CZTSSe interface and device performance, SCAPS device simulations were performed to study the effect of varying interface defect concentrations, N_{int}. In these simulations, experimentally determined absorption data for CZTSSe, CdS and In_2S_3 thin films were used. The effects of donor-like CZTSSe/In_2S_3 interface defects were tested on a Mo/CZTSSe/In_2S_3(CdS)/*i*-ZnO stack. A summary of all material parameters is listed in Table 6.4.2. The simulation results in Figure 6.4.8(a) show that a reduction in interface defect concentrations from 3.0 x10^{14} cm^{-3} to 0.1 x10^{14} cm^{-3} results in an overall increase in carrier collection over the whole wavelength spectrum with an enhanced extraction in the blue photon range (<

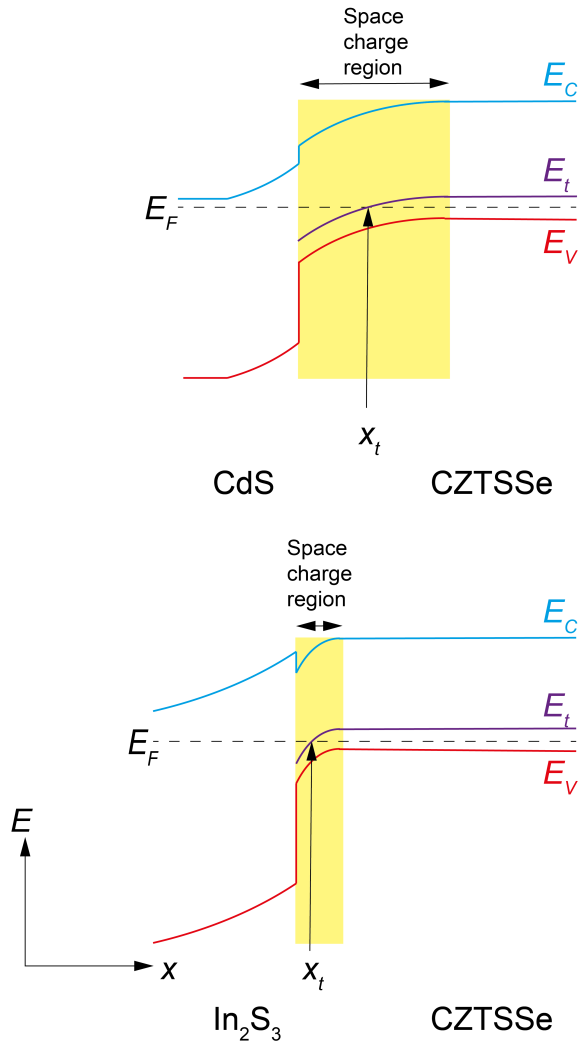

Figure 6.4.7: Band bending at interface of CdS and In_2S_3 buffers with CZTSSe absorber. Stronger band bending at the In_2S_3/CZTSSe interface due to the narrower space charge region width causes a larger shift in the position of point x_t (where Fermi level E_F crosses the defect level E_t) with increasing bias voltage, resulting in a change in f_{def}.

500 nm). Higher EQE in the 550 - 1050 nm range can be understood by increased photogeneration from an extended depletion region due to a reduction in interface defects. The simulated EQE curve at 3.0 x10^{14} cm^{-3} is in good agreement with experimental data (Figures 6.4.4(a) and 6.4.4(b)). The simulation results suggest a reduction in interface states in the In_2S_3-buffered device would lead to J_{sc} improvement and consequent efficiency enhancement. Simulated *J-V* measurements were performed with increasing concentrations of interface defects and extracted V_{oc} and efficiency, η parameters are plotted as a function of N_{int} in Figure 6.4.8(b). It is apparent that a reduction in N_{int} leads to a significant increase in V_{oc} together with a marked improvement in device efficiency.

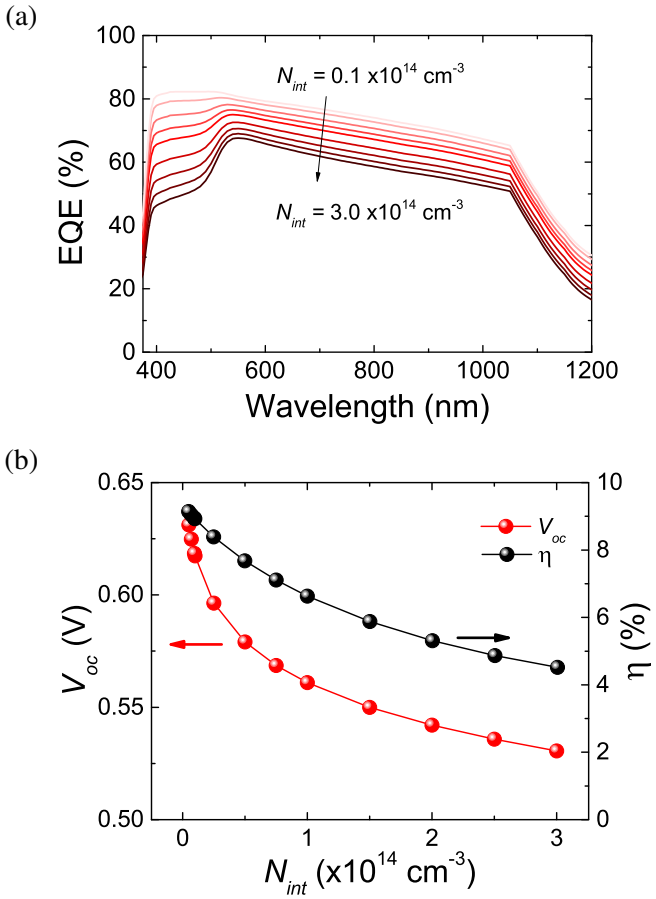

Figure 6.4.8: SCAPS device modeling showing (a) EQE of In_2S_3-buffered CZTSSe solar cell with varying concentration of interface defects and (b) V_{oc} and η versus N_{int} plots.

Table 6.4.2: Device simulation parameters, d: layer thickness, E_g: bandgap, χ: electron affinity, $\varepsilon/\varepsilon_0$: dielectric constant, m_e^*/m_0: effective mass, μ: carrier mobility, $N_{A/D}$: apparent doping density D:donor A:Acceptor, N_t:bulk defect density, E_t: defect energy level relative to VB, σ: capture cross section and N_{int}: interface defect concentration. Subscripts *e* and *h* are electron and hole, respectively.

Layer properties	CZTSSe	CdS	In_2S_3	*i*-ZnO
d (μm)	1.200	0.070	0.060	0.035
E_g (eV)	1.14[a]	2.42[a]	2.72[a]	3.37[b]
χ (eV)	4.6[c]	4.5[c]	4.7[d]	4.7[c]
$\varepsilon/\varepsilon_0$	8.5[e]	9.0[b]	13.5[d]	9.0[b]
m_e^*/m_0	0.1[e]	0.25[b]	0.25[d]	0.275[b]
m_h^*/m_0	0.32[e]	0.7[b]	0.7[d]	0.59[b]
μ_e (cm^2/Vs)	80[b]	160[b]	400[d]	200[b]
μ_h (cm^2/Vs)	25[b]	15[b]	210[d]	93[b]
$N_{A/D}$ (cm^{-3})	A: 5 x10^{16}[f]	D: 1 x10^{17}[b]	D: 1 x10^{18}	D: 1 x10^{18}[b]
Bulk defects (single level)				
N_t (cm^{-3})	A: 10^{14}[g]	D: 10^{17}[b]	D: 10^{18}	D: 10^{17}[b]
E_t (cm^{-3})	0.09[g]	0.10[b]	0.10	0.10[b]
N_t (cm^{-3})	A: 10^{14}[g]			
E_t (cm^{-3})	0.18[g]			
N_t (cm^{-3})	D: 10^{15}[b]			
E_t (cm^{-3})	0.63[b]			
σ_e (cm^2)	10^{-14}[b]	10^{-17}[b]	10^{-17}	10^{-12}[b]
σ_h (cm^2)	10^{-14}[b]	10^{-11}[b]	10^{-11}	10^{-15}[b]
Interface defects between CZTSSe and CdS/In_2S_3 (uniform distribution throughout interface)				
N_{int} (cm^{-3})		D: varied	D: varied	
σ_e (cm^2)		10^{-13}	10^{-13}	
σ_h (cm^2)		10^{-15}	10^{-15}	

[a] Experimentally determined from UV-VIS measurements

[b] Reference [201]

[c] Reference [202]

[d] Reference [203]

[e] Reference [16]

[f] Experimentally determined from *C-V* measurements

[g] Experimentally determined from PL measurements and DLTS in reference [17]

6.5 Summary

In summary, the interface properties between CdS and In_2S_3 buffer layers and kesterite CZTSSe absorber films fabricated from nanoparticle inks have been comprehensively investigated. XPS and IPES analysis revealed a preferential 'spike' conduction band offset of +0.39 eV at the In_2S_3/CZTSSe interface as opposed to a 'cliff' offset of -0.68 eV for the CdS/CZTSSe junction. PL studies of CdS- and In_2S_3-buffered CZTSSe thin films suggest the deposition of CdS induces chemical and electronic changes in the surface region of the CZTSSe film, probably caused by Cd diffusion into the absorber. As a consequence, the level of charge compensation is increased and free carrier concentration reduced from 1.2 x10^{17} cm^{-3} in the In_2S_3/CZTSSe device to 1.1 x10^{16} cm^{-3} in CdS/CZTSSe. Mott-Schottky analysis shows In_2S_3 based solar cells have increased doping density, however the optimised conduction band alignment and elevated carrier concentration does not translate to improved performance in this type of device (V_{oc} of 220(255) mV and η of 2.3(3.2) % for the In_2S_3(CdS)-buffered device). Mott-Schottky analysis also indicated a prevalence of interface defects in the In_2S_3-buffered solar cells, accounting for the reduced V_{oc} observed in these devices. SCAPS device modeling of both types of CZTSSe solar cells showed a reduction in the concentration of interface defects led to an improvement in the efficiency of the In_2S_3 based devices due not only to increased V_{oc} but also enhanced J_{sc} compared to that with a CdS buffer. The results demonstrate the potential of In_2S_3 as a buffer material for CZTSSe absorbers providing that interface defects are mitigated using suitable absorber surface passivation or barrier layer deposition.

Chapter 7

Conclusions and Outlook

7.1 Thesis summary

In this thesis, CZTSSe absorbers were prepared from CZTS nanoparticle inks synthesised by a hot injection method. Following selenisation of the CZTS nanoparticle thin films, CZTSSe solar cells were completed by deposition of buffer and window layers followed by metal contact grids. This fabrication method provides a low cost, industrially scalable approach to solar cell manufacture from Earth-abundant materials. However, this kesterite-based technology has failed to achieve device efficiencies comparable to chalcopyrite CIGSSe from which it was adapted. The deficit in open circuit voltage between these types of PV is often cited as the main reason for the suboptimal performance of kesterite-based devices.

The objectives of this investigation were to consider the material interfaces between the buffer/absorber, Mo/absorber back contact and also the bulk of the CZTSSe to identify areas which were adversely affecting device performance. In order to explore the performance-related issues in nanoparticle ink-based CZTSSe solar cells, a systematic bottom-up analysis of the materials and interfaces in the CZTSSe cell structure was adopted. The key objectives of the investigation were achieved and the results are summarised herein. Initially, possible loss mechanisms related to increased non-radiative charge carrier recombination are discussed in Chapter 2. A number of material and device characterisation techniques, such as PL spectroscopy and *J-V(T)* analysis, were employed to identify and quantify areas affecting device performance.

The first region in the CZTSSe device structure to be explored was the CZTSSe absorber-Mo back contact interface, detailed in Chapter 4. Typically, CZTSSe absorbers fabricated from

nanoparticle inks exhibit a bi-layer structure consisting of large grains on top of a layer of fine grains. GDOES measurements revealed the fine grain layer to be rich in carbon and selenium. This fine grain layer is a direct result of the use of a long carbon chain ligand, oleylamine, for the nanoparticle inks synthesis step. Whether the presence of the fine grain layer has a current-blocking effect due to the formation of a potential barrier at the back contact is still under debate. To investigate this issue, an alternate ligand with low carbon content (formamide) was used during CZTS nanoparticle ink fabrication. It was found that using formamide in CZTSSe absorber preparation completely eliminated the fine grain layer. PL analysis revealed the formamide-based CZTSSe absorber had a higher proportion of non-radiative defects compared to the standard oleylamine-based film. Despite the removal of the carbon-rich fine grain layer in the formamide-based absorber, it was not possible to produce a functioning device due to the porosity of the CZTSSe film. A working device was achieved by depositing an oleylamine-CZTSSe layer on top of a formamide CZTSSe layer. In this device a thin fine grain layer was sandwiched between large grain layers of formamide- and oleylamine-CZTSSe with no fine grains at the back contact interface. There was a 56% reduction in the back contact barrier height Φ_{BH} of the dual ligand based device compared to the standard oleylamine-CZTSSe (Φ_{BH}(OLA) $\sim$36 meV, Φ_{BH}(OLA+FA) $\sim$16 meV). As a consequnce the performance of the dual ligand CZTSSe device improved due lower series resistance, reverse saturation current, diode ideality factor and higher fill factor which can be attributed to a reduced barrier at the absorber/Mo interface.

The CZTSSe absorber bulk was the next component of the solar cell structure to be investigated. In Chapter 5, the use of lower purity precursor chemicals in the fabrication of nanoparticle-based CZTSSe absorbers and solar cells was considered. The aim was to improve the cost-effectiveness of the ink-based manufacturing process. ICPMS impurity analysis of dried and powdered CZTS nanoparticle inks made from lower/higher grade precursors revealed the lower grade CZTS inks contained additional elemental contaminants such as Pb and Hg. Defect analysis of the low and high purity CZTSSe absorber thin films was performed using PL spectroscopy. The same shallow donor and acceptor levels were identified in both types of absorber. Where the absorbers differed was the depth of the band edge fluctuations, which reduced from 59 meV in the lower purity film to 49 meV in the higher purity sample. This correlates to a reduction of around 40% in the total defect concentration in the higher purity absorber. TRPL measurements also revealed the minority carrier lifetime was greater in the higher purity film (0.44 ns compared to 0.20

ns). DLTS studies on complete CZTSSe solar cells detected the presence of a deeper acceptor defect (probably Sn-related) in the lower purity device. Sn loss was observed during the selenisation of the lower purity CZTS film precursor which could account for the presence of Sn-related defects in this absorber. Despite the apparent improvement in film quality of the higher purity CZTSSe absorber, solar cells fabricated from the different grade precursor chemicals showed similar performance. This indicates there is an underlying issue other than defects in the absorber bulk inhibiting device performance.

Finally, the interface between the *n*-type buffer and *p*-type CZTSSe absorber was examined. The band alignment at the *pn*-heterojunction in a CZTSSe solar cell can have a profound impact on device performance. In Chapter 6, In_2S_3 was used an alternative to the standard CdS buffer material in the CZTSSe device architecture and its' effects on optoelectronic device properties were studied. XPS/IPES analysis revealed In_2S_3 formed a 'spike'-like conduction band offset (+0.39 eV) at the interface with the CZTSSe absorber whereas CdS formed a 'cliff'-like offset. A small 'spike' offset at the buffer-absorber interface is favourable as it increases quasi Fermi-level splitting in the absorber which consequently increases device V_{oc}. The large 'cliff' offset (-0.68 eV) at the CdS-CZTSSe interface may increase interface recombination due to increased hole concentration at the interface.

PL measurements of In_2S_3- and CdS-buffered CZTSSe absorbers suggested there is a higher degree of charge compensation in the CZTSSe film with a CdS buffer. It is speculated Cd diffuses into the surface region of the CZTSSe absorber during CdS deposition, creating additional donor defects thereby increasing charge compensation and reducing free carrier concentration. Mott-Schottky analysis of CZTSSe solar cells showed the CdS-buffered device had a reduced apparent doping density compared to that of In_2S_3, which can be explained by the increased charge compensation in this film. However, analysis also indicated the In_2S_3-based device had higher concentrations of interface defects which was reflected in low V_{oc}. SCAPS modelling of the In_2S_3-buffered device showed that a reduction in the concentration of interface defects not only improved V_{oc} but increased J_{sc} leading to much-improved device efficiency. The results show the potential of In_2S_3 as a substitute for CdS in CZTSSe devices fabrcated from nanoparticle inks, providing interface defects are mitigated using suitable surface passivation or barrier layer application.

7.2 Outlook

A systematic investigation of nanoparticle-based CZTSSe absorbers and interfaces within the solar cell structure was performed to identify areas where the performance of CZTSSe solar cells could be advanced. The following are observations and salient points to achieve efficiency enhancements in CZTSSe devices based on the work done and results achieved in this thesis.

1. The presence of the carbon-rich CZTSSe fine grain layer often found at the Mo back contact in nanoparticle ink-based CZTSSe solar cells does not appear to be detrimental to device performance. In fact, the back contact barrier height in solar cellls fabricated using this method tends to be significantly lower than that seen in devices fabricated by other methods, such as electrodeposition and DC magnetron sputtering. The low barrier height in nanoparticle-based CZTSSe devices could be reduced even further if the fine grain layer is removed resulting in a quasi-ohmic CZTSSe/Mo contact.

2. Sn-related acceptor defects were detected in CZTSSe absorber films studied in this thesis. These defects tend to be deep in nature and act as efficient carrier recombination centres. Sn loss during the selenisation of stacked CZTS nanoparticle films was observed which would increase concentrations of V_{Sn}, Cu_{Sn} or Zn_{Sn} defects. Control of Sn composition during the selenisation step, for example by the addition of Sn in the furnace, would reduce concentrations of these detrimental defects.

3. In_2S_3 is a promising candidate to replace CdS as the *n*-type buffer in CZTSSe solar cells. The band alignment at the In_2S_3 buffer-CZTSSe absorber interface has a positive 'spike' conduction band offset which is favourable for efficient charge carrier extraction. Higher V_{oc} in CZTSSe devices could be achieved by optimisation of the In_2S_3 buffer layer. Preliminary work on incorporating a hybrid CdS-In_2S_3 layer into the device structure has shown encouraging results, see Figure 7.2.1 and Table 7.2.1.

Despite the issues regarding nanoparticle-based CZTSSe solar cells reported in this thesis, there is increasing enthusiasm around research into kesterite-based devices due to the considerable potential for improvements in device efficiency. With deeper understanding of the underlying causes of reduced performance in CZTSSe compared to CIGS PV, technological solutions can be developed. In doing so, the practical application of CZTSSe-based solar cells to fulfil the world's

growing energy demands will surely be brought closer to fruition.

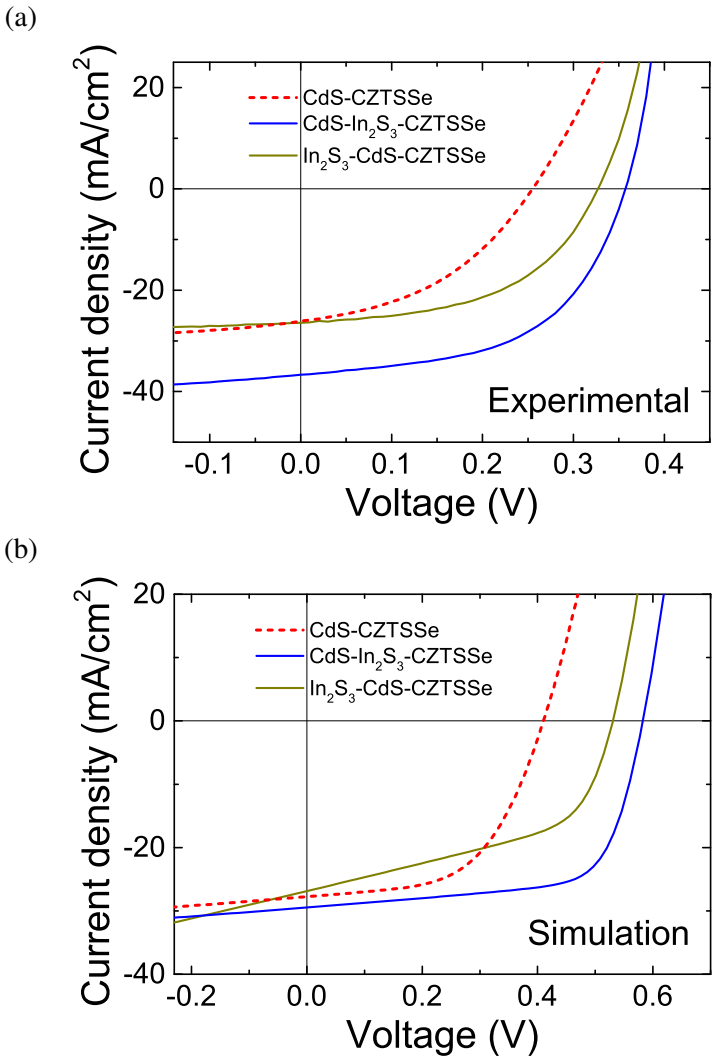

Figure 7.2.1: Preliminary results of (a) experimental and (b) simulated *J-V* analysis of CZTSSe solar cells with hybrid CdS/In_2S_3 layers.

Table 7.2.1: Experimental device parameters for CZTSSe cells with different buffers at room temperature with simulated values shown in brackets.

Buffer/absorber	V_{oc} (V)	J_{sc} (mA/cm^2)	FF (%)	η (%)
CdS/CZTSSe	0.26 (0.41)	26.1 (27.8)	42.6 (55.4)	2.78 (6.31)
CdS-In_2S_3/CZTSSe	0.35 (0.58)	36.7 (29.5)	54.96 (67.8)	7.06 (11.6)
In_2S_3-CdS/CZTSSe	0.32 (0.53)	26.5 (26.9)	52.2 (50.1)	4.42 (7.14)

Acronyms

BB	Band-to-Band 33, 34, 62
BGF	Bandgap fluctuations 41
BI	Band-to-Impurity 32, 34, 64, 65, 67, 74, 115
BIPV	Building-integrated photovoltaics 1
BT	Band-to-Tail 32, 34, 84
CB	Conduction band 17–19, 31, 32, 36, 43, 44, 76, 78, 84, 96, 97, 103, 104, 107, 112, 113, 115
CBM	Conduction band minimum 31, 78, 81, 82, 94, 99, 100
CBO	Conduction band offset 18, 19, 96, 99–102
DLTS	Deep level transient spectroscopy 53–55, 75, 76, 86, 94, 115, 131
DOS	Density of states 30
EDS	Energy-dispersive X-ray spectroscopy 45, 58, 90
EPF	Electrostatic potential fluctuations 41
EQE	External quantum efficiency 49–51, 78, 88–90, 122, 123, 125
FA	Formamide 23, 24, 57, 58, 60, 62–70, 72–74
FG	Fine grain 57, 60, 67

FWHM Full width at half maximum 78, 112

GBs Grain boundaries 17

GDOES Glow discharge optical emission spectroscopy 47, 48, 130

GIXRD Grazing incidence X-ray diffraction 41

ICPMS Inductively-coupled plasma mass spectroscopy 48, 76, 130

IPES Inverse photoemission spectroscopy 43, 44, 96, 99, 101, 102, 128, 131

IQE Internal quantum efficiency 40, 50, 51, 109, 113, 119, 121

ITO Indium tin oxide 6, 25

LG Large grain 57, 60, 67

OLA Oleylamine 23, 24, 57–60, 62–64, 66–70, 72–74

PL Photoluminescence 19, 20, 26, 27, 33–36, 60–63, 74–76, 78, 79, 81–86, 103, 104, 107–115, 121, 128–131

QDAP Quasi donor acceptor pair 31, 32, 34, 60–65, 67, 74, 79, 81, 82, 92–94, 107–109, 111, 115

SCAPS Solar cell capacitance simulations 97, 102, 124, 128, 131

SCR Space charge region 52, 53, 73, 95, 121, 123

SEM Scanning electron microscopy 44, 45, 97, 116

SLG Sodalime glass 5, 6, 45, 49

SRH Shockley-Read-Hall 15, 71, 72, 76

TCO Transparent conducting oxide 26

TFPV Thin film photovoltaic 1, 2, 11, 12, 20

TI Tail-to-Impurity 32, 34, 107, 113, 115

TRPL Time-resolved photoluminescence 35, 36, 84, 130

UHV Ultra-high vacuum 44

VB Valence band 17, 32, 36, 43, 76, 78, 84, 97, 103, 104, 113

VBM Valence band maximum 16, 31, 44, 78, 81, 82, 88, 91, 94, 99, 100

VBO Valence band offset 99

XPS X-ray photoelectron spectroscopy 42–44, 96, 99, 101, 102, 128, 131

XRD X-ray diffraction 41, 43, 58

Bibliography

[1] United Nations Framework Convention on Climate Change. Draft Paris Agreement. https://documents-dds-ny.un.org/doc/UNDOC/LTD/G15/278/26/PDF/G1527826.pdf?OpenElement, 2015. (Online; accessed 03-September-2019).

[2] Kunta Yoshikawa, Hayato Kawasaki, Wataru Yoshida, Toru Irie, Katsunori Konishi, Kunihiro Nakano, Toshihiko Uto, Daisuke Adachi, Masanori Kanematsu, and Hisashi et al. Uzu. Silicon heterojunction solar cell with interdigitated back contacts for a photoconversion efficiency over 26%. *Nature Energy*, 2(5), 2017.

[3] Jan Benick, Armin Richter, Ralph Muller, Hubert Hauser, Frank Feldmann, Patricia Krenckel, Stephan Riepe, Florian Schindler, Martin C. Schubert, and Martin et al. Hermle. High-Efficiency *n*-Type HP mc Silicon Solar Cells. *IEEE Journal of Photovoltaics*, 7(5):1171–1175, 2017.

[4] Martin A. Green, Yoshihiro Hishikawa, Ewan D. Dunlop, Dean H. Levi, Jochen Hohl-Ebinger, Masahiro Yoshita, and Anita W.Y. Ho-Baillie. Solar cell efficiency tables (version 53). *Progress in Photovoltaics: Research and Applications*, 27(1):3–12, 2018.

[5] William Shockley and Hans J. Queisser. Detailed Balance Limit of Efficiency of *p-n* Junction Solar Cells. *Journal of Applied Physics*, 32(3):510–519, 1961.

[6] Communication from the Commission to the European Parliament, the Council, the European Economic and Social Committee and the Committee of the regions on the 2017 list of Critical Raw Materials for the EU 2017. https://eur-lex.europa.eu/legal-content/EN/TXT/?uri=CELEX%3A52017DC0490, 2017. (Online; accessed 03-September-2019).

[7] L. L. Kazmerski, F. R. White, M. S. Ayyagari, Y. J. Juang, and R. P. Patterson. Growth

and characterization of thin-film compound semiconductor photovoltaic heterojunctions. *Journal of Vacuum Science and Technology*, 14(1):65–68, 1977.

[8] Takuya Kato, Jyh-Lih Wu, Yoshiaki Hirai, Hiroki Sugimoto, and Veronica Bermudez. Record Efficiency for Thin-Film Polycrystalline Solar Cells up to 22.9% achieved by Cs-Treated Cu(In,Ga)(Se,S)$_2$. *IEEE Journal of Photovoltaics*, 9(1):325–330, 2019.

[9] S.R. Hall, J.T. Szymanski, and J.M. Stewart. Kesterite, $Cu_2(Zn,Fe)SnS_4$, and stannite, $Cu_2(Fe,Zn)SnS_4$, structurally similar but distinct minerals. *The Canadian Mineralogist*, 16(2):131–137, 1978.

[10] Sergio Giraldo, Zacharie Jehl, Marcel Placidi, Victor Izquierdo-Roca, Alejandro Pérez-Rodríguez, and Edgardo Saucedo. Progress and Perspectives of Thin Film Kesterite Photovoltaic Technology: A Critical Review. *Advanced Materials*, 31(16):1806692, 2019.

[11] A. V. Mudryi, V. F. Gremenok, A. V. Karotki, V. B. Zalesski, M. V. Yakushev, F. Luckert, and R. Martin. Structural and optical properties of thin films of Cu(In,Ga)Se_2 semiconductor compounds. *Journal of Applied Spectroscopy*, 77(3):371–377, 2010.

[12] Byungha Shin, Yu Zhu, Nestor A. Bojarczuk, S. Jay Chey, and Supratik Guha. Control of an interfacial $MoSe_2$ layer in $Cu_2ZnSnSe_4$ thin film solar cells: 8.9% power conversion efficiency with a TiN diffusion barrier. *Applied Physics Letters*, 101(5):053903, 2012.

[13] Subba Ramaiah Kodigala. *Cu(In,Ga)Se_2 Based Thin Film Solar Cells*. Academic Press [Imprint], 1 edition, 2010.

[14] Lorelle M. Mansfield, Rebekah L. Garris, Kahl D. Counts, James R. Sites, Christopher P. Thompson, William N. Shafarman, and Kannan Ramanathan. Comparison of CIGS Solar Cells Made with Different Structures and Fabrication Techniques. *IEEE Journal of Photovoltaics*, 7(1):286–293, 2017.

[15] J. P. Liu, K. L. Choy, M. Placidi, J. López-García, E. Saucedo, D. Colombara, and E. Robert. Fabrication and characterization of kesterite Cu_2ZnSnS_4 thin films deposited by electrostatic spray assisted vapour deposition method. *physica status solidi (a)*, 212(1):135–139, 2014.

[16] Clas Persson. Electronic and optical properties of Cu_2ZnSnS_4 and $Cu_2ZnSnSe_4$. *Journal of Applied Physics*, 107(5):053710, 2010.

[17] S Campbell, Y Qu, J D Major, D Lagarde, C Labbé, P Maiello, V Barrioz, N S Beattie, and G Zoppi. Direct evidence of causality between chemical purity and band-edge potential fluctuations in nanoparticle ink-based $Cu_2ZnSn(S,Se)_4$ solar cells. *Journal of Physics D: Applied Physics*, 52(13):135102, 2019.

[18] Ingrid L. Repins, Manuel J. Romero, Jian V. Li, Su-Huai Wei, Darius Kuciauskas, Chun-Sheng Jiang, Carolyn Beall, Clay DeHart, Jonathan Mann, and Wan-Ching et al. Hsu. Kesterite Successes, Ongoing Work, and Challenges: A Perspective From Vacuum Deposition. *IEEE Journal of Photovoltaics*, 3(1):439–445, 2013.

[19] Oki Gunawan, Tayfun Gokmen, and David B. Mitzi. Suns-V_{oc} characteristics of high performance kesterite solar cells. *Journal of Applied Physics*, 116(8):084504, 2014.

[20] Weimin Li, Xia Yan, Armin G. Aberle, and Selvaraj Venkataraj. Effect of sodium diffusion on the properties of CIGS solar absorbers prepared using elemental Se in a two-step process. *Scientific Reports*, 9(1), 2019.

[21] N. Nicoara, Th. Lepetit, L. Arzel, S. Harel, N. Barreau, and S. Sadewasser. Effect of the KF post-deposition treatment on grain boundary properties in $Cu(InGa)Se_2$ thin films. *Scientific Reports*, 7(1), 2017.

[22] Enrico Avancini, Romain Carron, Thomas P. Weiss, Christian Andres, Melanie Bürki, Claudia Schreiner, Renato Figi, Yaroslav E. Romanyuk, Stephan Buecheler, and Ayodhya N. Tiwari. Effects of Rubidium Fluoride and Potassium Fluoride Postdeposition Treatments on $Cu(In,Ga)Se_2$ Thin Films and Solar Cell Performance. *Chemistry of Materials*, 29(22):9695–9704, 2017.

[23] Tzu-Ying Lin, Ishwor Khatri, Junpei Matsuura, Kosuke Shudo, Wei-Chih Huang, Mutsumi Sugiyama, Chih-Huang Lai, and Tokio Nakada. Alkali-induced grain boundary reconstruction on $Cu(In,Ga)Se_2$ thin film solar cells using cesium fluoride post deposition treatment. *Nano Energy*, page 104299, 2019.

[24] W.E. Devaney, W.S. Chen, J.M. Stewart, and R.A. Mickelsen. Structure and properties of high efficiency ZnO/CdZnS/CuInGaSe$_2$/Mo solar cells. *IEEE Transactions on Electron Devices*, 37(2):428–433, 1990.

[25] Carolin M. Sutter-Fella, Josua A. Stückelberger, Harald Hagendorfer, Fabio La Mattina, Lukas Kranz, Shiro Nishiwaki, Alexander R. Uhl, Yaroslav E. Romanyuk, and Ayodhya N. Tiwari. Sodium Assisted Sintering of Chalcogenides and Its Application to Solution Processed $Cu_2ZnSn(S,Se)_4$ Thin Film Solar Cells. *Chemistry of Materials*, 26(3):1420–1425, 2014.

[26] Tobias Abzieher, Thomas Schnabel, Michael Hetterich, Michael Powalla, and Erik Ahlswede. Source and effects of sodium in solution-processed kesterite solar cells. *Physica Status Solidi (a)*, 213(4):1039–1049, 2015.

[27] C. Andres, T. Schwarz, S.G. Haass, T.P. Weiss, R. Carron, R. Caballero, R. Figi, C. Schreiner, M. Bürki, and A.N. et al. Tiwari. Decoupling of optoelectronic properties from morphological changes in sodium treated kesterite thin film solar cells. *Solar Energy*, 175:94–100, 2018.

[28] Stefan G. Haass, Christian Andres, Renato Figi, Claudia Schreiner, Melanie Bürki, Yaroslav E. Romanyuk, and Ayodhya N. Tiwari. Complex interplay between Absorber Composition and Alkali Doping in High-Efficiency Kesterite Solar Cells. *Advanced Energy Materials*, 8(4):1701760, 2017.

[29] Yanchun Yang, Xiaojiao Kang, Lijian Huang, and Daocheng Pan. Tuning the Band Gap of $Cu_2ZnSn(S,Se)_4$ Thin Films via Lithium Alloying. *ACS Applied Materials & Interfaces*, 8(8):5308–5313, 2016.

[30] Antonio Cabas-Vidani, Stefan G. Haass, Christian Andres, Raquel Caballero, Renato Figi, Claudia Schreiner, José A. Márquez, Charles Hages, Thomas Unold, and Davide et al. Bleiner. High-Efficiency $(Li_xCu_{1-x})_2ZnSn(S,Se)_4$ Kesterite Solar Cells with Lithium Alloying. *Advanced Energy Materials*, 8(34):1801191, 2018.

[31] S. G. Haass, C. Andres, R. Figi, C. Schreiner, M. Bürki, A. N. Tiwari, and Y. E. Romanyuk.

Effects of potassium on kesterite solar cells: Similarities, differences and synergies with sodium. *AIP Advances*, 8(1):015133, 2018.

[32] Yaroslav E Romanyuk, Stefan G Haass, Sergio Giraldo, Marcel Placidi, Devendra Tiwari, David J Fermin, Xiaojing Hao, Hao Xin, Thomas Schnabel, and Marit Kauk-Kuusik. Doping and alloying of kesterites. *Journal of Physics: Energy*, 1(4):044004, 2019.

[33] Qiang Shu, Ji-Hui Yang, Shiyou Chen, Bing Huang, Hongjun Xiang, Xin-Gao Gong, and Su-Huai Wei. $Cu_2Zn(Sn,Ge)Se_4$ and $Cu_2Zn(Sn,Si)Se_4$ alloys as photovoltaic materials: Structural and electronic properties. *Physical Review B*, 87(11), 2013.

[34] M. Grossberg, K. Timmo, T. Raadik, E. Kärber, V. Mikli, and J. Krustok. Study of structural and optoelectronic properties of $Cu_2Zn(Sn_{1-x}Ge_x)Se_4$ (x = 0 to 1) alloy compounds. *Thin Solid Films*, 582:176–179, 2015.

[35] Sergio Giraldo, Markus Neuschitzer, Thomas Thersleff, Simón López-Marino, Yudania Sánchez, Haibing Xie, Monica Colina, Marcel Placidi, Paul Pistor, and Victor Izquierdo-Roca. Large Efficiency Improvement in $Cu_2ZnSnSe_4$ Solar Cells by Introducing a Superficial Ge Nanolayer. *Advanced Energy Materials*, 5(21):1501070, 2015.

[36] Shinho Kim, Kang Min Kim, Hitoshi Tampo, Hajime Shibata, and Shigeru Niki. Improvement of voltage deficit of Ge-incorporated kesterite solar cell with 12.3% conversion efficiency. *Applied Physics Express*, 9(10):102301, 2016.

[37] Shiyou Chen, Aron Walsh, Xin-Gao Gong, and Su-Huai Wei. Classification of Lattice Defects in the Kesterite Cu_2ZnSnS_4 and $Cu_2ZnSnSe_4$ Earth-Abundant Solar Cell Absorbers. *Advanced Materials*, 25(11):1522–1539, 2013.

[38] Gopalakrishnan Sai Gautam, Thomas P. Senftle, and Emily A. Carter. Understanding the Effects of Cd and Ag Doping in Cu_2ZnSnS_4 Solar Cells. *Chemistry of Materials*, 30(14):4543–4555, 2018.

[39] Rujun Sun, Daming Zhuang, Ming Zhao, Qianming Gong, Mike Scarpulla, Yaowei Wei, Guoan Ren, and Yixuan Wu. Beyond 11% efficient $Cu_2ZnSn(Se,S)_4$ thin film solar cells by cadmium alloying. *Solar Energy Materials and Solar Cells*, 174:494–498, 2018.

[40] Stephane Bourdais, Christophe Choné, Bruno Delatouche, Alain Jacob, Gerardo Larramona, Camille Moisan, Alain Lafond, Fabrice Donatini, Germain Rey, and Susanne Siebentritt. Is the Cu/Zn Disorder the Main Culprit for the Voltage Deficit in Kesterite Solar Cells? *Advanced Energy Materials*, 6(12):1502276, 2016.

[41] Congcong Wang, Shiyou Chen, Ji-Hui Yang, Li Lang, Hong-Jun Xiang, Xin-Gao Gong, Aron Walsh, and Su-Huai Wei. Design of I2-II-IV-VI4 Semiconductors through Element Substitution: The Thermodynamic Stability Limit and Chemical Trend. *Chemistry of Materials*, 26(11):3411–3417, 2014.

[42] Talia Gershon, Yun Seog Lee, Priscilla Antunez, Ravin Mankad, Saurabh Singh, Doug Bishop, Oki Gunawan, Marinus Hopstaken, and Richard Haight. Photovoltaic Materials and Devices Based on the Alloyed Kesterite Absorber $(Ag_xCu_{1-x})_2ZnSnSe_4$. *Advanced Energy Materials*, 6(10):1502468, 2016.

[43] Wei Wang, Mark T. Winkler, Oki Gunawan, Tayfun Gokmen, Teodor K. Todorov, Yu Zhu, and David B. Mitzi. Device Characteristics of CZTSSe Thin-Film Solar Cells with 12.6% Efficiency. *Advanced Energy Materials*, 4(7):1301465, 2013.

[44] Yongtao Qu, Guillaume Zoppi, Robert W Miles, and Neil S Beattie. Influence of reaction conditions on the properties of solution-processed Cu_2ZnSnS_4 nanocrystals. *Materials Research Express*, 1(4):045040, 2014.

[45] Rui Kamada, Takeshi Yagioka, Shunsuke Adachi, Atsushi Handa, Kong Fai Tai, Takuya Kato, and Hiroki Sugimoto. New world record Cu(In,Ga)$(Se,S)_2$ thin film solar cell efficiency beyond 22%. *2016 IEEE 43rd Photovoltaic Specialists Conference (PVSC)*, 2016.

[46] Kee-Jeong Yang, Dae-Ho Son, Shi-Joon Sung, Jun-Hyoung Sim, Young-Ill Kim, Si-Nae Park, Dong-Hwan Jeon, JungSik Kim, Dae-Kue Hwang, and Chan-Wook et al. Jeon. A band-gap-graded CZTSse solar cell with 12.3% efficiency. *Journal of Materials Chemistry A*, 4(26):10151–10158, 2016.

[47] A. D. Collord and H. W. Hillhouse. Germanium Alloyed Kesterite Solar Cells with Low Voltage Deficits. *Chemistry of Materials*, 28(7):2067–2073, 2016.

[48] Charles J. Hages, Mark J. Koeper, Caleb K. Miskin, Kevin W. Brew, and Rakesh Agrawal. Controlled Grain Growth for High Performance Nanoparticle-Based Kesterite Solar Cells. *Chemistry of Materials*, 28(21):7703–7714, 2016.

[49] Hongling Guo, Yong Cui, Qingwen Tian, Shang Gao, Gang Wang, and Daocheng Pan. Significantly Enhancing Grain Growth in $Cu_2ZnSn(S,Se)_4$ Absorber Layers by Insetting Sb_2S_3, $CuSbS_2$, and $NaSb_5S_8$ Thin Films. *Crystal Growth & Design*, 15(2):771–777, 2015.

[50] Huanping Zhou, Wan-Ching Hsu, Hsin-Sheng Duan, Brion Bob, Wenbing Yang, Tze-Bin Song, Chia-Jung Hsu, and Yang Yang. CZTS nanocrystals: a promising approach for next generation thin film photovoltaics. *Energy & Environmental Science*, 6(10):2822, 2013.

[51] Cyrus Wadia, A. Paul Alivisatos, and Daniel M. Kammen. Materials Availability Expands the Opportunity for Large-Scale Photovoltaics Deployment. *Environmental Science & Technology*, 43(6):2072–2077, 2009.

[52] Oki Gunawan, Teodor K. Todorov, and David B. Mitzi. Loss mechanisms in hydrazine-processed $Cu_2ZnSn(Se,S)_4$ solar cells. *Applied Physics Letters*, 97(23):233506, 2010.

[53] Susanne Siebentritt. Why are kesterite solar cells not 20% efficient? *Thin Solid Films*, 535:1–4, 2013.

[54] Tayfun Gokmen, Oki Gunawan, Teodor K. Todorov, and David B. Mitzi. Band tailing and efficiency limitation in kesterite solar cells. *Applied Physics Letters*, 103(10):103506, 2013.

[55] O. Vigil-Galán, Maykel Courel, J. A. Andrade-Arvizu, Y. Sánchez, M. EspÍndola-Rodríguez, E. Saucedo, D. Seuret-Jiménez, and Matthew Titsworth. Route towards low cost-high efficiency second generation solar cells: current status and perspectives. *Journal of Materials Science: Materials in Electronics*, 26(8):5562–5573, 2014.

[56] Jonathan J. Scragg, Phillip J. Dale, Diego Colombara, and Laurence M. Peter. Thermodynamic Aspects of the Synthesis of Thin-Film Materials for Solar Cells. *ChemPhysChem*, 13(12):3035–3046, 2012.

[57] Takuya Kato, Homare Hiroi, Noriyuki Sakai, Satoshi Muraoka, and Hiroki Sugimoto. *Characterization of Front and Back Interfaces on Cu_2ZnSn_S4 Thin-Film Solar Cells*, pages 2236–2239. EU PVSEC Proceedings, 2012.

[58] Tang Jiao Huang, Xuesong Yin, Guojun Qi, and Hao Gong. CZTS-based materials and interfaces and their effects on the performance of thin film solar cells. *physica status solidi (RRL) - Rapid Research Letters*, 08(09):735–762, 2014.

[59] Jonathan J. Scragg, Tomas Kubart, J. Timo Wätjen, Tove Ericson, Margareta K. Linnarsson, and Charlotte Platzer-Björkman. Effects of Back Contact Instability on Cu_2ZnSnS_4 Devices and Processes. *Chemistry of Materials*, 25(15):3162–3171, 2013.

[60] B. Ohnesorge, R. Weigand, G. Bacher, A. Forchel, W. Riedl, and F. H. Karg. Minority-carrier lifetime and efficiency of Cu(In,Ga)Se_2 solar cells. *Applied Physics Letters*, 73(9):1224–1226, 1998.

[61] Steven S. Hegedus and William N. Shafarman. Thin-film solar cells: device measurements and analysis. *Progress in Photovoltaics: Research and Applications*, 12(23):155–176, 2004.

[62] Xinya Xu, Yongtao Qu, Vincent Barrioz, Guillaume Zoppi, and Neil S. Beattie. Reducing series resistance in $Cu_2ZnSn(S,Se)_4$ nanoparticle ink solar cells on flexible molybdenum foil substrates. *RSC Advances*, 8(7):3470–3476, 2018.

[63] K. Wang, O. Gunawan, T. Todorov, B. Shin, S. J. Chey, N. A. Bojarczuk, D. Mitzi, and S. Guha. Thermally evaporated Cu_2ZnSnS_4 solar cells. *Applied Physics Letters*, 97(14):143508, 2010.

[64] Tayfun Gokmen, Oki Gunawan, and David B. Mitzi. Minority carrier diffusion length extraction in $Cu_2ZnSn(Se,S)_4$ solar cells. *Journal of Applied Physics*, 114(11):114511, 2013.

[65] Stener Lie, Joel Ming Rui Tan, Wenjie Li, Shin Woei Leow, Ying Fan Tay, Douglas M. Bishop, Oki Gunawan, and Lydia Helena Wong. Reducing the interfacial defect density of CZTSSe solar cells by Mn substitution. *Journal of Materials Chemistry A*, 6(4):1540–1550, 2018.

[66] JinWoo Lee, J. David Cohen, and William N. Shafarman. The determination of carrier mobilities in CIGS photovoltaic devices using high-frequency admittance measurements. *Thin Solid Films*, 480-481:336–340, 2005.

[67] Ingrid Repins, Carolyn Beall, Nirav Vora, Clay DeHart, Darius Kuciauskas, Pat Dippo, Bobby To, Jonathan Mann, Wan-Ching Hsu, and Alan et al. Goodrich. Co-evaporated $Cu_2ZnSnSe_4$ films and devices. *Solar Energy Materials and Solar Cells*, 101:154–159, 2012.

[68] Akihiro Nagoya, Ryoji Asahi, Roman Wahl, and Georg Kresse. Defect formation and phase stability of Cu_2ZnSnS_4 photovoltaic material. *Physical Review B*, 81(11), 2010.

[69] A. D. Collord, H. Xin, and H. W. Hillhouse. Combinatorial Exploration of the Effects of Intrinsic and Extrinsic Defects in $Cu_2ZnSn(S,Se)_4$. *IEEE Journal of Photovoltaics*, 5(1):288–298, 2015.

[70] Andrew Fairbrother, Mirjana Dimitrievska, Yudania Sánchez, Victor Izquierdo-Roca, Alejandro Pérez-Rodriguez, and Edgardo Saucedo. Compositional paradigms in multinary compound systems for photovoltaic applications: a case study of kesterites. *Journal of Materials Chemistry A*, 3(18):9451–9455, 2015.

[71] Shiyou Chen, X. G. Gong, Aron Walsh, and Su-Huai Wei. Defect physics of the kesterite thin-film solar cell absorber Cu_2ZnSnS_4. *Applied Physics Letters*, 96(2):021902, 2010.

[72] Shiyou Chen, Ji-Hui Yang, X. G. Gong, Aron Walsh, and Su-Huai Wei. Intrinsic point defects and complexes in the quaternary kesterite semiconductor Cu_2ZnSnS_4. *Physical Review B*, 81(24), 2010.

[73] Junwen Li, David B. Mitzi, and Vivek B. Shenoy. Structure and Electronic Properties of Grain Boundaries in Earth-Abundant Photovoltaic Absorber $Cu_2ZnSnSe_4$. *ACS Nano*, 5(11):8613–8619, 2011.

[74] Joel B. Li, Vardaan Chawla, and Bruce M. Clemens. Investigating the Role of Grain Boundaries in CZTS and CZTSSe Thin Film Solar Cells with Scanning Probe Microscopy. *Advanced Materials*, 24(6):720–723, 2012.

[75] Gee Yeong Kim, Ah Reum Jeong, Ju Ri Kim, William Jo, Dae-Ho Son, Dae-Hwan Kim, and Jin-Kyu Kang. Surface potential on grain boundaries and intragrains of highly efficient $Cu_2ZnSn(S,Se)_4$ thin-films grown by two-step sputtering process. *Solar Energy Materials and Solar Cells*, 127:129–135, 2014.

[76] S. Campbell, Y. Qu, L. Bowen, P. Chapon, V. Barrioz, N.S. Beattie, and G. Zoppi. Influence of OLA and FA ligands on the optical and electronic properties of $Cu_2ZnSn(S,Se)_4$ thin films and solar cells prepared from nanoparticle inks. *Solar Energy*, 2018.

[77] Jonathan J. S. Scragg, Jes K. Larsen, Mukesh Kumar, Clas Persson, Jan Sendler, Susanne Siebentritt, and Charlotte Platzer Björkman. Cu-Zn disorder and band gap fluctuations in $Cu_2ZnSn(S,Se)_4$ Theoretical and experimental investigations. *Physica Status Solidi (b)*, 253(2):247–254, 2015.

[78] D. P. Halliday, R. Claridge, M. C. J. Goodman, B. G. Mendis, K. Durose, and J. D. Major. Luminescence of $Cu_2ZnSnS4$ polycrystals described by the fluctuating potential model. *Journal of Applied Physics*, 113(22):223503, 2013.

[79] John K. Katahara and Hugh W. Hillhouse. Quasi-Fermi level splitting and sub-bandgap absorptivity from semiconductor photoluminescence. *Journal of Applied Physics*, 116(17):173504, 2014.

[80] Andrea Crovetto and Ole Hansen. What is the band alignment of $Cu_2ZnSn(S,Se)_4$ solar cells? *Solar Energy Materials and Solar Cells*, 169:177–194, 2017.

[81] Tao Song, Ana Kanevce, and James R. Sites. Emitter/absorber interface of CdTe solar cells. *Journal of Applied Physics*, 119(23):233104, 2016.

[82] R. Scheer. Activation energy of heterojunction diode currents in the limit of interface recombination. *Journal of Applied Physics*, 105(10):104505, 2009.

[83] K. C Mills and K. C Mills. *Thermodynamic data for inorganic sulphides, selenides and tellurides*. Butterworths, 1974.

[84] Jörn Timo Wätjen, Jessica Engman, Marika Edoff, and Charlotte Platzer Björkman. Direct evidence of current blocking by ZnSe in $Cu_2ZnSnSe_4$ solar cells. *Applied Physics Letters*, 100(17):173510, 2012.

[85] Rabie Djemour, Marina Mousel, Alex Redinger, Levent G$\breve{\text{u}}$tay, Alexandre Crossay, Diego Colombara, Phillip J. Dale, and Susanne Siebentritt. Detecting ZnSe secondary phase in $Cu_2ZnSnSe_4$ by room temperature photoluminescence. *Applied Physics Letters*, 102(22):222108, 2013.

[86] Haibing Xie, Yudania Sánchez, Simón López-Marino, Moisés Espíndola-Rodriguez, Markus Neuschitzer, Diouldé Sylla, Andrew Fairbrother, Victor Izquierdo-Roca, Alejandro Pérez-Rodriguez, and Edgardo Saucedo. Impact of Sn(S,Se) Secondary Phases in $Cu_2ZnSn(S,Se)_4$ Solar Cells: a Chemical Route for Their Selective Removal and Absorber Surface Passivation. *ACS Applied Materials & Interfaces*, 6(15):12744–12751, 2014.

[87] T. Schwarz, O. Cojocaru-Mirédin, P. Choi, M. Mousel, A. Redinger, S. Siebentritt, and D. Raabe. Atom probe study of $Cu_2ZnSnSe_4$ thin-films prepared by co-evaporation and post-deposition annealing. *Applied Physics Letters*, 102(4):042101, 2013.

[88] Shiyou Chen, Aron Walsh, Ji-Hui Yang, X. G. Gong, Lin Sun, Ping-Xiong Yang, Jun-Hao Chu, and Su-Huai Wei. Compositional dependence of structural and electronic properties of $Cu_2ZnSn(S,Se)_4$ alloys for thin film solar cells. *Physical Review B*, 83(12):125201, 2011.

[89] V. Nadenau, U. Rau, A. Jasenek, and H. W. Schock. Electronic properties of $CuGaSe_2$-based heterojunction solar cells. Part i. Transport analysis. *Journal of Applied Physics*, 87(1):584–593, 2000.

[90] Tang Jiao Huang, Xuesong Yin, Chunhua Tang, Guojun Qi, and Hao Gong. A low-cost, ligand exchange-free strategy to synthesize large-grained Cu_2ZnSnS_4 thin-films without a fine-grain underlayer from nanocrystals. *J. Mater. Chem. A*, 3(34):17788–17796, 2015.

[91] Yongtao Qu, Guillaume Zoppi, and Neil S. Beattie. Selenization kinetics in $Cu_2ZnSn(S,Se)_4$ solar cells prepared from nanoparticle inks. *Solar Energy Materials and Solar Cells*, 158:130–137, 2016.

[92] Jonathan J. Scragg, J. Timo Wätjen, Marika Edoff, Tove Ericson, Tomas Kubart, and Charlotte Platzer Björkman. A Detrimental Reaction at the Molybdenum Back Contact in $Cu_2ZnSn(S,Se)_4$ Thin-Film Solar Cells. *Journal of the American Chemical Society*, 134(47):19330–19333, 2012.

[93] Byungha Shin, Nestor A. Bojarczuk, and Supratik Guha. On the kinetics of $MoSe_2$ interfacial layer formation in chalcogen-based thin film solar cells with a molybdenum back contact. *Applied Physics Letters*, 102(9):091907, 2013.

[94] Steven P. Harvey, Ingrid Repins, and Glenn Teeter. Defect chemistry and chalcogen diffusion in thin-film $Cu_2ZnSnSe_4$ materials. *Journal of Applied Physics*, 117(7):074902, 2015.

[95] Feng Jiang, Chigusa Ozaki, Gunawan, Takashi Harada, Zeguo Tang, Takashi Minemoto, Yoshitaro Nose, and Shigeru Ikeda. Effect of Indium Doping on Surface Optoelectrical Properties of Cu_2ZnSnS_4 Photoabsorber and Interfacial/Photovoltaic Performance of Cadmium Free In_2S_3/Cu_2ZnSnS_4 Heterojunction Thin Film Solar Cell. *Chemistry of Materials*, 28(10):3283–3291, 2016.

[96] D Hariskos, M Ruckh, U Ruhle, T Walter, H Schock, J Hedstrom, and L Sstolt. A novel cadmium free buffer layer for Cu(In,Ga)Se_2 based solar cells. *Solar Energy Materials and Solar Cells*, 41-42:345–353, 1996.

[97] A P Levanyuk and V V Osipov. Edge luminescence of direct-gap semiconductors. *Soviet Physics Uspekhi*, 24(3):187–215, 1981.

[98] Boris Ionovich Shklovskij and Aleksej L Efros. *Electronic properties of doped semiconductors*. Springer, 1984.

[99] I. Dirnstorfer, Mt. Wagner, D.M. Hofmann, M.D. Lampert, F. Karg, and B.K. Meyer. Characterization of CuIn(Ga)Se_2 thin films. *Physica Status Solidi (a)*, 168(1):163–175, 1998.

[100] L. H. Thomas. The calculation of atomic fields. *Mathematical Proceedings of the Cambridge Philosophical Society*, 23(5):542–548, 1927.

[101] S. Siebentritt, N. Papathanasiou, and M.Ch. Lux-Steiner. Potential fluctuations in compensated chalcopyrites. *Physica B: Condensed Matter*, 376-377:831–833, 2006.

[102] Phil Won Yu. Excitation-dependent emission in Mg-, Be-, Cd-, and Zn-implanted GaAs. *Journal of Applied Physics*, 48(12):5043–5051, 1977.

[103] S. A. Schumacher, J. R. Botha, and V. Alberts. Photoluminescence study of potential fluctuations in thin layers of Cu($In_{0.75}Ga_{0.25}$)(S_ySe_{1-y})$_2$. *Journal of Applied Physics*, 99(6):063508, 2006.

[104] Talia Gershon, Byungha Shin, Nestor Bojarczuk, Tayfun Gokmen, Siyuan Lu, and Supratik

Guha. Photoluminescence characterization of a high-efficiency Cu_2ZnSnS_4 device. *Journal of Applied Physics*, 114(15):154905, 2013.

[105] Kong Fai Tai, Talia Gershon, Oki Gunawan, and Cheng Hon Alfred Huan. Examination of electronic structure differences between CIGSSe and CZTSSe by photoluminescence study. *Journal of Applied Physics*, 117(23):235701, 2015.

[106] Jüri Krustok, Heikki Collan, and Kari Hjelt. Does the low-temperature Arrhenius plot of the photoluminescence intensity in CdTe point towards an erroneous activation energy? *Journal of Applied Physics*, 81(3):1442–1445, 1997.

[107] F. Luckert, D. I. Hamilton, M. V. Yakushev, N. S. Beattie, G. Zoppi, M. Moynihan, I. Forbes, A. V. Karotki, A. V. Mudryi, and M. Grossberg. Optical properties of high quality $Cu_2ZnSnSe_4$ thin films. *Applied Physics Letters*, 99(6):062104, 2011.

[108] J. Krustok, H. Collan, M. Yakushev, and K. Hjelt. The role of spatial potential fluctuations in the shape of the PL bands of multinary semiconductor compounds. *Physica Scripta*, T79(1):179, 1999.

[109] Wyatt K. Metzger, Ingrid L. Repins, and Miguel A. Contreras. Long lifetimes in high-efficiency $Cu(In,Ga)Se_2$ solar cells. *Applied Physics Letters*, 93(2):022110, 2008.

[110] J. Tauc, R. Grigorovici, and A. Vancu. Optical properties and electronic structure of amorphous germanium. *Physica Status Solidi (b)*, 15(2):627–637, 1966.

[111] Franz Urbach. The long-wavelength edge of photographic sensitivity and of the electronic absorption of solids. *Physical Review*, 92(5):1324–1324, 1953.

[112] Julian Mattheis, Uwe Rau, and Jürgen H. Werner. Light absorption and emission in semiconductors with band gap fluctuations-a study on $Cu(In,Ga)Se_2$ thin films. *Journal of Applied Physics*, 101(11):113519, 2007.

[113] X. X. Liu and J. R. Sites. Solar-cell collection efficiency and its variation with voltage. *Journal of Applied Physics*, 75(1):577–581, 1994.

[114] J B Pendry. Theory of inverse photoemission. *Journal of Physics C: Solid State Physics*, 14(9):1381–1391, 1981.

[115] D. P. Woodruff, P. D. Johnson, and N. V. Smith. Inverse photoemission. *Journal of Vacuum Science & Technology A: Vacuum, Surfaces, and Films*, 1(2):1104–1110, 1983.

[116] Paul Whiteside, Jeffrey Chininis, and Heather Hunt. Techniques and challenges for characterizing metal thin films with applications in photonics. *Coatings*, 6(3):35, 2016.

[117] Joseph Goldstein, Dale E Newbury, Joseph R Michael, Nicholas W. M Ritchie, John Henry J Scott, and David C Joy. *Scanning electron microscopy and x-ray microanalysis*. Springer, 3 edition, 2003.

[118] W. Grimm. Eine neue glimmentladungslampe für die optische emissionsspektralanalyse. *Spectrochimica Acta Part B: Atomic Spectroscopy*, 23(7):443 – 454, 1968.

[119] J.R. Sites and P.H. Mauk. Diode quality factor determination for thin-film solar cells. *Solar Cells*, 27(1-4):411–417, 1989.

[120] O. Vigil-Galán, A. Arias-Carbajal, R. Mendoza-Pérez, G. Santana, J. Sastré-Hernández, G. Contreras-Puente, A. Morales-Acevedo, and M. Tufiño Velázquez. Spectral response of CdS/CdTe solar cells obtained with different S/Cd ratios for the CdS chemical bath. *Solar Energy Materials and Solar Cells*, 90(15):2221–2227, 2006.

[121] Maykel Courel, E. Valencia-Resendiz, F.A. Pulgarń-Agudelo, and O. Vigil-Galń. Determination of minority carrier diffusion length of sprayed-Cu_2ZnSnS_4 thin films. *Solid-State Electronics*, 118:1–3, 2016.

[122] Vikram L. Dalal and Allen Rothwarf. Comment on "A simple measurement of absolute solar cell efficiency". *Journal of Applied Physics*, 50(4):2980–2981, 1979.

[123] S. Weiss and R. Kassing. Deep Level Transient Fourier Spectroscopy (DLTFS) A technique for the analysis of deep level properties. *Solid-State Electronics*, 31(12):1733–1742, 1988.

[124] Moonsang Lee, Thi Kim Oanh Vu, Kyoung Su Lee, Eun Kyu Kim, and Sungsoo Park. Electronic states of deep trap levels in a-plane gan templates grown on r-plane sapphire by hvpe. *Scientific Reports*, 8(1), 2018.

[125] Wei Wang, Honglie Shen, Lydia Helena Wong, Zhenghua Su, Hanyu Yao, and Yufang Li.

A 4.92% efficiency Cu_2ZnSnS_4 solar cell from nanoparticle ink and molecular solution. *RSC Advances*, 6(59):54049–54053, 2016.

[126] Tang Jiao Huang, Xuesong Yin, Chunhua Tang, Guojun Qi, and Hao Gong. Influence of Ligands on the Formation of Kesterite Thin Films for Solar Cells: A Comparative Study. *ChemSusChem*, 9(9):1032–1041, 2016.

[127] Yanyan Cao, Michael S. Denny, Jonathan V. Caspar, William E. Farneth, Qijie Guo, Alex S. Ionkin, Lynda K. Johnson, Meijun Lu, Irina Malajovich, and Daniela Radu. High-Efficiency Solution-Processed $Cu_2ZnSn(S,Se)_4$ Thin-Film Solar Cells Prepared from Binary and Ternary Nanoparticles. *Journal of the American Chemical Society*, 134(38):15644–15647, 2012.

[128] Yongtao Qu, Guillaume Zoppi, and Neil S. Beattie. The role of nanoparticle inks in determining the performance of solution processed $Cu_2ZnSn(S,Se)_4$ thin film solar cells. *Progress in Photovoltaics: Research and Applications*, 24(6):836–845, 2016.

[129] T. Schmidt, K. Lischka, and W. Zulehner. Excitation-power dependence of the near-band-edge photoluminescence of semiconductors. *Physical Review B*, 45(16):8989–8994, 1992.

[130] S. Levcenko, J. Just, A. Redinger, G. Larramona, S. Bourdais, G. Dennler, A. Jacob, and T. Unold. Deep defects in$Cu_2ZnSn(S,Se)_4$ Solar Cells with Varying Se Content. *Physical Review Applied*, 5(2), 2016.

[131] M.V. Yakushev, M.A. Sulimov, J. Márquez-Prieto, I. Forbes, J. Krustok, P.R. Edwards, V.D. Zhivulko, O.M. Borodavchenko, A.V. Mudryi, and R.W. Martin. Influence of the copper content on the optical properties of CZTSe thin films. *Solar Energy Materials and Solar Cells*, 168:69–77, 2017.

[132] Oki Gunawan, Tayfun Gokmen, Charles W. Warren, J. David Cohen, Teodor K. Todorov, D. Aaron R. Barkhouse, Santanu Bag, Jiang Tang, Byungha Shin, and David B. Mitzi. Electronic properties of the $Cu_2ZnSn(Se,S)_4$ absorber layer in solar cells as revealed by admittance spectroscopy and related methods. *Applied Physics Letters*, 100(25):253905, 2012.

[133] Xianzhong Lin, Ahmed Ennaoui, Sergiu Levcenko, Thomas Dittrich, Jaison Kavalakkatt, Steffen Kretzschmar, Thomas Unold, and Martha Ch. Lux-Steiner. Defect study of $Cu_2ZnSn(S_xSe_{1-x})_4$ thin film absorbers using photoluminescence and modulated surface photovoltage spectroscopy. *Applied Physics Letters*, 106(1):013903, 2015.

[134] D. O. Toginho Filho, I. F. L. Dias, E. Laureto, J. L. Duarte, S. A. Lourenço, L. C. Poças, S. S. Prabhu, and J. Klem. Quasi-donor-acceptor pair transitions in GaAsSb and AlGaAsSb on InP. *Journal of Applied Physics*, 97(12):123702, 2005.

[135] R. Bacewicz, P. Żuk, and R. Trykozko. Photoluminescence study of ZnO/CdS/Cu(In,Ga)Se_2 solar cells. *Opto - Electronics Review*, Vol. 11, No. 4:277–280, 2003.

[136] Souhaib Oueslati, Guy Brammertz, Marie Buffière, Christine Köble, Touayar Oualid, Marc Meuris, and Jef Poortmans. Photoluminescence study and observation of unusual optical transitions in $Cu_2ZnSnSe_4$/CdS/ZnO solar cells. *Solar Energy Materials and Solar Cells*, 134:340–345, 2015.

[137] B.E. McCandless, J.E. Phillips, and J. Titus. *Characterizing contacts to p-type CdTe in CdS/CdTe solar cells*, pages 448–452. 1998.

[138] U. Rau. Tunneling-enhanced recombination in Cu(In,Ga)Se_2 heterojunction solar cells. *Applied Physics Letters*, 74(1):111–113, 1999.

[139] T. Walter, R. Herberholz, C. Müller, and H. W. Schock. Defect Distribution and Metastability in Chalcopyrite Semiconductors. *MRS Proceedings*, 426, 1996.

[140] Maykel Courel, E. Valencia-Resendiz, J.A. Andrade-Arvizu, E. Saucedo, and O. Vigil-Galán. Towards understanding poor performances in spray-deposited Cu_2ZnSnS_4 thin film solar cells. *Solar Energy Materials and Solar Cells*, 159:151–158, 2017.

[141] G.A.M. Hurkx, D.B.M. Klaassen, and M.P.G. Knuvers. A new recombination model for device simulation including tunneling. *IEEE Transactions on Electron Devices*, 39(2):331–338, 1992.

[142] Charles J. Hages, Nathaniel J. Carter, Rakesh Agrawal, and Thomas Unold. Generalized current-voltage analysis and efficiency limitations in non-ideal solar cells: Case

of $Cu_2ZnSn(S_xSe_{1-x})_4$ and $Cu_2Zn(Sn_yGe_{1-y})(S_xSe_{1-x})_4$. *Journal of Applied Physics*, 115(23):234504, 2014.

[143] B G Mendis, M D Shannon, M C J Goodman, J D Major, A A Taylor, D P Halliday, and K Durose. The nature of electrostatic potential fluctuations in Cu_2ZnSnS_4 and their role on photovoltaic device performance. *Journal of Physics: Conference Series*, 471:012014, 2013.

[144] Seung Min Lee, Bhaskar Chandra Mohanty, Yeon Hwa Jo, Deuk Ho Yeon, and Yong Soo Cho. Phase development, microstructure and optical properties of $Cu_2ZnSnSe_4$ thin films modified with Pb and Ti. *Surface and Coatings Technology*, 231:389–393, 2013.

[145] Guohua Zhong, Kinfai Tse, Yiou Zhang, Xiaoguang Li, Li Huang, Chunlei Yang, Junyi Zhu, Zhi Zeng, Zhenyu Zhang, and Xudong Xiao. Induced effects by the substitution of Zn in Cu_2ZnSnX_4 (X = S and Se). *Thin Solid Films*, 603:224–229, 2016.

[146] A. Bauknecht, S. Siebentritt, J. Albert, and M. Ch. Lux-Steiner. Radiative recombination via intrinsic defects in $Cu_xGa_ySe_2$. *Journal of Applied Physics*, 89(8):4391–4400, 2001.

[147] Susan Schorr. The crystal structure of kesterite type compounds A neutron and X-ray diffraction study. *Solar Energy Materials and Solar Cells*, 95(6):1482–1488, 2011.

[148] Léo Choubrac, Michaël Paris, Alain Lafond, Catherine Guillot-Deudon, Xavier Rocquefelte, and Stéphane Jobic. Multinuclear (^{67}Zn, ^{119}Sn and ^{65}Cu) NMR spectroscopy an ideal technique to probe the cationic ordering in Cu_2ZnSnS_4 photovoltaic materials. *Physical Chemistry Chemical Physics*, 15(26):10722, 2013.

[149] Michaël Paris, Léo Choubrac, Alain Lafond, Catherine Guillot-Deudon, and Stéphane Jobic. Solid-State NMR and Raman Spectroscopy to Address the Local Structure of Defects and the Tricky Issue of the Cu-Zn Disorder in Cu-Poor, Zn-Rich CZTS Materials. *Inorganic Chemistry*, 53(16):8646–8653, 2014.

[150] M.V. Yakushev, I. Forbes, A.V. Mudryi, M. Grossberg, J. Krustok, N.S. Beattie, M. Moynihan, A. Rockett, and R.W. Martin. Optical spectroscopy studies of $Cu_2ZnSnSe_4$ thin films. *Thin Solid Films*, 582:154–157, 2015.

[151] Talia Gershon, Byungha Shin, Tayfun Gokmen, Siyuan Lu, Nestor Bojarczuk, and Supratik Guha. Relationship between Cu_2ZnSnS_4 quasi donor-acceptor pair density and solar cell efficiency. *Applied Physics Letters*, 103(19):193903, 2013.

[152] M. Grossberg, T. Raadik, J. Raudoja, and J. Krustok. Photoluminescence study of defect clusters in Cu_2ZnSnS_4 polycrystals. *Current Applied Physics*, 14(3):447–450, 2014.

[153] Prashant K. Sarswat and Michael L. Free. A study of energy band gap versus temperature for Cu_2ZnSnS_4 thin films. *Physica B: Condensed Matter*, 407(1):108–111, 2012.

[154] Y.P. Varshni. Temperature dependence of the energy gap in semiconductors. *Physica*, 34(1):149–154, 1967.

[155] M. Grossberg, J. Krustok, J. Raudoja, and T. Raadik. The role of structural properties on deep defect states in Cu_2ZnSnS_4 studied by photoluminescence spectroscopy. *Applied Physics Letters*, 101(10):102102, 2012.

[156] Taavi Raadik, Jüri Krustok, M. Kauk-Kuusik, K. Timmo, M. Grossberg, K. Ernits, and J. Bleuse. Low temperature time resolved photoluminescence in ordered and disordered Cu_2ZnSnS_4 single crystals. *Physica B: Condensed Matter*, 508:47–50, 2017.

[157] L. Dobaczewski, A. R. Peaker, and K. Bonde Nielsen. Laplace-transform deep-level spectroscopy: The technique and its applications to the study of point defects in semiconductors. *Journal of Applied Physics*, 96(9):4689–4728, 2004.

[158] Yongtao Qu, Guillaume Zoppi, Laurence M. Peter, Sophie Jourdain, and Neil S. Beattie. Enhanced external quantum efficiency from $Cu_2ZnSn(S,Se)_4$ solar cells prepared from nanoparticle inks. *Japanese Journal of Applied Physics*, 57(8S3):08RC01, 2018.

[159] M. Ganchev, J. Iljina, L. Kaupmees, T. Raadik, O. Volobujeva, A. Mere, M. Altosaar, J. Raudoja, and E. Mellikov. Phase composition of selenized $Cu_2ZnSnSe_4$ thin films determined by X-ray diffraction and Raman spectroscopy. *Thin Solid Films*, 519(21):7394–7398, 2011.

[160] Richard Haight, Xiaoyan Shao, Wei Wang, and David B. Mitzi. Electronic and elemental properties of the $Cu_2ZnSn(S,Se_4$ surface and grain boundaries. *Applied Physics Letters*, 104(3):033902, 2014.

[161] G. Rey, A. Redinger, J. Sendler, T. P. Weiss, M. Thevenin, M. Guennou, B. El Adib, and S. Siebentritt. The band gap of $Cu_2ZnSnSe_4$: Effect of order-disorder. *Applied Physics Letters*, 105(11):112106, 2014.

[162] G. Rey, G. Larramona, S. Bourdais, C. Choné, B. Delatouche, A. Jacob, G. Dennler, and S. Siebentritt. On the origin of band-tails in kesterite. *Solar Energy Materials and Solar Cells*, 179:142–151, 2018.

[163] Alain Lafond, Léo Choubrac, Catherine Guillot-Deudon, Philippe Deniard, and Stephane Jobic. Crystal Structures of Photovoltaic Chalcogenides, an Intricate Puzzle to Solve: the Cases of CIGSe and CZTS materials. *Zeitschrift für anorganische und allgemeine Chemie*, 638(15):2571–2577, 2012.

[164] G. Gurieva, M. Dimitrievska, S. Zander, A. Pérez-Rodriguez, V. Izquierdo-Roca, and S. Schorr. Structural characterisation of $Cu_{2.04}Zn_{0.91}Sn_{1.05}S_{2.08}Se_{1.92}$. *Physica Status Solidi (c)*, 12(6):588–591, 2015.

[165] Philip Jackson, Roland Wuerz, Dimitrios Hariskos, Erwin Lotter, Wolfram Witte, and Michael Powalla. Effects of heavy alkali elements in $Cu(In,Ga)Se_2$ solar cells with efficiencies up to 22.6%. *Physica Status Solidi (RRL) - Rapid Research Letters*, 10(8):583–586, 2016.

[166] Douglas M. Bishop, Brian McCandless, Talia Gershon, Michael A. Lloyd, Richard Haight, and Robert Birkmire. Modification of defects and potential fluctuations in slow-cooled and quenched $Cu_2ZnSn(S,Se)_4$ single crystals. *Journal of Applied Physics*, 121(6):065704, 2017.

[167] D. Aaron R. Barkhouse, Oki Gunawan, Tayfun Gokmen, Teodor K. Todorov, and David B. Mitzi. Device characteristics of a 10.1% hydrazine-processed $Cu_2ZnSn(Se,S)_4$ solar cell. *Progress in Photovoltaics: Research and Applications*, 20(1):6–11, 2011.

[168] M. Bär, B.-A. Schubert, B. Marsen, R. G. Wilks, S. Pookpanratana, M. Blum, S. Krause, T. Unold, W. Yang, and L. et al. Weinhardt. Cliff-like conduction band offset and kcn-induced recombination barrier enhancement at the $CdS/Cu_2ZnSn(S,Se)_4$ thin-film solar cell heterojunction. *Applied Physics Letters*, 99(22):222105, 2011.

[169] M.G. Sandoval-Paz, M. Sotelo-Lerma, J.J. Valenzuela-Jáuregui, M. Flores-Acosta, and R. Ramiírez-Bon. Structural and optical studies on thermal-annealed In_2S_3 films prepared by the chemical bath deposition technique. *Thin Solid Films*, 472(1-2):5–10, 2005.

[170] D. Aaron R. Barkhouse, Richard Haight, Noriyuki Sakai, Homare Hiroi, Hiroki Sugimoto, and David B. Mitzi. Cd-free buffer layer materials on $Cu_2ZnSn(S_xSe_{1-x})_4$: Band alignments with ZnO, ZnS, and In_2S_3. *Applied Physics Letters*, 100(19):193904, 2012.

[171] Jeehwan Kim, Homare Hiroi, Teodor K. Todorov, Oki Gunawan, Masaru Kuwahara, Tayfun Gokmen, Dhruv Nair, Marinus Hopstaken, Byungha Shin, and Yun Seog et al. Lee. High Efficiency $Cu_2ZnSn(S,Se)_4$ Solar Cells by Applying a Double In_2S_3/CdS Emitter. *Advanced Materials*, 26(44):7427–7431, 2014.

[172] Andrii Omelianovych, Ji Hye Kim, Larina Liudmila, and Byung Tae Ahn. Effect of post annealing on the characteristics of In_2S_3 buffer layer grown by chemical bath deposition on a CIGS substrate. *Current Applied Physics*, 15(12):1641–1649, 2015.

[173] E. A. Kraut, R. W. Grant, J. R. Waldrop, and S. P. Kowalczyk. Precise determination of the valence-band edge in x-ray photoemission spectra: Application to measurement of semiconductor interface potentials. *Physical Review Letters*, 44(24):1620–1623, 1980.

[174] K. Sawangsri, P. Das, S.N. Supardan, I.Z. Mitrovic, S. Hall, R. Mahapatra, A.K. Chakraborty, R. Treharne, J. Gibbon, and V.R. Dhanak. Experimental band alignment of Ta_2O_5/GaN for MIS-HEMT applications. *Microelectronic Engineering*, 178:178–181, 2017.

[175] J. T. Gibbon, L. Jones, J. W. Roberts, M. Althobaiti, P. R. Chalker, Ivona Z. Mitrovic, and V. R. Dhanak. Band alignments at Ga_2O_3 heterojunction interfaces with Si and Ge. *AIP Advances*, 8(6):065011, 2018.

[176] Hui-Ju Chen, Sheng-Wen Fu, Shih-Hsiung Wu, Tsung-Chieh Tsai, Hsuan-Ta Wu, and Chuan-Feng Shih. Structural and photoelectron spectroscopic studies of band alignment at the Cu_2ZnSnS_4/CdS heterojunction with slight Ni doping in Cu_2ZnSnS_4. *Journal of Physics D: Applied Physics*, 49(33):335102, 2016.

[177] A Santoni, F Biccari, C Malerba, M Valentini, R Chierchia, and A Mittiga. Valence band offset at the CdS/Cu_2ZnSnS_4 interface probed by x-ray photoelectron spectroscopy. *Journal of Physics D: Applied Physics*, 46(17):175101, 2013.

[178] Mattias L. N. Palsgaard, Andrea Crovetto, Tue Gunst, Troels Markussen, Ole Hansen, Kurt Stokbro, and Mads Brandbyge. Semiconductor band alignment from first principles: A new nonequilibrium Green's function method applied to the CZTSe/CdS interface for photovoltaics. *2016 International Conference on Simulation of Semiconductor Processes and Devices (SISPAD)*, 2016.

[179] Takashi Minemoto, Takuya Matsui, Hideyuki Takakura, Yoshihiro Hamakawa, Takayuki Negami, Yasuhiro Hashimoto, Takeshi Uenoyama, and Masatoshi Kitagawa. Theoretical analysis of the effect of conduction band offset of window/CIS layers on performance of CIS solar cells using device simulation. *Solar Energy Materials and Solar Cells*, 67(1-4):83–88, 2001.

[180] M. Gloeckler and J.R. Sites. Efficiency limitations for wide-band-gap chalcopyrite solar cells. *Thin Solid Films*, 480-481:241–245, 2005.

[181] Peter Y Yu and Manuel Cardona. *Fundamentals of semiconductors*. Springer, 2005.

[182] Eliam Zacks and A. Halperin. Dependence of the peak energy of the pair-photoluminescence band on excitation intensity. *Phys. Rev. B*, 6:3072–3075, Oct 1972.

[183] Chang Yan, Jialiang Huang, Kaiwen Sun, Steve Johnston, Yuanfang Zhang, Heng Sun, Aobo Pu, Mingrui He, Fangyang Liu, and Katja et al. Eder. Cu_2ZnSnS_4 solar cells with over 10% power conversion efficiency enabled by heterojunction heat treatment. *Nature Energy*, 3(9):764–772, 2018.

[184] M.G. Sousa, A.F. da Cunha, J.P. Teixeira, J.P. Leitão, G. Otero-Irurueta, and M.K. Singh. Optimization of post-deposition annealing in Cu_2ZnSnS_4 thin film solar cells and its impact on device performance. *Solar Energy Materials and Solar Cells*, 170:287–294, 2017.

[185] Dong-Hau Kuo and Moges Tsega. Electrical conduction and mobility enhancement in *p*-type In-doped $Cu_2ZnSnSe_4$ bulks. *Japanese Journal of Applied Physics*, 53(3):035801, 2014.

[186] Yingli Pei, Jing Guo, Dongxing Kou, Wenhui Zhou, Zhengji Zhou, Qingwen Tian, Yuena Meng, and Sixin Wu. Precise-tuning the In content to achieve high fill factor in hybrid buffer structured $Cu_2ZnSn(S,Se)_4$ solar cells. *Solar Energy*, 148:157–163, 2017.

[187] M. Pilvet, M. Kauk-Kuusik, M. Altosaar, M. Grossberg, M. Danilson, K. Timmo, A. Mere, and V. Mikli. Compositionally tunable structure and optical properties of $Cu_{1.85}$ $(Cd_xZn_{1-x})_{1.1}SnS_{4.1}$ (0 = x = 1) monograin powders. *Thin Solid Films*, 582:180–183, 2015.

[188] Markus Neuschitzer, Moises Espindola Rodriguez, Maxim Guc, Jose A. Marquez, Sergio Giraldo, Ian Forbes, Alejandro Perez-Rodriguez, and Edgardo Saucedo. Revealing the beneficial effects of Ge doping on $Cu_2ZnSnSe_4$ thin film solar cells. *Journal of Materials Chemistry A*, 6(25):11759–11772, 2018.

[189] Shoushuai Gao, Yi Zhang, Jianping Ao, Xiuling Li, Shuang Qiao, Ying Wang, Shuping Lin, Zhaojing Zhang, Dongxiao Wang, and Zhiqiang et al. Zhou. Insight into the role of post-annealing in air for high efficient $Cu_2ZnSn(S,Se)_4$ solar cells. *Solar Energy Materials and Solar Cells*, 182:228–236, 2018.

[190] Jüri Krustok, Taavi Raadik, Reelika Kaupmees, Maarja Grossberg, Marit Kauk-Kuusik, Kristi Timmo, and Arvo Mere. Observation of band gap fluctuations and carrier localization in $Cu_2CdGeSe_4$. *Journal of Physics D: Applied Physics*, 52(28):285102, 2019.

[191] Q Li, S. J Xu, M. H Xie, and S. Y Tong. A model for steady-state luminescence of localized-state ensemble. *Europhysics Letters (EPL)*, 71(6):994–1000, 2005.

[192] Huining Wang, Ziwu Ji, Shuang Qu, Gang Wang, Yongzhi Jiang, Baoli Liu, Xiangang Xu, and Hirofumi Mino. Influence of excitation power and temperature on photoluminescence in InGan/GaN multiple quantum wells. *Optics Express*, 20(4):3932, 2012.

[193] Petr G. Eliseev, Piotr Perlin, Jinhyun Lee, and Marek Osinski. Blue temperature-induced shift and band-tail emission in InGaN-based light sources. *Applied Physics Letters*, 71(5):569–571, 1997.

[194] M. Grossberg, T. Raadik, J. Krustok, M. Kauk-Kuusik, K. Timmo, R. Kaupmees, V. Mikli, and A. Mere. Optical and structural properties of orthorhombic and tetragonal polymorphs of $Cu_2CdGeSe_4$. *Thin Solid Films*, 666:44–47, 2018.

[195] Zhen-Kun Yuan, Shiyou Chen, Hongjun Xiang, Xin-Gao Gong, Aron Walsh, Ji-Sang Park, Ingrid Repins, and Su-Huai Wei. Engineering Solar Cell Absorbers by Exploring the Band Alignment and Defect Disparity: The Case of Cu- and Ag-based Kesterite Compounds. *Advanced Functional Materials*, 25(43):6733–6743, 2015.

[196] J. E. Moore, S. Dongaonkar, R. V. K. Chavali, M. A. Alam, and M. S. Lundstrom. Correlation of Built-In Potential and I–V Crossover in Thin-Film Solar Cells. *IEEE Journal of Photovoltaics*, 4(4):1138–1148, July 2014.

[197] U. Rau and H.W. Schock. Electronic properties of $Cu(In,Ga)Se_2$ heterojunction solar cells-recent achievements, current understanding, and future challenges. *Applied Physics A: Materials Science & Processing*, 69(2):131–147, 1999.

[198] Chang Yan, Fangyang Liu, Kaiwen Sun, Ning Song, John A. Stride, Fangzhou Zhou, Xiaojing Hao, and Martin Green. Boosting the efficiency of pure sulfide CZTS solar cells using the In/Cd-based hybrid buffers. *Solar Energy Materials and Solar Cells*, 144:700–706, 2016.

[199] Jonathan J. Scragg, Philip J. Dale, Laurence M. Peter, Guillaume Zoppi, and Ian Forbes. New routes to sustainable photovoltaics: evaluation of Cu_2ZnSnS_4 as an alternative absorber material. *physica status solidi (b)*, 245(9):1772–1778, 2008.

[200] R. Herberholz, M. Igalson, and H. W. Schock. Distinction between bulk and interface states in $CuInSe_2$ CdS ZnO by space charge spectroscopy. *Journal of Applied Physics*, 83(1):318–325, 1998.

[201] Ana Kanevce, Ingrid Repins, and Su-Huai Wei. Impact of bulk properties and local secondary phases on the $Cu_2(Zn,Sn)Se_4$ solar cells open-circuit voltage. *Solar Energy Materials and Solar Cells*, 133:119–125, 2015.

[202] Mehmet Eray Erkan, Vardaan Chawla, and Michael A. Scarpulla. Reduced defect density at the CZTSSe/CdS interface by atomic layer deposition of Al_2O_3. *Journal of Applied Physics*, 119(19):194504, 2016.

[203] Mohammad Istiaque Hossain, Puvaneswaran Chelvanathan, Mukter Zaman, M. R. Karim, M. A. Alghoul, and Nowshad Amin. Prospects of indium sulphide as an alternative to cad-

mium sulphide buffer layer in CIS based solar cells from numerical analysis. *Chalcogenide Letters*, 8(5):315–324, 2011.